Structural, Dielectric and Raman Spectroscopic Investigations of the composites of Alkaline Niobates ($NaNbO_3$, $KNbO_3$) and Mott-Insulators (NiO, MnO_2)

A Thesis Submitted to
Indian Institute of Technology Guwahati
for the degree of

Doctor of Philosophy

By

Robin T. George

Department of Physics
Indian Institute of Technology Guwahati
Guwahati-781039, Assam (India)

Dedicated to

My Father Mr. Thanjan Thoma George,

My Mother Mrs. Baby George,

My Wife Mrs. Maryjo M. George,

My Brother Robert and My Sister Rosemary.

INDIAN INSTITUTE OF TECHNOLOGY GUWAHATI

Department of Physics

Guwahati – 781039

Declaration

"*Structural, dielectric and Raman Spectroscopic investigations of the composites of alkaline niobates ($NaNbO_3$, $KNbO_3$) and Mott-Insulators (NiO, MnO_2)*" is the result of my own doctoral research work. This work was carried out under the supervision of Dr. Subhash Thota at the Department of Physics, Indian Institute of Technology Guwahati. To the best of my knowledge, the work presented in this thesis has not been submitted to any other Institute/University for the award of any degree.

Robin T. George
Research Scholar (Roll No: 146121015)
Department of Physics
Indian Institute of Technology Guwahati
Guwahati-781039, India

INDIAN INSTITUTE OF TECHNOLOGY GUWAHATI

Department of Physics

Guwahati – 781039

Certificate

It is certified that the work described in this thesis, entitled "*Structural, dielectric and Raman Spectroscopic investigations of the composites of alkaline niobates ($NaNbO_3$, $KNbO_3$) and Mott-Insulators (NiO, MnO_2)*", done by Mr. Robin T. George, a Ph.D. student of Department of Physics, Indian Institute of Technology Guwahati, for the award of degree of Doctor of Philosophy has been carried out under my supervision. This work has not been submitted elsewhere for the award of any degree.

Dr. Subhash Thota
Associate Professor
Department of Physics
Indian Institute of Technology Guwahati
Guwahati-781039, India

Synopsis

Owing to the toxicity, the commercially used lead and lead-based materials will be expelled from many commercial microelectronic applications. Therefore, lead-free ferroelectric (FE) and antiferroelectric (AFE) materials have attracted a lot of attention as they intrinsically couple mechanical and electrical degrees of freedom. Among many FE/AFE oxides that crystallize into perovskite structure (ABO_3), alkaline niobates ($ANbO_3$, A = Alkaline metals) and their composite have drawn immense attention due to their promising applications in modern-day electronics. Among these lead-free alkaline niobates, potassium niobate ($KNbO_3$) and sodium niobate ($NaNbO_3$) along with their composites has been widely investigated to replace the High-κ dielectrics. It is well-known fact that structural transitions are usually accompanied by a finite change in polarization of the system. Tuning such transitions either by doping with other elements or by mixing with binary transition-metal oxides is a typical approach employed by many researchers to enhance the overall physical properties of the system. Both the compounds $KNbO_3$ and $NaNbO_3$ are the two simplest lead-free perovskite systems that undergo several temperature and pressure-driven structural transitions in a wide temperature range 190-920K. Both these crystals vary from low symmetric rhombohedral to high-symmetry cubic structure with increasing temperature. The present research work has primarily motivated us to develop the two-phase composites comprising of $KNbO_3$ and $NaNbO_3$ with wide energy band-gap Mott insulators such as NiO and MnO.

Sodium Niobate comes under the class of AFE oxides which crystallizes into orthorhombic structure at room temperature. However, as the temperature increases from 30°C to 575°C, the crystal structure gradually changes from orthorhombic to tetragonal (with space group *P4/mbm*), and further changes to high symmetry cubic structure (space group *Pm3m*) above 630°C. Also, a series of intermediate phase transitions in $NaNbO_3$ without altering its orthorhombic structure reported in the literature. Two such transitions occur in $NaNbO_3$: the first transition takes place at 360°C where orthorhombic-P phase changes to orthorhombic-R phase without altering the AFE ordering, and the second one take place at 480°C (associated to the orthorhombic-R to S phase change) where the AFE domains collapse to disordered paraelectric (PE) state (T_{AFE}). Moreover, in the PE state, the system undergoes yet another transition from orthorhombic-S to T_1 at 520°C before transforming itself into a more symmetric tetragonal structure (orthorhombic-T_1 to tetragonal-T_2) at 575°C. In addition to these transitions, $NaNbO_3$ also undergoes a low-temperature transition (at 190K) from rhombohedral-N phase (phase group *R3c*) to orthorhombic-P phase. Few researchers also reported room temperature monoclinic phase in $NaNbO_3$. Neutron diffraction studies carried out on single-crystal $NaNbO_3$ reports the existence of monoclinic phase at room temperature and that orthorhombic crystal structure exists above 370°C with space group *Cmcm*. Using thermo-optical and photoelectron emission spectroscopic studies, it has been revealed that $NaNbO_3$ can also exhibit FE phase between 100K and 830K. Depending on the synthesis procedure, $NaNbO_3$ exhibits a wide

range of physical properties which is yet to be understood to a depth that this compound and its composites can be fully utilized on an industrial scale for different applications. On the other hand, its sister compound $KNbO_3$ belongs to the family of ferroelectric lead-free crystals which also predominantly crystalizes into orthorhombic crystal structure at room temperature with ferroelectric Curie Temperature as high as 430°C. Like in the case for $NaNbO_3$, $KNbO_3$ also undergoes a similar series of structural transitions rhombohedral → orthorhombic → tetragonal→ cubic. High density, high dielectric permittivity, mechanical strength and improved microstructure can be achieved in this compound by means of novel heat treatment conditions like microwave sintering, sintering aids and extra additives during the synthesis process. It was discovered that additives such as $LaFeO_3$, $BiFeO_3$ and MnO_2 improve the mechanical and electrical properties significantly. Using the liquid phase sintering method, high density (~ 95%), enhanced relative-dielectric permittivity (ε_r > 540), superior electromechanical coupling factor (k_p = 29%) and high piezoelectric coefficient (d_{33}= 109pC/N) have been accomplished. However, the main drawbacks of both these compounds are that they are moisture sensitive and exhibit less density. Although, there are numerous studies devoted to overcome such hygroscopic nature of these compounds, very little success is achieved till now. Therefore, in the current thesis, we focus on this issue as one of the main objectives of the research work. By incorporating the binary or ternary transition metal oxides with these lead-free niobates one can easily achieve enhanced dielectric properties with low leakage current and improved mechanical strength with good piezoelectric properties (d_{33}~ 125pC/N) near the morphotropic phase boundary. Making the composites with one or more perovskites along with denser binary transition metal oxides resulted in a massive reduction in the deliquescence.

The present research work is primarily motivated by all the above-mentioned studies with vigour to understand the dielectric, structural and optical properties of both $KNbO_3$ and $NaNbO_3$ when combined with the Mott-Insulators such. When we initiated this problem, no report was available focusing on these aspects either in the form of both bulk or nanostructures. Hence, an attempt was made here to understand the global dielectric behavior, ac-conductivity mechanism and vibrational excitations of above-mentioned composites. The detailed layout of the thesis is given below.

Chapter 1 provides an introduction to the dielectric materials and their applications. Also, this chapter gives a brief outlook into the family of perovskites along with their high-frequency dielectric properties. This chapter also includes basic concepts of ferroelectric and antiferroelectric systems along with magnetism in transition metal oxides. Further, it contains discussion on various types of electrical conduction mechanisms and behaviour of High-κ dielectrics under high ac-fields. This chapter also reviews few important concepts like: Mott-Insulators, Lyddane-Sachs-Teller relation $\left[\frac{\epsilon_0-S'}{\epsilon_\infty}=\left(\frac{\omega_l}{\omega_t}\right)^2\right]$, Debye-relaxation and various dielectric polarization mechanisms including Maxwell–Wagner–Sillars and defect-dipole polarization with special emphasis on the influence of

domain-wall displacement, microstructure, depletion and depolarization effects. This chapter also presents important up-to-date research on the Relaxor-dynamics of lead-free systems and the governing mathematical models such as Vogel-Fulcher law and Uchino-Nomura Criterion.

Chapter 2 presents a detailed overview of the various experimental techniques employed in the current research work including the synthesis procedure and characterization techniques. Material synthesis involving the Ball-milling process, optimization of the heat-treatment conditions such as calcination and sintering temperatures to achieve the maximum relative density and reduce the hygroscopic nature of the parent compounds have been discussed. The working principles of various instruments employed in the current study are also emphasized. For example, details of preliminary characterization techniques like X-ray diffraction (XRD) followed by Rietveld refinement using Fullprof software to determine the crystal structure, electronic structure using X-ray photoelectron spectroscopy (XPS), and microstructure/morphology using Field-Emission Scanning Electron Microscope (FESEM) are presented. Since the current work is vastly focused on the dielectric properties, the working principle of high-frequency (100Hz-20MHz) impedance analyser (which is capable of operating up to 650°C) has been discussed in great detail. The local environment of the cations using Electron Spin Resonance spectroscopy has also been discussed. In addition to these techniques, a detailed explanation related to the Raman spectroscopy (80-723K operation conditions) has been narrated. Various other commercial characterization techniques like Differential Scanning Calorimetry and Thermo-Gravimetric analysis (DSC-TGA), and superconducting quantum interference device (SQUID) based magnetometer are elucidated.

Chapter 3 focuses on the structural and dielectric properties of NiO substituted $NaNbO_3$ ceramics synthesized by the standard solid-state reaction technique. This chapter also gives an overview of the current research activities in the area of $NaNbO_3$ based lead-free dielectric systems. Incorporation of NiO inside the $NaNbO_3$ matrix led to significant lattice distortion from an orthorhombic (*Pmna*) to a monoclinic (*Pbma*) crystal structure at room temperature. The electronic structure and elemental analyses of (1-*x*) $NaNbO_3$ + *x* NiO composites have been discussed with the help of XPS data. These studies reveal the pentavalent and monovalent nature of the cations 'Nb' and 'Na' respectively, and in addition to this, Ni-2*p* doublet with binding energy separation of 17.82eV signifying the presence of divalent Ni. The temperature dependence of relative-dielectric permittivity $\varepsilon_r(T)$ of these composites exhibits two cusps associated with T_{AFE} and T_{O-M} for lower compositions ($x \leq 0.10$). Along with these transitions in this chapter, we unveil a feeble but lucid anomaly across 170°C in $\varepsilon_r(T)$ which is seldom discussed in the literature. Relative dielectric permittivity as high as 10^7 was observed as a single giant hump, engulfing multiple structural transitions (T_{AFE}, T_N and T_{O-M}) in $NaNbO_3$-NiO composites. The temperature dependence of ac-resistivity ($\rho_{ac}(T)$) provides strong evidence for the variable-range-hopping of charge carriers. The frequency dependence of ac-conductivity follows Jonscher's power law (JPL), $\sigma_{ac} = \sigma_{dc} +$

$A\omega^s$, which exhibits dispersive nature at high frequencies. The temperature dependence of the frequency exponent '*s*' obtained from the JPL analysis has been discussed which provides insights into various charge transport mechanisms and the dominance of universal dielectric response (UDR) at different temperatures. This chapter concludes with the demonstration of Mott's variable range hopping (VRH) of charge carriers between the localized states.

Chapter 4 presents a systematic study of the dielectric spectroscopy and temperature-dependent (80K ≤ T ≤ 300K) Raman spectroscopy of $NaNbO_3$ having dilute dispersion of NiO. The first part of this chapter discusses the temperature dependence of relative-dielectric permittivity, $\varepsilon_r(T)$, which exhibits an anomalous change in its magnitude across three distinct phase transitions of $NaNbO_3$ at 176°C, 392°C and 478°C. These are respectively associated with a second-order phase transition occurring due to incommensurate phase between two orthorhombic AFE orderings, change from orthorhombic P to R-phase (T_{P-R}) without altering AFE structure, and an orthorhombic R to S-phase transition accompanied by a change from AFE to paraelectric (PE) transition. A large thermal hysteresis ($\Delta T_{hys} \sim$ 38K) was evident in ε_r and ac-resistivity (ρ_{ac}) between the temperatures 200°C and 400°C signifying the first-order nature of the T_{P-R} transition. The second part of this chapter deals with a detailed analysis of vibrational excitations probed by means of the Raman spectroscopy for various compositions (*x*) of $NaNbO_3$–NiO composites ((1-*x*) $NaNbO_3$ + *x* NiO (0.05 ≤ *x* ≤ 0.95)). Such a systematic analysis and novel interpretation of Raman spectra on this system is completely new and has not been reported in the literature until now. At room temperature, for higher NiO content, a new mode centered at 838cm^{-1} was observed in Raman spectra along with the two-Magnon mode at 1496cm^{-1}, a broad longitudinal optical mode (2LO) at 1096cm^{-1}, and a weak translational optical mode (2TO) at 726cm^{-1}. At low temperatures, down to 80K, several peculiar features are evident in the Raman spectra of NbO_6 octahedra which are associated with the structural and antiferromagnetic transitions of $NaNbO_3$ and NiO respectively. Temperature dependence of DSC data collected under heating cycle in the presence of Ar gas, shows two weak anomalies: the first anomaly appears in the temperature range 500–550°C which is associated with T_{AFE} and the second one takes place between 320°C and 395°C, which is close to the structural phase transition T_{P-R} (370°C) observed in the dielectric data. Moreover, a giant cusp was evident in the DSC data at 150°C which is linked to the second-order incommensurate phase transition T_{p1} noticed in $\varepsilon_r(T)$. These studies reveal that any change in $\varepsilon_r(T)$ is accompanied by a definite change in the thermodynamic order parameter of the investigated system. Finally, this chapter ends with the discussion on low-temperature phonon and magnon modes that have emerged due to the presence of antiferromagnetic (AFM) NiO.

Chapter 5 focuses on MnO_2 containing $NaNbO_3$ polycrystalline composites. Structural analysis of the undoped system prepared after the heat treatment of the ball-milled precursors, Na_2CO_3 and Nb_2O_5, reveal the emergence

of orthorhombic phase of $NaNbO_3$ with space group *P21ma*. This phase is slightly different compared to *Pbcm* space group of $NaNbO_3$ and *R3c* space group of ferroelectric $NaNbO_3$. The key feature that sets apart *Pbcm* from *P21ma* is the diffraction peak occurring at the Bragg angle $2\theta \sim 36.5°$. X-ray diffraction analysis also reveals that samples heat-treated at 1000°C has Mn_2O_3 as the major phase along with $NaNbO_3$, however, samples heat-treated at 1040°C contains Hausmannite Mn_3O_4 along with Mn_2O_3. Using the Williamson-Hall analysis of X-ray line broadening, we estimated the micro-strain (η) and the average grain size (D) of all the compositions ($0.02 \leq x \leq 0.7$). This analysis reveals that few compositions having a significant amount of Mn_3O_4 which exhibits non-uniform strain effects on the lattice planes within the matrix. Since Mn_3O_4 exhibits long-range magnetic ordering with high magneto-crystalline anisotropy below 43K, we performed the vibrational Raman spectroscopy measurements down to 10K from room temperature. The room temperature vibrational Raman spectra show an anomalous change in the location of vibrational and liberational modes of NbO_6 octahedra due to the manganese ions that might have occupied the interstitial positions. This allows us to understand their role on the rhombohedral (FE) to orthorhombic (AFE) phase transition of $NaNbO_3$. With decreasing temperature, most of the NbO_6 modes are found to shift towards the higher wavenumbers as a result of contraction of bond length, and hence resulting in an increase in force constant. The anomalous changes occurring in the Raman shift between 80K and 300K for all the compositions reveal the existence of yet another possible structural transition. In particular, the Raman modes of NbO_6 octahedra, ν_6 (109-200cm^{-1}) and ν_5 (200-310cm^{-1}) exhibits anomalies in their position (X_C) between 275K and 290K. It is interesting to note that these modes exhibit positive temperature coefficients and shows significant hysteresis in their positions (4cm^{-1} across 80K). For the compositions, $x = 0.04$ and $x = 0.10$, the rotational degree of freedom of NbO_6 liberational modes are drastically affected as the temperature approaches to 300K from 80K. For $x = 0.02$ and $x = 0.30$, the ν_6 mode clearly deconvolutes into two distinct peaks with decreasing temperature. For the former, these peaks get sharper whereas, for the latter, the deconvoluted peaks soften with cooling and for $x = 0.04$, the ν_6 mode diminishes gradually with decreasing the temperature. For all the compositions, ν_5 and ν_6 modes display anomalous changes in its position between 170K and 220K which is associated with the structural phase transition of $NaNbO_3$ from rhombohedral to orthorhombic structure accompanied by the FE to AFE phase transition. The high-temperature impedance spectroscopic studies ($\varepsilon_r(T)$ and $\rho_{ac}(T)$) of these composites exhibits anomalies at orthorhombic-P to -R phase transition together with a new soft-anomaly across 150°C associated with the second-order incommensurate phase. Such anomalies are also present in the temperature dependence of dissipation factor similar to the systems $NaNbO_3$-NiO, $KNbO_3$-NiO, $KNbO_3$-$NaNbO_3$, and (Li/K,Na)NbO_3. A small but distinct hump was observed in $\varepsilon_r(T)$ and $\rho_{ac}(T)$ at 735K for frequencies greater than 105kHz which is associated with the standard AFE to disorder PE (T_{AFE}) phase transition accompanied by a change from orthorhombic-R to S phase. Furthermore, the ρ_{ac} analysis provided substantial evidence to the variable range

hopping mechanism of charge carriers in all these samples.

Chapter 6 describes a detailed study on the structural, dielectric, Raman scattering and ac-conductivity of ferroelectric $KNbO_3$ and antiferromagnetic NiO two-phase composites [(1-*x*) $KNbO_3$ + *x* NiO, $0.005 \leq x \leq 0.95$]. The first section of this chapter deals with the series of dielectric transitions. In this system, we noticed two major transitions in $\varepsilon_r(T)$ — the first at 445°C (T^*) and the second at 220°C (T_1) — respectively associated with the structural transitions from tetragonal to cubic and orthorhombic to tetragonal phases. In addition, a new anomaly across $T_2 \sim$ 320°C has been observed in $\varepsilon_r(T)$, and the loss-tangent ($Tan\delta(T)$), which may be associated with the combined effect of antiferromagnetic ordering of NiO and ferroelectric coupling of $KNbO_3$. The dispersive nature of T^*, and the Vogel–Fulcher temperature dependence of its characteristic relaxation frequency reveals the existence of relaxor-like behavior, which is further supported by Uchino–Nomura criteria (for $x \leqslant 0.10$) but departs from relaxor behavior for $x > 0.10$. In the second section of this chapter we discuss $\rho_{ac}(T)$ analysis which provides strong evidence for Mott's Variable range hopping process of charge carriers between localized states, with average hopping length of 4.2nm and hopping energy 0.72eV. The variation of T^*, T_1 and T_2 as a function of *x*, in consonance with the crystal structure, has been discussed. The final section of this chapter deals with the Raman spectroscopic studies aiming to probe the local structure of the investigated system, which shows significant increase of tilt-angle between adjacent NbO_6 octahedra as the divalent Ni occupies octahedral sites of the $KNbO_3$ matrix. All the Raman-active modes of these composites are indexed as lattice translations, specifically with the motion of K^+ ($190cm^{-1}$), the core vibrations of the NbO_6 octahedra ($220cm^{-1} \leqslant \nu \leqslant 320cm^{-1}$) and their collective modes ($50cm^{-1} \leqslant \nu \leqslant 150cm^{-1}$), and Magnon modes (two-magnon $\sim 1500cm^{-1}$) associated with the antiferromagnetic ordering of NiO.

Chapter 7 presents a brief summary of important results of the research work carried out in this thesis. In this chapter, we also identify some open issues which are potentially interesting for the future studies.

***Work Published in International Journals*:**

[1] "*Dielectric properties of (1-x) $KNbO_3$ – x NiO two phase composites*"
R. Soni, **R. T. George**, D.C. Joshi, S. Nayak, P. Pramanik, P. Suresh, T.A. Dar and S. Thota,
Journal of Physics D: Applied Physics, **50**, 415305 (2017).

[2] "*Effect of NiO substitution on the structural and dielectric behavior of $NaNbO_3$*",
R.T. George, D.C. Joshi, S. Nayak, N. Tiwari, R.N. Chauhan, T.A. Dar and S. Thota,
Journal of Applied Physics, **123**, 054101(2018).

[3] "*Thermal hysteresis and vibrational excitations in NiO containing $NaNbO_3$*",
R.T. George, T.A. Dar, D.C. Joshi, V. Sathe, A.K. Rathore and S. Thota,
Journal of Physics D: Applied Physics, **52**, 115301(2019).

[4] "*Nature of magnetic ordering in nanocomposites of $Zn_{(1-p)}Ni_pO$ and NiO*"
D.C. Joshi, P. Pramanik, **R.T. George**, T. Sarkar and S. Thota,
Physica E: Low Dimensional Systems and Nanostructures, **103**, 46(2018).

[5] "*Dielectric and Thermo-Raman spectroscopic studies on $NaNbO_3$-MnO_2 two phase composites*"
R.T.George, V. Sathe and S. Thota (*Under Preparation*).

[6] "*Low- temperature magnetic and ac-susceptibility studies of $NaNbO_3$-MnO_2 two phase composites*"
R.T.George, S. Ghosh, P. Pramanik, R.J. Choudhary and S. Thota (*Under Preparation*).

Conferences and Poster Presentations

[1] *"A dynamical study of lead-free $KNaNbO_3$-MnO_2"*
R.T. George, R. Soni, D.C. Joshi, P. Pramanik, S. Nayak, S. Pittala and S. Thota, International Conference on Nanomaterials and Nanotechnology (ICNANO-2017), 01 - 03 March, 2017 at Vinoba Bhave Research Institute, Allahabad, India.

[2] "*Thermal Hysteresis in $NaNbO_3$-NiO Two-Phase Composites*"
R.T. George, R. Soni, D. C. Joshi, S. Nayak, P. Pramanik, S. Ghosh, and S. Thota, National Seminar on Advances in Material Science, March 24-25, 2017; Gauhati University, Assam, India.

[3] "*Dielectric behaviour of lead free ferroelectric $NaNbO_3$-NiO two-phase composite*"
R.T. George, D. C. Joshi, R. Soni, P. Pramanik, S. Nayak, and S. Thota Research Conclave 2017; IIT Guwahati, Assam, India.

[4] "*Raman Spectroscopic Studies of Piezoelectric Alkaline Niobate*"
R.T. George, S. Nayak, D.C. Joshi, T.A. Dar and S. Thota, National Workshop on Fluorescence and Raman Spectroscopy (FCS 2017), December 17-21 2017, Indian Institute of Technology Guwahati, Guwahati, Assam, India.

[5] "*Structural and ac-electrical transport of Antiferroelectric $NaNbO_3$ and NiO composites*"
R.T. George, T.A. Dar, D.C. Joshi, S. Nayak and S. Thota, International Conference on Systems and Processes in Physics, Chemistry and Biology (ICSPPCB- 2018), 1-3 March 2018, Assam University, Silchar, Assam, India.

[6] "*High Temperature Dielectric Behaviour of $KNaNbO_3$ and CuO composites*"
T.A. Dar, D.C. Joshi, **R.T. George**, and S. Thota, International Conference on Advanced Nanomaterials and Nanotechnology (ICANN 2017), 17-21 December 2017, Indian Institute of Technology Guwahati, Guwahati, Assam, India.

[7] "*On the Vibrational Excitations of Ferroelectric $KNbO_3$ and Antiferromagnetic $MgMnO_3$*"
S. Nayak, R. Soni, **R.T. George**, T.A. Dar, D.C. Joshi and S. Thota International Conference on Advanced Nanomaterials and Nanotechnology (ICANN 2017), 17-21 December 2017, Indian Institute of Technology Guwahati, Guwahati, Assam, India.

[8] "*High Frequency ac-electrical resistivity studies on $KNaNbO_3$ + CuO composites*"
T.A. Dar, D.C. Joshi, S. Nayak, **R.T. George**, S. Ghosh and S. Thota, International Conference on Systems and Processes in Physics, Chemistry and Biology (ICSPPCB- 2018), 1-3 March 2018, Assam University, Silchar, Assam, India.

[9] "*Mott Variable-Range Hopping Conduction Mechanism in Ferroelectric $KNbO_3$-NiO*"
R. Soni, **R.T. George**, D.C. Joshi, P. Pramanik1, S. Nayak and S. Thota,

International Conference on Nanomaterials and Nanotechnology (ICNANO-2017), 1-3 March 2017, VBRI Allahabad, India.

[10] "*On the nature of diffused first-order phase transition in $NaNbO_3$-MnO_2 two-phase composites*"
R. Soni, D. C. Joshi, S. Nayak, P. Pramanik, **R.T. George**, S. Ghosh, and S. Thota,
UGC-SAP (DRS III) Sponsored National Seminar on Advances in Materials Science, 24-25 March 2017, Gauhati University, Guwahati-781014, Assam, India.

Acknowledgments

First and foremost, I would like to thank my supervisor Dr. Subhash Thota for providing his valuable suggestions and support during my Ph.D. career without whom this Ph.D. thesis would not exist. Without his constant support and faith, I would not have reached the end of this educational journey. I am truly grateful for his patience and help for my scientific writing regardless of the time of the day. His guidance and quick suggestions at the right time guided me through my tough times especially when I had no answers to the problems faced. I am immensely grateful to him for providing me unique opportunities that significantly broadened my research experience that will undoubtedly be crucial for pursuing an academic career in the future.

My deepest and heartfelt thanks to the members of my Doctoral Committee Dr. A.K. Sharma (Chairman), Dr. T. Mishra and Dr. V. Ramakrishnan for the time they spent on this dissertation as well as for their guidance and insightful comments, which was undoubtedly for the betterment of this thesis, I am immensely grateful to all. I would also like to extend my sincere thanks to Dr. S. Ghosh, Head of Physics Department for his dynamicity and for looking into the needful matters in time in a department level, thus making sure my work in the department went smoothly and comfortably. In particular, I have my deepest gratitude to Prof. P. Poulose, former Head of the Department, who was there to confront me during the tough times of my Ph.D. career. He was there for me keeping aside his valuable time, to look into the difficulties I faced.

My sincere thanks to my collaborators Dr. N. Tiwari, Dr. R.N. Chauhan for providing rich instrumental data without which this work would not have acquired what it has achieved. I would also like to thank Dr. V. Sathe and Dr. R.J. Choudary who also extended their help by providing me the instrumental facilities in their esteemed institute (UGC-DAE CSR, Indore). I am also grateful to Mr. A.K. Rathore (Technical staff, UGC-DAE CSR), who was of great help during my visit to his institute, sharing various technical ideas regarding the instrument. Without their help, I would not be able to complete this thesis work. I acknowledge the financial support for this thesis provided by the Indian Institute of Technology Guwahati and MHRD and funding agencies DST-FIST and DAE-BRNS.

Behind the big picture, there is a group of enthusiastic people who worked seamlessly making sure all the requirements are met smoothly on an administrative level. So, with immense pleasure, an honourable mention to all the administrative staff for all their effort, though small, but yet worth to be mentioned. Special thanks to D. Talukdar (Research and Development Section) for his swift and timely assistance for my travel allowance without which my research-related travel would not be possible on time. I am thankful from the fathoms of my heart to The Central Instruments Facility (CIF) provided by the Indian Institute of Technology Guwahati for giving an outstanding platform for research, offering various sophisticated instruments for various scientific experiments. I would also like to extend my sincere gratitude to, Prof. M. Qureshi (Head of CIF), Prof. G. Krishnamoorty (former Head), and the rest of the team who are involved in

the smooth functioning of CIF. A special thanks to Mr. C. Borgohain who helped me gain technical ideas about Vibrating Sample Magnetometer (VSM) and Quantum Dynamics – Physical Property Measurement System (QD-PPMS) during my operational hours, Mr. S.K. Deb for providing timely slots for Raman measurements whenever in case of emergency. I also want to thank the XRD facility provided by DST, New Delhi, through the FIST program in our department which was a key instrument for the completion of this thesis. My sincere thanks to two other people, Dr. Yashwant G. and Mr. Soumik G. who taught me various technical knowledge about Dynacool-PPMS, with great discussions about its working principles, technology and ideas that was put together to give this instrument its form, sharing some of the most insightful moments during his work visits inside the campus

I am also grateful to all the faculty members of the Physics department, IIT Guwahati, especially to one Dr. C.Y. Kadolkar, who has been one stand-out person for me in the department whose support, guidance, exceptional knowledge and witty humour always helped. Be in sports or academics, he is there training me which helped me carve a different person out of me each day. Also, I would like to thank Dr. Sidananda Sarma for his technical assistance and friendly discussions. My special thanks to all the diligent scientific officers and staff members for their hard work they have put forward during office hours in the department.

I am thankful to my lab mates, D.C. Joshi, S. Nayak, Dr. T.A. Dar, R.K. Yadav, R. Soni, S.Ghosh, P. Pramanik, Suchit, Shaona, Ravi, Soumya, Atyant, Shweta and Pragya for their help and company, especially Deep and Sanjib who have helped and worked with me rigorously day and night. I am also thankful to my seniors, Arun Mathew, Prahlad, Ranganadh, Ramakrishna. Many thanks to my friends and colleagues, too many to list, but each in their own way played an important part in my research life in Guwahati.

I want to present my special thanks to all my teachers from KG who gifted me the ability to read and write, to my 12th from my school, Nirmalamatha Central School, Thrissur without whom this thesis would have seen the light of this day. I would also like to thank my teachers from Loyola College, Chennai (B.Sc.) and Pondicherry Central University (M.Sc.) who have inspired me through my academic career. My special thanks to Mr. Nageswara Rao, Director UV Physics Academy, who inspired me by his way of teaching, dedication and sincerity. I must thank all my friends whom I came across in all the above-mentioned realms of my academic career.

Last but not least, I want to give my greatest acknowledgements to my family. My parents are always supportive of me. They comforted me when I was frustrated, encouraged me when I felt unconfident, and motivated me when I was struggling. I must show my deepest gratitude to my wife, Maryjo M. George, without her care, patience, encouragement, and support, I would not have accomplished my Ph. D.

By

Robin T. George

Contents

List of Figures

Chapter 4

Table No. **List of Tables** **Page No.**

Chapter 3

Chapter 4

Chapter 5

Chapter 6

Chapter 1
General Introduction with Theoretical Background

In this chapter, general background to the physics of dielectric materials is presented in order to allow proper discussion of the experimental results presented in the later chapters. This material is based on the text-books by Dekker [1], Richerson [2] and the other reference cited in this chapter.

1.1 Ideal Dielectrics:

Dielectrics are type of insulator that virtually does not contain any free charge carriers (they are bound to the atoms), however, they become polarized when exposed to an external Electric Field (**E**). Hence dielectric materials are good insulators which means they exhibit high electrical resistivity. There is no actual flow of charge in these systems (with external field) but move slightly from their original position. Thus, by application of external field, one can create a relative displacement between the charge centres (the negatively charged electron cloud and positively charged nucleus), the state which is termed to be as polarized, and this effect collectively termed as polarization (**P**), which can generate electric dipole moments ($\boldsymbol{p}$) within the material and are aligned in the direction of electric field. Dipole moment ($\boldsymbol{p}$), when two equal and opposite charges ('*q*') are displaced by a distance **d**, is given by,

$$\boldsymbol{p} = q\boldsymbol{d} \tag{1.1}$$

Electric polarization, by definition is the net dipole moment per unit volume (*V*) and can be represented as,

$$\mathbf{P} = \sum_i \frac{\boldsymbol{p_i}}{V} \tag{1.2}$$

As the charge inside cancels out, there is a finite amount of charge on both sides of the dielectric medium (known as the surface charge σ_s). This quantity may be small if this space is filled with vacuum or air (ε_r = 1), but this can be improved considerably with the help of a dielectric medium (figure 1.1). This property of the dielectric medium is exploited vastly in capacitors to store charge/energy.

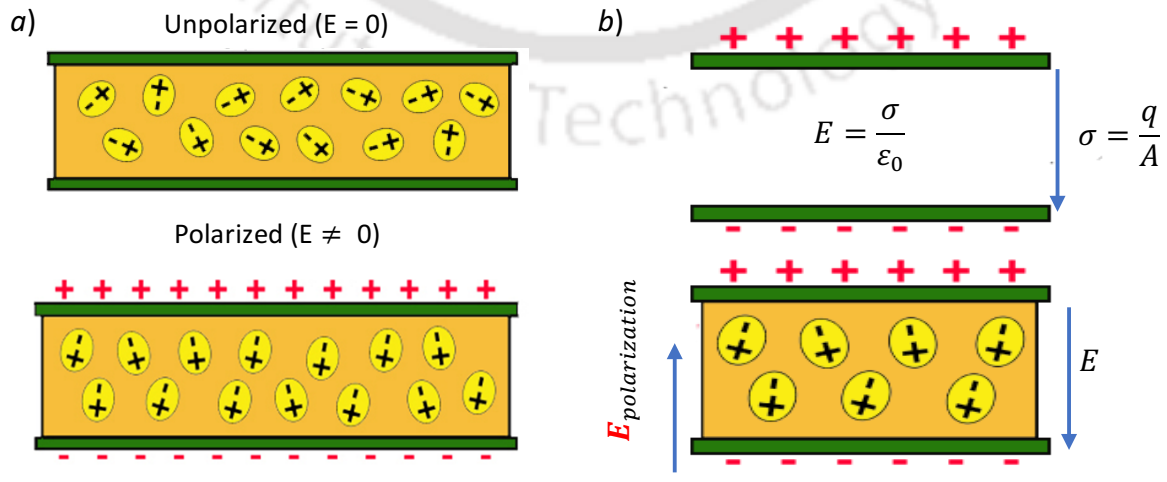

Figure 1.1. (*a*) Schematic view of a dielectric when placed in an electric field E ≠ 0 and E = 0, and (*b*) Field directions in a dielectric medium when placed between the parallel plates of area A and each carrying a charge

A capacitor is an arrangement where an electric field **E** is applied across a parallel plate with common area A and separated by a distance *t*, hence, one plate becomes positive (or negative) relative to other. This means that a surface charge density, σ_s, is stored on each plate and thus resulting in an effective Capacitance C_0 in vacuum which is given by,

$$C_0 = \frac{\varepsilon_0 A}{d} \tag{1.3}$$

where ε_0 is the permittivity of free space, and is a constant which takes the value 8.85×10^{-12}F/m. With dielectric medium placed between the parallel plate capacitor arrangement, the resultant capacitance increases by a factor $(1+\chi_s)$, where χ_s is the susceptibility of the material. This is where the concept of relative dielectric permittivity, ε_r, comes into picture.

$$\varepsilon = \varepsilon_0(1+\chi_s) \tag{1.4}$$

$$\varepsilon_r = (1+\chi_s) = \varepsilon/\varepsilon_0 \tag{1.5}$$

$$C = \varepsilon_0 \varepsilon_r A/d \tag{1.6}$$

Relative permittivity ε_r is defined as the ratio of the permittivity of the material (ε) to that of the free space (ε_0). It is in other words a measure of ability of the material to store energy with the application of electric field (figure 1.2).

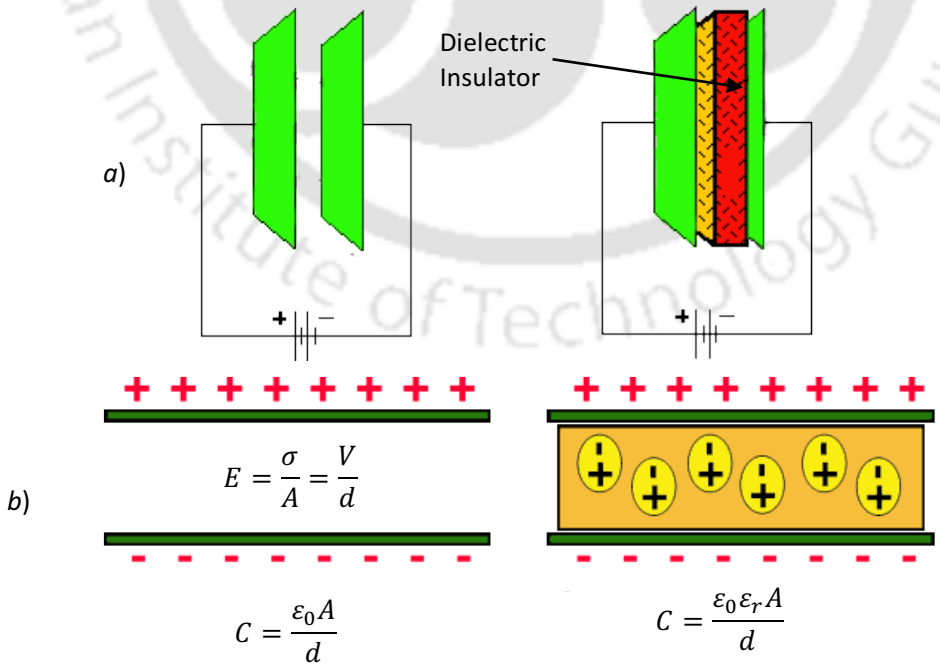

Figure 1.2. (*a*) Schematic representation of a parallel plate capacitor arrangement without and with a dielectric. (*b*) Polarity on the electrodes with and without dielectric medium.

As discussed above, in the presence of an external electric field, dielectrics (insulators) can be electrically polarized and this property is used in the capacitor applications. In a parallel plate arrangement, the surface charge, σ_s is

$$\sigma_s = \varepsilon_0 \mathbf{E} \tag{1.7}$$

where **E** = V/d, or vectorially **E** = $-\nabla V$. So, consequent to the applied electric field, there can be some surface charge due to the dielectric medium placed between the parallel plate arrangement. Hence, the total charge accumulated can be defined using a new parameter, also known as the *Displacement vector,* **D** which accounts for the free and the bound charge within the medium. Hence **D** can be written as,

$$\mathbf{D} = \varepsilon_0 \mathbf{E} + \mathbf{P} = \varepsilon \mathbf{E} \tag{1.8}$$

$$\therefore \mathbf{P} = \varepsilon_0(\varepsilon_r - 1)\mathbf{E} = \varepsilon_0 \chi_s \mathbf{E} = \alpha \mathbf{E} \tag{1.9}$$

Hence, for a linear homogenous stretch of dielectric medium, **P** depends linearly on the applied field **E**. The quantity 'α' equation 1.9 is called the ***Polarizability***, which gives the tendency of the material to be polarized.

1.2 Dielectrics in presence of ac-field:

All of the above discussion is on an assumption that the medium behaves as an ideal dielectric, where there is no power loss during charging and discharging of charge. However, when the dielectric medium is placed in an alternating field, dielectric-loss comes into play. Dielectric losses occur mainly due to the dissipation of energy because of dipole rotation in an alternating field and there is some inertia due to the mass these dipoles possess. Hence, all of the previously discussed permittivity, ε_r, is the real component (ε'). There are hence two components for permittivity of a material: ε', the real component and ε", the imaginary component and they are related with the below equation.

$$\varepsilon_r = \varepsilon' - i\varepsilon" \tag{1.10}$$

The imaginary part represents the energy-loss or in other words the dissipation factor. For most of the dielectrics D_0 is proportional to E_0 (where D_0 and E_0 are the amplitudes of the time varying **E** and **D** given by $E_0\sin(\omega t)$ and $D_0\cos(\omega t - \delta)$), but their ration D_0/E_0 is generally frequency dependent [1]. By working out the differential equation for the current density in a capacitor, one can readily show that the energy (W) dissipated in a dielectric in the form of heat per second per unit volume is

$$W = \left(\frac{\omega}{8\pi}\right) E_0 D_0 sin\delta = \left(\frac{\omega}{8\pi}\right) E_0^2 \varepsilon" \tag{1.11}$$

In the above expression, the energy losses are proportional to $sin\delta$, which is called the *loss-factor*, and δ is the *loss-angle*. However, dissipation factor is also represented as $tan\delta$, called the *loss-tangent* [2]. This is only correct for small angles when $sin\delta \cong Tan\delta \cong \delta$. Loss-tangent is that quantity that can be expressed as the ratio of imaginary component of the permittivity to that of the real.

$$Tan\ \delta = \varepsilon"/\varepsilon' \tag{1.12}$$

1.2.1 Debye Relaxation and its evolution:

In circuit physics, it is well known that the voltage of the electric field **E** always lags behind the current by $\theta = \pi/2$, however, in reality, with the dielectrics, this angle (or lag) is not exactly $\pi/2$, but the current leads by an angle $(\pi/2 - \delta)$. Naturally, δ will be zero if there is no loss present. Individually, the real and the imaginary components can be expressed as a function of frequency (ω) as,

$$\varepsilon'(\omega) = \varepsilon_\infty + \left(\frac{\varepsilon_s - \varepsilon_\infty}{1+\omega^2\tau^2}\right) \; and \; \varepsilon"(\omega) = \; \omega\tau \left(\frac{\varepsilon_s - \varepsilon_\infty}{1+\omega^2\tau^2}\right) \qquad (1.13)$$

Here, τ represents the characteristic *relaxation time* of the medium, ε_s the static or the low-frequency permittivity and ε_∞ is the permittivity at high-frequencies. These expressions are frequently referred to as the *Debye equations*. Dielectric relaxation is a momentary lag caused by the delay in molecular polarization in responding to the dynamically changing electric field. The variation of real and the imaginary part of permittivity is shown in figure 1.3.

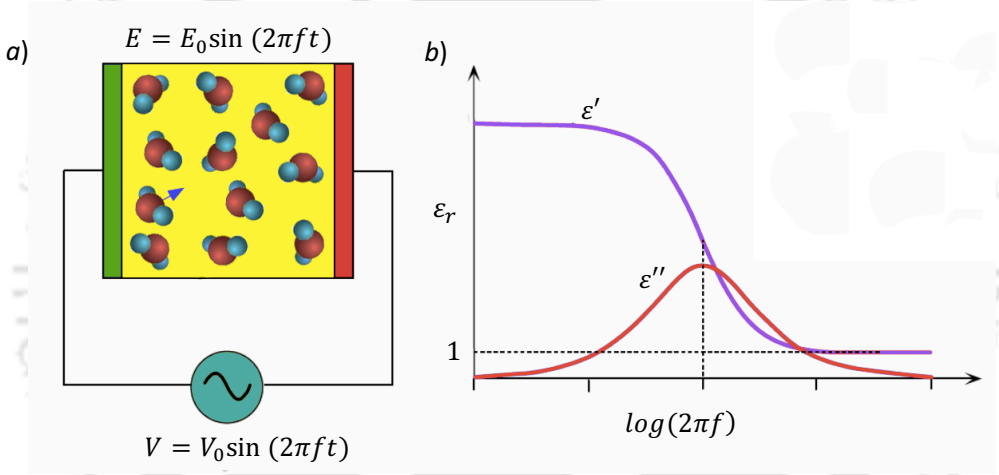

Figure 1.3. (*a*) Schematic diagram of a parallel plate capacitor with dielectric medium in the presence of ac-voltage. (*b*) Frequency (*f*) dependence of the real (ε') and imaginary (ε'') components of relative dielectric permittivity (often called as Debye curves, equation 1.13).

It is observed that the dielectric loss, which is proportional to ε" according to equation 1.13, exhibits a maximum for $\omega\tau = 1$, i.e., when angular frequency is equal to $1/\tau$. Also, for frequencies appreciably less than $1/\tau$, the real part of the dielectric constant ε' becomes equal to the static dielectric constant. Also, in this frequency range, the losses vanish and the dipoles contribute their full share to the polarization. On the other hand, for frequencies greater than $1/\tau$, the dipoles can no longer follow the field variations, and the dielectric constant ε' approaches ε_∞.

One of the most important assumptions made by Debye for the relaxation theory was that the molecules are of spherical geometry and that the dipoles were independent of the angular frequency ($\omega = 2\pi f$). Another assumption for Debye theory of relaxation was that the system consisted of non-interacting polar molecules. But in reality, dipoles for majority of materials are interactive and their response is field

dependent, unlike how Debye had assumed for the formulation the theory of relaxation [3]. Later in 1941, an improved form for the Debye equations were proposed by K.S. Cole and R.H. Cole, popularly known as the *Cole-Cole equation* [3,4]. The modified Debye equation, or in other words, the Cole-Cole equation can be expressed as

$$\varepsilon^*(\omega) = \varepsilon_\infty + \frac{(\varepsilon_s - \varepsilon_\infty)}{[1+(i\omega\tau)^{1-\alpha}]} \tag{1.14}$$

where $\varepsilon^*(\omega)$ is the complex permittivity, α is a constant that depends on the material property lies in the range $0 \leq \alpha \leq 1$ and rest having the same meaning as in the Debye formulation (equation 1.13), where $\alpha = 0$ is the case when Cole-Cole approaches Debye relaxation [4]. Here α should not be confused with polarizability as in equation 1.9. Furthermore, in 1951 a new variation of the Debye expression was proposed by Davidson *et al.* known as the *Cole-Davidson equation* [5]. Later in 1966, S. Havriliak and S. J. Negami investigating the complex dielectric behaviour proposed by Cole-Davidson, consequently, the Cole-Cole equations can be empirical and can be considered as a consequence of the existence of distribution of relaxation times, rather than a single relaxation time. Further, the relaxation equation can be modified to result in the *Havriliak-Negami equation* or in short, known as the HN equation as shown below [6].

$$\varepsilon^*(\omega) = \varepsilon_\infty + \frac{(\varepsilon_s - \varepsilon_\infty)}{[1+(i\omega\tau)^{1-\alpha}]^\beta} \tag{1.15}$$

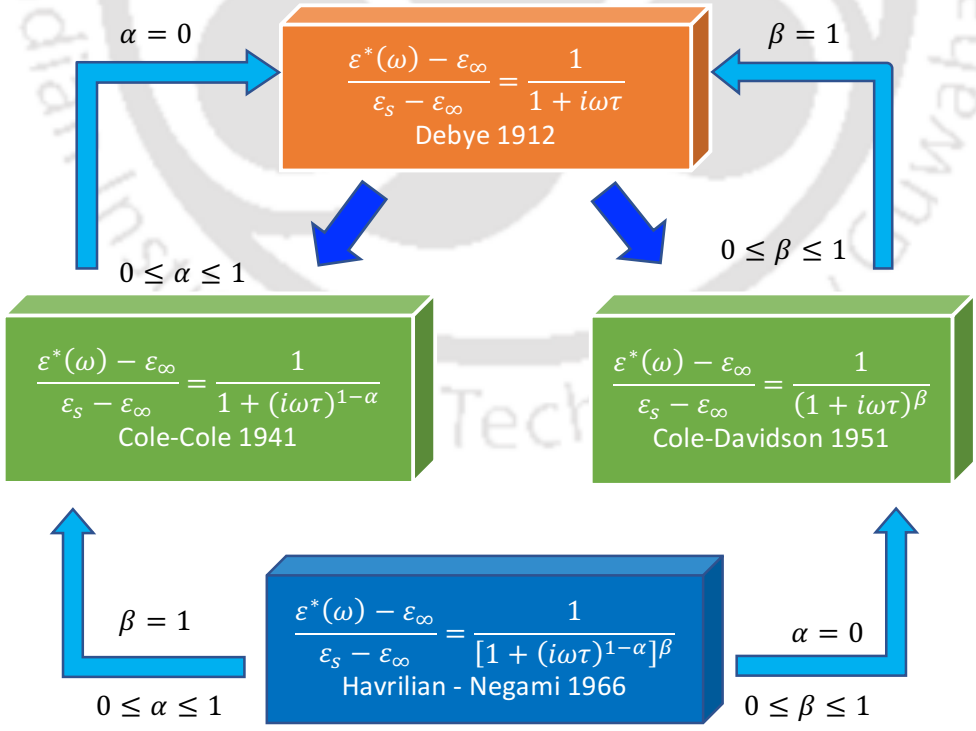

Figure 1.4. Evolution Cole-Cole, Cole-Davidson and Havrilian-Negami relaxation mechanism from of the Debye relaxation and the corresponding mathematical expressions.

where $0 \leq \alpha, \beta \leq 1$. Debye model with single relaxation can be obtained from $\alpha = 0$ and $\beta = 1$, Cole-Cole with $\beta = 1$ and $0 \leq \alpha \leq 1$ and Cole-Davidson with $0 \leq \beta \leq 1$ and $\alpha = 0$. Evolution of the relaxation models is described in figure 1.4. By eliminating τ from equation 1.12, one can arrive at an equation,

$$\left[\varepsilon' - \frac{(\varepsilon_s - \varepsilon_\infty)}{2}\right]^2 + (\varepsilon'')^2 = \left[\frac{(\varepsilon_s - \varepsilon_\infty)}{2}\right]^2 \qquad (1.16)$$

which is of the form $(x-h)^2 + (y-k)^2 = a^2$ (i.e. a circle whose centre is at (h, k) and radius a). Thus, plotting between ε' against ε" results in a semicircle of radius $\frac{(\varepsilon_s - \varepsilon_\infty)}{2}$ with its centre $\left(\frac{(\varepsilon_s - \varepsilon_\infty)}{2}, 0\right)$ as shown in figure 1.5. Such plots are called *Cole-Cole Plots*.

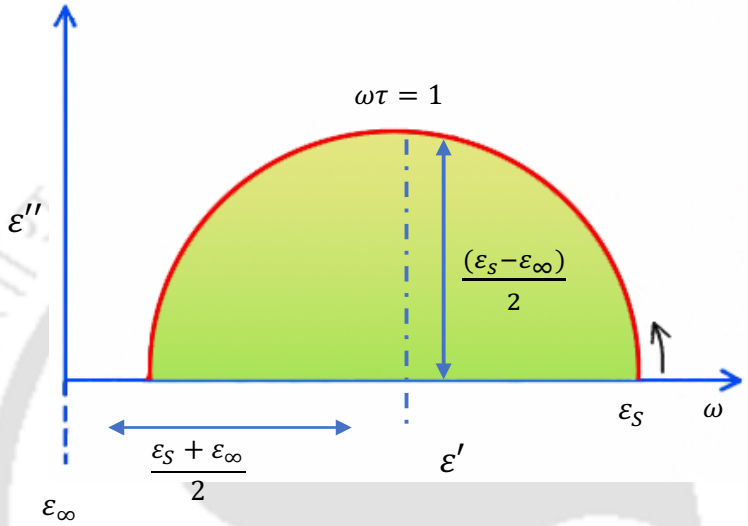

Figure 1.5. Cole-Cole plot (i.e. Imaginary component of the dielectric permittivity ε'' versus real component of the relative dielectric permittivity ε'). Here the static and high-frequency dielectric permittivity are represented by ε_s and ε_∞ , and angular frequency $\omega = 2\pi f$ and the τ represents the relaxation time.

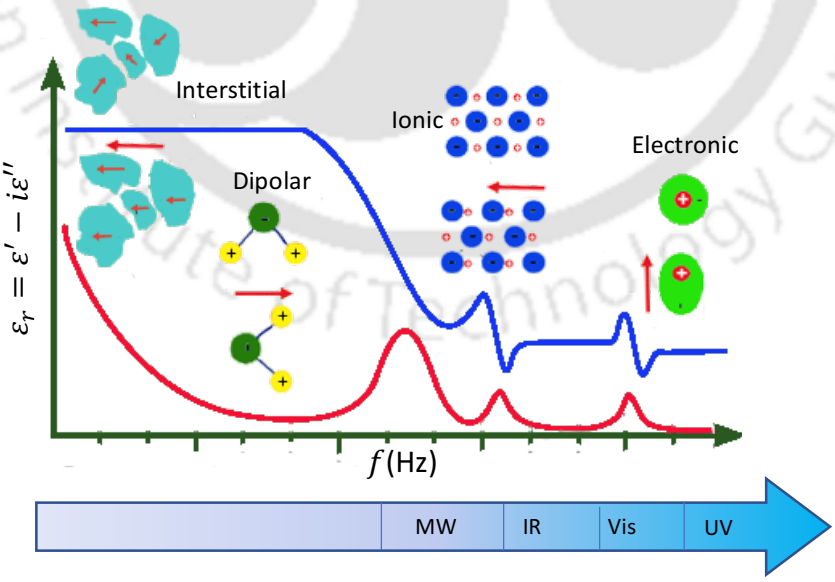

Figure 1.6. Frequency dependence of relative dielectric permittivity representing various polarization mechanism low-frequency space-charge polarization, ionic, dipolar, atomic and high-frequency electronic polarization. Arrow denotes the direction of electric field.

1.3 Types of Polarization in High-κ dielectric systems:

There are mainly four mechanisms of polarization that are involved and they are: (*i*) Electronic or Atomic Polarization, (*ii*) Ionic Polarization (*iii*) Dipolar or Orientation Polarization, (*iv*) Interface or space charge polarization, and (v) Maxwell-Wagner Polarization. Figure 1.6 shows the frequency variation of the dielectric permittivity $\varepsilon(f)$ representing the onset of all the above-mentioned polarization mechanisms.

1.3.1 Atomic or Electronic Polarization:

Electronic polarization occurs in a dielectric medium when placed in an electric field resulting in a relative displacement of electron cloud to that of the positive charge centre or nuclei (figure 1.7).

1.3.2 Ionic Polarization:

This type of polarization mostly occurs in ionic compounds. Application of electric field leads to small displacement of ions from their equilibrium position, which is sufficient to induce a net dipole moment (figure 1.8).

1.3.3 Dipolar or Orientation Polarization:

This is primarily due to the orientation of molecular dipoles in the direction of electric field without which the dipoles would be randomly oriented due to thermal agitation (figure 1.9).

1.3.4 Interface or Space Charge Polarization:

This polarization involves very little movement of charges associated with the application of electric field. This polarization is mostly confined to the grain boundaries or between any other interface (figure 1.10). The range of diffusion of ions/charge for this polarization is appreciably large compared to other types of polarization. For all the above polarization, we can see that the masses that get displaces vary for different polarization, with masses increasing from electronic to interface polarization. Hence, we can say that heavier the entity that is getting displaced, more time will be spent in displacing them. Hence the atomic polarization is the fastest which typically persist in between 10^{13} to 10^{15}Hz, and interfacial or space charge polarization is the slowest which occurs at frequency below 10Hz.

1.3.5 Maxwell-Wagner Polarization:

On the basis of the difference in the charge carrier relaxation times, the Maxwell-Wagner effect accounts for the charge accumulation at the boundaries of the two-material interface (figure 1.11). Basically, the ratio of the permittivity to the conductivity will result in the relaxation ($\tau = \varepsilon/\sigma$), i.e. at the steady state, the charge accumulation at the boundaries after a time $\tau = \varepsilon/\sigma$. Charge accumulation across the interface of the two materials with different relaxation times is called the *Maxwell-Wagner effect*. This effect is pronounced in all material interfaces such as metal-insulator, metal-semiconductor, insulator-semiconductor and many others.

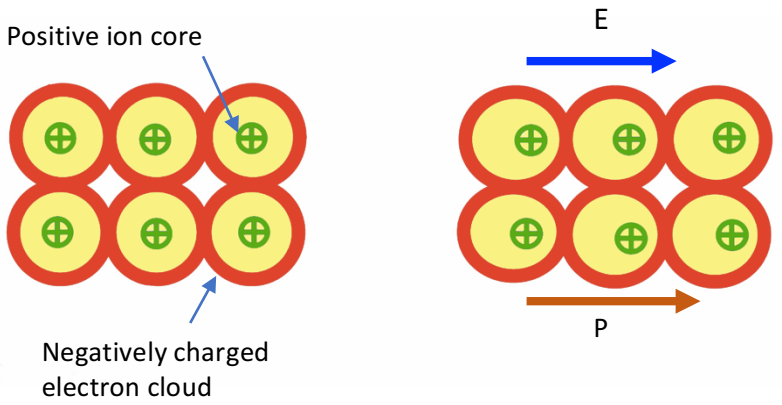

Figure 1.7. Schematic representation of electronic polarization in the presence of electric field E.

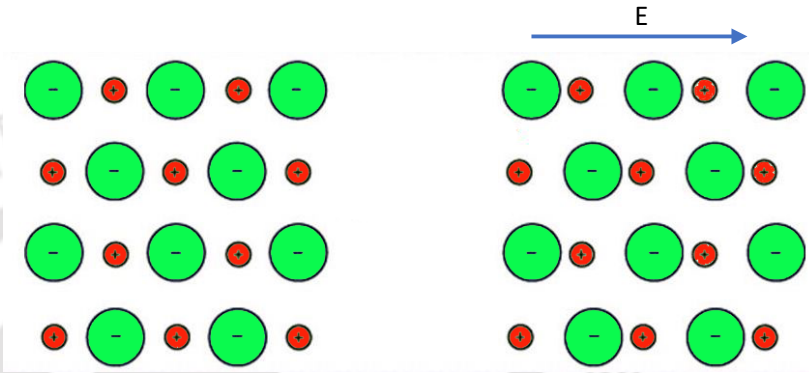

Figure 1.8. Schematic representation of ionic polarization in the presence of electric field E.

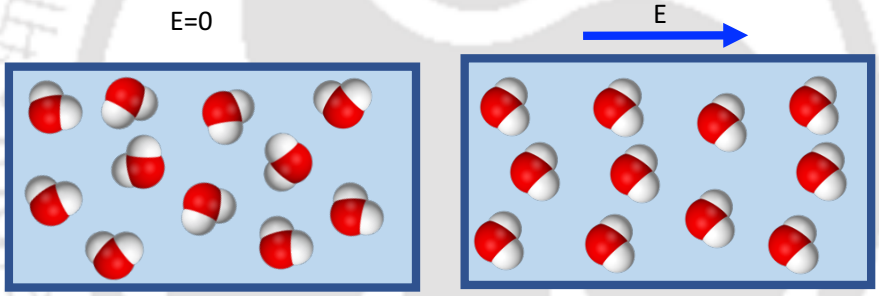

Figure 1.9. Schematic representation of dipolar or orientation polarization in the presence of electric field E.

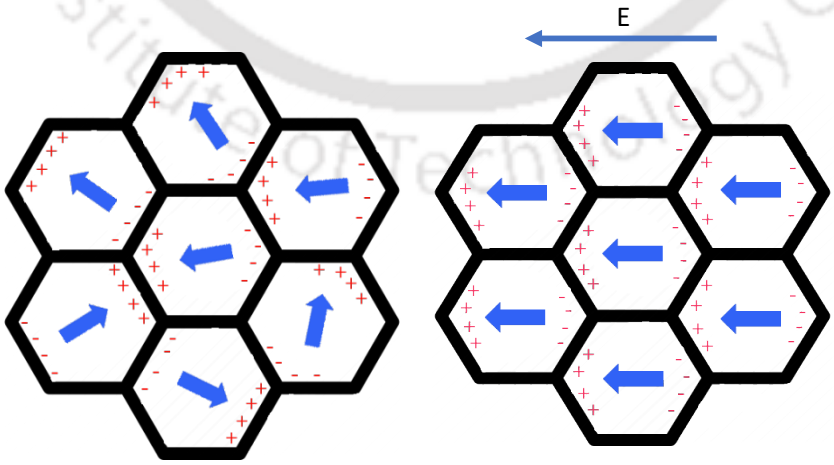

Figure 1.10. Schematic representation of the interface polarization in the presence of electric field E.

According to Maxwell ("*A Treatise on Electricity and Magnetism*" [7]), the divergence of **D** under a steady-state condition between two-material interface is

$$\boldsymbol{\nabla}.\mathbf{D} = \boldsymbol{\nabla}.\varepsilon\mathbf{E} = \boldsymbol{\nabla}.\left(\frac{\varepsilon}{\sigma}\right)\boldsymbol{j} = \boldsymbol{\nabla}\tau.\boldsymbol{j} = q \neq 0 \qquad (1.17)$$

here q is the accumulated charge density at the interface. This equation reveals that the charge accumulated in the interface of two materials with different relaxation times is not zero. Maxwell's theory points out that, for the current to flow across any materials, it has to follow two paths which can be described using a parallel equivalent circuit.

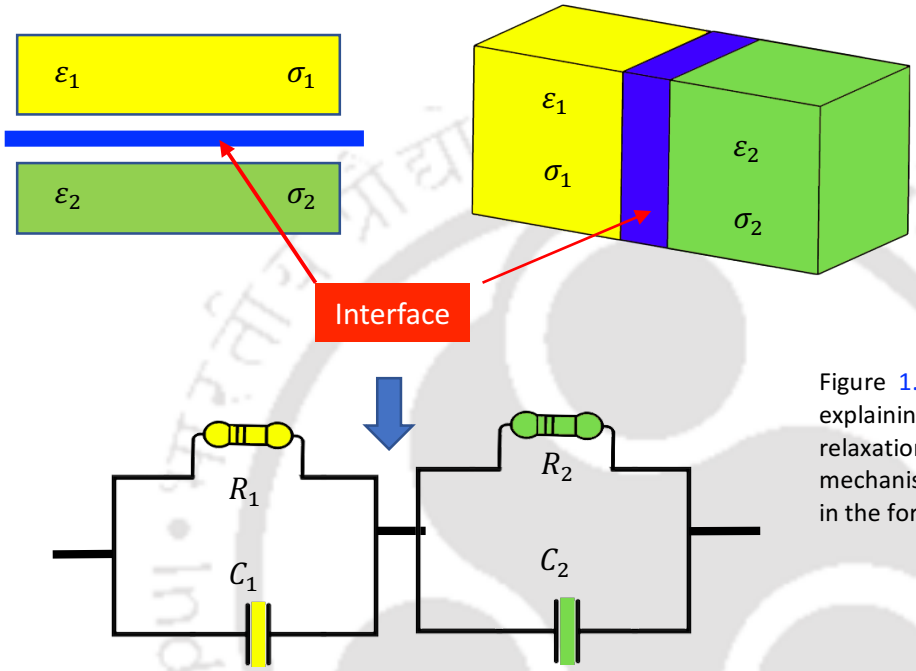

Figure 1.11. Schematic circuit diagram explaining the Maxwell-Wagner (M-W) relaxation mechanism. M-W relaxation mechanism in bi-layers can be visualized in the form of a RC parallel circuit.

This circuit consists of a resistor $R\ (= l/A\sigma)$ for representing the path for flow of current due to conduction, and a capacitor $C\ (= \varepsilon A/l)$ representing the second path for Maxwell's displacement current [8]. Hence, the response time for the equivalent circuit can be written as

$$RC = \frac{l}{A\sigma} \times \frac{\varepsilon A}{l} = \frac{\varepsilon}{\sigma} = (\tau_2 - \tau_1)J = \sigma_s \neq 0 \qquad (1.18)$$

where $\tau_1 (= \varepsilon_1/\sigma_1)$ and $\tau_2 (= \varepsilon_2/\sigma_2)$ are the relaxation times of material 1 and 2 respectively, J is the steady-state current density, and σ_s the charge accumulated per unit area at the interface. Maxwell-Wagner effect is an important phenomenon that often appears in Metal-Insulator-Metal based FET systems and many other memory devices.

1.4 Lattice Vibrations and Lyddane-Sachs-Teller (LST) Relation:

In this section, we discuss about the basic concepts of atomic motion (lattice vibrations) and importance of LST relation which are linked to the frequency response of dielectric permittivity of any dielectric material [9-12]. Before we look into *Lyddane-Sachs-Teller* (or commonly known as the LST relation), it is important to know about electronic polarization mechanism, little more than that just the displacement

of negatively charged electron cloud relative to positively charged nucleus (section 1.3.1). Electronic polarization is one of the most common type of polarization. The weakly bound electrons will be the first to respond towards the applied electric field and this process is quick which occur in a time frame of 10^{-14}-10^{-15} sec [9]. Static dielectric constant, ε_r , is the sum of electronic (ε_e) and lattice contributions (ε_l), $\varepsilon_r = \varepsilon_e + \varepsilon_l$. The electronic component ε_e is also equal to the optical dielectric constant ε_∞ which in turn equivalent to the square of the refractive index (n) of the material as shown in equation 1.19. Typically, the magnitudes of ε_∞ lies between 4 and 5 [10]. However large static dielectric constant can arise due to lattice contributions and can be expressed as,

$$\varepsilon_r - n^2 = \sum \frac{Ne^2 Z_T^{*2}}{m\omega_{TO}^2} \qquad (1.19)$$

In the above equation, N represents the number of ions per unit volume, e is the electronic charge, Z_T^* the transverse effective charge, m is the reduced mass of the ion and ω_{TO} denotes the frequency of the transverse optical phonon [12].

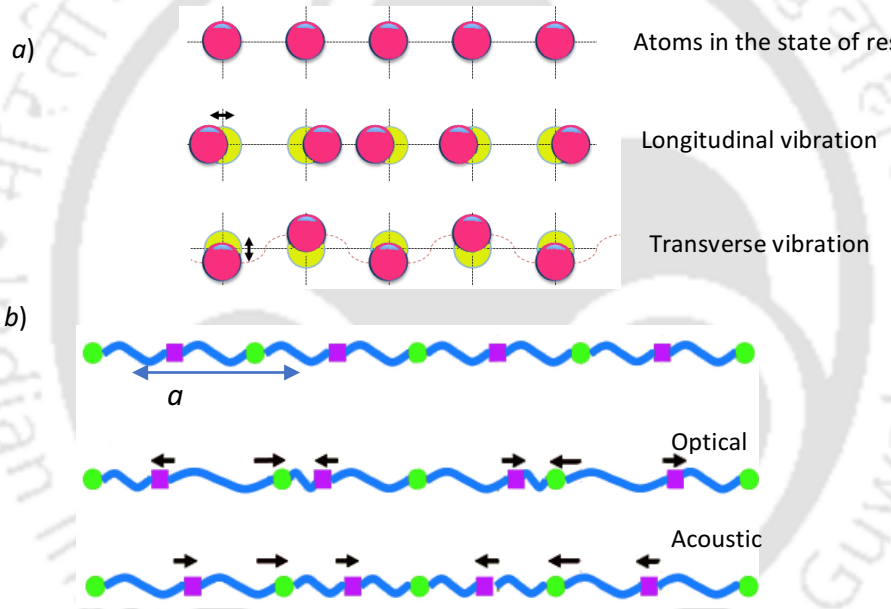

Figure 1.12. Visual representation of (*a*) Transverse and longitudinal mode of vibrations and (*b*) optical and acoustic modes. The double-headed arrow in (*a*) represents the direction of vibration of the particle.

1.4.1 Concept of Optical and Acoustical modes:

At equilibrium, every single atom in the lattice is positioned at its lattice site. But when an atom at equilibrium is displaced by a small amount, by the laws of nature, the restoring force developed will tend to return the atom back to its equilibrium position. This results in *lattice vibrations*. Since all the atoms are bound together by chemical bonds that acts like a spring that can stretch and compress, movement of one will cause the movement of its neighbouring atoms. This can result in many atoms to vibrate in unison with energy governed by the temperature. These lattice vibrations are responsible for the characteristic properties of matter such as Specific Heat, Thermal Conductivity, Dielectric properties and Electrical

Conductivity, Optical, etc. There are many elementary excitations with an associated particle that mediates the excitation. In the case for lattice vibrations, the mediating particle which carries the Quanta of mechanical vibrations and are collectively called as *Phonons*. The energy of this elastic mode of angular frequency ω and is excited by n phonons can be written as,

$$\epsilon = \left(n + \frac{1}{2}\right)\hbar\omega \tag{1.20}$$

The lattice vibration also gives rise to the concept of Longitudinal Wave (direction of displacement of the particle and direction of wave propagation are the same) and Transverse Wave (direction of propagation and direction of displacement are mutually perpendicular) [11]. It is assumed that the elastic response of the crystal is a linear function of these forces [13]. Bringing together the Hooke's law, we also assume that the force on the n^{th} plane caused due to displacement of the $n+q$ plane (q = ± 1) is proportional to the difference of their respective displacements. Total force and the equation of motion turn out to be as,

$$F_n = k(x_{n+1} - x_n) + k(x_{n-1} - x_n) \tag{1.21}$$

$$M\frac{d^2x_n}{dt^2} = k(x_{n+1} + x_{n-1} - 2x_n) \tag{1.22}$$

Where k is the force constant. These equations are for monatomic i.e. all the atoms have the same mass M and its solution between the zonal boundaries $K = 0$ to $K = \pm\frac{\pi}{a}$ comes out to be

$$\omega = \left(\frac{4k}{M}\right)^{\frac{1}{2}} |\sin\left(\frac{1}{2}Ka\right)| \tag{1.23}$$

With diatomic basis with different masses M_1 and M_2 the scenario completely changes. There are two equations of motion for each mass with displacements x and y respectively. This basis also gives rise to possibility for the *Optical* and *Acoustical* modes of vibration (figure 1.12). Acoustical phonons are lattice waves that occur due to in-phase displacement of the atoms in the crystal and can travel with the velocity of sound. The frequency of acoustical phonons is generally non-zero at the zone (Brillouin Zone) boundaries. Also, the optical phonons observed in multi-atom system where the lattice waves occur due to the displacement of atoms in the opposite direction, exhibits non-zero frequency in the zone boundaries. By solving the equation of motion, one can obtain the frequency for acoustical mode (ω_{act}) and the optical mode (ω_{opt}) for the long wavelength approximation ($Ka \ll 1$) as given below.

$$\omega_{opt}^2 = 2k\left(\frac{1}{M_1} + \frac{1}{M_2}\right);\ \omega_{act}^2 = \frac{ka^2K^2}{2(M_1+M_2)} \tag{1.24}$$

1.4.2 LST Relation:

R.H. Lyddane, R.G. Sachs and E. Teller studied the polar vibrations of alkali halides and reported important relation between the dielectric permittivity and phonon frequency [11,14]. Without making any specific hypothesis or any assumptions, these authors proposed a relation which connects the lattice vibrations to the dielectric permittivity. LST relation determines the ratio of the natural frequency of the longitudinal optical (LO) lattice vibrations (phonons) (ω_{LO}) to the natural frequency of the transverse optical

(TO) lattice vibration (ω_{TO}) for long wavelengths (or negligible wave vectors) which is equal to the ratio of static dielectric permittivity (ε_s) and permittivity at frequencies in the visible range (ε_∞).

$$\frac{\varepsilon_s}{\varepsilon_\infty} = \left(\frac{\omega_{LO}}{\omega_{TO}}\right)^2 \qquad (1.25)$$

Common applications of the LST relation are; (*i*) to predict one of the missing parameters among the four, (*ii*) to check the consistency of the experimental and the theoretically obtained values of phonon modes and dielectric permittivity, and (*iii*) conditions when phonon modes branches out multiple times [14,15].

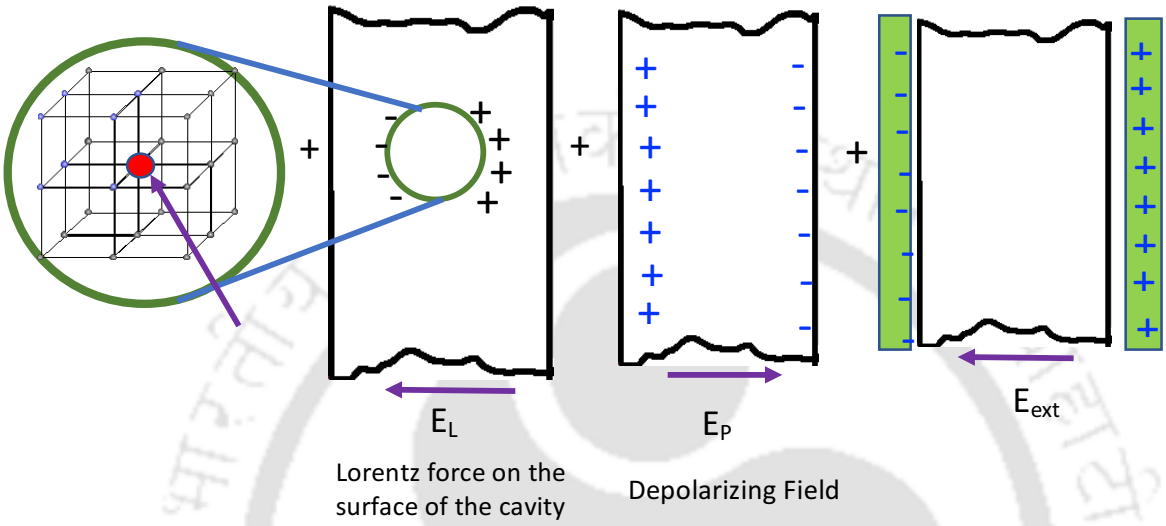

Figure 1.13. Schematic representation of the depolarizing field (E_P) and Lorentz force on the surface of the spherical cavity (Lorentz sphere) in the presence of external magnetic field (E_{ext}). This representation is useful in the determination of local electric field at the center of the spherical cavity.

1.5 Local Field Effects and the Clausius-Mossotti Relationship:

The *Clausius-Mossotti* relation is named after the Italian physicist Ottaviano - Fabrizio Mossotti who analysed the relationship between the dielectric constant of different media and was later confirmed by the German physicist Rudolf Clausius. In this context, the concept of *Local Electric Field* comes into the picture. Local Electric Field arrives on the fact that the electric field, **E**, is not expected to be same for a dipole on a microscopic level, when **E** = **V**/d is the average electric field over a macroscopic scale. This local electric field (E_{loc}) varies from the external electric field (E_{ext}) owing to the polarization of the surrounding medium (figure 1.13). The electric field experienced by a dipole, or in other words the local electric field can be expressed as,

$$\mathrm{E}_{loc} = (\mathrm{E}_{ext} - \mathrm{E}_{dep}) + \mathrm{E}_L + \mathrm{E}_{cen} \qquad (1.26)$$

where, E_{dep} is the depolarization field due to dielectric polarization, E_L is the Lorentz field due to the charges on the surface of the spherical cavity and E_{cen} (=0) is the contribution to the field due to charges within the sphere surrounding the dipole, which is zero for isotropic crystals. Lorentz field E_L and the depolarization field E_{dep} can be expressed as,

$$\mathrm{E}_L = \boldsymbol{P}/3\varepsilon_0 \; ; \mathrm{E}_{dep} = -\boldsymbol{P}/\varepsilon_0 \qquad (1.27)$$

Hence, $\mathrm{E}_{loc} = \mathrm{E} - \mathrm{P}/\varepsilon_0 + \mathrm{P}/3\varepsilon_0$ and substituting from equation 1.9, we obtain,

$$\mathrm{E}_{loc} = \frac{\mathrm{E}}{3}(\varepsilon_r + 2) \tag{1.28}$$

Here the macroscopic polarization $\boldsymbol{P}$ (dipole moment per unit volume) can be expressed as sum total of dipole moments of individual atom in the given volume. Hence,

$$\boldsymbol{P} = Np = N\alpha E_{loc} \tag{1.29}$$

$$(\varepsilon_r - 1)\varepsilon_0 \mathbf{E} = \frac{N\alpha \mathbf{E}(\varepsilon_r+2)}{3} \iff \alpha = \frac{3\varepsilon_0}{N}\left(\frac{\varepsilon_r-1}{\varepsilon_r+1}\right) \tag{1.30}$$

also,

$$\chi_s = \frac{\frac{N\alpha}{\varepsilon_0}}{1-\frac{N\alpha}{3\varepsilon_0}} \tag{1.31}$$

Equation 1.30 is also known as the *Clausius-Mossotti* relation. This relates the dielectric constant to the electronic polarizability [13]. Dielectric constant at optical frequencies arises almost entirely from the electronic polarizability. Hence this relation reduces to

$$\left(\frac{n^2-1}{n^2+1}\right) = \frac{4\pi}{3}N\alpha \qquad \text{(CGS)} \tag{1.32}$$

Above relation is also known as *Lorentz-Lorenz* equation.

1.6 Crystals Symmetries:

It is well known that the point symmetry groups in three dimensions require 14 different types of

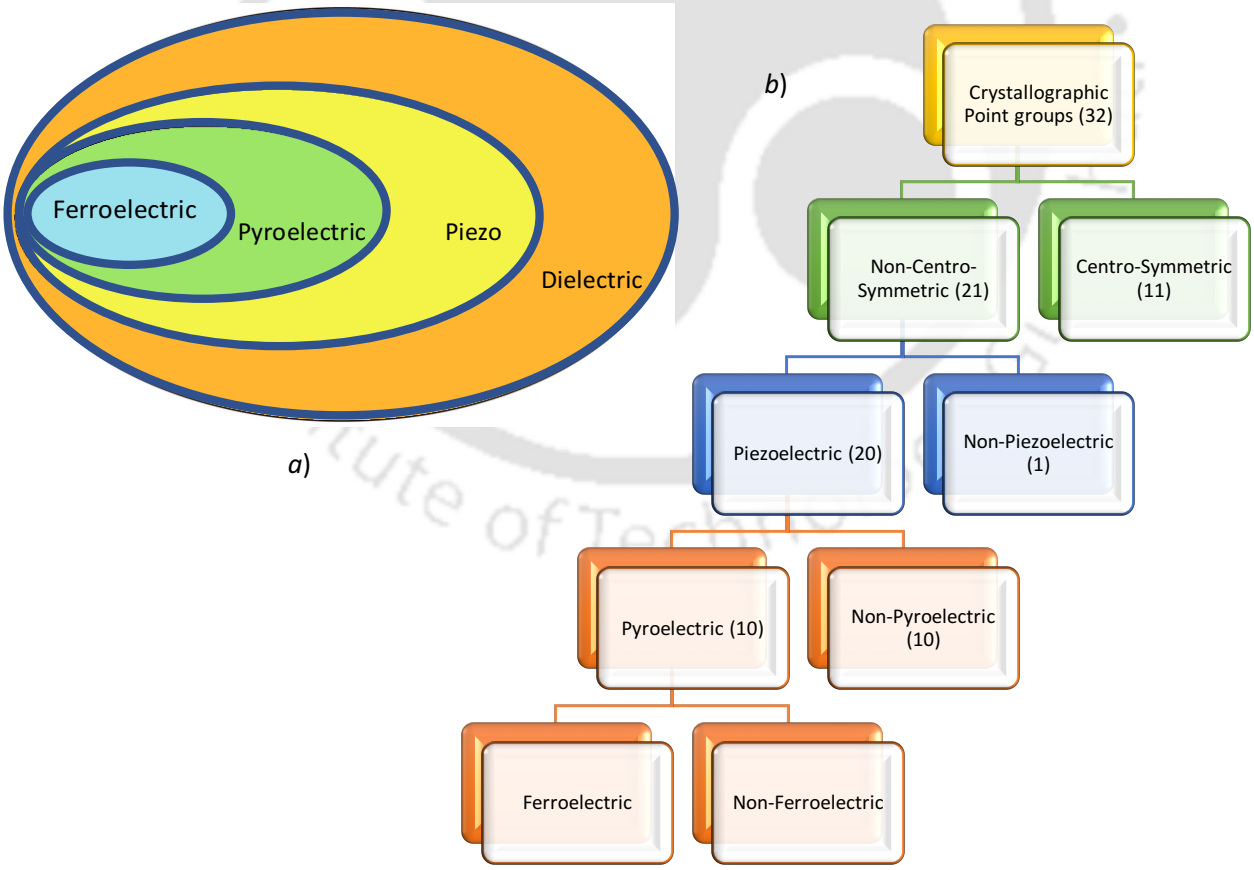

Figure 1.14. (*a*) Pie-chart representation of the classification of dielectrics, Pyroelectrics, and Piezoelectrics. (*b*) Flowchart representing the classification of crystallographic point groups based on their symmetries.

lattice with 7 crystal systems. Based on the symmetry, rotation and mirror planes of the crystals that determine the main features of the crystals, there are 32 crystallographic point groups defined by different *symmetry* operations [16,17]. Symmetry can be understood as consistency or the repetition of something in space and/or time bringing back to its original form. Symmetry is used to characterize the crystals and hence identify the repeating parts of the molecule which helps in simplifying the data collection since the physical properties includes symmetry of the crystals [18]. The most common symmetry operators are Identity, Mirror (reflection), Centre of Symmetry (inversion) and Rotation.

a)

Crystal Class	Centro-Symmetric		Non-Centro-Symmetric				
			Polar		Non-Polar		
Cubic	*m*3	*m*3*m*	none		**432**	$\bar{3}m$	23
Tetragonal	4 or *m*	4 or *mmm*	4	4*mm*	$\bar{4}$	$\bar{4}2m$	22
Orthorhombic	*mmm*		*2mm*		222		
Hexagonal	6 or *m*	6 or *mmm*	6	6*mm*	$\bar{6}$	$\bar{6}2m$	622
Trigonal	$\bar{3}$	$\bar{3}m$	3	3*m*	32		
Monoclinic	2 or *m*		2	*2m*	none		
Triclinic	$\bar{1}$		1		none		
TOTAL	11		10		11		

b)

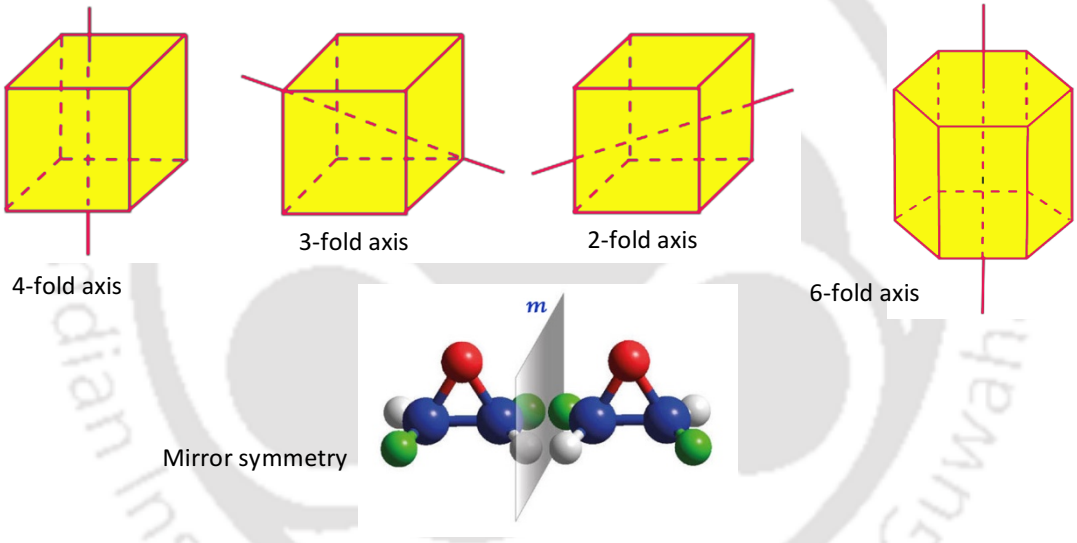

Figure 1.15. (*a*) List of crystal symmetries along with their point groups for all the seven crystal systems (cubic class 432 (in red) does not possess piezoelectricity), and (*b*) Representation of different symmetry operations including mirror symmetry.

Among the 32 crystallographic point groups, only 11 contain the centre of symmetry, these are Centro-Symmetric class of crystals (they are also known as *Laue groups*), and the rest of 21 are Non-Centro-Symmetric class of crystals, which exhibits ferroelectricity (figure 1.14). Out of the 21 Non-Centro-Symmetric point groups, 10 belong to polar crystals and the rest non-polar. Among the Non-Centro-Symmetric structures, 20 exhibit piezoelectric properties, and only 1 which does not. By the definition of the piezoelectric effect, all components of the piezoelectric tensor should vanish inside the crystal possessing the centre of symmetry. In the remaining 21 Non-Centro-Symmetric crystallographic classes, the piezoelectricity may exist, except for the cubic class 432, where the piezoelectric charges developed along the ⟨111⟩ polar axes cancel each other [19]. Crystal class along with their point groups is shown in figure

1.15. Combining a total of 32 crystallographic point groups and 14 *Bravais lattices*, there are about 230 different ways to arrange a finite object in 3-dimensional space. In the following sections, we have provided a brief outlook into piezoelectricity, pyroelectric and ferro/-antiferroelectricity.

1.6.1 Piezoelectricity:

Piezoelectricity follows the direct translation from the Greek word *piezein* meaning 'pressure electricity' was discovered by Jacques Curie and Pierre Curie in 1880 (Curie Brothers). This phenomenon was observed in crystals such as tourmaline, topaz, cane sugar and Rochelle Salt [19]. Curie brothers, however, could not predict a converse piezoelectric effect, i.e., deformation or stress under applied electric field. This property was later mathematically solved from the fundamental thermodynamic principles by Lippmann (1881) which was followed by the experimental confirmation by Curie brothers [19]. Piezoelectric crystals are one of the important classes of materials that convert mechanical energy into electrical energy and vice versa [20,21]. These materials make up the basis of scientific instruments like atomic force microscopy which can analyse the topology of the material on nanoscale. When the application of mechanical energy results in the generation of electrical energy, this is termed as *Direct piezoelectric effect* [21].

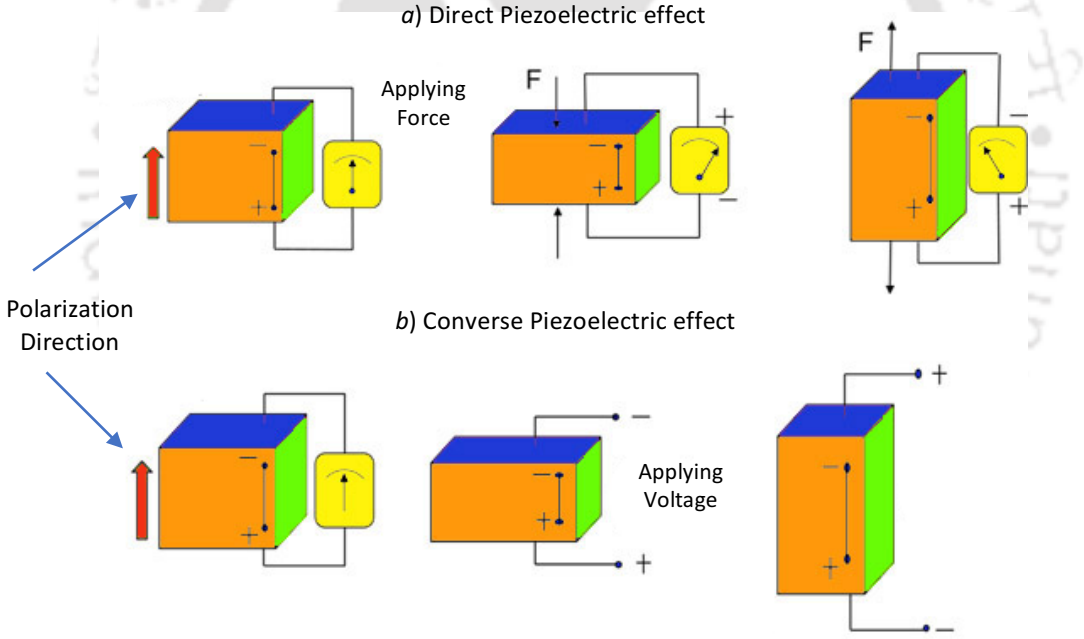

Figure 1.16. Direct and Converse Piezoelectric effects showing the direction of applied stress (force) and the resulting direction of field (or voltage) for direct piezoelectric effect (*a*). Also, the direction of applied field and the strain developed for converse piezoelectric effect (*b*).

The linear relationship between the applied stress σ_{jk} and the resulting charge density D_i may be written as,

$$D_i = d_{ijk}\sigma_{jk} \tag{1.33}$$

where d_{ijk} is a rank-three tensor with unit CN^{-1} and D_i is the induced charge density. Its matrix form turns out to be,

$$\begin{bmatrix} D_1 \\ D_2 \\ D_3 \end{bmatrix} = \begin{bmatrix} 0 & 0 & 0 & 0 & d_{15} & 0 \\ 0 & 0 & 0 & d_{24} & 0 & 0 \\ d_{31} & d_{32} & d_{33} & 0 & 0 & 0 \end{bmatrix} \times \begin{bmatrix} \sigma_1 \\ \sigma_2 \\ \sigma_3 \\ \sigma_4 \\ \sigma_5 \\ \sigma_6 \end{bmatrix} \quad (1.34)$$

Piezoelectric materials also have another interesting phenomenon i.e. they change their dimensions (i.e. they contract or expand) with the application of the electric field. This is also known as The *Converse piezoelectric effect*. Figure 1.16 shows the direct and converse piezoelectric effects. The relation between the strain, s_{ij} developed and the electric field E_k applied is,

$$s_{ij} = d_{ijk} E_k \quad (1.35)$$

where d_{ijk} is with unit mV^{-1}, and its matrix form is,

$$\begin{bmatrix} x_1 \\ x_2 \\ x_3 \\ x_4 \\ x_5 \\ x_6 \end{bmatrix} = \begin{bmatrix} 0 & 0 & d_{31} \\ 0 & 0 & d_{32} \\ 0 & 0 & d_{33} \\ 0 & d_{42} & 0 \\ d_{51} & 0 & 0 \\ 0 & 0 & 0 \end{bmatrix} \times \begin{bmatrix} E_1 \\ E_2 \\ E_3 \end{bmatrix} \quad (1.36)$$

The matrix forms are the result of the reduced form of the equations 1.33 and 1.35. These equations can be simplified using the *Voigt conversion* [22]. The piezoelectric coefficients for direct and converse are thermodynamically identical. It is to be observed that the sign of the piezoelectric charge D_i and strain x_{ij} produced due to the applied mechanical and electrical field, respectively depend greatly on the direction with which they are applied. The coefficient d is sometimes referred to as the *piezoelectric charge constant*, which is the polarization generated per unit of mechanical stress applied to the piezoelectric material or alternatively, is the mechanical strain experienced by the piezoelectric material per unit of electric field [22].

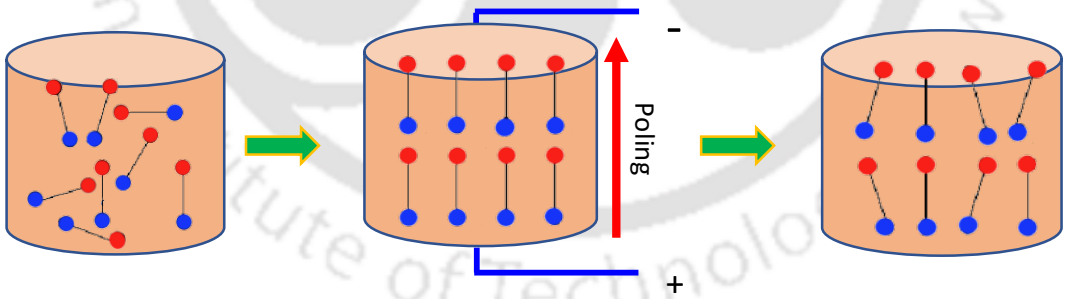

Figure 1.17. Schematic diagram showing the alignment of dipoles before and after the application of electric field (or poling voltage). Red dots represent positive pole/charge and blue dots represents the negative pole/charge.

We can now understand that for piezoelectric interaction to occur, it is in fact necessary that certain axes of the medium intrinsically possess a directionality or polarity. In some crystals, this polarity is inherent by the symmetry of crystal classes, but for some isotropic crystals and other crystal classes, this inherent polarity is absent. In these crystal types, the polarity that is needed to induce piezoelectric properties more or less permanent by momentarily applying a strong electric field near T_C, orienting the dipoles/domains in a particular direction even after the removal of the applied field (figure 1.17). This process is called *Poling*

(This is analogous to magnetizing of a permanent magnet) [23]. Most of the ferroelectrics have to be poled to be useful as piezoelectric crystals. In the undisturbed state, the polarization directions are so randomly oriented resulting a net polarization. However, the amount of polarization also depends on the structure of the material due to the counteracting internal strains i.e. for example tetragonal structures can reach up to more than 80% polarization, whereas orthorhombic can reach up to 90% [24].

1.6.2 Pyroelectricity:

Pyroelectricity is one among the useful and active research areas of the High-κ dielectrics [23]. Pyroelectricity is the capacity of some materials to generate a voltage when they are subjected to heat (thermal energy).

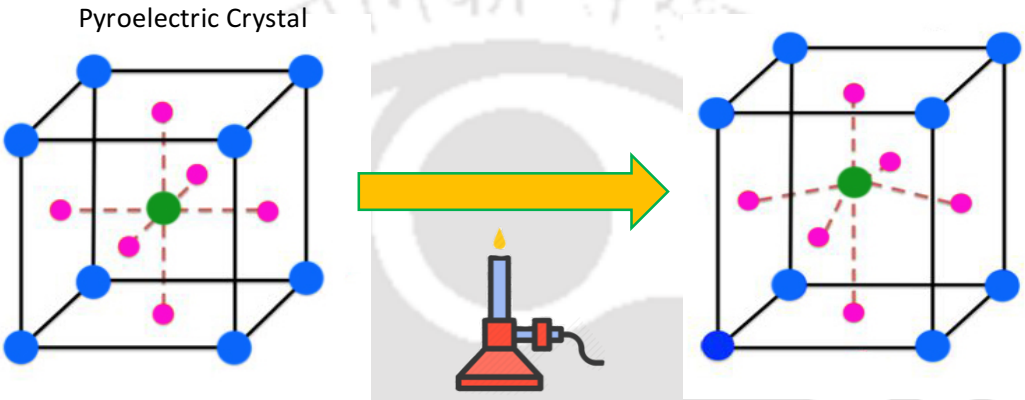

Figure 1.18. Schematic representation of Pyroelectric effect showing the displacement of center of symmetry.

We had previously 21 out of the 32 crystal classes are classified as piezoelectrics. Out of these 20 point groups of piezoelectric materials, 10 crystal classes exhibit a unique polar axis in the unstrained condition for which the polarization changes with the temperature [23,24]. The term pyroelectricity has originated from the Greek word '*Pyr*' meaning fire and electricity. Pyroelectrics are those class of materials in which spontaneous polarization is developed by the change in temperature and the property is called as *pyroelectricity* (figure 1.18). This change in spontaneous polarization (ΔP) with a change in temperature (ΔT) can be expressed as

$$\Delta P = -\boldsymbol{p}\Delta T \qquad (1.37)$$

In the above expression, $\boldsymbol{p}$ is the pyroelectric coefficient and is a vector quantity and remains invariant under all symmetry operations of crystal [25]. Thus, by symmetry, all pyroelectric crystals are piezoelectric, but the converse is not true and hence there can be two possible contributions towards pyroelectricity. That is one can experimentally observe pyroelectricity just by heating the crystal, but can be performed in two different ways. One is to fix the shape or size of the crystal while heating, and in the other way is to allow the crystal to expand freely without restricting its appetite for thermal expansion. In the former case, the effect observed can be considered to be as the *primary pyroelectricity* and the latter is known as *secondary pyroelectricity* (where the piezoelectric contributions come in the picture). Hence, in the case of free-crystal total expression for pyroelectricity can be written as

$$\left(\frac{d\boldsymbol{P}}{dT}\right)_{\sigma,E} = \left(\frac{d\boldsymbol{P}}{dT}\right)_{s,E} + \left(\frac{d\boldsymbol{P}}{ds}\right)_{T,E} \times \left(\frac{ds}{dT}\right)_{\sigma,E} \quad (1.38)$$

Few limited number of pyroelectrics has an additional property by which it can change the direction of polarization with the application of electric field or mechanical stress. When the change is primarily due to electric field, it is often called *ferroelectric*, and when it is primarily due to stress, then the material is said to be *ferroelastic*.

1.6.3 Ferroelectricity and Curie Temperature:

Among the pyroelectrics, some exhibits spontaneous polarization and the direction of polarization can be reversed by the application of electric field. This property is called *ferroelectricity*. A ferroelectric material has permanent dipole moment analogous to ferromagnetic materials (which has permanent magnetic dipoles). The phenomenon of ferroelectricity was first observed in 1917, while A.M. Nicholson, J.A. Anderson and W.G. Candy noted some anomalies in its dielectric behaviour while investigating the piezoelectric properties of Rochelle salt ($KNaC_4H_4O_6.4H_2O$) [26]. Also, these scientists also observed sudden change in the piezoelectric activity at ~ 298K which is now recognized as the first observation of *ferroelectric Curie Point*. Later in 1921 these properties were described in detail by J. Valasek [26]. This is also the reason why ferroelectricity is also referred to as *Rochelle Electricity* or *Signette Electricity* [27]. The term ferroelectricity was given to this phenomenon due to its similarity with ferromagnetism in magnetics, and not because it is observed in iron and iron-based materials. Another phenomenon that is common to both ferroelectric and ferromagnetic materials is the existence of a critical temperature popularly known as the *Curie Temperature* (T_C). At T_C, the permittivity reaches its maximum and beyond this temperature permittivity drops significantly. This amount of drop beyond the Curie temperature is governed by the Curie-Weiss Law which is given by

$$\varepsilon_r = \frac{A}{T - T_C} \quad (1.39)$$

where A is the material constant, T is the measuring temperature above T_C (different sources can give different form of the same equation. The one provided here is from [28]). Hence at this temperature, the material generally transforms from polar, non-centrosymmetric ferroelectric phase to non-polar, centrosymmetric paraelectric phase. One of the striking features of ferroelectric materials is that Polarization ($\boldsymbol{P}$) versus electric field ($\mathbf{E}$) hysteresis loop. All the ferroelectrics in small fields behave like a normal dielectric and exhibits a linear relationship between polarization and electric field. However, as the field increases, more and more randomly oriented domains reorient themselves in the direction of the applied field which increases in polarization. After certain field value, there will be no more domains left to orient in the direction of field resulting in a full-saturation, commonly known as *Saturation polarization* (P_{sat}). It can be noticed that when the field is removed, not all domains returns to its state of randomness and thus resulting in a *Remanent polarization* (P_r). Thus, some additional field is to be applied in the opposite direction to bring the system back to its original state (i.e. $\boldsymbol{P} = 0$). The additional amount of electric field required for this switching of the polarization is called the *Coercive field* (E_C). Figure 1.19 shows the ideal ferroelectric P-E hysteresis

loop. Among the ferroelectric materials, perovskite related compounds have been studied most, primarily due to their exciting properties and reasonably high transition temperatures, making them attractive for various applications.

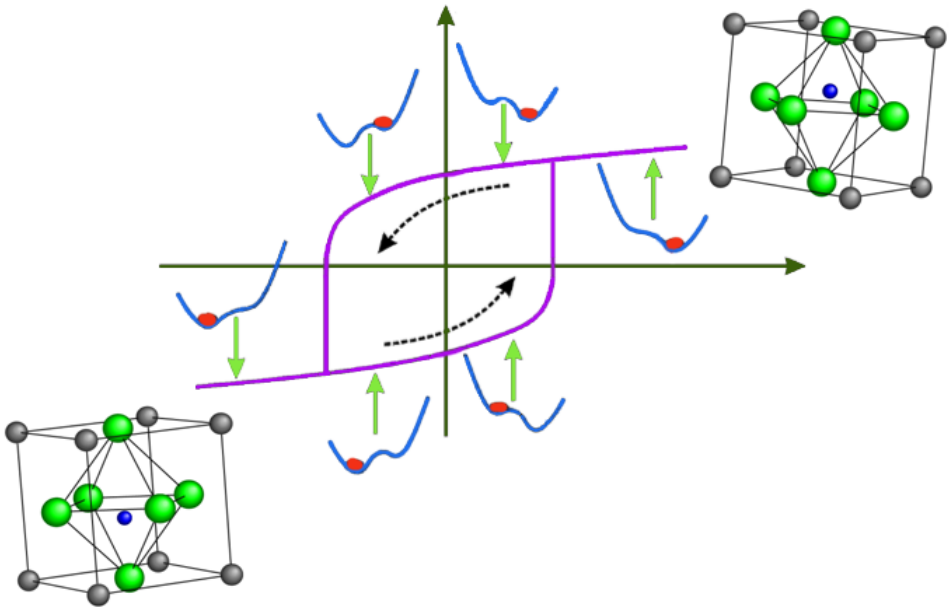

Figure 1.19. Typical P-E hysteresis-loop observed for an ideal ferroelectric system along with the schematic of energy band diagram resulting from the atomic displacement [30].

1.6.3.1 Landau Theory:

Ferroelectricity was explained by three different theories and they are (*i*) first principle theory (*ii*) soft-mode theory and (*iii*) Phenomenological theory [29]. But the bridge between these theories and the experiments were established based solely on symmetry considerations by Landau [30-33]. Landau's theory provides a reliable description of the equilibrium of a system around its phase transition. Landau, in his papers, noted that a 'system cannot change smoothly between two phases of different symmetry; the continuous path that a system can take between its transition from liquid to gaseous around a first-order critical point is possible because of no involvement of symmetry change [30,34]. Landau characterizes an order parameter to define transition in such a way that this parameter is zero at its maximum symmetry (disordered state), and gradually gains a finite value when the system achieves low-symmetry. This order parameter for paraelectric-ferroelectric transition is polarization ($\boldsymbol{P}$). The free-energy parameter $\mathcal{F}(\boldsymbol{P})$ is expanded near the transition as power series and the state of the system is found by minimizing $\mathcal{F}(\boldsymbol{P})$. Landau's theory thus gives a conceptual bridging between the microscopic models with the macroscopic phenomena since the theory assumes the spatial average of local functions. The free-energy function $\mathcal{F}(\boldsymbol{P})$ can be written as

$$\mathcal{F}(\boldsymbol{P}) = \frac{1}{2}a\boldsymbol{P}^2 + \frac{1}{4}b\boldsymbol{P}^4 + \frac{1}{6}c\boldsymbol{P}^6 + \cdots \qquad (1.40)$$

were a, b and c are temperature dependent parameters and takes part in deciding the nature of the phase transition and dielectric behaviour near the Curie temperature (T_C). For the ferroelectric phase the

coefficients a and c are positive. These coefficients can be determined from experiments or from *First-Principle calculations*. Landau theory works better for those systems which has high coordination number and long-range ordered systems [30].

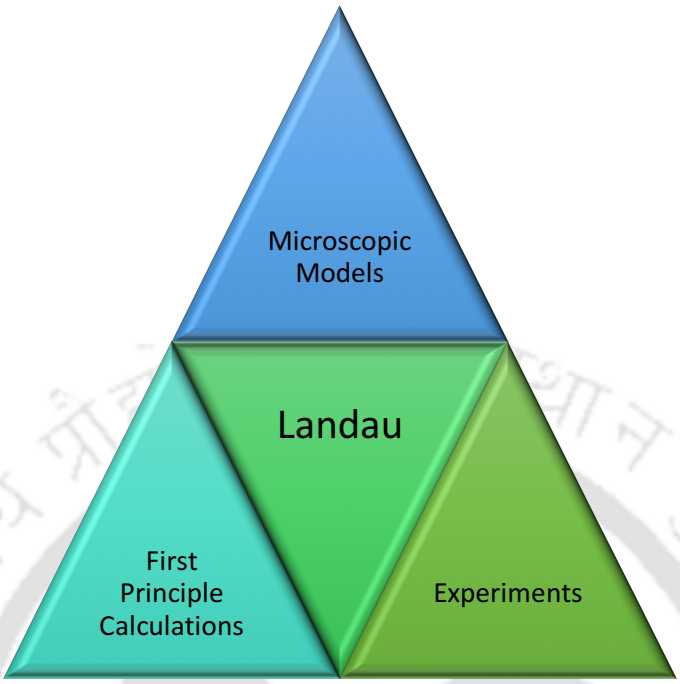

Figure 1.20. Schematic picture showing the relationship between the first principle theory, experiment and the microscopic model with Landau theory in the vicinity of phase transition.

1.6.3.2 General Phenomenology or the Landau-Devonshire Theory:

The symmetry-based treatment of phase transition put out by Landau was first applied to ferroelectric systems by Devonshire [35,36]. Landau theory employs two main fundamental postulates of thermodynamics, one is that free energy can be generally expressed as a function of ten variables and the second being the value of the dependent variable that can be obtained from the free energy minima. Choosing the origin for the free-energy for an unpolarised, unstrained crystal to be zero, we truncate the power series to the sixth power with the key approximation that one can expand the free energy in the powers of dependent variables as below.

$$\mathcal{F}(\boldsymbol{P}) = \frac{1}{2}a\boldsymbol{P}^2 + \frac{1}{4}b\boldsymbol{P}^4 + \frac{1}{6}c\boldsymbol{P}^6 - \mathrm{E}\boldsymbol{P}\,,\ where\ \mathcal{F} = dF/dV \qquad (1.41)$$

In the above equation, F is the total free-energy and $\mathcal{F}$ is the free-energy density. By determining the minima of the above expression at $d\mathcal{F}/d\boldsymbol{P} = 0$, we obtain the linear susceptibility to be,

$$\mathbf{E} = a\boldsymbol{P} + b\boldsymbol{P}^3 + c\boldsymbol{P}^5 \Rightarrow \chi = \frac{P}{E} = \frac{1}{a} \qquad (1.42)$$

Landau Theory also assumes that around Curie point ($T \sim T_0$), except for a, other coefficients of the free-energy expansion are independent of temperature. Hence,

$$\mathcal{F}(\boldsymbol{P}) = \frac{1}{2}a_0(T - T_0)\boldsymbol{P}^2 + \frac{1}{4}b\boldsymbol{P}^4 + \frac{1}{6}c\boldsymbol{P}^6 - \mathbf{E}\boldsymbol{P} \qquad (1.43)$$

Here the temperature T_0 is defined as that temperature when the sign of $'a'$ changes, and this is close to the T_C, but not equal to T_C. The sign of $'b'$ will determine the nature of transition between the two configurations (ferroelectric to paraelectric) along with the free-energy. Also, a_0 and c are both positive in every known ferroelectric [37,38]. Both ferroelectric and paraelectric phases co-exists at T_C and are associated with the latent heat. Generally, for first-order transition $b < 0$ and for second-order transition $b > 0$. When considering a second-order transition where $b > 0$, spontaneous polarization is estimated by setting $\mathbf{E} = 0$ in the equation 42. Retaining the two low-order terms we obtain

$$\boldsymbol{P}_0 = \left[\frac{a_0}{b}(T_0 - T)\right]^{\frac{1}{2}} \quad (1.44)$$

$$\kappa = \frac{1}{\chi} = \frac{E}{P} = 2a_0(T - T_0)\ at\ T < T_0 \quad (1.45)$$

here κ is the *dielectric stiffness coefficient*. Furthermore, strain as a function of polarization ($s(\boldsymbol{P})$) was also brought into consideration for deducing the free-energy ($\mathcal{F}(\boldsymbol{P}, s(\boldsymbol{P}))$).

1.6.3.3 The Soft-Mode and First Principle Theory:

In 1959, Cochran made a break-through relating the instability of the crystal with the lattice dynamics and considered lattice mode as the basic variable. This came out to be the *soft-mode theory* [39]. Cochran pointed out that at second order ferroelectric transitions where the dielectric constant diverges, there must be a transverse optical lattice vibration mode whose frequency goes to zero as the transition is approached. This idea turned out to be an outstanding contribution towards ferroelectric theory and research [40]. It cannot be denied that the soft-mode concept was put out by several other scientists prior to Cochran, were one of the earliest mentionings about soft phonon is in the paper of C.V. Raman and T.M.K. Nedungadi [40,41]. According to this theory, the transition of the ferroelectric phase takes place due to lattice instability because of the softening of optical phonon modes. Once this softening occurs, the atoms will be displaced from its original position or in other words its equilibrium position, and there are no more restoring forces acting on the atoms to bring them back to their original position. This theory was successful in explaining the structural and ferroelectric transitions in perovskites (ABO_3). Later in 1990, ferroelectricity was better and clearly explained by first principle theory. According to this theory, off-centring of the atom is favoured by long-range Coulomb forces which can, in turn, result in larger electrostatic energy that can displace the atoms from their ideal position of the perovskite structure. The core of this theory is mostly *Density Function theory* and specifically *Local Density Approximation* [42].

1.6.4 Antiferroelectricity:

According to the standard definition provided by Lines and Glass, an antiferroelectric phase is that state obtained by the condensation of non-polar lattice modes which can exhibit large dielectric anomalies near the transition temperature and can transform itself into a ferroelectric state by the application of electric field [43]. This is because the ferroelectric phase is close in energy to the antiferroelectric phase whose transitions can be induced with the help of electric field which is characterized by a double hysteresis

loop [44,45]. Antiferroelectrics are generally antipolar materials that develop long-range order but do not possess spontaneous polarization. Charles Kittel, in 1951 remarks antiferroelectric state as one in which lines of ions in the crystal are spontaneously polarized, but has their neighbouring lines polarized in the antiparallel direction in such a way that the net macroscopic polarization is zero [46].

Spontaneous polarization in ferroelectrics is believed to be present as a result of *Lorentz Catastrophe* in which the constant of proportionality between applied electric field and polarization exhibits singularity [46]. Contributions from Slater, Devonshire and Wul to this theory reveals that this phenomenon can also be responsible for the arrangement of the dipoles in an antiferroelectric fashion [47-49]. Here we assume the lattice to be made of two identical interpenetrating lattices x and y with polarizations $\boldsymbol{P}_x$ and $\boldsymbol{P}_y$ respectively. The free-energy (Helmholtz) expression per unit volume comes out to be,

$$\mathcal{H}(\boldsymbol{P}_x, \boldsymbol{P}_y, T) = \mathcal{H}_0 + f(\boldsymbol{P}_x^2 + \boldsymbol{P}_y^2) + g\boldsymbol{P}_x\boldsymbol{P}_y + h(\boldsymbol{P}_x^4 + \boldsymbol{P}_y^4) \qquad (1.46)$$

Where f, g and h are temperature dependent functions, so that the spontaneous polarization ($\mathbf{E} = 0$) in the antiferroelectric state ($\boldsymbol{P}_{sx} = -\boldsymbol{P}_{sy}$) can be given by,

$$\boldsymbol{P}_{sx}^2 = (g - 2f)/4h \qquad (1.47)$$

at Curie temperature $\boldsymbol{P}_{sx} = \boldsymbol{P}_{sy} = 0 \Longrightarrow g = 2f$

Assuming that f, related to the atomic polarizabilities, varies with temperature near the Curie point is

$$f = \frac{1}{2}g + \lambda(T - T_C) \qquad (1.48)$$

where, λ is a constant. If λ >0, the antiferroelectric region lies on the low temperature side of the Curie point and the dielectric constant changes slope slightly. If λ < 0, the antiferroelectric state lies on the high temperature side of the Curie point with dielectric constant achieving local minima [46]. Above discussion is for a second-order transition. Devonshire commented that, for greater flexibility into the treatment of dielectric constant near Curie point, it is easier to account for the transition of ferroelectric from polarized to unpolarized as a first-order transition rather than second-order. Later Kittel concludes that "if the ferroelectric transition is first-order, there will be a discontinuity in dielectric constant, whereas on the other hand, if it is second-order, the crystal will have high dielectric constant at Curie point.

1.7 Transition Metal Oxides:

This section deals with the physics of first-row transition metal oxides (TMO) because the current thesis is dedicated to the composites made-up of alkaline niobates ($NaNbO_3$ and $KNbO_3$) and TMO based Mott insulators. According to Schrödinger's wave equation for the hydrogen atom, three main quantum numbers are needed to define the shape, size and orientation in 3D space, and they are principal (n), angular (l) and magnetic (m). For d-orbitals the value of principle and the angular quantum number are 3 and 2 respectively, and d-orbital results in five sub-orbitals with magnetic quantum number m_j as -2, -1, 0, 1, 2. These five d-orbitals are called d_{xy}, $d_{xz}, d_{yz}, d_{x^2-y^2}$ and d_{z^2} (figure 1.21) with the transition metal atom placed in the origin $(x, y, z) = (0,0,0)$. Three of these five d-orbitals (d_{xy}, d_{xz}, d_{yz}) are degenerate and orients in between the Cartesian axes, whereas the remaining two orients along the axes. The five d-oribital

energy splits into two bands in which the orbitals aligned between the Cartesian axes constitute the t_{2g} band. The other two which are aligned along the axes constitute the e_g band and the energy difference between these two bands is termed as the *crystal field splitting*.

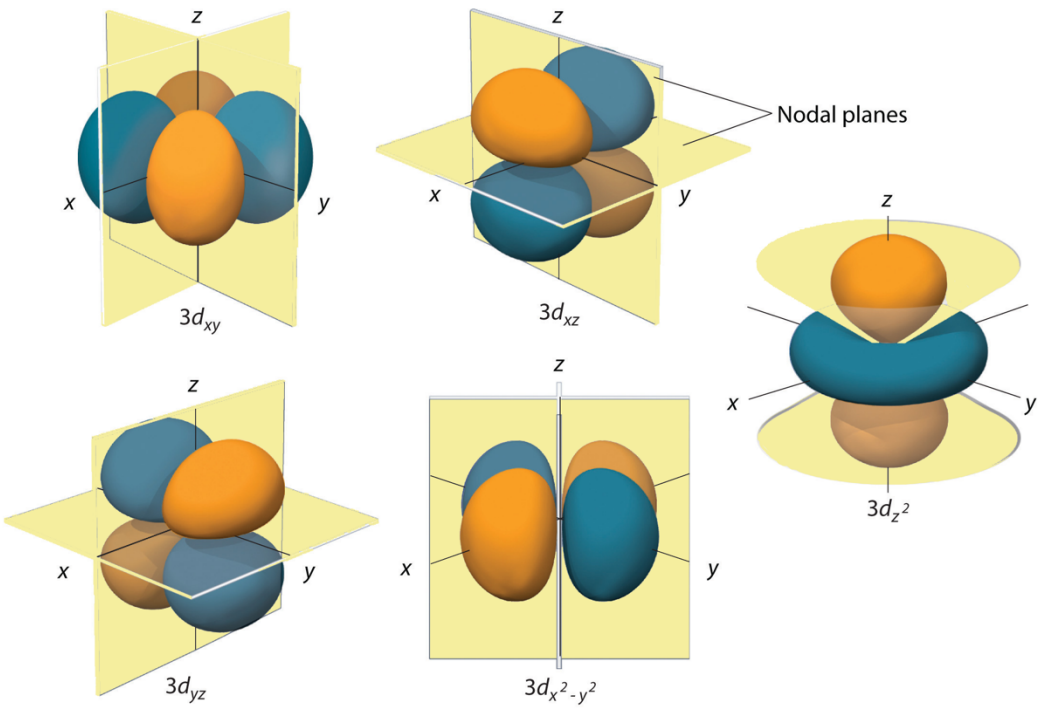

Figure 1.21. Five *d*-orbital along with their shapes and conventional designations.

The International Union for Pure and Applied Chemistry (IUPAC) defines transition metals as those elements whose atoms have partially filled d-orbital or those whose cations with an incomplete d shell [50]. This mostly includes the elements from the group 3-12. The f-block elements- the lanthanides and actinides also comes under the category of transition metals and are commonly referred to as the *inner transition metals* because they have atomic numbers that fall between the first and second element of the last two rows. Hence the main difference of this category of metals is that the valence electron can be present in more than one shell and hence most of the transition metals have more than one *oxidation state*. In the first transition series, the oxidation state range from one to seven in which Manganese, with electronic configuration [Ar]$4s^2 3d^5$ shows the maximum oxidation state (+7), in the second, oxidation state range between one to eight, in the third from two to eight and so on [51]. One of the reasons for this varying oxidation state takes you back to one of the basic concepts that say 'Half-filled and full-filled orbitals are more stable than partially filled orbitals. This is because the electrons in each orbital of the same subshell which has similar spin can exchange their positions leading to a decrease in overall energy known as the *exchange energy*. More the number of these exchanges more is the energy released through exchanges, and hence more stability. Keeping aside the fact that these oxides are easily tunable for their electric and magnetic properties, they possess a variety of properties which includes superconductivity [52]. Although

superconductivity has been understood and studied from long, high-temperature superconductivity was the ground-breaking discovery and was discovered in cuprates [53,54]. Hence, transition metals constitute one of the interesting class of materials which exhibits a variety of structural and physical properties whose origin is not yet clearly known which has turned out to be an alluring factor for much ongoing research in the field of condensed matter physics and material science.

1.7.1 Magnetism in TMOs:

In most of the TMOs, the magnetic interactions are mostly due to mixed-valence state i.e. more than one valence state in the same atom on crystallographically equivalent sites [55]. Some of the basic interaction which are important to possess magnetism in the localized $3d$ electrons are intra-atomic Coulomb interaction, crystal and ligand field, spin-orbit coupling, Jahn-Teller Effect and exchange Interaction (J_{EX}). The Inter-Atomic interaction makes it energetically unfavourable to occupy two electrons in the same orbital state. This is one of the reasons for the birth of *Mott-Insulators* (section 1.7.2). Crystal and ligand field splitting is of the order of electron-volts and the interaction is comparable to that of the interatomic Coulombic interaction. Whereas, in the case of Spin-Orbit interaction, the interaction energy is smaller compared to that of inter-atom and the crystal field. The structure and properties of a system are determined by the motion of its electron and nuclei and also by their interaction. Jahn-Teller effect is the name applied to the phenomenon that generally occurs in systems with electronic states that are degenerate and can lead to unstable symmetry configurations. This can give rise to a strong electron-vibrations (*vibron*), which can lower the symmetry through structural transitions [56]. However, it does not predict the direction of distortion. Moreover, the exchange interaction (direct, or super-exchange) mechanism between the magnetic ions is a dominant interaction in magnetic oxides where the transfer of electrons occurs via an oxygen ligand which depends on the mutual orientation of the spins. In ferrites, this is the strongest interaction leading to the formation of ferrimagnetism and antiferromagnetism [55].

1.7.2 Mott-Insulators:

Band theory predicts a state that will not conduct electricity (insulating) when all the bands are fully occupied or entirely empty. It has come to notice that it is possible to have an insulating system even when the band theory predicts a metallic state, due to Coulombic interactions. These compounds which are theoretically conductors, but insulators in real, are collectively termed as *Mott-Insulators*. This was the consequence of the theoretical approach carried out by N.F. Mott on the effect of the electron-electron interaction (later awarded Nobel Prize for Physics in 1977) [57]. Typically, this happens when the bandwidth W is smaller than the intra-orbital Coulomb matrix element U and thus the stronger Coulombic force restricts the electron from hoping to another atom [58]. The idea of “Metal” and “Insulator” are strictly limited down to temperatures close to zero, as a matter of fact, “insulators” displays small finite amount of conductivity. One of the striking difference from that of the normal band insulators is that the internal degrees of freedom

such as spin and orbit still survive in Mott-Insulator. These insulators also possess a peculiar property in which the conductivity vanishes as the temperature tends to zero even though the band theory predicts it to be metallic [59]. Among such large class of Mott insulators, TMO based Mott-Insulators having wide-energy band-gap such as NiO, CoO and MnO are considered as potential materials for the applications in solar cells, thin-film transistors (TFTs), Spin-Valves, Magnon Transistors, lithium-ion batteries and gas-sensors [60-62]. Some important properties of TMO based Mott insulators are flexibility in production, low cost and simplicity in use, and large number of detectable gases which make them reliable for gas sensors devices which can be widely used in controlling industrial emission, household security, vehicle emission control, environmental monitoring and food nutrition and safety [62-65]. In particular, NiO, a wide $d-d$ energy-gap Mott insulator, is a very interesting material for its various applications in super-capacitor, exchange bias controlled spin valve and electrochromic devices [65]. Bulk NiO exhibits an antiferro- to paramagnetic transition across the Néel temperature T_N(~ 523 K) associated with the low-temperature rhombohedral phase (space-group R-3m) to high-temperature cubic phase (space-group *Fm-3m*) transition. Such a high value of T_N (T_N > Room Temperature) which can be tuned to near room temperature makes NiO as a potential candidate for spin-valve device applications [62]. These reasons motivated us to work in the field of Mott insulators and high-κ dielectric composites both from fundamental and applications point-of-view. The results and analysis of such composites will be discussed in the coming chapters.

भारतीय प्रौद्योगिकी संस्थान गुवाहाटी
Indian Institute of Technology Guwahati

Chapter 2
Materials and Methods

In this chapter, details of the experimental procedures and experimental techniques employed in this work are presented. First the procedures used to synthesize the samples are presented. This is followed by adequate description of the experimental techniques used for characterization and measuring the various properties of the sample.

2.1 Synthesis of the bulk $ANbO_3$ (A = Na, K) ceramics:

The standard solid-state reaction technique is the conventional method widely adapted for the preparation of alkaline niobates which involves multiple steps such as Ball-Milling, pre-calcination which leads to the volatilisation of alkaline species and crystallizing water resulting in the formation of the precursor. This product upon further heat-treatment for long duration at high temperatures (sintering) yields the final perovskite product. This final product is usually very soft, less dense, hygroscopic and brittle which makes it a challenge in handling for further characterization (discussed from section 2.3) [66].

2.2 Standard Solid State Reaction Technique:

The solid-state reaction technique is one of the easiest, cost-effective and thermodynamically stable method to synthesize the ceramic systems [67]. One of the main advantages of this technique is that one can choose a wider spectrum of precursors such as oxides and carbonates. As the name suggests, the starting materials are mostly in solid form (powder). Starting materials should be mixed thoroughly to obtain a homogenous mixture, and then they have to be heated as the solids will not react with each other at room temperature. In the following sections, the different steps involved in this solid-state reaction technique is discussed in detail.

2.2.1 Precursors and their processing:

In the first step, the raw materials are heat-treated at 150°C for removing the moisture content. This temperature is so set to just remove the undesirable water content (moisture) and not to induce any chemical change (change in the oxidation state) in the atomic level for the choice of the cation. In the second step, we synthesized the undoped $NaNbO_3$ and $KNbO_3$ by mixing the stoichiometric amounts of Niobium pentoxide (Nb_2O_5), sodium carbonate (Na_2CO_3) or potassium carbonate (K_2CO_3) in the planetary Ball-Mill with ethanol as milling medium. The balanced reaction for both $NaNbO_3$ and $KNbO_3$ is shown below.

$$\left.\begin{aligned} Na_2CO_3 + Nb_2O_5 &\rightarrow 2NaNbO_3 + CO_2 \uparrow \\ K_2CO_3 + Nb_2O_5 &\rightarrow 2KNbO_3 + CO_2 \uparrow \end{aligned}\right\} \quad (2.1)$$

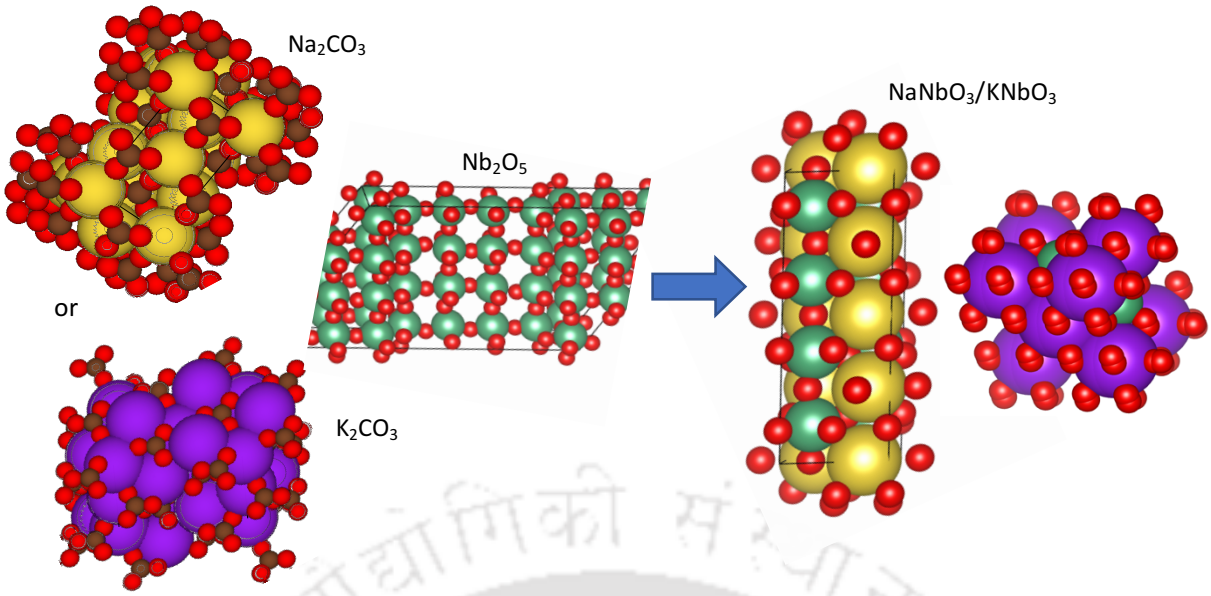

Figure 2.1. Above is the 3D structural layout of individual compounds that are used as precursors for the preparation of $NaNbO_3$ and $KNbO_3$. Structures are generated using VESTA software. Red spheres represent oxygen, green is Niobium (Nb), violet is Potassium (K), Yellow is Sodium (Na) and brown is Carbon (C) atoms.

Weight of each material required to make the desired amount of final parent counterpart was mathematically determined and then weighed accurately up to third decimal using high precession electronic weighing balance which is capable of measuring weight to the fourth decimal.

2.2.2 Homogenizing of the precursors using Ball-Milling:

Using the planetary Ball-Milling all the precursors Nb_2O_5, and Na_2CO_3/K_2CO_3 are homogenized/mixed uniformly. The schematic diagram of the planetary Ball-Mill that we used is shown in figure 2.2. This is used for mechanical alloying (or for mixing) which can result in perfect homogenising of emulsions and pastes. In the present case, we employed the Planetary Mono Mill model PULVERISETTE 6 classic line from FRITSCH GmbH. This is a high-performance Planetary Ball-Mill with a single grinding bowl mount and practical, easily adjustable imbalance compensation. This instrument is capable of reaching speeds of up to 650rpm, ensuring a constant high grinding performance. This coupled with extremely low space requirements for loss-free grinding results in the comminution of hard, medium-hard, brittle and moist materials, which is then dried in suspension or in inert gas atmosphere. Ball-Mill arrangement generally consists of a hollow cylinder with zirconia balls in it. These milling balls can be occupying about 35-45% of the milling medium. Generally, Ball-Milling is carried out by placing constituent chemicals in the jar made of high-dense ceramic materials such as zirconia or alumina (or tungsten carbide) with milling balls made up of same material as that of the jar each weighing about 3-5g and has a diameter of 10mm. The chemical composition of Mg Stabilized Zirconium oxide grinding bowls (250ml volume) and balls should be between 94.2% and 95.2% of Zirconium Oxide (ZrO_2), 1 – 2% of Hafnium oxide (HfO_2), 3.5% Magnesium oxide (MgO), 0.1% of Silicon dioxide (SiO_2), 0.1% Aluminium oxide. The fact behind using different sized balls is that the larger balls help to breakdown the coarse feed material and the smaller balls help to produce finer powder by reducing the voids between the

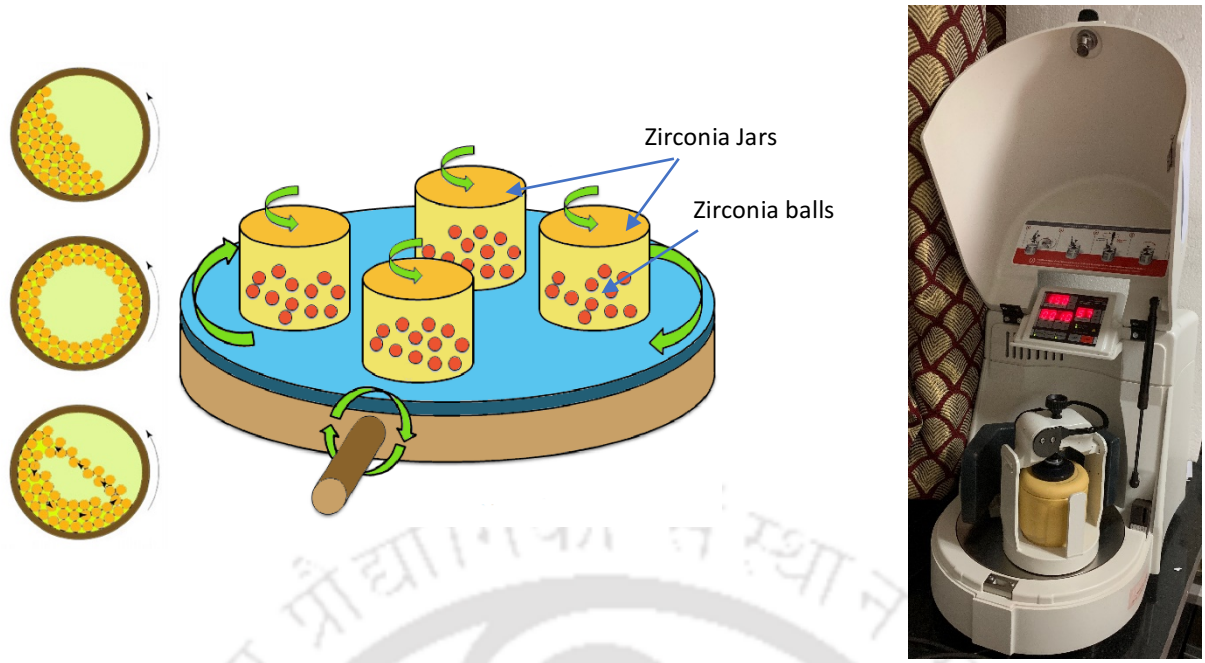

Figure 2.2. Schematic representation of how a planetary Ball Mill works. Image on the left shows the cascade action that happens inside the zirconia jar during the operation and the image on the right shows the photograph of the Ball-Mill that was used in this work.

larger ones. It is a well-known fact that smaller particle offers large area because they possess greater surface to volume ratio compared to larger particle, and thus improving the reaction probability. Another advantage of ball-milling is that it can improve the density of the ceramics during sintering due to reduced particle size. Ball-milling was carried out using distilled water as the milling medium, with a speed of 120rpm for 5h and a periodic break of two minutes. Thus, in the present case an appropriate amount of above mentioned raw materials will be mixed by using Ball-Milling method for 5hrs with distilled water as the grinding medium. The slurry thus formed will be heated at 120^{o}C in air to remove the water content. This slurry is from what one obtains the parent niobates after heat treatment which is discussed below.

2.2.3 Calcination:

The IUPAC definition for calcination is 'heating to high temperature in the atmosphere or in the presence of air or oxygen [68]. Calcination is a pre-heating treatment prior to sintering (section 2.2.5) which is carried out at a much lower temperature than the melting point of the material in a controlled environment. This is the step where decomposition of the precursors by the elimination of carbonates as carbon dioxide (CO_2), sulphates as sulphur dioxide (SO_2), moisture, water of hydrates and in the case for metallurgy, also to remove organic matter from the ore. Calcination is also known to provide better thermal and weather stability. The duration of calcination, gas ambiance (either Air, Ar, N_2 or O_2) and the temperature also plays an important role in the phase formation. Calcination temperature or the phase formation temperature is generally decided from the differential scanning calorimetry (discussed in section 2.3.1).

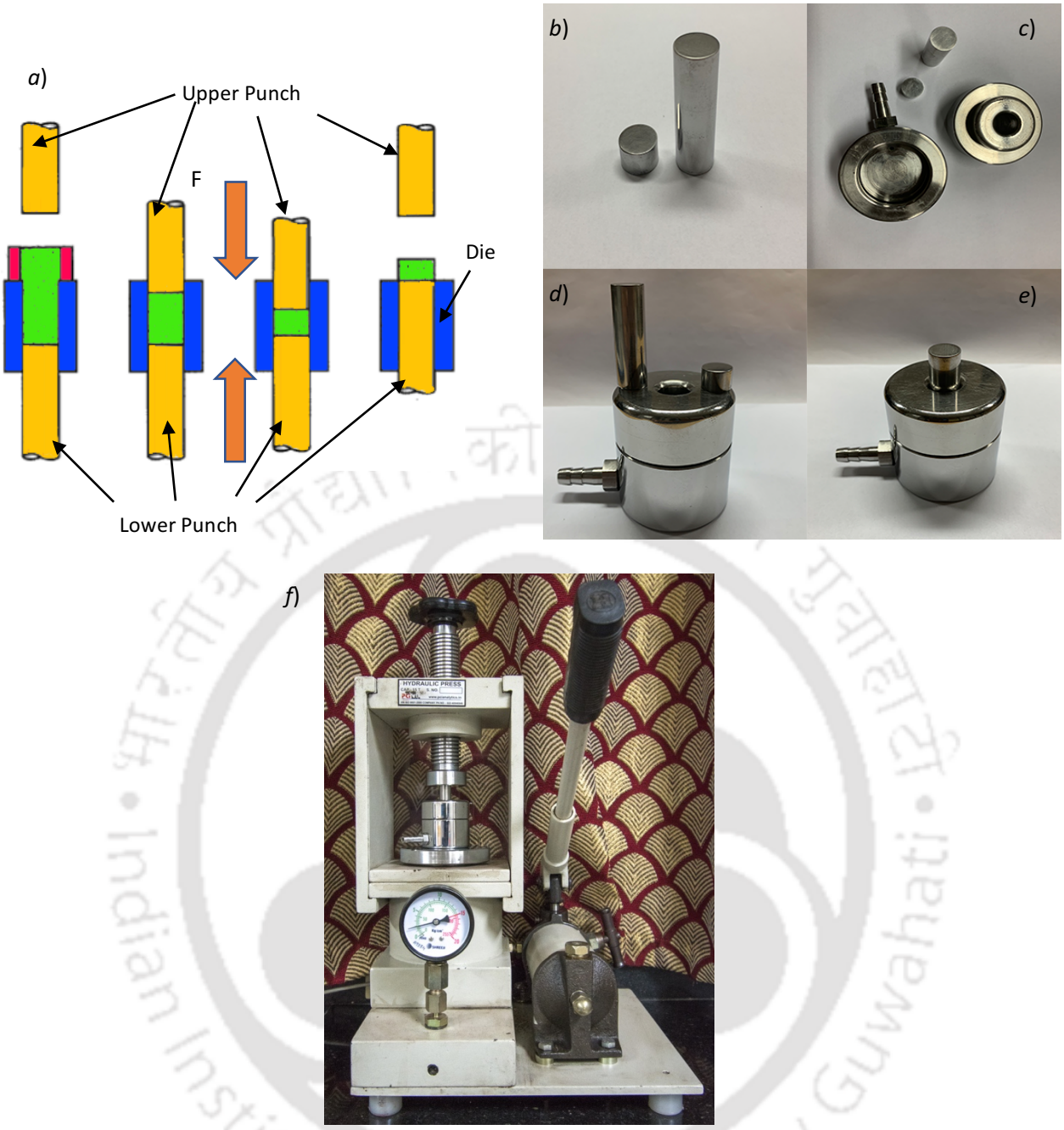

Figure 2.3. (*a*) Shows the schematic representation of Pelletization of sample using a die, (*b*) Picture of upper and lower punch, (*c*) Top view of the complete die set, (*d*) lateral view of die set, and (*e*) view of how a die set appears after sample loading and ready to be installed in a hydraulic press and (*f*) shows the Hydraulic press that we used for the palletization of the samples with loaded die.

2.2.4 Densification or Pelletization:

After calcination, phase formation of $NaNbO_3$/$KNbO_3$ is complete which can be confirmed by the X-ray diffraction technique (discussed in section 2.3.2) for the presence of any secondary phase (or impurities). A desired amount of the sample (after calcination) and the addenda (NiO/MnO_2) is weighed accurately to the third decimal and mixed using an agate mortar and pestle for 4h in a dust-free environment. This is to ensure uniform mixing of the sample and thus resulting in a homogenous mixture of the sample. Before pelletizing, this mixture is mixed with an appropriate amount of polyvinyl alcohol (PVA) which acts as a

binder. After thoroughly mixing the sample with the binder, the sample is then transferred part by part as per the requirement to prepare pellets. After transferring the required amount of sample for a pellet into the die, it is then placed on a hydraulic press. It is made sure that the pressure is applied at a slow rate to allow the escape of the trapped air. If the applied pressure is P_a, then the gradient of pressure P_z at the top of the pellet dies out exponentially as shown below.

$$P_z = P_a \exp\left(-\frac{4\mu\xi l}{d}\right) \quad (2.2)$$

In the above equation μ is the coefficient of friction along the die wall, ξ is arbitrary constant that accounts for the particle friction, l and d are the length and diameter of the pellet respectively. Using of binder, we can reduce the coefficient of friction between the walls of the die during the application of uniaxial pressure. Figure 2.3 shows the process of pelletization and the die that was used for this work. Green compacts lack mechanical strength to withstand even small physical stress and has high porosity. Hence one can proceed for further heat treatment, commonly referred as sintering which is discussed in the following section.

2.2.5 Sintering:

The consolidation of powder compacts by the application of heat is known as sintering. By the thermal energy supplied close to its melting point (usually 3/4th of the melting point), inter-particle bonding occurs by the process of inter-particle diffusion due to which the powder densifies and average grain size increases. This phenomenon that occurs during sintering is called densification and grain growth [4].

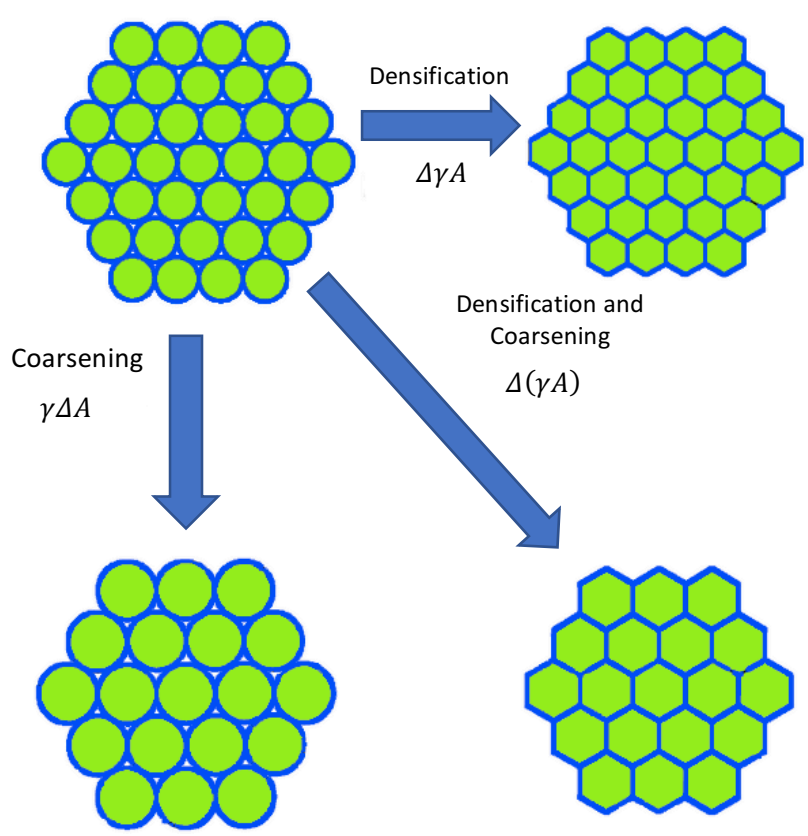

Figure 2.4. Schematic diagram showing the variation in the interfacial energy parameters γ and A with sintering.

There are basically, two types of sintering – liquid phase sintering and solid-state sintering. As the name suggests, when the thermal treatment is done entirely to solid content, then it is called solid-state sintering. If the temperature of sintering exceeds the melting temperature of one of the chemical constituent, then it is commonly known as liquid phase sintering. Along with the temperature, the atmosphere also plays a vital role on densification. One of the most driving force for researchers to do sintering is the fact of reducing surface area. The green compact (or in other words, the homogenous mixture) consists of many individual particles itself, each possessing its own surface area. By controlled supply of heat energy, one can facilitate a good amount of grain growth which results in a decrease of surface area. It is this reduction in the surface area that results in the densification, or in other words, we can say that larger the surface to volume ratio, larger is the driving force for agglomeration. During a conventional sintering, following processes are known to occur to the powder compact: (*i*) Particle bonding via necking, (*ii*) neck growth, (*iii*) Pore channel closure and (*iv*) pore shrinkage. All these processes can be accounted by total interfacial energy represented as γA, where γ is the specific energy of the interface and A is the total interfacial surface area of the powder compact. Reduction in the total interfacial energy can be written as

$$\Delta(\gamma A) = \Delta\gamma A + \gamma\Delta A \qquad (2.3)$$

In the above equation, $\Delta\gamma$ is due to densification and ΔA is due to grain growth [69]. Figure 2.4 shows the variation of interfacial energy or in other words, the driving force during sintering. Grain growth and lattice diffusion are the important aspects for eliminating porosity. This elimination in one way important in the increase of overall density. Sintering temperature is thus an important factor to obtain highly dense material.

2.3 Characterization Techniques:

In this section, various characterization techniques that were employed to investigate the physical properties of $NaNbO_3$/$KNbO_3$ ceramics are described along with brief discussions of the working principle of each technique.

2.3.1 Differential Scanning Calorimetry and Thermo-Gravimetric Analysis (DSC-TGA):

Differential Scanning Calorimetry and thermo-gravimetric analysis are the most widely used thermal analysis techniques that provides a fast and easy method for extracting wealthy information about the thermal properties of the material. These techniques are used to study the heat-flow and the resulting mass-loss of the material due to the its temperature-dependent properties. A DSC is capable of measuring the energy changes that occur in the material during the heat treatment (whether it may be heating or cooling) or may be held isothermally [70]. Using DSC, one can measure the flow of energy in or out of the sample as a function of temperature or time and are usually expressed in the units mW. For the measurement, two alumina crucibles are used with one as reference. This standard reference sets the baseline for the measurement against which any change is calculated. The furnace is then heated at a constant heating rate in an inert atmosphere. An inert atmosphere is preferred for the measurement to avoid any circumstances

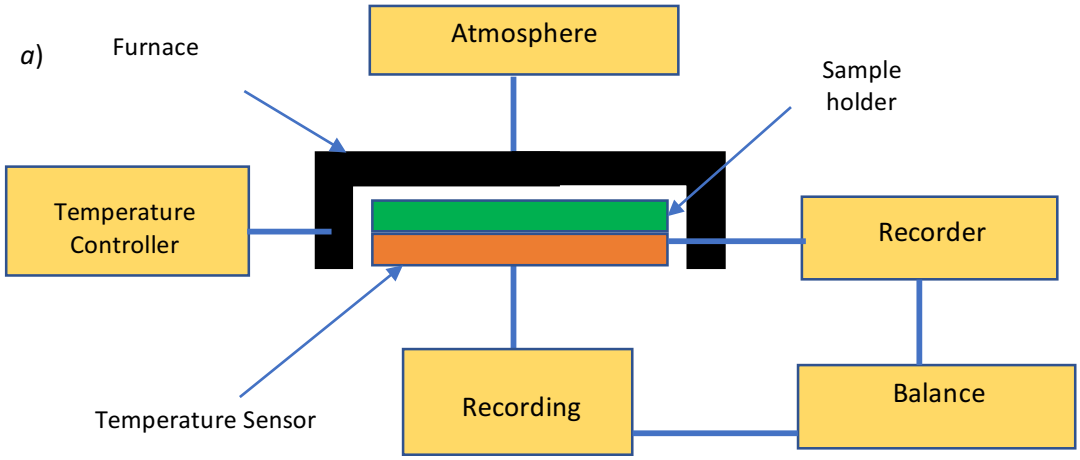

Figure 2.5. (*a*) Shows the block diagram of a thermobalance, (*b*) Photograph of the DSC-TGA setup with which measurements were carried out for this thesis.

that the sample reacts with the environment itself giving out an exothermic peak in the heat-flow data (oxidation). In these situations, one cannot point out that the sample transitions are solely responsible for the peak appeared. Depending on the phase transition of the material, it can result in either an exothermic peak or an endothermic peak. From the nature and position of the peak, one can say whether the heat signatures are related to glass transition (T_g), crystallization, fusion, melting, solid-solid transition, oxidation, etc. Specific heat (C_p) of a material can also be determined quantitatively from DSC. Specific heat is denoted with p because the measurement is in constant pressure. Thus, this characterization technique also allows one to have an idea to choose the temperature for calcination and sintering.

Thermogravimetry is a branch of thermal analysis which is used to examine the change in mass as a function of temperature in the scanning mode and as a function of time in isothermal mode. In other words, thermogravimetric analysis is that it measures change in the weight of the sample which could be due to a chemical reaction or loss of moisture. It can also measure the rate of change of reaction in different gases if the sample is heated at different rates. A material can lose its mass due to various thermal events like desorption, absorption, sublimation, vaporization, oxidation, reduction, etc. Generally, the initial mass of the

sample will be positioned as 100%, and further change in mass will be recorded against percentage mass lost during heat treatment. The main measuring principle of a TG is the use of a thermobalance. A thermobalance is used to measure the change in the sample mass as a function of temperature in a controlled atmosphere in constant heating rate with controlled gas flow and crucible. Figure 2.5 shows the block diagram of a thermobalance.

2.3.2 X-Ray Diffraction Spectrometer (XRD):

X-ray diffraction technique is one of the most common yet powerful tool which has its uniqueness in determining the crystal structure because the wavelength λ of monochromatic X-ray beam is of the order of interplanar spacing *d*. One can visualize the atomic planes are plane mirrors obeying the laws of reflection, reflecting a small fraction of the incident beam. Depending on atomic arrangement (thus the crystal planes), the reflected beam can undergo either constructive or destructive interference due to the path difference between two reflected beams. English physicists W.H. Bragg and W.L. Bragg came up with the empirical relation that could explain the possible interference pattern of X-rays that was observed when scattered by a crystal. For this work, they were awarded Nobel prize in 1915 [71]. The Bragg's law is given below

$$2d\ sin\theta = n\lambda \qquad (2.4)$$

A schematic view of a diffractometer is shown in figure 2.6. The angle between the X-ray source and the sample is θ, and 2θ is the angle between the incident beam and the detector. The incident angle θ is always half of the detector angle 2θ. The general function of a diffractometer is to detect the X-rays diffracted from materials and to record the diffraction intensity as a function of the diffraction angle (2θ). The X-ray radiation generated by an X-ray tube passes through Soller slits which collimates the X-ray beam which then strikes the specimen. X-rays are then diffracted by the specimen and form a convergent beam at the receiving slits before they enter the detector. The diffracted X-ray beam passes through a monochromatic filter to suppress wavelengths other than K_α radiation and decrease any background radiation, before being received by the detector. The K_α radiation is generated by bombarding of target surface (Cu, Fe, Cr) by accelerated electrons. Most common targets that are used in generating K_α radiation are Copper (Cu), Molybdenum (Mo) and Cobalt (Co) target. When there are n number of equidistant atomic planes separated by a distance d, under most angles of incidence, θ, the waves reflected from neighbouring planes will show a phase difference. But at great distance from the crystal, where all the reflected waves come together, the superposition of these waves of systematically increasing phases will lead to cancellation of amplitudes. There exists only the transmitted wave. However, if the phases of all the reflected waves have a phase difference of less than one half wavelength, then all reflected amplitudes will build up together to an optical field in the direction of reflection, without any actual cancellations of contributions. Should all waves arrive in the same phase, then full reinforcement of the waves takes place to an amplitude of n times that of the single reflected wave. Thus, XRD is a direct evidence for the periodic arrangement of atoms inside a lattice [72].

a)

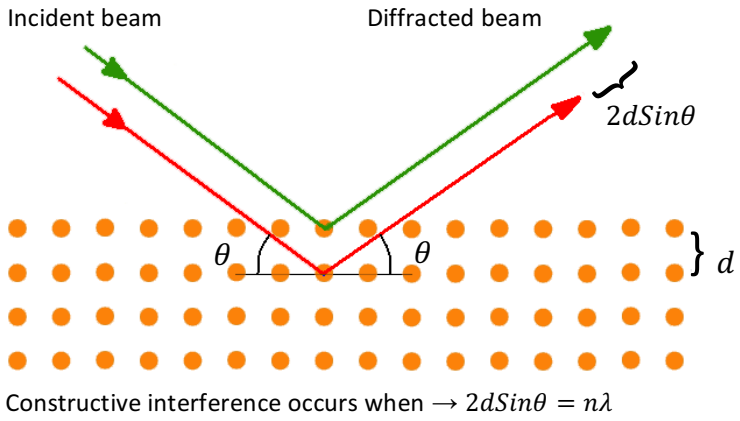

Constructive interference occurs when $\rightarrow 2dSin\theta = n\lambda$

b)

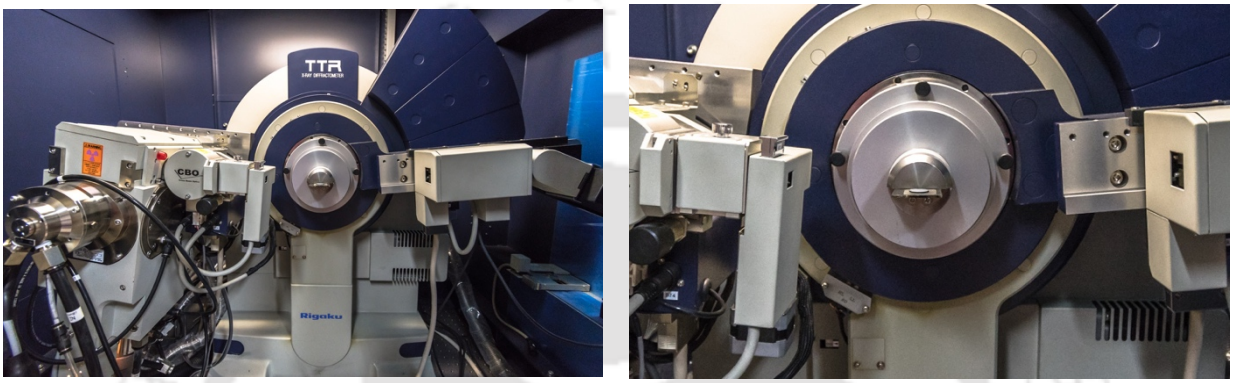

Figure 2.6. (*a*) Pictorial representation of the underlying principle of the XRD - Bragg's law, (*b*) Photograph of the Rigaku X-ray Diffractometer (with sample loaded) used for the current work.

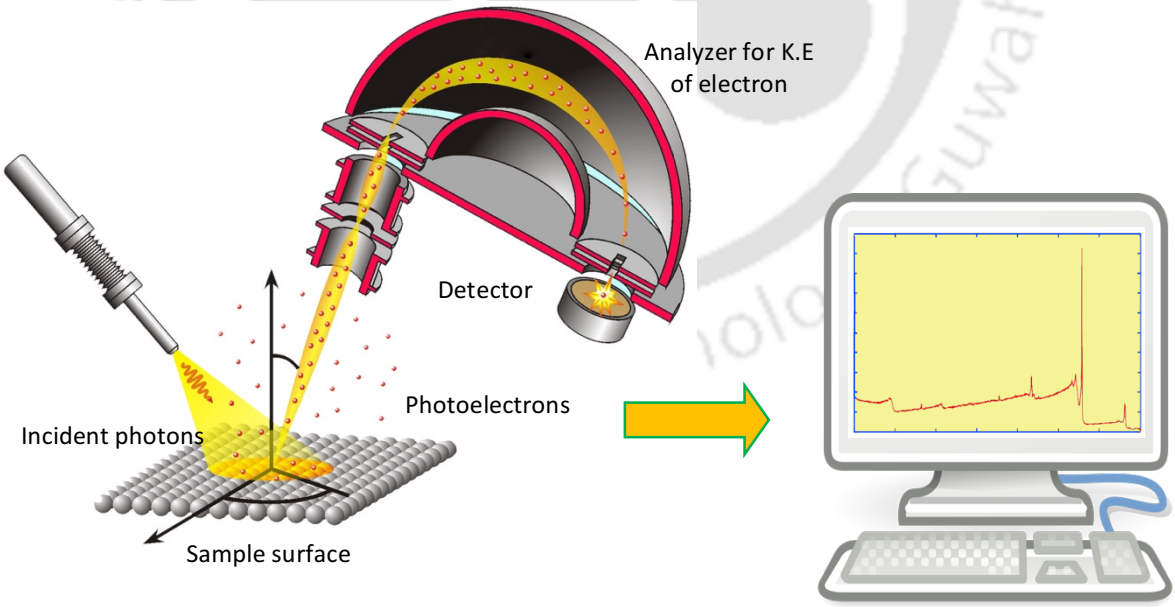

Figure 2.7. Schematic diagram of XPS showing the electrons ejection from the surface of the material due to the incident photons that are collected by the energy analyzer. Here the kinetic energy of the electron is measured by the detectors and the resultant output is shown as energy spectrum (survey scan).

In the present work, a Japanese make X-ray Diffractometer Rigaku (model: TRAX-III) with Cu-K_α source radiation of wavelength λ = 1.54056Å was used for the characterization of $NaNbO_3$ and $KNbO_3$ based two-phase composites. Further, Rietveld refinement was carried out for these experimentally obtained diffraction results using FullProf program [73,74]. All the XRD measurements for this thesis has been carried out with fixed experimental conditions such as the step size and scanning rate was fixed to be 0.03° and 3°/min between the 2θ margin of 10°-80°. At first, the calibration of the diffraction angle was made using a standard silicon sample for any possible instrumental line broadening. Figure 2.6 shows the photograph of the XRD machine that was used for the structural characterization.

2.3.3 X-Ray Photoelectron Spectroscopy (XPS):

X-ray Photoelectron Spectroscopy (XPS) is also commonly known as Electron Spectroscopy for Chemical Analysis (ESCA). This technique is a widely-used surface analysis which provides both elemental and chemical state of the material. As the name suggests, the basic underlying principle of this technique is the *Photoelectric effect* which was enunciated by Albert Einstein in the year 1905 [75] for which he was awarded the Nobel Prize in 1921. If $E(M)$ denotes the energy of the neutral atom of the material, and $E(M^+)$ denotes the energy for the ionized atom, then by conservation of energy, one can write,

$$E(M) + h\nu = E(M^+) + K.E.(e^-)$$

where $K.E.(e^-)$ is the kinetic energy of emitted electron. One can re-arrange the above equation as shown below.

$$K.E.(e^-) = h\nu - [E(M^+) - E(M)] \quad (2.5)$$

The final term in the above equation is the difference in the energy between the neutral and ionized atom which is generally known as *binding energy*. The photoelectric effect is that phenomenon when photons of suitable energy $h\nu$ (threshold energy) strikes the surface of a metal whose *work function* is (or binding energy) ϕ_0, electrons are emitted from the surface of the metal with kinetic energy (K.E = $\frac{1}{2}mv^2$). A simple yet famous expression that explains photoelectric effect is as shown below.

$$K.E = h\nu - \phi_0 \quad (2.6)$$

Thumb rule for one to observe photoelectric effect is that the energy of the photon incident on the material should be greater than the work function of the material i.e. $h\nu > \phi_0$. A Schematic view of a typical XPS is shown in figure 2.7. Typical X-ray source for an XPS is Magnesium and Aluminium Inside an ultra-high vacuum (UHV) chamber of the order of 10^{-7}Pa, a heated filament (cathode) ejects electrons which are accelerated towards an anode [76]. Due to these electron bombardments onto the anode, holes are generated which are radioactively filled by the electrons from higher level resulting in the X-ray. To remove unwanted radiation from the source, the Al-K_α is often monochromatized using a quartz crystal. For the current work, we have employed an XPS capable of producing X-rays of energy 1487eV (Al-K_α) and 1254eV (Mg-K_α) equipped with an ultra-high-vacuum (UHV ~ 10^{-10}Torr) with a pass energy of 100eV. When these X-rays with sufficient energy are incident on the surface of the material, electrons from specific bound states gets

ejected. Once these photo-electrons are ejected, they are collected by an electron analyser which measures the kinetic energy. Here the electron-optics consist of an electric lens and a magnetic lens which allows only electrons of particular energy to pass through (*pass energy*). By adjusting the field of the lens system, one can thus measure the kinetic energy of these ejected photo-electrons from the radius of the trajectory of electrons through the analyser. An energy analyser produces an energy spectrum of intensity in which each peak corresponds to a specific element at a particular oxidation state.

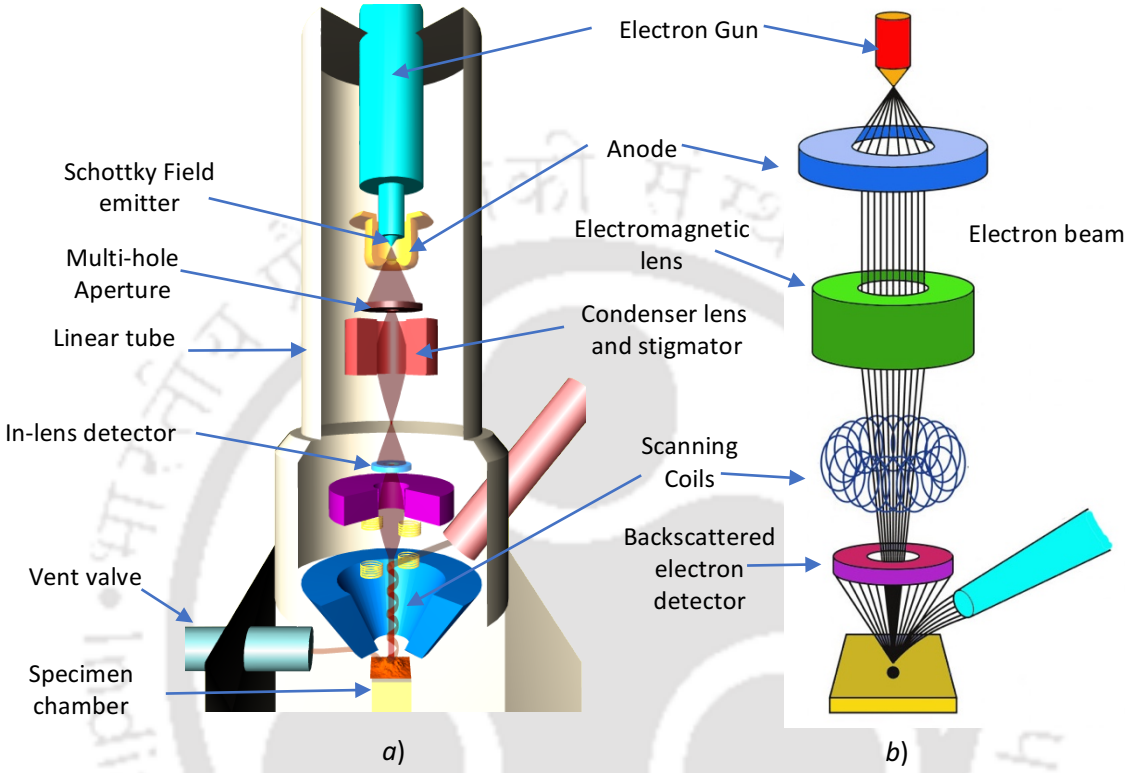

Figure 2.8. (*a*) Pictorial representation of various parts of FESEM, and (*b*) Schematic representation electromagnetic lens.

2.3.4 Field Emission Scanning Electron Microscope (FESEM):

Field emission scanning electron microscopy is one modern tool for research that provides the topological and elemental information of the material. Comparing to the conventional microscopes, FESEM provides much more clear and less electrically distorted with enhanced spatial resolution. Biggest different between FESEM and SEM lies in their innate ability to generate electrons. When the latter engages heated tungsten or Lanthanum Hexaboride filament as the cathode source which is also known as the thermionic emitter [77]. However, FESEM uses a field emission gun (FEG, also known as cold-cathode field emitter) which is made of tungsten. This provide a super focussed electron beam which overcomes the drawbacks of SEM for relatively low brightness and evaporation of filament (by thermal drift) and provides higher spatial resolution of about ~ 1 nm even at low working potentials. Hence FESEM limits the charging effect of non-conductive and avoids damage to samples that are sensitive to electron beam. Thus, an SEM that uses a Field emission gun is called FESEM [78]. In our present work, we have used FESEM which is equipped with energy dispersive X-ray spectrometer (EDS or EDAX) from Sigma Zeiss using secondary electron mode which can

provide a magnification from 10x to 300,000x. Figure 2.8 shows the lateral section of an FESEM along with a schematic representation of the internal lens system of the same.

One of the remarkable features of FESEM is the use of its in-lens electron optic system. FESEM uses a focussed beam of electron to image the specimen. The electron beam column is what defines the electron-optic system which accommodates FEG and the lenses in high-vacuum. Probe size is also an important factor for the resolution. Smaller probe size is achieved with the help of electron-optics which demagnify the electron source to result in a smaller probe and hence achieves higher resolution [79].

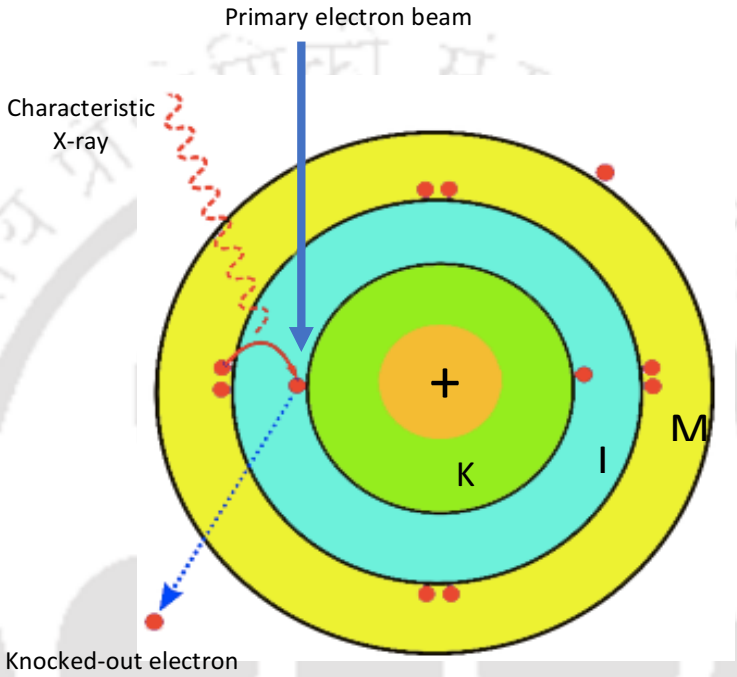

Figure 2.9. Schematic view of atomic levels representation of the basic principle of EDS/EDAX.

The electron beam from the FEG is accelerated through a high voltage which then passes through an electromagnetic objective lens to produce a thin electron beam. This beam is then used to scan the surface of the sample using scan coils. Since, electrons interact with the material, the sample must be conducting, if not, then a conducting coating is given to the material before loading it to the instrument. These electrons bombards on the surface of the sample which dislodges electrons from the sample. These dislodged electrons are called as secondary electrons, which is then collected by a detector and converts into signals. Furthermore, these signals are amplified, analysed and converted into topographical images.

Energy-dispersive X-ray spectrometer (EDS/EDAX) allows one to determine the what individual elements and their relative proportion within the scan area. It is one of the analytical techniques used for the chemical characterization of the material. The underlying principle is that an electron beam can interact with matter generating various signals that possess information about the material such as backscattered electrons can give information about difference in atomic number, topographic information can be given by

secondary electrons, also the transmitted electrons can give information about the internal structure. Each element has its own uniqueness to its structure, which when they interact with the electron beam produces distinctive characteristic X-ray and EDS make use of this characteristic X-ray signal (figure 2.9). When a high-energy electron bombards the atom, it knocks out the electron from the inner shell resulting in an electron vacancy with an excited atom. This excited atom returns to its ground state by filling this vacancy by an electron from a higher energy level resulting in the emission of X-rays characteristic to that element. Each peak in the EDS spectrum corresponds to a particular element and the intensity of the peak defines the concentration of that element in the material.

2.3.5 Vibrational Raman Spectroscopy:

Raman spectroscopy technique is based on the inelastic scattering of monochromatic light (usually a laser source) by which one can probe transitions among the vibrational quantum levels of atoms or molecules by absorption or emission of photons [80,81]. When monochromatic light rays of particular frequency ν_0 interact with matter, majority of the incident light undergoes elastic scattering (Rayleigh Scattering). Here the excited molecule returns to the initial state thus emitting a photon of the same frequency i.e. ν_0 (figure 2.10). However, a small fraction of the incident light (< 10^{-7}) can undergo inelastic scattering and resulting a molecule in a different quantum state, ν_m. These in-elastically scattered photons are having frequency either shifted up, $\nu_0 + \nu_m$ (anti-stokes line) or down, $\nu_0 - \nu_m$ (stokes lines). This effect is referred to as the Raman Effect (Noble prize in the year 1930 was awarded to Sir C.V. Raman for discovering this phenomenon). This shift according to Raman could give information about vibrational, rotational and other low-frequency transitions in the molecule. [82]

A molecule is said to be Raman active if the change in energy of the molecule is associated with the change in its polarizability (α). A classical approach to Raman scattering can be explained below. For a laser that can emit photons of frequency ν_0, the electric field strength of electromagnetic (EM) wave that oscillates with time can be written as,

$$E = E_0 Cos 2\pi\nu_0 t \qquad (2.7)$$

where E_0 is the amplitude of vibration. When a diatomic molecule is exposed to this EM wave, dipole moment P gets induced:

$$P = \alpha E = \alpha E_0 Cos 2\pi\nu_0 t \qquad (2.8)$$

If the molecule is vibrating with a frequency ν_m and amplitude x_0, then the displacement x can be written as shown below.

$$x = x_0 \cos 2\pi\nu_m t \qquad (2.9)$$

One can easily assume that for small amplitude of vibration, α is going to be linearly dependent on x. Thus, one can write,

$$\alpha = \alpha_0 + \left(\frac{\partial\alpha}{\partial x}\right)_0 . x_0 + \cdots \qquad (2.10)$$

where α_0 is the polarizability in the equilibrium position and the derivative term inside the brackets is the rate of change of α w.r.t. change in x at equilibrium. Combining the above equations, we obtain:

$$P = \alpha_0 E_0 Cos2\pi\nu_0 t + \left(\frac{\partial\alpha}{\partial x}\right)_0 . x_0 E_0 Cos2\pi\nu_0 t . Cos2\pi\nu_m t$$

$$\Rightarrow P = \alpha_0 E_0 Cos2\pi\nu_0 t + \frac{1}{2}\left(\frac{\partial\alpha}{\partial x}\right)_0 . x_0 E_0 [2\pi(\nu_0 + \nu_m)t + 2\pi(\nu_0 - \nu_m)t] \qquad (2.11)$$

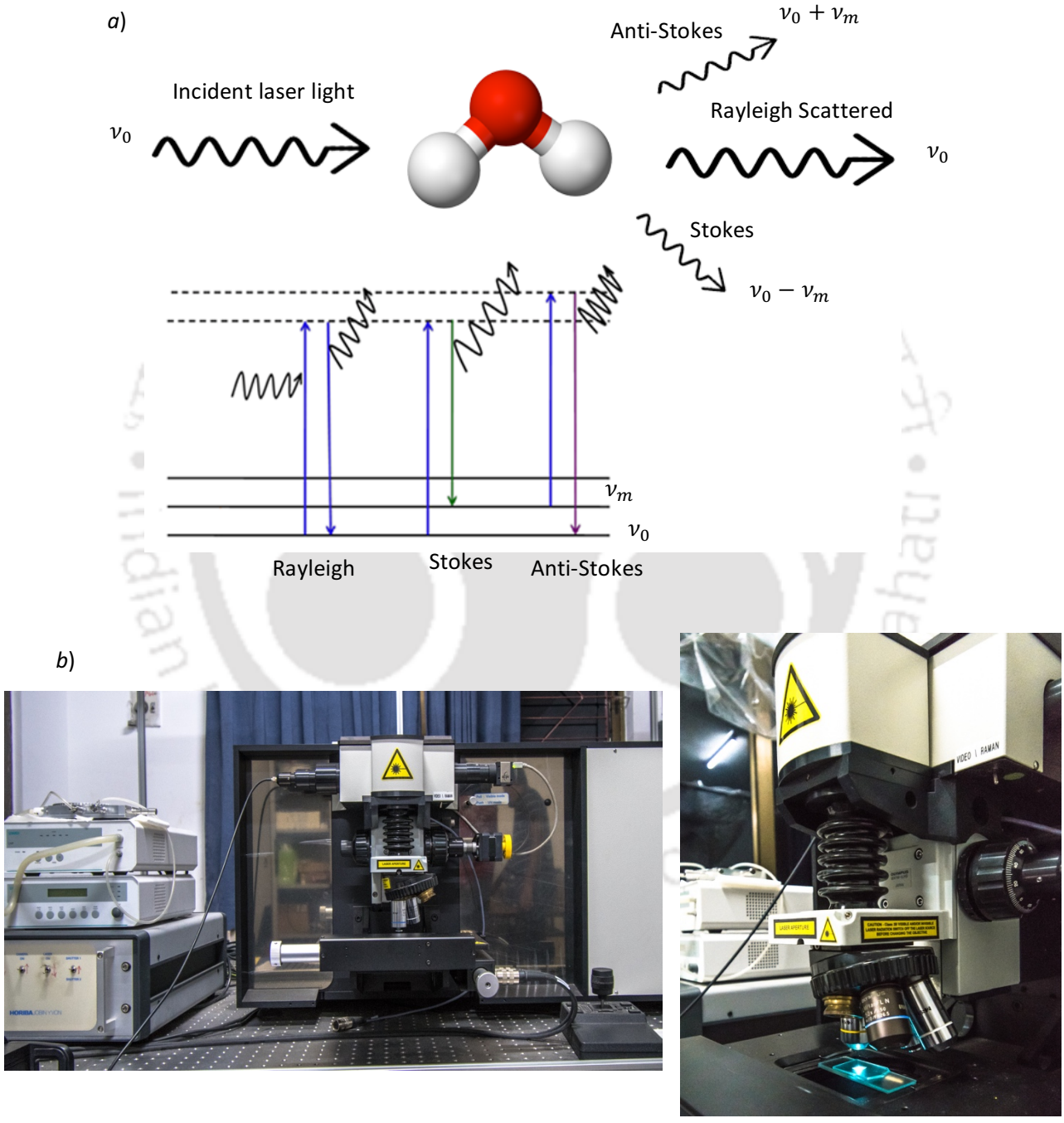

Figure 2.10. (*a*) Schematic representation of the light scattering on material and resulting in Rayleigh and Raman scattering, and (*b*) Photograph of the Raman spectrometer that was used in this work.

The first term represents Rayleigh scattering, second and third represents anti-stokes and stokes line respectively. It can be noted that if $\left(\frac{\partial \alpha}{\partial x}\right)_0 = 0$, then there is no stokes and anti-stokes term and hence not Raman-active.

A typical Raman spectroscopy consist of a monochromatic light source (generally laser), focused onto a sample. The scattered light though very weak, is collected with the help of monochromators with excellent stray-light rejection and sensitive detectors. This is one reason why detection of low-frequency Raman modes becomes difficult as the Rayleigh scattering intensity may exceed the intensity of the useful Raman signal. In many case, this problem is resolved by eliminating the spectral range close to the frequency of the laser source. In general, the intensity of Raman scattering is found to be proportional to the square of the derivative of polarizability.

$$I \propto \left|\left(\frac{\partial \alpha}{\partial x}\right)_0\right|^2 \qquad (2.12)$$

In this work, we used LABRAM HR800 Raman spectrometric analyser developed by Horiba Jobin Yvon which uses an Argon laser of wavelengths 480nm, 532nm and 633nm (figure 2.10). The microscope coupled confocally to a 800nm focal length spectrograph equipped with two switchable gratings. A beam splitter is used to reflect the laser beam and split into two equal parts. The notch filter is used to allow only the Raman scattered signal and to block the incident signal. Further, this Raman signal passes through a grating which resolves weak Raman signal. Finally, the beam falls on the charge-coupled device (CCD) where the change in polarizability w.r.t. change in the displacement is measured and later converted to Raman spectra.

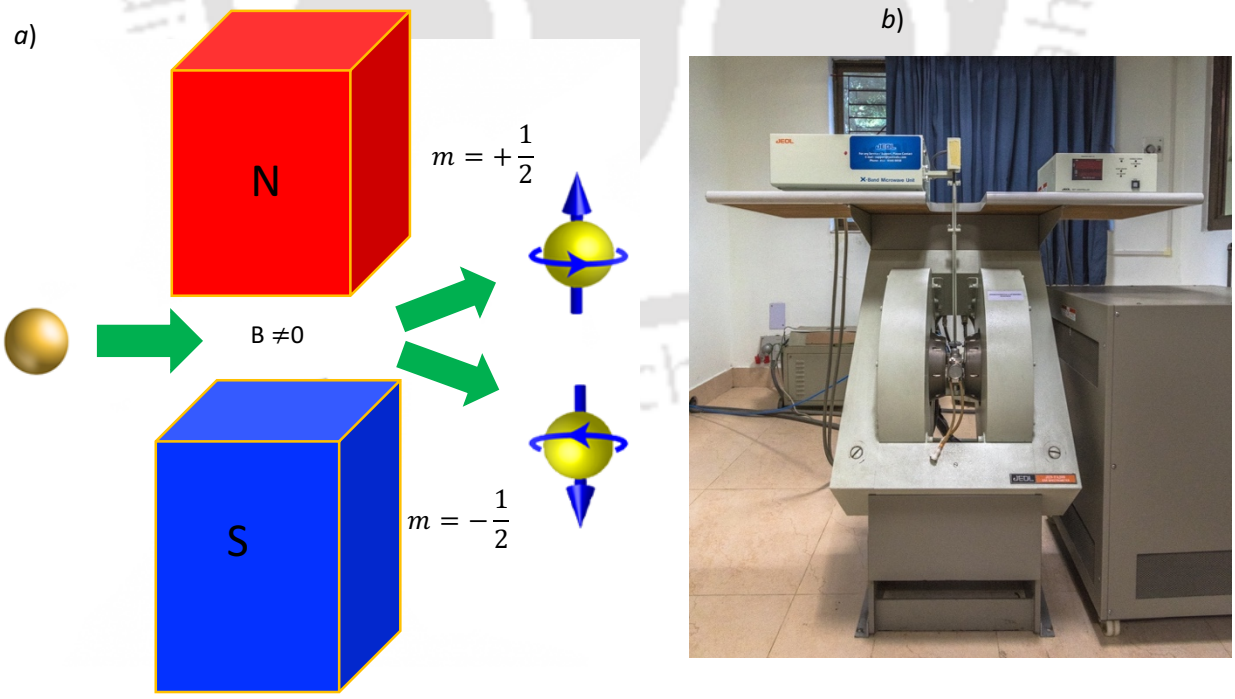

Figure 2.11. (*a*) Schematic diagram showing the underlying principle of ESR in which splitting of the energy levels of up and down spins of electron in the presence of magnetic field **H**. (*b*) Photograph of an Electron Spin Resonance spectrometer that we used in the current study.

2.3.6 Electron Spin Resonance Spectroscopy (ESR):

Electron spin resonance, also known as Electron Paramagnetic Resonance (EPR), is a very important tool through which one can probe the local structure within the molecule. This is one of the modern research technique used to study the behaviour of material which possess unpaired electron, free radicals, and other paramagnetic centres (atom with odd number of electrons). Such material property leads to significant absorption of input microwave radiation in the presence of magnetic field. Every atom possesses the negatively charged electrons and every electron mainly has two types of motions. One being orbiting around the nucleus, and the other is spinning around its axis. The magnetic moment of most of the molecule is mostly due to spin magnetic moment of electron. For a single unpaired electron, there can be only two possible spin states (±1/2), and thus the energy difference between the two possible energy states is given by

$$\Delta E = E_{\uparrow} - E_{\downarrow} = g\mu_B B \qquad (2.13)$$

In the above equation, g is the Lande's g-factor (=2 for free electron) or sometimes referred to as the spectroscopic factor, μ_B is Bohr magneton ($= 9.27\times10^{-24} JT^{-1}$) and B is the applied magnetic field. Thus, for the resonance condition (given by below equation) a perfect balance between the microwave energy and magnetic energy is required.

$$h\nu = g\mu_B B \qquad (2.14)$$

where ν is the frequency of the microwave. For practical application in ESR, the frequency of the microwave is generally kept constant and the magnetic field strength is varied so as to obtain resonance.

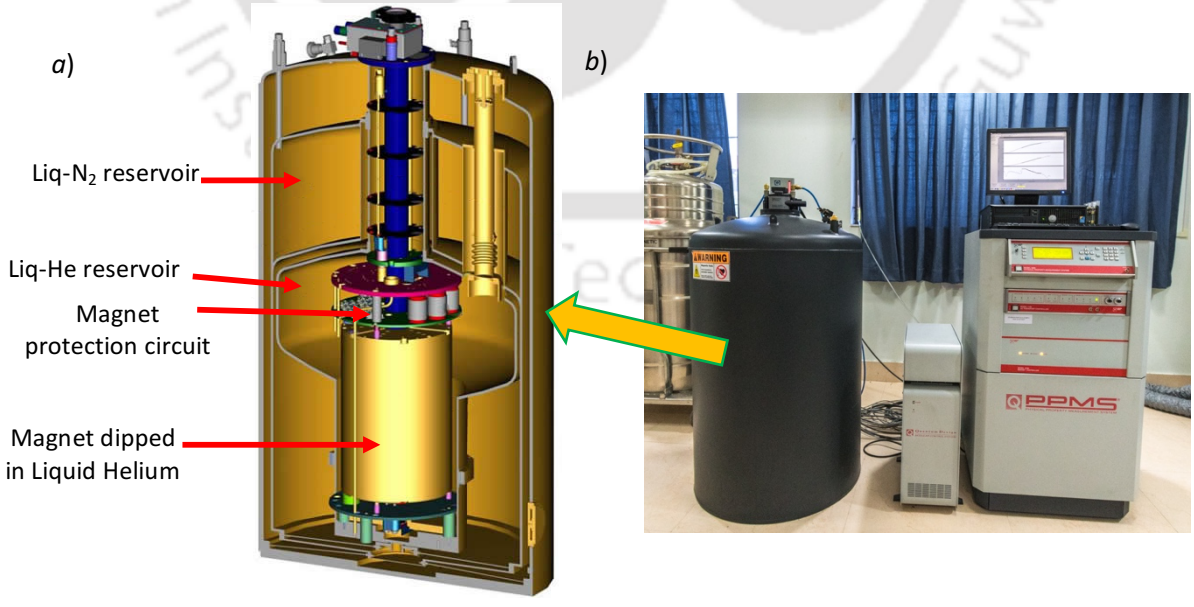

Figure 2.12. (*a*) Cross-sectional view of the PPMS Dewar where the superconducting magnets are dipped in a pool of liquid helium encapsulated by liquid nitrogen container. (*b*) Photograph of PPMS from Quantum Design that has been used for the current work.

When the magnetic field satisfies the resonance condition, energy is absorbed and thus the power reaching the detector is reduced [83,84]. The ESR measurements for this thesis were carried out using a JEOL JES-FA200 spectrometer which operates in X-band frequency of 9.45GHz (figure 2.11). EM waves are sent from the microwave bridge to the resonant cavity where the sample is loaded and modulation of magnetic field is done with the help of modulators.

2.3.7 Physical Property Measurement System (PPMS):

Heat capacity, often abbreviated as C_p, is defined as the heat energy required to raise the temperature of unit mass by unit degree. It can also be defined as the ability of the material to retain heat and rate at which it cools. For example, a substance with low specific heat (example iron (Fe)) will heat up quickly, also at the same time it loses the heat quickly. Whereas, on the other hand, those materials with higher specific heat (like water 4.186J/g-K), requires more energy to heat up, as well as it cools slowly.

$$Q = Cm\Delta T \Rightarrow C = Q/m\Delta T \qquad (2.15)$$

where Q is the heat energy absorbed or released by a material of mass m. Measuring the heat capacity, one can obtain enthalpy and entropy which in a way is the measure of the stability of the material [85]. In case of gaseous material, it is also important to fix the physical parameters, pressure and volume, as the heat energy supplied can be expelled out by the gas in the form of change in volume or pressure ($PV = nRT$). Hence, we have two different specific heat capacity for gases: C_P which is at constant pressure and C_V at constant volume.

In the current thesis, we have only solid samples, and the measurements were carried out in Quantum Design Physical Property measurement system (QD-PPMS). A typical PPMS is capable of reaching measuring temperatures from 400K down to 1.8K, and the superconducting magnets capable of magnetizing the sample chamber to a magnitude of ±9T (figure 2.12). The instrument is programmed to supply controlled amount of heat for a fixed time followed by a cooling phase of same duration, during which thermal changes in the material is being monitored. At temperatures below the Debye temperature, one can directly probe the electronic and magnetic specific-heats of a material and hence allow comparison between theory and experiment.

2.3.8 Impedance Spectroscopy:

One of the most vital characterization tool used in the field of ferroelectrics and high-κ dielectrics is the Impedance Analyser with which one can probe the different relaxation mechanism and transition temperatures. The frequency and temperature dependence of ac-resistivity and dielectric permittivity of the $NaNbO_3$ and $KNbO_3$ based samples were measured using two different high precision RF Impedance analysers: one from Solartron (Model: SI-1260) and the other from Wayne-Kerr Electronics Pvt. Ltd. (Model WK-3030B). These instruments are equipped with temperature controller (Eurotherm-2204e) and heater

capable of reaching 600℃. For the dielectric measurements, the two sides of the sample in the form of pellet will be fashioned like a parallel-plate-capacitor geometry with silver as electrical contacts. Temperature dependent relative dielectric permittivity 'ε_r' and loss-tangent 'δ' are measured using impedance analysers (mentioned above) attached to a temperature controller. Constant ac-peak-to-peak sinusoidal potential of 100mV with frequencies varying between 100Hz and 20MHz has been used as input signal. In order to match the input/output impedances of the instrument and investigating sample under high frequency limits, a 50Ω feedthrough terminator cable was connected at the input and simultaneously a 50Ω power splitter was used at output terminal as shown in figure 2.13.

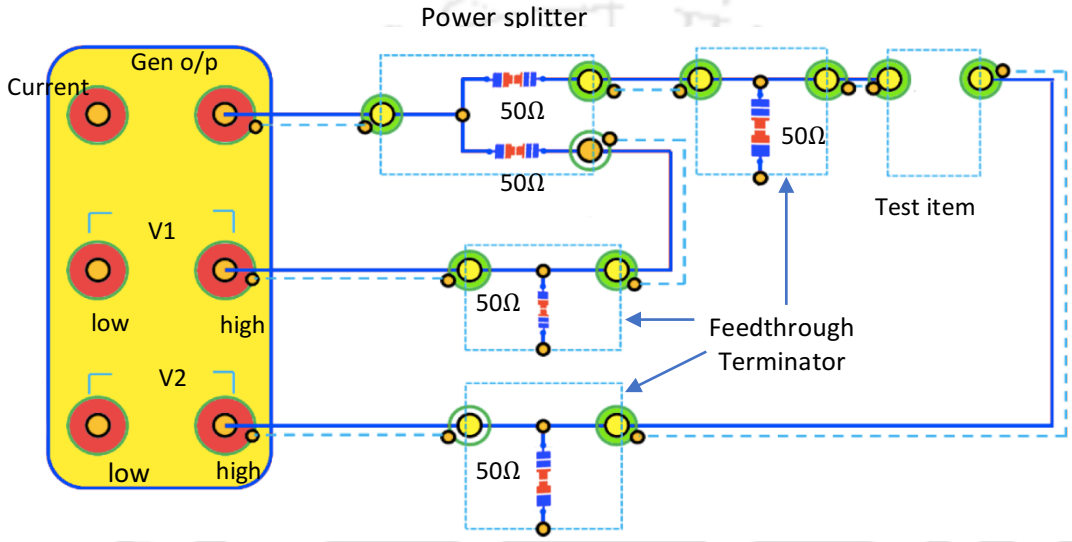

Figure 2.13. Typical connections for high frequency voltage measurements using Impedance Analyzer.

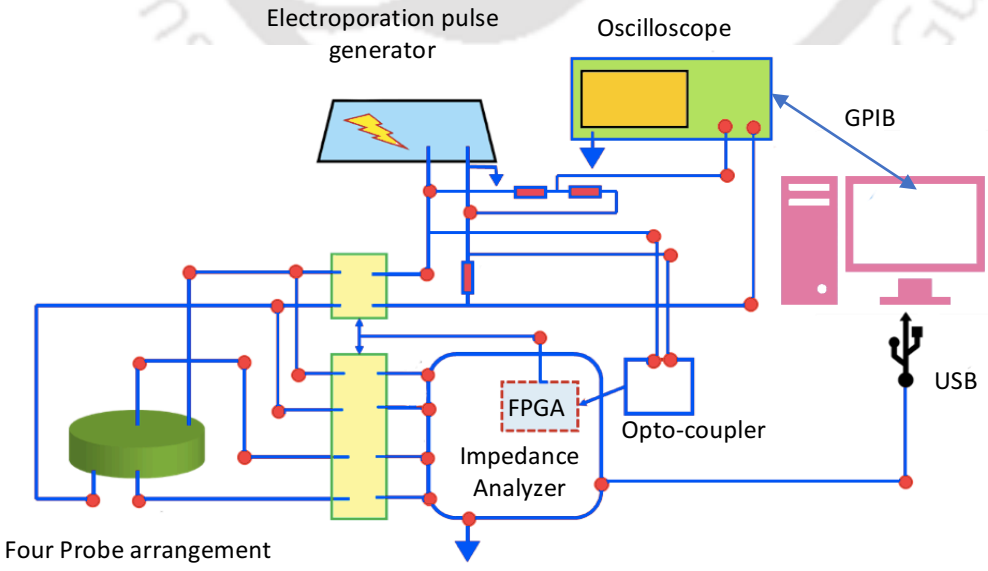

Figure 2.14. Schematic connections along with the circuit representation of an Impedance Analyzer.

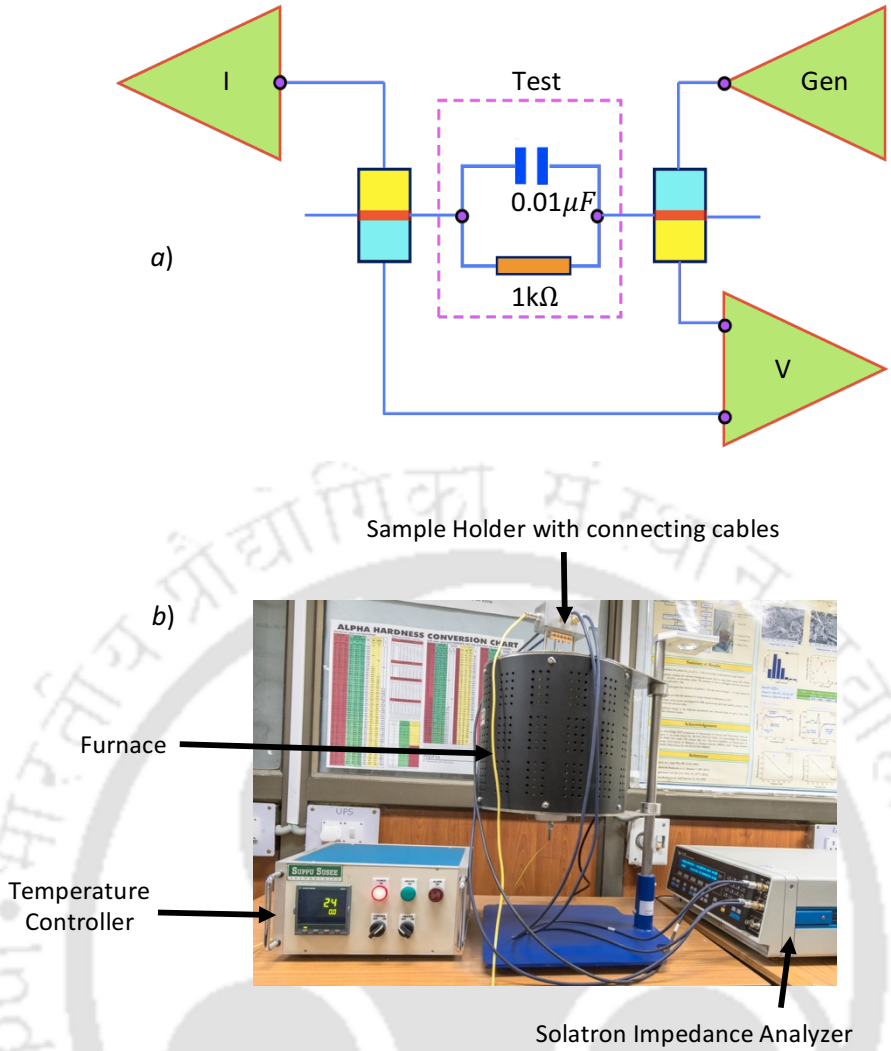

Figure 2.15. (*a*) Circuit level connections for a simple impedance measurement setup and (*b*) Photograph of the Impedance Analyser setup that we used in this work.

The most common and standard technique to measure impedance is by applying a single-frequency voltage (V) or current (I) to the interface and measuring the phase shift and amplitude (or real and imaginary parts) of the resulting current at that frequency using either analogue circuit or fast Fourier transform (FFT) analysis of the response. Generally, three different types of electrical stimulations can be used: (*i*) For the transient measurements, a step function of voltage [$V(t) = V_0$ for $t > 0$, $V(t) = 0$ for $t < 0$] may be applied at $t = 0$ to the system and the resulting time-varying current *I(t)* measured. The ratio $V_0/I(t)$, often called the indicial impedance or the time varying resistance, measures the impedance resulting from the step function voltage perturbation at the electrochemical interface. (*ii*) The second technique is to apply a signal $V(t)$ composed of random noise to the interface and measure the resulting current. Fourier- transformation of the results is required to pass into the frequency domain and obtain definite value of the impedance. This approach offers the advantage of fast data collection because only one signal is applied to the interface for a short time. The technique has the disadvantages of requiring true random noise. (*iii*) The third approach is the most common

and standard one, in this mode the impedance is measured by applying a single-frequency voltage or current to the interface and measuring the phase shift and amplitude, or real and imaginary parts, of the resulting current. Figure 2.14 shows the general architecture of any commercial Impedance-Gain-Phase Analyser. Figure 2.15 shows the simplest way of connecting the capacitance (C) and resistance (R) network of the measurement.

Chapter 3
Structural and Dielectric properties of $NaNbO_3$-NiO composites

This chapter deals with the structural, dielectric and elemental analysis of selected composites of $NaNbO_3$-NiO composites. This chapter provides a systematic comparative analysis of the dielectric spectroscopy of two specific compositions (0.10 and 0.95) such as Jonscher's Power Law. Towards the end of this chapter, we have provided detailed discussion providing substantial evidence for Mott's Variable Range Hopping Mechanism in both the systems.

3.1. Introduction:

As we have seen in Chapter 1, lead and lead-based ceramics will be gradually expelled in the future from many commercial applications and materials owing to concerns regarding their toxicity [86-88]. Among various lead-free materials which crystallize into Perovskite crystal structure (ABX_3 as general formula), alkaline niobates such as $NaNbO_3$ and $KNbO_3$ and $CaTiO_3$ have drawn immense attention due to their promising applications in modern microwave electronic devices, sensors, piezoelectric actuators, etc [89-92]. Interest in this family of oxides arises due to their large band-gap with surprising physical properties and their flexibility to incorporate in its lattice with many of the elements as substituents [93]. Owing to the structure flexibility, lattice distortions are achieved easily resulting in a broad range of novel functional properties which opens up a constructive approach of designating novel electronic devices. The three main factors responsible for lattice distortions in perovskites are (*i*) size effects, (*ii*) deviation from the ideal perovskite structure, and (*iii*) Jahn-Teller Distortion [94]. According to Goldschmidt's classification the '*Tolerance Factor*', t, was defined on the basis of ionic radii which is given below equation [95,96].

$$t = \frac{R_A + R_O}{\sqrt{(2(R_B + R_O)}} \qquad (3.1)$$

Where R_A, R_B and R_O represents the average ionic radii of the A-site and B-site cation, and the oxygen anion. This factor helps us to get a better picture and understanding of the geometrical close-packing in the perovskite lattice. For an ideal cubic structure, the tolerance factor should be 1. Depending on the size of A-ion and the B-ion, the value of the tolerance factor can be greater than or less than one, which can give an idea of whether the structure will be taking up orthorhombic or tetragonal symmetry. For the structure to be stable, any perovskite should have the tolerance factor in the range $0.9 < t < 1.1$ [97]. In a way, the tolerance factor is a measure of how good the A-site cation can fit into the perovskite framework, and value towards the lower part of the permissible range for stability (tolerance factor) only tells that BO_6 octahedra is tilted or not. Few important findings that have been drawn from analysing vast number of perovskites are, (*i*) when $t \approx 1$, the structure exhibited low distortion as well as low Curie temperature, (*ii*) $t > 1$, favours tetrahedral distortion due to large A-site cation, however, large number of perovskites are cubic and hence are not ferroelectric at room temperature, and (*iii*) if $t < 1$, implies that A-site cation is small, and so this is common with structures containing rare-earth elements [97,98].

In 2004, Saito *et al.* reported the enhanced piezoelectric charge coefficient $d_{33}\sim$ 400pC/N in the Li and Ta doped $K_{0.5}Na_{0.5}NbO_3$ system which is competitive with that of the $Pb(Zr_xTi_{(1-x)})O_3$ system [86]. Among the above two alkali niobates, $NaNbO_3$ and its composites have drawn considerable attraction due to their wide range of applications including high-density optical data storage, hologram recording materials, and radio-telephone engineering [99-104]. $NaNbO_3$ is the only perovskite that undergoes the most complicated temperature and pressure-driven structural phase transitions which are not completely understood to date. The structural and dielectric behaviours of $NaNbO_3$ have been refined several times following the improvement of the characterization techniques for both single and polycrystalline samples[105-110]. The low-temperature powder neutron diffraction measurements revealed the coexistence of ferroelectric and antiferroelectric phases over a wide temperature range and the anomalous smearing of dielectric permittivity over the temperature range 12K $\leq T \leq$ 350K, consistent with the competing ferroelectric and antiferroelectric interactions [105].

Recently, Almeida *et al.* [111] reported the population accumulation effect of silicate glasses containing $NaNbO_3$ nano-crystals useful for the optical limiting behaviour which finds applications in laser power regulation devices and stabilization of signal levels in optical data transmissions [112]. The incorporation of In_2O_3 within the $NaNbO_3$ matrix exhibits enhanced photocatalytic activity which makes them a promising candidate for hydrogen fuel cells [113]. Raevski *et al*. reported the diffuse first-order phase transition near 150℃ in 9at.% of Gd doped $NaNbO_3$ with a significant decrease in the domain size across this transition which is tunable by incorporating the Gd-ions; also, dipoles of Gd-ions contribute significantly to the frequency dependence of dielectric permittivity [114,115]. However, the single crystals of $0.9NaNbO_3$-$0.1Gd_{1/3}NbO_3$ exhibit different prehistories and dielectric aging in the low-frequency range with a smeared phase transition whose frequency-dependent characteristics are different as compared with the standard relaxor ferroelectrics [116]. Titov *et al.* reported a dramatic decrease in the mean size of twin domains in (1–*x*) $NaNbO_3$+ *x* $Gd_{1/3}NbO_3$ with an increasing Gd content (*x*) as observed using the Metripol microscope system [117]. When *x* exceeds a certain threshold value $x_C \approx 0.11$, an abrupt drop occurs in the permittivity maximum $\varepsilon_r(T)$ by more than 100℃. These authors also noticed that the dielectric permittivity maximum ($\varepsilon_r \geq 1600$) diffuses markedly with an increase in the value of "*x*" due to the difference in the sizes of Na^+ and Gd^{3+} ions [117]. In the case of (1–*x*) $NaNbO_3$ + *x* $BiCrO_3$ ceramics, a mixed-phase consisting of both perovskite and the pyrochlore lattice was noticed by Hsiao *et al*. [118] Increasing the heat treatment conditions from 950℃ (for 5h) to 1250℃ (for 3h) reveals that there is a reduction in the pyrochlore content in the mixed phases for the compositions between 0.1 and 0.4. For *x* = 0.4, a very high (10^4) magnitude of ε_r with less dissipation (< 1) was observed across 50℃ in the $NaNbO_3$ + $BiCrO_3$ composites [118].

The doping of transition metals such as Ti, Mn, Co, Ni, or Cu inside the $NaNbO_3$ matrix has generated great interest (as discussed in section 1.7) because of their ability to alter their band structure and electrical conductivity [119-124]. Molak *et al*. reported that Mn-doped $NaNbO_3$ exhibits nine orders change in the

resistance (10^{13}-$10^{4}\Omega$) without altering its antiferroelectric behaviour [124]. These authors observed the activation energy E_a= 0.08eV in the temperature range of 17℃–127℃ and E_a = 0.5eV–0.6eV for T > 177℃. Such a change in the magnitude of E_a is associated with the energy levels introduced by the Mn dopant and/or due to oxygen vacancies [124]. On the other hand, the two-phase composites of binary transition metal oxides (TMO) can exhibit very high dielectric permittivity, and such systems have seen great interest in gas sensor applications [121-126]. For example, Wu *et al*. reported giant relative dielectric permittivity (ε_r > 10^5) near room temperature in $Li_{0.05}Ti_{0.02}Ni_{0.93}O$ due to an enhanced grain-boundary layer mechanism across the periphery of the capacitor geometry layers [125]. Similarly, some recent studies reported colossal dielectric permittivity in donor-acceptor (Nb, In) co-doped rutile TiO_2 and in (Li, In) doped ZnO [127,128] by increasing the Nb doping concentration in TiO_2 ceramics, two different dielectric responses were observed by Li *et al*. in the frequency dependence of dielectric properties which are associated with the space charge polarization and the electron-pinned defect-dipole effect [120].

Focusing on the antiferroelectric $NaNbO_3$ system, very limited literature is available dealing with the doping of TMOs inside $NaNbO_3$. Erünal *et al*. reported that at low sintering temperatures (937℃), Na_3NbO_4 emerges out as a secondary phase when 0.25 mol % Cu^{2+} doped in $NaNbO_3$. This system exhibits a distinctly diverse stoichiometry with two kinds of mutually compensating defect structures as represented by the Kroger-Vink notation (Cu''' – $V_O^{\bullet\bullet}$)' and ($V_O^{\bullet\bullet}$- Cu_{Nb}'''- $V_O^{\bullet\bullet}$)$^{\bullet}$ [129]. In this notation, the subscript indicates the lattice site occupied by the defect and the superscript corresponds to the electronic charge of the defect. The '••' symbol indicates a single positive charge, and the symbol <'> signifies a negative charge. The electron paramagnetic resonance studies of $Na_{0.98}[Nb_{0.9975}Cu_{0.0025}]O_3$ and $Na[Nb_{0.9975}Cu_{0.0025}]O_3$ systems reveal the quartet hyperfine coupling of S= 1/2 spin with the nucleus of isospin I= 3/2, indicating the $3d^9$ electronic configuration of Cu^{2+} [129]. Nevertheless, the two-phase composites comprising antiferromagnetic NiO and antiferroelectric $NaNbO_3$ have not been investigated till when we initiated this work. Both the systems (NiO and $NaNbO_3$) exhibit structural transitions above room temperature, one can tune such transitions for the modern electronic applications such as ferroelectric memories and magneto-electronic devices. Such structural transitions are usually accompanied by a change in the long-range ferroic-order (anti-ferromagnetic/ferrielectric) to a disordered (para-magnetic/ para-electric) state [130]. In particular, NiO exhibits a high temperature cubic to low temperature rhombohedral phase transition across 250℃, which plays an important role in the development of spin-valve devices, and $NaNbO_3$ exhibits a series of transitions below 480℃, e.g., orthorhombic to tetragonal across 480℃ and tetragonal to cubic at 370℃ [130-132]. Therefore, in order to gain a comprehensive understanding of the changes occurring in crystal structure and dielectric behaviour of NiO containing $NaNbO_3$, an attempt has been made here to study the two-phase composite system (1–x) $NaNbO_3$ + x NiO, over a wide composition range ($0.05 \leq x \leq 0.95$). This chapter deals with some intriguing dielectric properties and structural changes in $NaNbO_3$ + NiO composites.

3.2 Experimental Details:

In this section, we provide a detailed synthesis procedure and discuss various characterization techniques and their results pertaining to the $NaNbO_3$+NiO two-phase composites. Initially, various compositions (x) of the samples (1–x) $NaNbO_3$ + x NiO ($0 \leq x \leq 1$) were synthesized by the standard solid-state reaction method by taking stoichiometric amounts of $NaNbO_3$ and NiO. For this, undoped $NaNbO_3$ was first prepared by highly pure sodium carbonate (Na_2CO_3, EMPLURA, 99%) and niobium pentoxide (Nb_2O_5, SRL Pvt. Ltd., 99.95%). Appropriate amounts of these materials were mixed and blended by the Ball-Milling method for 5h with distilled water as the milling medium (Detailed discussion related to the synthesis is discussed in section 2.2). The Ball-Milled products were heated above 100℃ in air overnight to remove the water content and then calcined at 700℃ for 4h in air to obtain pure $NaNbO_3$. After this, stoichiometric amounts of pure NiO powder were added to pure $NaNbO_3$ for different desired compositions of (1–x) $NaNbO_3$ + x NiO ($0.10 \leq x \leq 0.95$). These mixed powders were pressed into cylindrical pellets of diameter 13mm using a hydraulic press with a maximum load of 5ton-cm^{-2}. All these pellets were finally sintered at 1040℃ for 4h in air.

The phase purity and crystal structure were examined using X-ray diffraction (XRD) measurements using a Rigaku X-ray diffractometer (model: TTRAX-III) with Cu-K_α radiation (λ = 1.541Å), followed by Rietveld refinement of the obtained diffraction patterns by means of FullProf programme. The microstructure of the samples was examined using a field emission scanning electron microscope (FESEM, Sigma, Zeiss) using a secondary electron mode. For the elemental analysis of the samples, a dual source X-ray photoelectron spectroscope (XPS, Al-K_α at 1486.8eV and Mg-K_α at 1253.6eV) from VG Microtech equipped with an ultra-high vacuum (8×10^{-10}Torr) chamber with a pass energy of 100eV was employed. The XPS spectra were recorded using monochromatized Al-K_α radiation, and the binding energies were calibrated against the advantageous C-1s peak 294eV. For the dielectric measurements, two sides of the sintered pellet were fashioned into a parallel-plate electrode geometry using silver coating. An impedance analyser from Solartron (Model SI1260) assembled with the high-temperature accessory (layout given in Chapter 2) was used for the dielectric measurements in the frequency range of 100Hz–20MHz with 100mV ac peak-to-peak amplitude of the ac-signal.

3.3 Results and Analysis:

3.3.1 Phase evolution and Microstructure:

Figure 3.1 shows the XRD pattern of the composites (1-x) $NaNbO_3$ + x NiO for different compositions ($0 \leq x \leq 1$) recorded at room temperature. The Rietveld refinement data for these diffraction patterns are shown in the figure 3.2. For dilute substitution of NiO ($x < 0.10$), all the diffraction patterns are analogous to the orthorhombic crystal structure similar to that of pure $NaNbO_3$ without any significant deviation in the lattice parameters and bond angles. All these diffraction patterns were corresponding to the space group *Pbcm*(57). However, with an increase in the composition, a slight increase in the lattice parameters (a = 5.51Å b = 5.52Å, and c = 15.58Å) was noticed when compared with the standard values of $NaNbO_3$ (a =

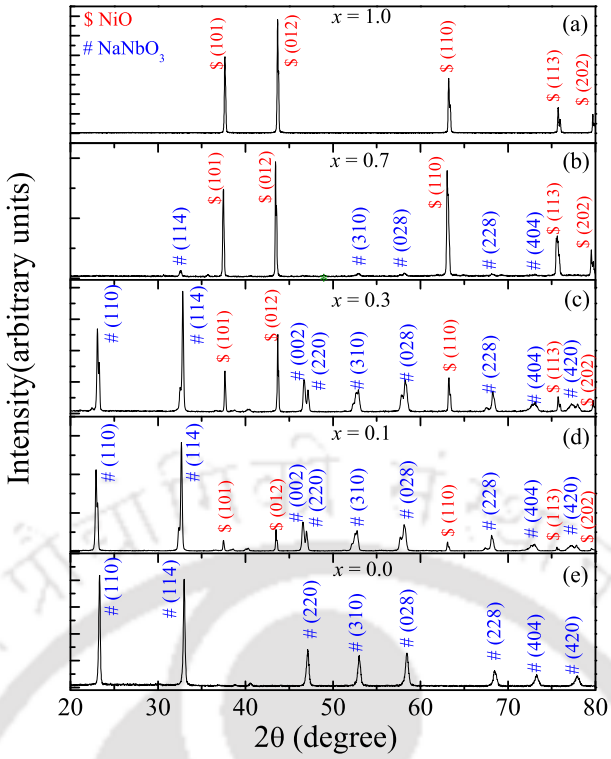

Figure 3.1 The X-ray diffraction data of (1-*x*) $NaNbO_3$ + *x* NiO samples for (*a*) *x* = 1.0, (*b*) *x* = 0.7, (*c*) *x* = 0.3, (*d*) *x* = 0.1, and (*e*) *x* = 0.0, sintered at 1040°C for 4 h in air. The blue colour Miller indices (#) represent the lattice plane of $NaNbO_3$, and the red colour Miller indices ($) represent the lattice plane of NiO.

5.50Å , b = 5.56Å, and c = 15.58Å) (figure 3.3). This change in the lattice parameter is expected with the increase in the dopant concentration because the divalent Ni^{2+} ions (ionic radius, $r_{Ni^{2+}}$= 0.69Å) are likely to occupy the Nb-sites (ionic radius, $r_{Nb^{5+}}$= 0.64Å) in the octahedra. As the composition '*x*' increases, the diffraction peaks corresponding to the rhombohedrally distorted NiO become more prominent (the Miller indices are indexed in red in figure 3.1); this secondary phase has been refined using the space group *R-3m*(166). It is interesting to observe that the diffraction peak at the Bragg angle $2\theta\sim$ 46.5° (220) splits into a doublet corresponding to Miller indices (220) and (002) for *x* = 0.10 and *x* = 0.30 (as shown in figure 3.4). Such peak- splitting usually occurs due to significant distortion from the orthorhombic crystal structure and transfers to a lower- symmetry monoclinic structure due to the cationic displacement [133,134]. Hence, the threshold between orthorhombic and monoclinic crystal symmetry for the $NaNbO_3$+NiO composite lies in between *x* = 0.3 and *x* = 0.5.

Earlier studies reported a similar type of peak-splitting across $2\theta\sim$ 45.7° in Li-doped $KNbO_3$ and $NaNbO_3$ and Li/ Ta co-doped $KNbO_3$ and $NaNbO_3$ [135]. Other ferroelectric systems such as $PbZr_{0.52}Ti_{0.48}O_3$ and $Pr_{0.5}Eu_{0.5}MnO_3$ also undergo such lower symmetry structural phase transitions; in particular, the tetragonal crystal structure transforms to the monoclinic phase [136]. In the present case, we observed that the interaxial angle 'β' deviates from 90.0° to 90.19° as the composition increases from 0.10 to 0.30, along with the decrease in the lattice parameter. This occurs due to the structural transition from tetragonal to

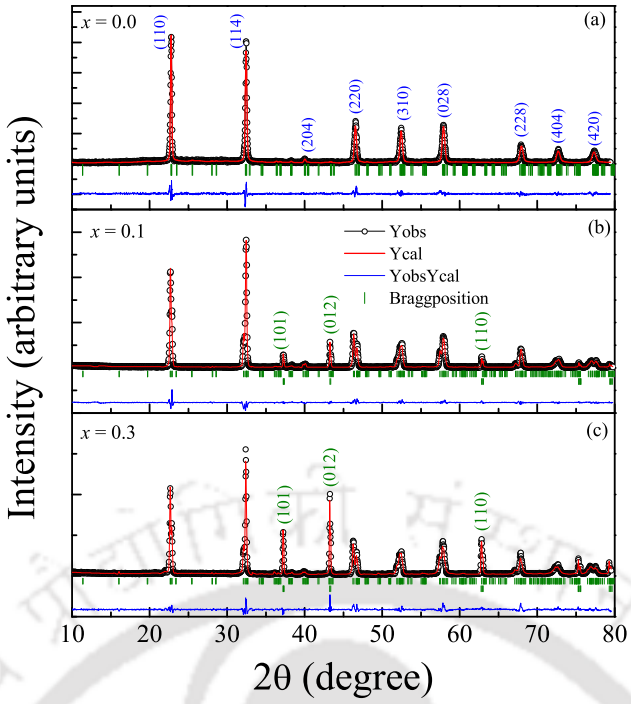

Figure 3.2. X-ray diffraction pattern together with the Rietveld Refined data of (1-*x*) $NaNbO_3$ + *x* NiO for (*a*) *x* = 0.0 (*b*) *x* = 0.1 and (*c*) *x* = 0.3 sintered at 1040℃ for 4h in air. Blue colour indexing corresponds to the Miller indices of $NaNbO_3$ and green colour indexing corresponds to that of NiO.

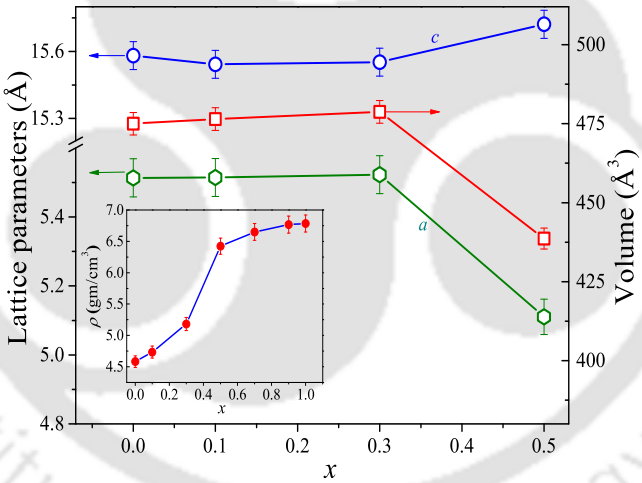

Figure 3.3. Variation in the lattice parameters and volume of the unit cell for (1 - *x*) $NaNbO_3$+ *x* NiO composite with a change in the NiO concentration (*x*). The inset shows the variation of density (ρ) with change in (*x*).

monoclinic. Such distortions were not traceable in these composites for the $x \geq 0.50$ system due to the domination of the rhombohedral NiO phase, and for $x \geq 0.80$, the signature of $NaNbO_3$ peaks gradually diminish and completely vanishes. From figure 3.3, it can be noticed that the lattice parameter 'a' decreases with an increase in *x* from 0.0 to 0.50, whereas the c-axis increases with gradual decrease in the volume of the unit cell. Since the ionic radius of the octahedrally occupied divalent Ni ion ($r_{Ni^{2+}}$ = 0.69Å) is greater than the ionic radii of the pentavalent Nb ion ($r_{Nb^{5+}}$0.64Å), one can expect larger unit cell parameters for the present investigated two-phase composites. Using the Rietveld refinement data, we have also calculated the density of the unit-cell for different concentrations of NiO ($0 \leq x \leq 1$) of the (1–*x*) $NaNbO_3$ + *x* NiO two-phase

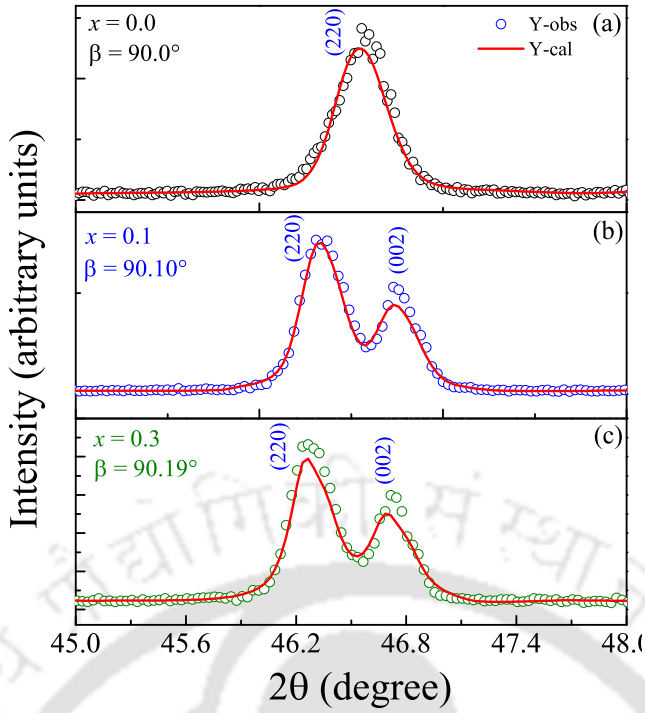

Figure 3.4. Diffraction peak at Bragg angle $2\theta \sim 46.55°$ (220) splitting from (*a*) *x* = 0.0 to a doublet corresponding to Miller indices (220) and (002) for (*b*) *x* = 0.1 and (*c*) *x* = 0.3.

composites (as depicted in the inset of figure 3.3). A significant increase in the unit-cell density from 4.58gm/cm^3 to 6.42gm/cm^3 for *x* = 0 to 0.50 was noticed due to the incorporation of NiO. The average grain size (D) and micro-strain (η) have been estimated using the Williamson-Hall (W-H) analysis using the equation $\beta Cos\theta = \kappa\lambda/D + \eta Sin\theta$. In the above equation 'β' is the full width at half maximum (FWHM) of diffraction peak intensity, and the constant 'κ' represents the shape parameter and is equal to 0.89 for spherical particles, and λ is the wavelength of X-ray source. The average grain size 'D' (73–490nm) and micro-strain (η = 10^{-3}) have been obtained from the intercepts and slopes of $\beta Cos\theta$ versus $Sin\theta$ for different compositions of (1-*x*) $NaNbO_3$ + *x* NiO. As the NiO concentration increases, the FWHM of the diffraction peaks increases, which signifies the contribution of decrease in the grain size and an increase in the lattice strain in these $NaNbO_3$+NiO composites. Identical behaviour was also observed in systems like CdO+ZnO and NiO+ZnO composites [123,137-141].

The FESEM micrographs shown in figures 3.5(*a*) and 3.5(*b*) were recorded in the secondary- electron (SE) mode for the compositions *x* = 0.10 and 0.95, respectively. These micrographs depict the polygonal shape morphology of average grain sizes 344nm and 380nm, with clear grain boundaries of widths 42nm and 53nm for *x* = 0.10 and 0.95, respectively. A thorough statistical analysis has been carried out, in order to understand the detailed and precise distribution of the grains in $NaNbO_3$-NiO two-phase composites. The inset of figure 3.5 represents the histograms of the particle size distribution where maximum number of particles lie in the range 350-400nm and 300-400nm for *x* = 0.10 and *x* = 0.95 respectively.

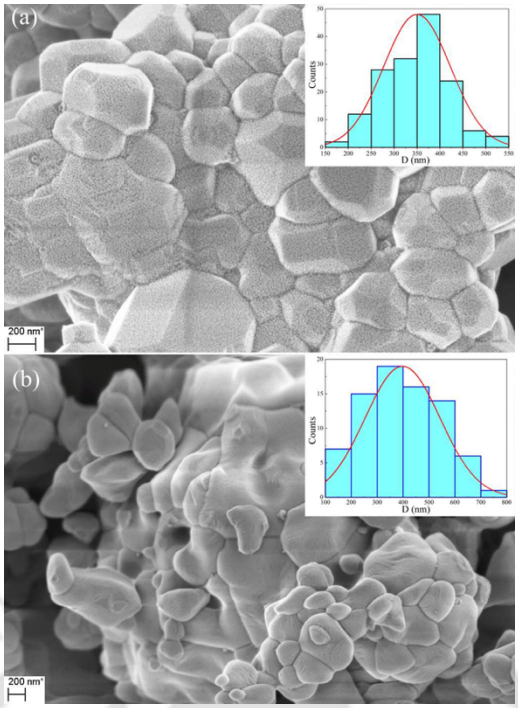

Figure 3.5. FESEM micrographs recorded under secondary-electron mode for (*a*) *x* = 0.10 and (*b*) *x* = 0.95 respectively. Inset of (*a*) and (*b*) shows the histogram analysis for average grain size for respective compositions.

3.3.2 Elemental Analysis using X-ray Photoelectron Spectroscopy:

The electronic structure of the synthesized composites was examined by using XPS (a detailed description about the XPS has been given in section 2.3.3). The entire XPS spectrum for O-1s, Na-1s, Ni-2p, and Nb-3d core levels was calibrated by using the binding energy (BE) of advantageous carbon (C-1s) orbitals positioned at 284eV [142-145]. Figure 3.6(*a*) shows the X-ray photoelectron intensity versus binding energy (BE) spectra of the Na-1s core levels for *x* = 0.70. From this figure, we observe that Na-1s spectra exhibit a single peak centred at 1070.22eV, indicating that 'Na' ions possess +1 oxidation state [146-148]. The 3d-core-level XPS spectra of Nb [figure 3.6(*b*)] exhibit two peaks associated with the 3d doublet states 3$d_{5/2}$ and 3$d_{3/2}$ without any signatures of satellite peaks, signifying the presence of pentavalent oxidation of Nb. On the other hand, the XPS spectra of Ni-2p show four peaks between 853.96eV and 879.05eV [figure 3.6(*c*)]. This spectrum is further deconvoluted into five Gaussian-Lorentzian (GL) peaks centred at 845.47eV, 853.96eV, 860.35eV, 871.78eV, and 879.05eV, respectively. The two main peaks centred at 853.96eV and 871.78eV are associated with the doublets Ni-2$p_{3/2}$ and Ni-2$p_{1/2}$, respectively [142-145]. The binding energy separation (ΔE) between these doublets (ΔE = $Ep_{1/2}$- $Ep_{3/2}$) is 17.82eV, signifying the presence of the divalent oxidation state of Ni [142-145,149]. This binding energy difference is slightly higher as compared with the binding energy of the metallic state of Ni (17.4eV), however, less than the stoichiometric value of pure NiO (18eV) [142-145,149]. Along with these two main peaks, we also observed additional three more satellite peaks centred at 845.47eV, 860.35eV, and 879.05eV designated by S1, S2, and S3 in figure 3.6(*c*), respectively. These satellite peaks shifted toward the lower binding-energy scale as compared to pure NiO

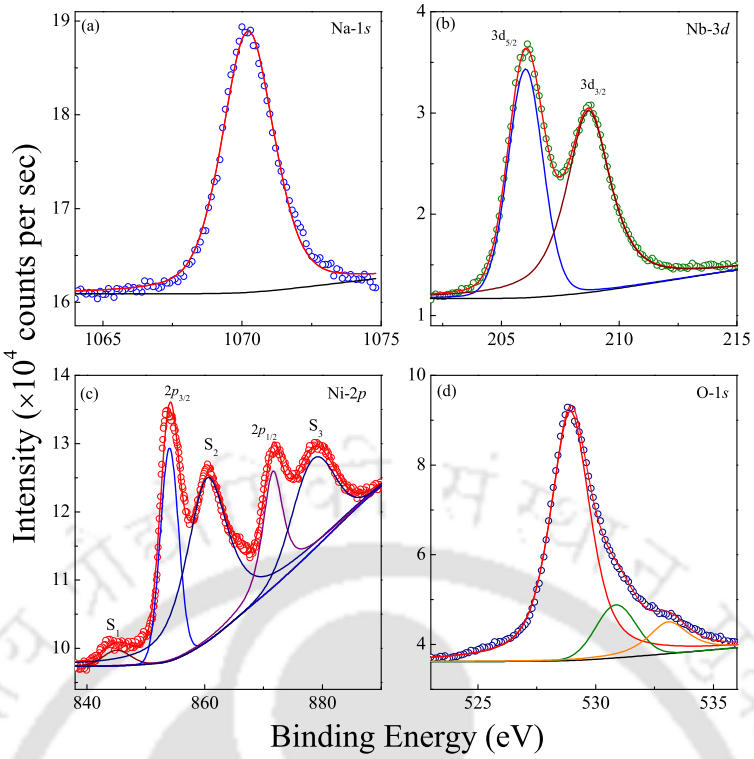

Figure 3.6. The core level X-ray photo- electron spectra of (*a*) Na-1s, (*b*) Nb- 3d, (*c*) Ni-2p, and (*d*) O-1s core-level spectra of (1-*x*) $NaNbO_3$ + *x* NiO for *x* = 0.70.

[144,150]. This shift in the satellite peaks is associated with the non-local screening of Ni^{2+}. The charge transfer nature of the valance band states leads to the screening of Ni^{2+}, which can be analysed in terms of a simplified model based on final state effects where photoemission is accompanied by the rearrangement of electrons in the valance band [151].

$$2p^6 3d^8 + h\nu \rightarrow 2p^5 3d^8 + e^- \quad (3.2)$$

$$2p^5 3d^8 + e^- \rightarrow 2p^5 3d^9 L + e^- \quad (3.3)$$

The above equation 'L' represents a hole in the O-2p band. Using this model, the main Ni-2$p_{3/2}$ peak is observed across 853.9eV associated with the local screening of lattice oxygen along with a satellite peak at 860.3eV caused by the non-local screening effect [150,151]. Finally, the O-1s XPS spectrum shown in figure 3.6(*d*) is partially resolved into three GL peaks centred at 528.93eV, 530.86eV, and 533.09eV, which indicates that oxygen is in a different environment in the $NaNbO_3$-NiO composites [128,129]. The main peak centred at 528.93eV arises due to the oxygen bonded with the cations, i.e., Na^+, Nb^{5+}, and Ni^{2+}, whereas the second peak at 530.86eV is related to the surface oxygen presence in the system with a small amount of vacancies [152-154]. The third peak at 533.09eV is associated to the additional oxygen present in the system in the form of a hydroxyl group adsorbed by either Na or Ni from the surface [155].

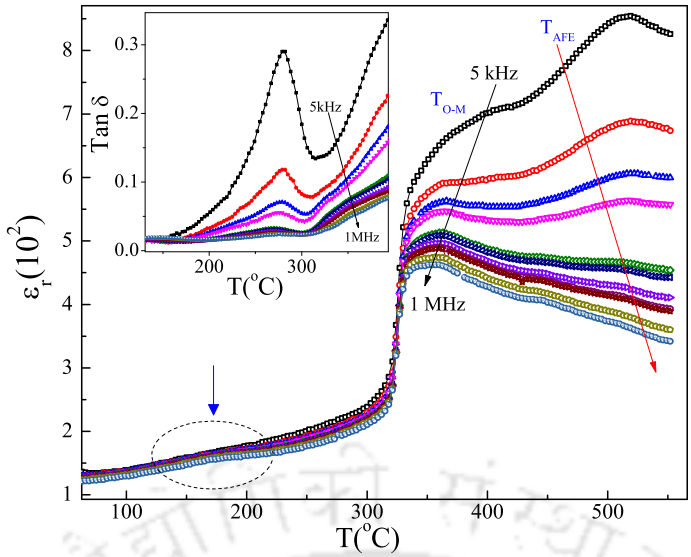

Figure 3.7. Temperature dependent relative dielectric permittivity $\varepsilon_r(T)$ measured at various frequencies (5kHz ≤ f ≤ 1MHz) for $NaNbO_3$ + 0.10 NiO with very closely spaced temperature intervals (T = 3°C) and temperature ranging from 30°C to 550°C. The inset shows the temperature dependence of dissipation factor $Tan\ \delta$ recorded for the same range of frequencies. The encircled region shows the feeble anomaly that emerged at T~ 170°C.

3.3.3 High-temperature Dielectric Spectroscopy:

In order to understand the role of NiO on the global dielectric behaviour of $NaNbO_3$, we measured the variation in the relative dielectric permittivity ε_r as a function of temperature, $\varepsilon_r(T)$ at different frequencies (*f*) of the ac-signal for two different compositions *x* = 0.10 and 0.95. Figures 3.7 and 3.8 show ε_r versus T measured between the temperatures 30°C and 550°C for different *f* in the range 5kHz–20MHz for *x* = 0.10 and *f* = 100Hz – 20MHz for *x* = 0.95, respectively. Two major humps were observed in $\varepsilon_r(T)$; the first hump appears across 520°C and the second hump across 398°C for *x* = 0.10 at low frequencies. These two transitions are associated with the antiferroelectric to paraelectric transition (T_{AFE}) and orthorhombic (*Pmna*) to monoclinic (*Pbma*) crystal structure transition (T_{O-M}) within the antiferroelectric region, respectively. For low frequencies, the antiferroelectric transition is more prominent than the crystallographic transition (21% increase in the dielectric permittivity was noticed). For the case of undoped $NaNbO_3$, the above transitions take place at 570°C and 375°C, clearly indicating the dominant role of antiferromagnetic NiO, signifying the effect on the antiferroelectric long range ordering. These transitions are strongly dependent on the ac-driving frequency; in particular, T_{AFE} for these composites gradually smeared-off with an increasing frequency from 5kHz to 1MHz (indicated by the red arrow in figure 3.7), whereas the structural transition T_{O-M} shifts from 398°C to 345°C as the measuring frequency increases from 5kHz to 1MHz.

It is interesting to note that a feeble anomaly close to 170 ± 5°C was observed for the *x* = 0.10 composite (figure 3.7). A similar type of anomaly was reported previously by Shirane *et al.* in $NaNbO_3$ with a small amount of ferroelectric $KNbO_3$ [131]. Raevski *et al.* reported such a weak anomaly across 150°C in

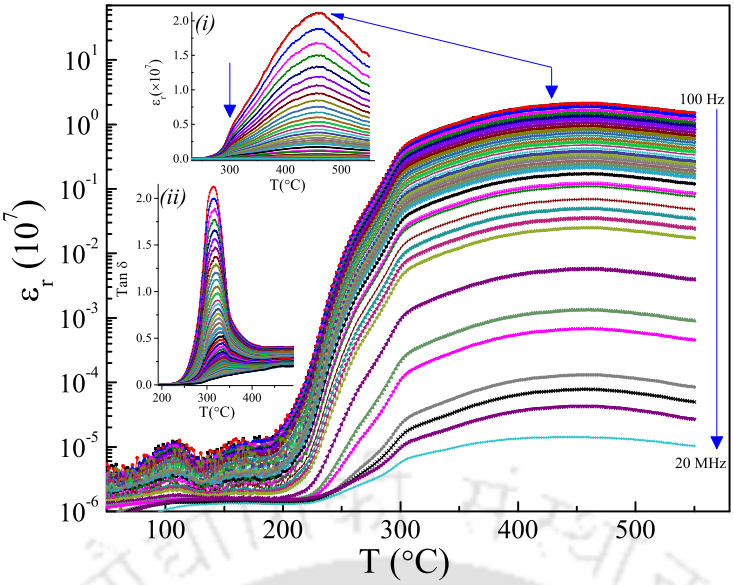

Figure 3.8. Log-scale representation of temperature dependent relative dielectric permittivity $\varepsilon_r(T)$ measured at various frequencies (100Hz ≤ f ≤ 20MHz) for $NaNbO_3$ + 0.95NiO with very closed spaced temperature intervals (T = 2°C) and temperature ranging from 50°C to 550°C. The inset (*i*) shows the variation in the same in linear scale. Inset (*ii*) shows the variation of loss-tangent versus temperature.

$\varepsilon_r(T)$ of single crystals of $NaNbO_3$, (Na,Li)NbO_3, and (K,Na)NbO_3 solid solutions. From the temperature dependence of lattice parameters [$a(T)$, $b(T)$, and $c(T)$], these authors concluded that such an additional phase transition in the vicinity of second-order transition is due to the rhombohedral distortion of the perovskite structure (1% lattice hysteresis between $a(T)$ and $b(T)$ across 150°C with a change in the interaxial angle $\Delta\beta\sim$ 0.3) [156,157]. On the other hand, the temperature dependence of loss-tangent ($Tan\ \delta$ versus T) shows a cusp like feature across 279°C and increases continuously beyond this temperature (inset of figure 3.7); across the same, ε_r, starts rising. For *x* = 0.95, the giant values of $\varepsilon_r(T)$ were noticed for all the frequencies with a very broad maximum in $\varepsilon_r(T)$ [inset (*i*) of figure 3.8] where a major contribution from NiO is anticipated. Moreover, the transitions pertaining to $NaNbO_3$ (T_{O-M} and T_{AFE}) were untraceable in figure 3.8, and the global dielectric behaviour is dominated by NiO. Interestingly, a shoulder-like feature is evident between 250°C and 320°C [indicated by the arrow mark in the inset (*i*) of figure 3.8], which is linked with the antiferromagnetic to paramagnetic transition of NiO; such a change in the magnetic ordering is usually accompanied by a structural change from rhombohedral to high temperature cubic crystal structure of NiO. In the case of undoped NiO (with perfect stoichiometry), such a transition usually occurs across 253 ± 6°C [121,158]. The temperature dependence of loss-tangent for *x* = 0.95 [inset (*ii*) of figure 3.8] exhibits a giant frequency independent peak centred at 314°C associated with the change in the crystal structure and magnetic ordering as discussed above. Nevertheless, the additional phase transition noticed across 170°C for lower compositions (*x* ≤ 0.10) is very feeble in *x* = 0.95 system due to the dominance of the antiferromagnetic NiO.

The divergence of $\varepsilon_r(T)$ across the ferroelectric phase transition is directly connected with the softening of the phonon mode and can be explained by the Lyddane-Sachs-Teller (LST) relation (Section 1.4 gives a brief outlook into the origin of lattice vibrations and history of formulation LST relation). The generalized LST relation contains all the dielectric dispersion terms

$$\left(\frac{\varepsilon_0 - S'}{\varepsilon_\infty}\right) = \left(\frac{\omega_l}{\omega_t}\right)^2 \tag{3.4}$$

where ε_0 and ε_∞ are static and high frequency dielectric permittivity, respectively, and S' is the strength of the permanent dipole moments [159]. As the ferroelectric transition is approached, the suppression of long-range harmonic modes occurs and a short-range anharmonic ordering takes place, leading to the softening of optical phonon frequencies ($\omega_l \rightarrow 0$) [159]. Under these circumstances, the high frequency dielectric permittivity (ε_∞) attains its maximum value. Such a singular behaviour of 'ε_r' can also be understood from the thermodynamic free energy model: the nonlinear free energy expression contains the terms polarization P and temperature T in the form $F(T,\ P) = F_0(T) + \mathcal{A}P^2 + BP^4 + CP^6$, where $\mathcal{A}$, B, and C are the phenomenological coefficients [159]. According to the theoretical description given by Landau and Lifshitz, the coefficients '$\mathcal{A}$' and 'T' are linked to the dielectric constant as given by the following relation [160]:

$$\varepsilon = \frac{1}{\left(\frac{\partial^2 F}{\partial T^2}\right)_{P=0}} = \frac{1}{2\mathcal{A}} \tag{3.5}$$

Across the phase transition, coefficient $\mathcal{A} \rightarrow 0$ leads to the divergence in dielectric constant [160]. Although the validity of the above equation is for a second-order phase transition, even for a first-order phase transition, the magnitude of '$\mathcal{A}$' significantly drops from its maximum value but does not vanish completely.

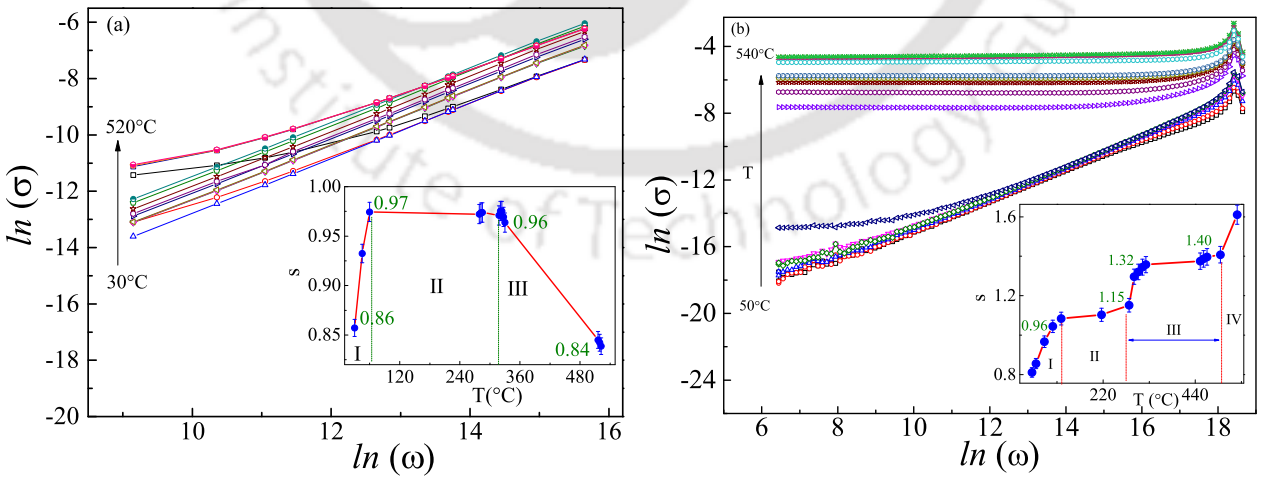

Figure 3.9. The log-log plot of ac-conductivity (σ_{ac}) against angular frequency (ω) measured at various temperatures for (*a*) *x* = 0.10 and (*b*) *x* = 0.95. The inset shows the variation in the frequency exponent "*s*" calculated from Jonscher's universal power law.

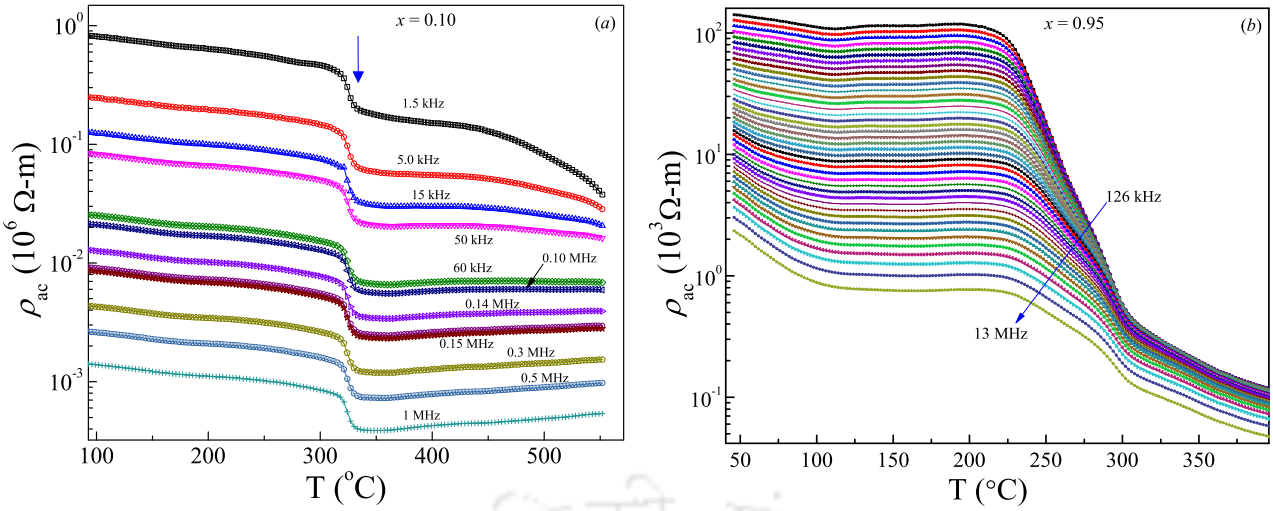

Figure 3.10. Temperature variation in ac-resistivity ($\rho_{ac}(T)$) for (*a*) *x* = 0.10 and (*b*) *x* = 0.95 for frequency ranging between 1.5kHz and 13MHz.

3.3.4 Conductivity Analysis and Jonscher's Power law:

A. K. Jonscher, in his review article in 1977 reported a '*universality of frequency and time response*' while inspecting the dielectric response suggesting a dominating role of many-body interaction [161]. This law shows that the ac-conductivity can be expressed as sum of frequency independent part (dc-conductivity) and frequency dependent part. This law is sometimes referred to as *Universal Power Law* and it can be written as

$$\sigma_{ac} = \sigma_{dc} + A\omega^{s} \quad (3.6)$$

where A is the temperature dependent constant which is known as the pre-exponential factor and can be written as

$$A = \omega_C^{-s}\sigma_{dc} \quad (3.7)$$

and ω_C is the frequency of onset for dispersive behaviour [162] and can be written as

$$\omega_C = \omega_{ph}\exp\left(-\frac{E_a}{k_B T}\right) \quad (3.8)$$

where ω_{ph} is the vibration frequency of atoms in the solids and usually taken as 10^{12}rad/sec, E_a is the activation energy. Moreover, Funke, in his *Jump Relaxation Model* points out that it is important to note that for a non-zero dc-conductivity, the power-law exponent should be smaller than one, which otherwise would imply that there would be no successful hops [163]. Also, the jump relaxation model gives an expression for the exponent in the power-law as:

$$s = \frac{backhop\ rate}{site\ relaxation\ rate} \quad (3.9)$$

In order to understand the frequency (1.5kHz ≤ *f* ≤ 13MHz) dependence of the charge transport mechanism in the present composite system, we measured the ac-conductivity, σ_{ac} at various temperatures with 100mV constant peak-to-peak driving potential of varying frequency. The scattered symbols shown in figure 3.9(*a*) and (*b*) are the frequency dependence of σ_{ac} values obtained experimentally for both *x* = 0.10

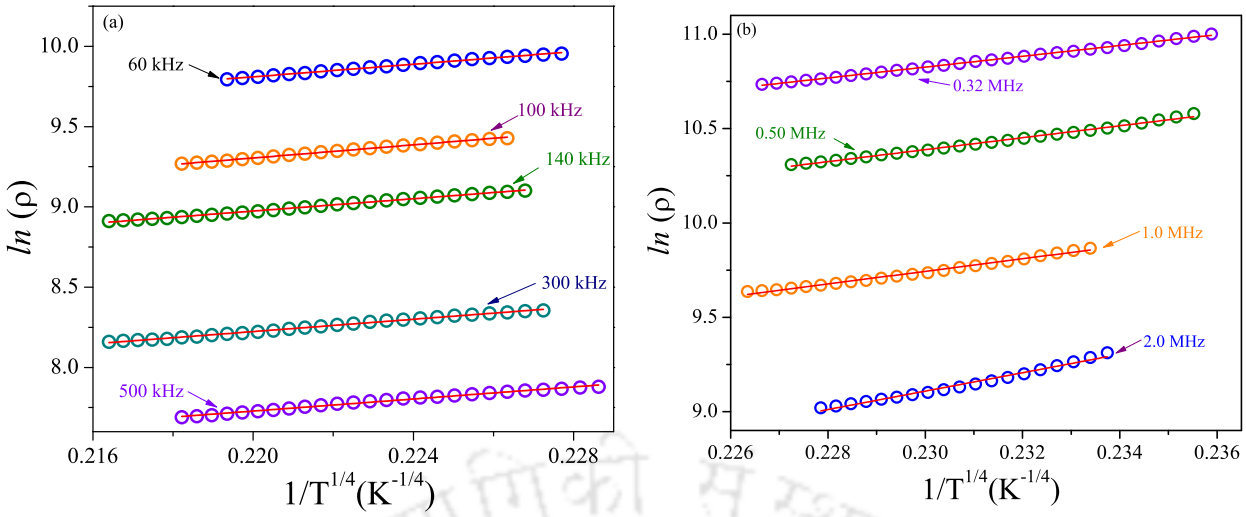

Figure 3.11. Logarithmic variation in ac-resistivity [$ln(\rho_{ac})$] versus $T^{-1/4}$ for (*a*) *x* = 0.10 and (*b*) *x* = 0.95 for few selected frequencies.

and 0.95. In the present case, $\sigma_{ac}(f)$ was plotted only for selected temperatures between 30°C and 540°C. In figure 3.9, solid lines represent the best fit of the experimental data with Jonscher's universal power law (JPL) ($\sigma_{ac} = \sigma_0 + A\omega^s$) [164,165]. In this equation, the quantity σ_0 is the frequency independent conductivity, the coefficient 'A' is the dispersion parameter, and the dimensionless frequency exponent 's' represents the measure of the degree of the interaction and is a temperature dependent parameter. For ceramics and high-κ dielectric composites, the above-mentioned power law is extensively used to understand the frequency dependent behaviour although different models are available in the literature [125,158,166]. For the general case, the value of "s" should lie between 0 and 1, popularly known as the "universal dynamic response" (UDR) [165,167,168]. Some systems also follow the double power law behaviour with $s > 1$ [169-171].

From figure 3.9, it can be observed that for both the compositions, σ_{ac} increases with an increase in the frequency, signifying the trapping of localized charge carriers. The origin of the frequency dependence of conductivity lies in the relaxation phenomena arising due to the mobile charge carriers. Generally, at low frequencies, there exists a frequency independent plateau region [i.e., dc-conductivity σ_0]; however, for *x* = 0.10, the frequency independent σ_0 plateau region is not clearly visible since the measurements were performed between the frequencies 1.5kHz and 1MHz (for many polycrystalline systems, σ_0 is dominated for *f* < 1kHz [172]). At low frequencies [the plateau region in figure 3.9(*b*)], the charge conduction process occurs through infinite paths via long-range translational motion of the charge carriers. This behaviour can be explained using the jump relaxation model. According to this model, the electrons undergo successful hopping to its neighbouring vacant site at low frequencies for a long period of time and lead to the long range translational motion of charge carriers which contributes to the dc-conductivity σ_0.

T(℃)	x = 0.10		x = 0.95	
	s	$A\times10^{-11}$	s	$A\times10^{-11}$
50	0.932	29.768	0.81	13.13
100	0.974	16.485	1.04	0.460
304	0.971	34.759	1.32	0.013
500	0.845	340.17	1.41	0.006

Table 3.1. The list of measured parameters "A" and frequency exponent "s" obtained from Jonscher's power law analysis for x = 0.10 and x = 0.95.

On the other hand, in the frequency dependence region, the charge transport occurs mainly by hopping of the charges. In the present case for f > 7kHz, two competing relaxation processes occur; (*i*) successful hopping where the charge carriers relax into its neighbourhood site and (*ii*) unsuccessful hopping where the charge carrier jumps back to its initial position. The ratio of successful hopping over unsuccessful hopping creates the dispersion in conductivity at high frequencies, and the term $A\omega^s$ dominates. In most polycrystalline samples, two different dispersion regimes can be observed in σ_{ac}. Such regions are associated with the grain boundaries (low-frequency dispersion) and grains (high-frequency dispersion) which can be explained by the double power law related to the JPL discussed above.

$$\sigma_{ac} = \sigma_0 + A_1\omega^{s_1} + A_2\omega^{s_2} \qquad (3.10)$$

In the above equation, the second term $A_1\omega^{s_1}(0 \leq s_1 \leq 1)$ is assigned to the low-frequency dispersion region (2kHz ≤ f ≤ 3MHz) corresponding to the short-range hopping process, whereas the contribution of the third term $A_2\omega^{s_2}(0 \leq s_2 \leq 2)$ is significant in the high frequency region (f > 3MHz) which is associated with the hopping of charge carriers back and forth between the localized states. From the linear fitting analysis ($\sigma = A\omega^s$), we obtained the values of 'A' and 's' for the two compositions, and these values are listed in Table 3.1. The temperature dependence of the experimentally determined 's' values can be used to examine the validity of charge transport by a specific hopping model for the current system [173-176]. For example, if the transport is through the variable range hopping mechanism, the magnitude of the exponent $s \sim 0.8$ is expected which is consistent with the current result 0.838 ≤ s ≤ 0.974 for x = 0.10 [121,174]. Nevertheless, a significant deviation is often observed from the standard JPL behaviour ω^s for x > 0.10, which is associated with the feeble frequency dependence of the exponent s [173,177].

The variation in 's' as a function of temperature for both the compositions is shown in the inset of F figure 3.9(*a*) and 3.9(*b*). Generally, the conduction behaviour exhibits a remarkable relationship with the obtained exponent 's'. The temperature independent behaviour of 's' suggests that the charge transport process is mainly dominated by tunnelling of the charge carriers by thermal energy [170]. Previous reports on the frequency and temperature dependent ac-conductivity studies of the $NaNbO_3$ reveals that the 's'

values derived from the power law lie between 0.15 and 0.44. These values signify that the charge conduction mechanism is dominated by the small and Large Polaron hopping process with a high effective mass of electron m_e^* due to the localization of electrons [170]. For Small Polaron hopping conduction, the value of $'s'$ increases with temperature, while for Large Polaron hopping, $'s'$ decreases with an increase in the temperature. For *x* = 0.10, we noticed three different regions in the $s(T)$ curve [inset of figure 3.9(*a*)]: from 30℃ to 60℃ (Region-I), from 60℃ to 310℃ (Region- II), and from 310℃ to 520℃ (Region-III). It is clearly evident that in the plateau region-II, $'s'$ is almost independent and decreases to 0.83 on either side of the temperature window. From this analysis, we conclude that the conduction mechanism below 60℃ is mainly dominated by the hopping of Small Polarons. The concept of Polaron hopping is discussed below.

3.3.5 Polaron Hopping and VRH Mechanism:

When a conduction electron interacts with self-induced polarization in an ionic crystal, a quasiparticle called a Polaron will form [179]. The concept of *Polaron* can also be used to understand the nature of interaction between electrons and atoms. Previous reports by Fröhlich in 1954 gave insight to a category of Polarons whose spatial extension was found to be larger than that of the lattice parameter itself [180]. The coupling constant for α was expressed as,

$$\alpha = \frac{e^2}{\hbar c}\sqrt{\frac{m_b c^2}{2\hbar\omega_{LO}}}\left(\frac{1}{\varepsilon_\infty}-\frac{1}{\varepsilon_0}\right) \tag{3.11}$$

were ε_∞ and ε_0 are the electronic and static dielectric constant of the crystal, m_b is the band mass of electron. This Polaron was dedicated to categorize the interaction between charge carrier and long-wavelength optical phonons. The Fröhlich Polarons are also referred to as *Large Polarons*.

First theoretical breakthrough for the concept of *Small Polaron* conduction was established by Yamashita and Kurosawa in 1958, when the band theory failed to explained the conduction mechanism by usual localized electron when effective mass of electron m^* is large (when the induced lattice polarization and polarization field generated by self-trap are significant) [181,182]. Small Polaron on the contrary to large Polarons, are responsible for short range forces. Mobility of Small Polaron is governed by Einstein's relation,

$$\mu = \frac{eD}{k_B T} \tag{3.12}$$

Here, Diffusion constant $D = < v^2\tau >$, $< v^2 > = 2J^2a^2/\hbar^2$, $J = \hbar/\tau$. Here $< v >$ is the averaged carrier velocity, J is the electron transfer integral. After applying the condition for self-trapping ($\tau \gg \tau_0$; τ_0 is the time period for lattice vibration) which leads to the upper limit for the mobility in the hopping region (given by the below equation),

$$\mu \ll \frac{ea^2}{2\tau_0 k_B T} = \left(\frac{1}{4\pi}\right)\left(\frac{ea^2}{\hbar}\right)\left(\frac{\hbar\omega_0}{kT}\right) \tag{3.13}$$

Later in 1963, Hall effect over the non-adiabatic Polaron hopping was first developed by Friedman and Holstein in 2D equilateral triangle lattice [183]. Further in 1969, Emin and Holstein came up with the

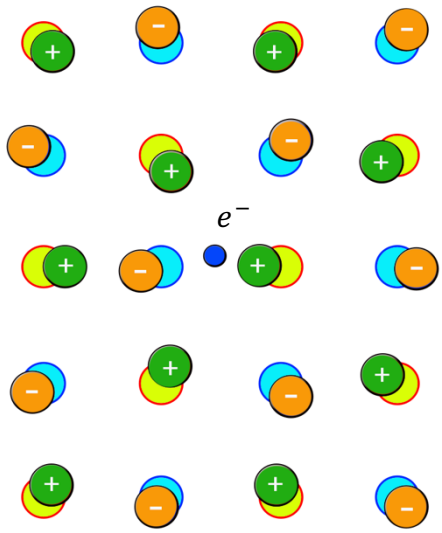

Figure 3.12. Schematic picture describing the interaction between electron and atoms within a crystal (i.e. Polaron).

adiabatic theory for the Small Polaron motion [184]. Emin and Holstein arrived at an expression for mobility of small Polaron for *adiabatic* analogue which was valid at high temperatures.

$$\mu = \frac{3}{4\pi}\left(\frac{ea^2}{\hbar}\right)\left(\frac{\hbar\omega_0}{kT}\right)\exp\left(-\frac{\{U-J\}}{k_BT}\right);\ U = \frac{1}{2}\gamma\hbar\omega_0 \qquad (3.14)$$

In the above equation γ is known as the *Holstein constant*. In the present system (for x = 0.10), the formation of Small Polarons occurs due to the incomplete d-orbital of Nb^{4+} caused by the oxygen vacancies above room temperature, reducing Nb^{5+} to Nb^{4+}. With an increase in the temperature (> 310°C), these Small Polarons dissociate into residual carriers and interact with the positive ions present in the system. Such an interaction between the lattice and charges leads to the formation of Large Polarons whose mobility is inversely proportional to the square root of temperature ($\propto T^{-1/2}$). Due to this interaction, the slope of the $s(T)$ curve decreases significantly. For a very high composition, $x \geq 0.95$ [inset of figure 3.9(*b*)], we observed the UDR behaviour in Region-I from 50°C to 100°C (with 's' values between 0.81 and 1.04), whereas, the double power law behaviour was noticed in three different temperature regimes: Region-II from 100°C to 280°C (1.04 to 1.15), Region-III from 280°C to 450°C (1.15 to 1.36), and Region-IV from 450°C to 540°C (1.36 to 1.61). Normally, the ac-component of $\sigma(\omega)$ in JPL exhibits a weaker temperature dependence than the dc part, which often follows a thermally activated Mott's variable-range-hopping process [173,174]. Recent studies dealing with the temperature and frequency dependent ac-conductivity of $KNbO_3$ based composites reported the dominance of Mott's variable range hopping of charge carriers between Nb^{5+} and Nb^{3+} ions [158].

f ($\times 10^3$Hz)	x = 0.10			x = 0.95		
	$N(\xi_F)$ $\times 10^{39}$J^{-1}cm^{-1}	r_h nm	ϵ_h meV	$N(\xi_F)$ $\times 10^{39}$J^{-1}cm^{-1}	r_h nm	ϵ_h meV
1.5	8.22	1.780	32.0	2.25	2.58	38.0
500	9.27	1.727	31.2	1.15	3.05	30.7
1000	10.40	1.678	30.4	0.94	3.21	48.3

Table 3.2. List of parameters: density of states [$N(\xi_F)$], average hopping length (r_h), and average hopping energy (ϵ_h), obtained from VRH analysis for x = 0.10 and x = 0.95.

3.3.6 Confirmation of Mott's VRH mechanism:

Figures 3.10(*a*) and 3.10(*b*) show the temperature dependence of ac-resistivity $\rho_{ac}(T)$ measured at various frequencies (1.5kHz ≤ f ≤ 1MHz) for x = 0.10 and for frequencies (126kHz ≤ f ≤ 13MHz) for x = 0.95, respectively. For (126kHz ≤ f ≤ 13MHz) for x = 0.95, respectively. For x = 0.10, the system exhibits a large value of resistivity $\rho_{ac} \sim 10^5\Omega$-m at room temperature for f = 1.5kHz. As the temperature increases, ρ_{ac} starts to decrease and exhibits a sudden drop across 350°C [indicated by arrow in figure 3.10(*a*)] due to the phase-transition from the monoclinic to the orthorhombic crystal structure of $NaNbO_3$. Additionally, a small hump across T_{AFE} was noticed, which is associated with the antiferroelectric to paraelectric transition of $NaNbO_3$ [177]. For the higher compositions (x ≥ 0.95), the $\rho_{ac}(T)$ curves exhibit a hundred fold drop across 210°C due to the inter-mixture of antiferromagnetic domains of NiO with the morphotropic phase boundary of the $NaNbO_3$ matrix [121,158]. In order to understand the charge conduction mechanism in these composites, we further analysed the temperature dependence of ac-resistivity data in detail. Figure 3.11 shows the plots of $ln(\rho_{ac})$ against $T^{-1/4}$ for selected frequencies for both the compositions x = 0.10 and 0.95. The linear behaviour of these curves provides the signature of Mott's variable-range hopping of charge carriers; this result supports the frequency dependence of σ_{ac} analysis discussed above. Before moving into the interpretation of experimental data, it is important to know about the formulation of VRH. In 1969, N.F. Mott came up with this revolutionizing theory that is used even today to understand the low temperature conduction of localized charge carriers [185]. According to Mott's VRH model, the electrical resistivity in d-dimenional hopping can be written as,

$$\rho = \rho_0 \, exp\left(\frac{T_0}{T}\right)^{\frac{1}{1+d}} \tag{3.15}$$

which reduces to equation 3.16.

$$\rho = \rho_0 \, exp\left(\frac{T_0}{T}\right)^{\frac{1}{4}} \tag{3.16}$$

where ρ_0 is the pre-exponent factor, T_0 is the characteristic temperature which depends on the density of states ($N(\xi_F)$) near the Fermi level and can be written as

$$T_0 = \frac{16\alpha^3}{k_B N(\xi_F)} \tag{3.17}$$

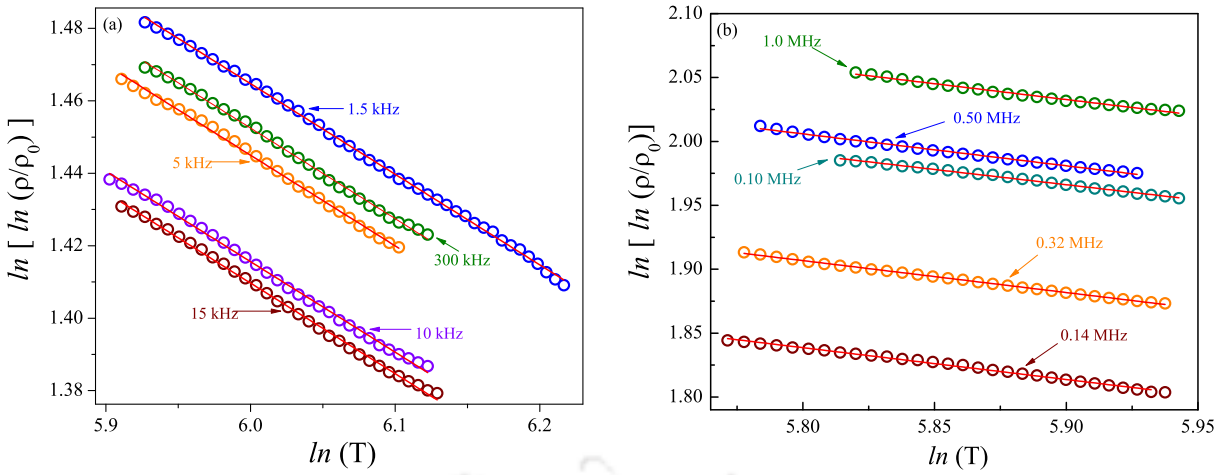

Figure 3.13. The double logarithmic variation of (ρ/ρ_0) as a function of $ln(T)$ for few selected frequencies for (*a*) x = 0.10 and (*b*) x = 0.95.

were α is the spatial extension of the wave function $\psi = \exp(-\alpha R)$. He noted that the conduction due to hopping from energy states that are in close range to the Fermi Level. Thus, Mott came up with an argument that Fermi energy lies in the hopping regime and that $k_B T$ is small compared to band-width [185]. He stated that if the electron is to jump to a distance less than R_H, then the number of states in the range dE can be written as,

$$\left(\frac{4}{3}\pi R^3\right) N(E) dE \tag{3.18}$$

where the maximum probable distance of hopping can be written as

$$2\alpha = \frac{9}{4\pi R^4 N(E) k_B T} \tag{3.19}$$

and thus, the average spacing between the energy of hopping or the activation energy when $R < R_H$ is,

$$W_H = \frac{3}{4\pi R_H^3 N(\xi_F)} \tag{3.20}$$

These equations have now evolved to take different forms in order to so as to explain the hopping mechanism in various materials. Below, we provide a detailed discussion that explains the rigorous analysis involving the current experimental results providing the evidence for the VRH mechanism present in the system. According to the Mott's variable-range hopping model, the charge conduction mechanism should follow the relation $\rho_{ac} = \rho_0 \exp\left(\frac{T}{T_0}\right)^n$, where ρ_0 is the pre-exponent factor, 'n' is the exponential factor, and T_0 is the characteristic temperature coefficient. These parameters were extracted from the intercepts and slopes of the logarithmic plots shown in figure 3.11 [121,186].

The variation in the exponential factor 'n' in the above equation decides the nature of the hopping process and the validity of the variable-range hopping mechanism in which the value of 'n' should be approximately -0.25 [187,188]. In order to confirm this, we have plotted the double logarithm curves of (ρ/ρ_0) as a function of $ln(T)$ (shown in figure 3.13). Consequently, the magnitude of the slope obtained

from the above graphs was found to be ~ -0.25, affirming the validity of equation $\rho_{ac} = \rho_0 \exp\left(\frac{T}{T_0}\right)^n$ and thus providing substantial evidence to variable-range hopping of charge carriers for both the systems *x* = 0.10 and 0.95. Usually, the formation of localized charge carriers (generated by the defects such as oxygen vacancies and interstitial Ni^{3+} ions) plays a major role in the hopping conduction mechanism [121,156]. These localized charge carriers accumulates across the Fermi level and provides a finite number of electronic states near the Fermi level. The density of electronic states ($N(\xi_F)$) near the Fermi level depends upon the characteristic temperature T_0 (obtained from the slope of figure 3.11) which is given by the relation $N(\xi_F) = 16\alpha^3/k_B T_0$. In this relation, the decay length α^{-1} signifies the spatial extension of the wave function $e^{-\alpha R}$. Moreover, using the magnitude of $N(\xi_F)$, we have calculated the average hopping length r_h and hopping energy ϵ_h using the expressions [121,158].

$$r_h = \left[\frac{3}{(2\pi\alpha N(\Sigma_F)k_B T)}\right]^{1/4} \quad (3.21)$$

$$\epsilon_h = \frac{3}{4\pi\alpha N(\Sigma_F)\mathcal{R}_H^3} \quad (3.22)$$

All the calculated values of $N(\xi_F)$, r_h, and ϵ_h are listed in Table 3.2. For *x* = 0.10, the average hopping length (r_h) decreases from 1.78nm to 1.68nm as the frequency increases from 1.5kHz to 1MHz. On the other hand, the addition of NiO significantly increases the average hopping length from 1.78 nm to 3.00nm for *x* = 0.10 and 0.95, respectively.

3.4. Summary:

To summarize this chapter, incorporation of NiO inside the $NaNbO_3$ matrix (*x* ≥ 0.05) leads to a significant lattice distortion from an orthorhombic (*Pmna*) to a monoclinic (*Pbma*) crystal structure at room temperature, which is associated with the off-centre displacement of cations. The electronic structure and elemental analyses of these composites were studied by means of XPS, which provides evidence of pentavalent and monovalent nature of 'Nb' [$3d_{5/2}$ (206.1eV) and $3d_{3/2}$ (208.7eV)] and 'Na' [1s (1070.2eV)], respectively. However, the Ni-2p XPS spectra exhibits a doublet with binding energy separation 17.82eV, signifying the presence of a divalent state of Ni together with the satellite peaks centered at 853.96eV and 879.05eV. The temperature dependence of relative-dielectric permittivity $\varepsilon_r(T)$ exhibits two cusps across 520℃ (T_{AFE}) and 398℃ (T_{O-M}) for lower compositions of NiO (*x* ≤ 0.10). The first transition, T_{AFE}, is associated with the antiferroelectric to paraelectric transition, and the second one, T_{O-M}, is associated with the orthorhombic to monoclinic crystal structure transition. Along with these two major transitions, we noticed a feeble but lucid anomaly across 170℃ in low-frequency ε_r curves which accompanies the second-order transition. Such an anomalous change in ε_r (T < 200℃) is in-line with the previously reported ε_r versus T data of undoped $NaNbO_3$ and $NaNbO_3$+$KNbO_3$ mixture [131]. For higher compositions of NiO (*x* ≥ 0.95), all the above two transitions are merged into a single giant hump with ε_r as high as 10^7.

Our results demonstrate that frequency dependent ac-conductivity $\sigma_{ac}(f)$ follows the JPL [$\sigma_{ac} = \sigma_0 + A\omega^s$], and the frequency independent term (σ_0) behaviour was explained by using Funke's Jump-Relaxation Model. For high frequencies ($f \geq 7$kHz), a dispersive nature of σ_{ac} was observed mainly due to the competition between two different relaxation processes related to successful and unsuccessful hopping of charge carriers. Moreover, the temperature dependence of the frequency exponent 's' obtained from the JPL analysis provides two different phonon-assisted charge transport mechanisms applicable for the current systems: (*i*) the formation of Small Polarons in the range 40°C ≤ T ≤ 60°C due to incomplete d-shells of Nb^{4+} and (*ii*) the formation of Large Polarons due to the interaction of residual charge carriers with the positive ions (charge–lattice interaction) at high temperatures. Conversely, for $x \leq 0.95$, we observed the double power law behaviour between 100°C and 540°C ($1.04 \leq s \leq 1.61$) and the dominance of universal dielectric response between 50°C and 100°C ($0.81 \leq s \leq 1.04$). From the logarithmic variation of ρ_{ac} versus $T^{-1/4}$ and $ln[ln(\rho/\rho_0)]$ versus $ln[T]$ plots, we demonstrated Mott's variable range hopping of Polarons between the localized states.

Chapter 4
Vibrational Excitations and Thermal Hysteresis in $NaNbO_3$-NiO

This chapter deals with the vibrational excitations and thermal hysteresis in $\varepsilon_r(T)$ of $NaNbO_3$-NiO composites. This chapter provides a systematic comparative analysis of the phase transitions probed for one dilute composition (x = 0.05) by the dielectric spectroscopy with the differential scanning calorimetry technique which is the extension of the previous chapter. At the end of this chapter we discuss the magnetic properties of these composites using VSM and ESR measurement techniques.

4.1 Introduction:

It is well known that at room temperature, $NaNbO_3$ generally exhibits an orthorhombic crystal structure with space group *Pbma*. However, as the temperature increases the crystal structure changes to tetragonal (space group *P*4/*mbm*) at 575°C and further changes to a higher-symmetry cubic phase (space group *Pm*3*m*) above 640°C [105,189-194]. The first transition occurs at T ~ 360°C from the orthorhombic P-phase to the R-phase, followed by the orthorhombic R-phase to the S-phase at 480°C [189,194]. The collapse of antiferroelectric domains to a disordered paraelectric state occurs at the same temperature (T_C ~ 480°C). Yet, in the paraelectric state, the crystal structure changes from orthorhombic-S to T_1 at 520°C and orthorhombic T_1 to tetragonal T_2 at 575°C [189,105]. Furthermore, $NaNbO_3$ undergoes a transition from an orthorhombic to a rhombohedral crystal structure at 193K (T > 163K) with space group *R*-3*c* [189,194,177] and lattice parameters $a = b = c$ = 7.8147Å [195]. The room temperature monoclinic phase (with lattice parameters a = 3.9092Å, b = 3.8713Å and c = 3.9092Å) has been previously reported in the literature [177,196,173]. These transitions are slightly different from the single crystal work to polycrystalline samples [177]. Here the transition from the monoclinic P-phase to the orthorhombic R-phase occurs at T~ 370°C without changing its antiferroelectric ordering. Neutron diffraction studies carried out on $NaNbO_3$ reveal that above 370°C the orthorhombic (with space group *Cmcm*) [177,197] crystal structure of $NaNbO_3$ accommodates an antiferroelectric-ordered domain structure with a crossover of two distinct multiplicities of the pseudocubic phase (R, S and T_1) [173]. It is interesting to note that all these transitions have their signatures in the other physical properties including broadband dielectric, heat capacity and vibrational spectroscopy [105,115,198–201]. Earlier studies by Pardo *et al.* [202] reported large thermal hysteresis (~ 100°C) in $\varepsilon_r(T)$ for $NaNbO_3$ + $LiNbO_3$ ceramics between 250°C and 350°C due to the first-order nature of the ferroelectric to paraelectric transition. Similar type of results has been reported for a Gadolinium (Gd) substituted $NaNbO_3$ system and $Ag_{0.4}Na_{0.6}NbO_3$ ceramics [115,200]. Recently Gao *et al.* demonstrated that the antiferroelectric P-phase can be stabilized in $CaHfO_3$ + $NaNbO_3$ perovskites which can exhibit large thermal hysteresis of ΔT_{hys} ~ 200°C (for x = 0.03 in $Na_{(1-x)}Ca_xNb_{(1-x)}Hf_xO_3$). These authors also observed dynamic switching of the active ferroelectric phase into the antiferroelectric phase at room temperature [203].

These studies motivated us to investigate the thermal hysteresis behaviour in $\varepsilon_r(T)$ of an NiO-$NaNbO_3$ system which is missing in the literature. Thus, in the present work, we focus on the high-temperature (30℃ ≤ T ≤ 550℃) frequency dependent dielectric properties (only dilute composition x = 0.05) and low-temperature (80K ≤ T ≤ 300K) vibrational excitations in this system. Our main aim is to probe the changes occurring in the Raman spectra and thermal hysteresis in $\varepsilon_r(T)$ and the ac-resistivity $\rho_{ac}(T)$ as we incorporate NiO (which has T_N~ 250℃) in the $NaNbO_3$ lattice [204]. Giant atomic displacement due to (*i*) off-centring of Nb-ions in its octahedron, (*ii*) tilting of NbO_6 octahedra and (*iii*) rhombohedral distortion in NiO may collectively result in ferroelastic properties. Such atomic displacement may lead to the formation of a finite dipole moment, which in turn contributes to the overall polarization of the system [189]. Bouziane *et al.* investigated low-frequency Raman scattering in $NaNbO_3$ and reported the existence of dynamic polarized clusters in the antiferroelectric state [198]. These authors also pointed out that the phase transition from the P-phase to the R-phase (T ~ 370℃) in $NaNbO_3$ crystals may be due to dipole relaxation around the off-centre Nb-ions, resulting in an order–disorder character of the antiferroelectric phase [198].

Soni *et al.* recently reported a new anomaly across 320℃ in $\varepsilon_r(T)$ along with the two known transitions at 445℃ and 220℃ in the ferroelectric $KNbO_3$ and antiferromagnetic NiO composites [158]. These authors also studied the role of NiO in the vibrational spectra of $KNbO_3$ and reported the emergence of Two-Magnon mode at 1500cm^{-1} [158]. Moreover, a very recent study reported structural distortion from orthorhombic to monoclinic phase at room temperature in $NaNbO_3$ + NiO two-phase composites [199]. Also, the incorporation of NiO inside the $KNbO_3$ and $NaNbO_3$ compounds leads to some major changes in their global dielectric behaviour and ac-conductivity [158,199]. Although there have been numerous studies of $NaNbO_3$ and its composites, detailed Raman spectroscopy down to a temperature of 80K in NiO-substituted $NaNbO_3$ is still lacking in the literature; thus, we fulfilled this gap in the literature. Our experimental results reveal large thermal hysteresis in dielectric and ac-resistivity data in the range 200–400℃ and the emergence of several new phonon and Magnon modes in the low-temperature Raman spectra of $NaNbO_3$ + NiO composites.

4.2 Experimental Details:

We have used the same synthesis procedure as discussed in earlier chapter. For room temperature Raman spectroscopy, we used a HORIBA Jobin Yvon Raman spectrometer (model LabRam HR) with a laser source of wavelength 514nm. Temperature dependent vibrational Raman spectroscopy was performed in the backscattering geometry using a He–Ne laser of wavelength 432nm coupled with a Labram-HR800 micro Raman spectrometer equipped with a 50× objective. An appropriate notch filter and a Peltier cooled charge coupled device detector was used in the above equipment. The laser power was kept at 25mW for excitation. No melting or phase transformation was found in the sample due to this power. For the low-temperature measurements, the sample was mounted on a THMS600 stage from Linkam UK and a grating with 1800gr-

mm^{-1} was used in a high-resolution dispersive geometry. The samples were first mounted in the cold stage setup, equipped with a temperature controller capable of maintaining a steady temperature of 80K. Samples were no more than 1mm thick so as to reduce the temperature gradient. Cooling was provided by passing dry nitrogen gas from a thermally sealed container containing liquid nitrogen. By regulating this gas flow the temperature controller was able to hold the temperature fluctuations within a range of ±1°C. In order to achieve very high positional accuracy, the grating was kept stationary during the entire temperature scan. A spectral window of ~1800cm^{-1} was employed with a positional accuracy of 0.08cm^{-1} (Si peak 520.623cm^{-1}). Thermal analysis of the sintered products was carried out using a high temperature differential scanning calorimetry (DSC)/thermogravimetric (TG) system (Netzsch, model STA449F3A00). Thermal stability of the sintered product was studied from room temperature to 1100°C with a heating rate of 10°C-min^{-1} under a constant Argon gas ambient (flow rate 60ml-min^{-1}). The observed accurate shift in Raman modes and Raman linewidths were obtained from the best fit to a Lorentzian line shape and pseudo-Voigt approximation after baseline correction. Magnetic hysteresis measurements were performed using a Lakeshore vibrating sample magnetometer (VSM; model 7410). This instrument was first calibrated using standard nickel sample (6.20emu at 5000Oe magnetic field) at room temperature. These measurements were carried out at room temperature, for a field window of −15kOe to +15kOe. The electron spin resonance (ESR) spectra were recorded at room temperature using a JEOL JES-FA200 spectrometer operating at the X-band frequency of 9.45GHz.

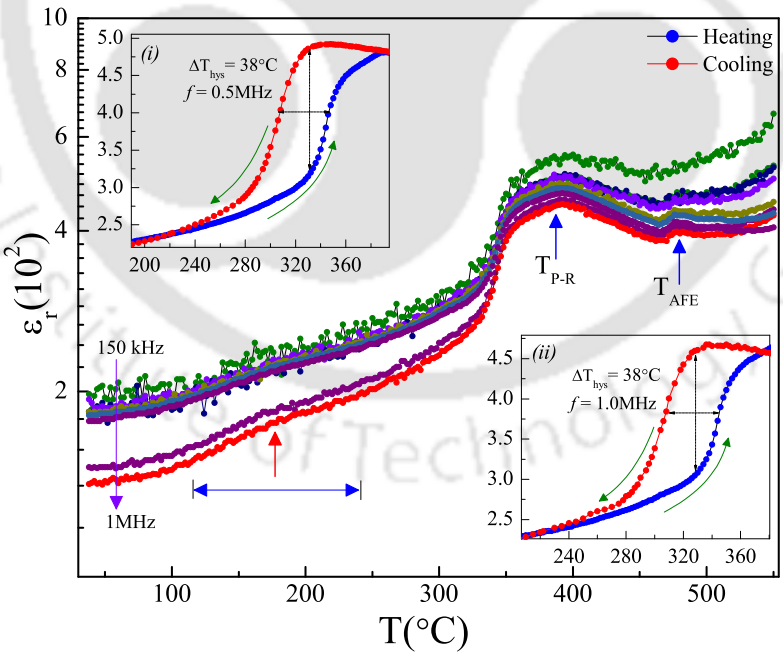

Figure 4.1. Temperature dependence of dielectric permittivity $\varepsilon_r(T)$ measured at various frequencies (150kHz ≤ f ≤ 1MHz) for temperatures from 30°C to 550°C with a temperature interval ΔT = 2°C for the sample NNO5. Insets (*i*) and (*ii*) show the thermal hysteresis (ΔT_{hys}) in $\varepsilon_r(T)$ for f = 0.5MHz and f = 1.0MHz, respectively. The red arrow points to the feeble anomaly at T ~ 180°C, T_{P-R} denotes the phase transition from orthorhombic P- to R-phase and T_{AFE} denotes the antiferroelectric to paraelectric transition.

4.3 Evidence for Thermal Hysteresis:

Figure 4.1 shows the variation of dielectric permittivity, ε_r, as a function of temperature measured for various frequencies (f) between 150kHz and 1MHz for 5wt% NiO containing $NaNbO_3$ (this composition will be referred to as NNO5 hereafter). The measurements start at 40°C and the data were recorded with a 2°C interval for heating and cooling cycles. The magnitude of ε_r increases progressively with increasing temperature and takes a cusp shape between 370°C and 480°C, with a maximum value of ε_r (554 at f = 150kHz) occurring at 392°C (shown by the vertical blue arrow). Such a change in ε_r is linked with the phase transition from orthorhombic P-phase to R-phase (T_{P-R}) without altering its antiferroelectric properties. For undoped $NaNbO_3$ this transition occurs at 370°C [105,189,200]. For f > 10^5Hz, a small but distinct hump (vertical blue arrow) at 478°C is visible in $\varepsilon_r(T)$, which is close to the standard antiferroelectric to paraelectric transition (T_{AFE} ~ 480°C) of $NaNbO_3$ which is accompanied by the orthorhombic-R to S phase transition [105,189,200]. Such a hump is also associated with the softening of phonon modes related to the tilt of NbO_6 octahedra due to the thermally driven off-centred Nb-ions [205]. It is interesting to note that between the temperatures 120°C and 220°C, a broad anomaly was noticeable in ε_r at 176°C (shown by the red arrow mark). This type of anomaly was previously reported at 150°C for undoped $NaNbO_3$ and shifts towards higher temperatures (~180°C) when Li or K is substituted at Na sites of the perovskite lattice [156]. On the basis of detailed temperature dependent structural, optical and dielectric studies, Raevskii *et al.* concluded that such an additional phase transition can be close to a second-order transition taking place between two orthorhombic antiferroelectric rhombohedral phases (between 150°C and 180°C) [156,206,207]. The solid-state phase transitions occurring in the investigated system have definite signatures in their differential scanning calorimetry (DSC) data.

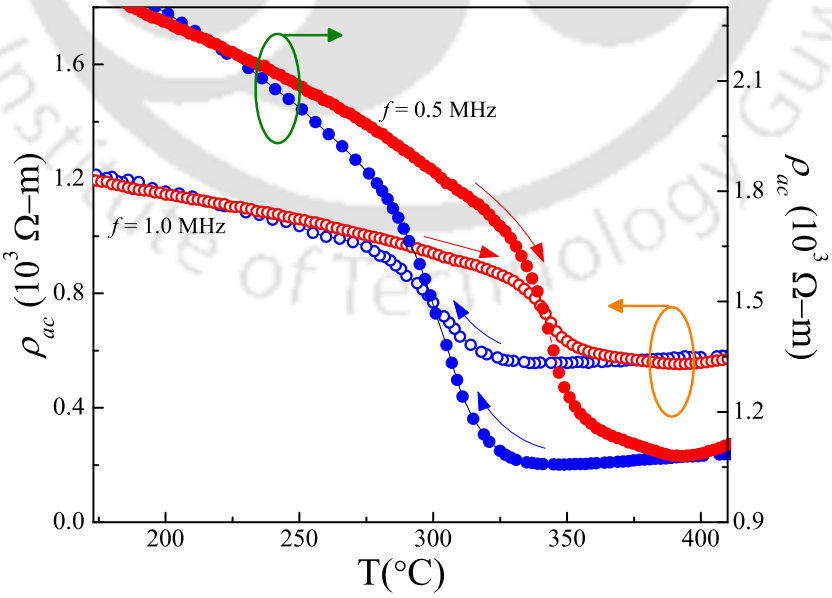

Figure 4.2. Hysteresis behaviour of ac resistivity (ρ_{ac}) for NNO5 ceramics obtained at two different frequencies, f = 0.5MHz and 1.0MHz. Red squares represent data recorded for the heating cycle and the blue circles represent the cooling cycle.

Figure 4.3 shows the temperature dependence of heat flow in mW-mg^{-1} for x = 0.05. This temperature dependence of DSC data collected under a heating cycle in the presence of an Argon gas ambient shows two weak anomalies: the first is in the temperature range 497℃–546℃ and is associated with T_{AFE} and the second anomalous change in heat flow takes place between 321℃ and 395℃, which is close to the structural phase transition T_{P-R} (370℃) observed in the dielectric data. Moreover, a giant cusp was evident in the DSC data at 156℃ which is linked to the second-order incommensurate phase transition T_{p1} noticed in $\varepsilon_r(T)$ [206–208]. These studies reveal that any change in the $\varepsilon_r(T)$ is accompanied by a definite change in the thermodynamic order parameter of the investigated system. A weak broad exothermic hump just above may arise due to sodium volatilization in $NaNbO_3$ [209–213].

The insets of figure 4.1 show ε_r versus T measured under cooling and heating cycles for (*i*) f = 0.5MHz and (*ii*) 1.0MHz. From these plots, one can clearly notice a large thermal hysteresis (ΔT_{hys} ~ 38℃) in permittivity which is consistent with the stoichiometric $NaNbO_3$. In the case of single crystal $NaNbO_3$, Molak reported much smaller ΔT_{hys} values (≤ 10℃) which increase substantially (33℃) with increase in the defect concentration n_{vo} (at low pressure ~2×10^{-2}Pa), leading to a non-stoichiometric sample $NaNbO_{3-\delta}$ with much lower phase transition temperature ($T \sim$ 341℃) [208]. A detailed pressure dependent study of Mn-substituted $NaNbO_3$ by Molak [214] revealed that reduction in the Nb valency due to the presence of oxygen vacancies (or induced by Mn-substitution) leads to the development of a local electric field (E_{loc}) due to charge accumulation in the vicinity of defects (as discussed in section 1.5 related to the local electric field). As a consequence, local fluctuations in the order parameter may be expected in the system which may lead to giant atomic displacement (Nb-ions), thus resulting in larger ΔT_{hys} values [214]. In the present case, thermal hysteresis is also evident in the temperature dependence of ac resistivity as shown in figure 4.2.

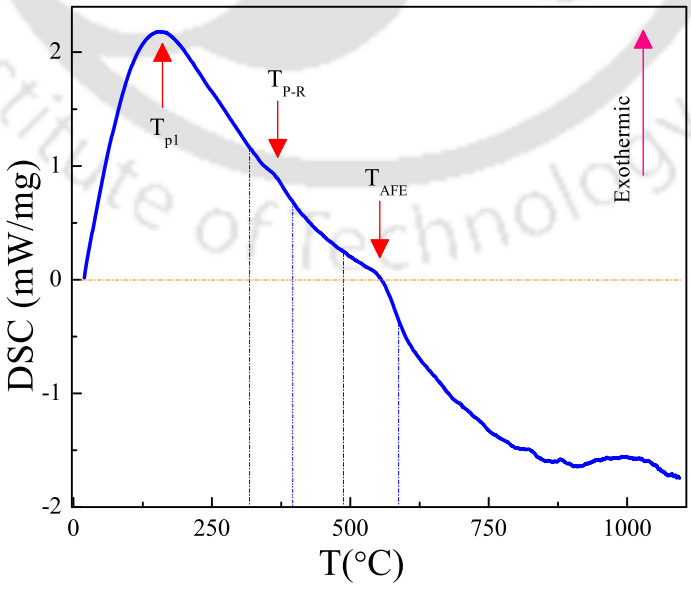

Figure 4.3. The DSC curve for NNO5 recorded during the heating cycle. The arrows indicate possible anomalies associated with the solid-state phase transitions. The vertical lines represent the temperature window.

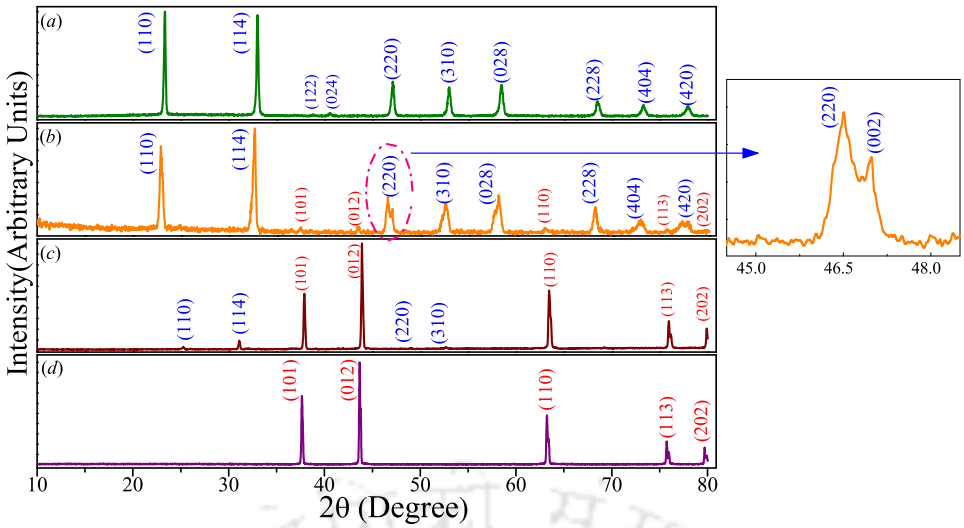

Figure 4.4. X-Ray diffraction pattern of (1-*x*) $NaNbO_3$ + *x* NiO for (*a*) *x* = 0.0, (*b*) *x* = 0.05, (*c*) *x* = 0.90 and (*d*) *x* = 1.0, sintered at 1040°C for 4h in air. Blue colour indexing corresponds to the Miller Indices of $NaNbO_3$ and red colour indexing corresponds to that of NiO. Inset shows zoomed view of (220) peak splitting into a doublet (220) and (002) at 2θ~ 46.5°.

Previous studies by Kania and Kwapulinski reported much larger ΔT_{hys} values (~ 90°C) across the M_3–O_1 transition in Ag containing $NaNbO_3$ ($Na_{0.6}Ag_{0.4}NbO_3$) due to the internal and external stresses occurring across the martensitic type (P–R) phase transition in $NaNbO_3$ [200]. In the present case, incorporation of antiferromagnetic NiO inside the $NaNbO_3$ matrix may lead to compositional inhomogeneity in the perovskite lattice due to mismatched ionic radii ($r_{Ni^{2+}}$ = 0.69Å and $r_{Nb^{5+}}$ = 0.64Å) and increased imperfections, thus causing significant internal stresses. Such effects collectively altered crystallographic and ferroelectric transition temperatures including a large ΔT_{hys} as compared with undoped $NaNbO_3$. Recent studies by Gao *et al.* reported ΔT_{hys} = 62°C (for undoped $NaNbO_3$) and 105°C in the solid solution $Ca_{0.04}Hf_{0.04}O_3$–$Na_{0.96}Nb_{0.96}O_3$ [203]. On the other hand, no signatures of magneto-dielectric coupling were observed in the present system because NiO is a type-II antiferromagnet, which shows an ordering temperature T_N ~ 250°C [215–217].

Our preliminary X-ray diffraction studies on the dilutely doped systems reveal that all the diffraction patterns corresponded to the orthorhombic crystal structure (space group *Pbcm*(57)). However, a slight increase in the lattice parameters was observed as the secondary phase pertaining to the rhombohedrally distorted NiO emerged out as the dominant phase in the $NaNbO_3$ matrix with increasing *x*. The NiO phase was refined using space group *R*-3*m* [199]. The changes occurring in the lattice parameters may be due to differences in the ionic radii of Ni^{2+} (0.69Å) which is likely to occupy the Nb-sites (0.64Å) in the NbO_6 octahedra. Moreover, at the Bragg angle 2θ~ 46.51° we observed splitting of the (220) X-ray reflection into a doublet corresponding to the Miller indices (220) and (002) in the NNO5 system due to the orthorhombic to low-symmetry monoclinic structural distortion (as shown in figure 4.4) [199].

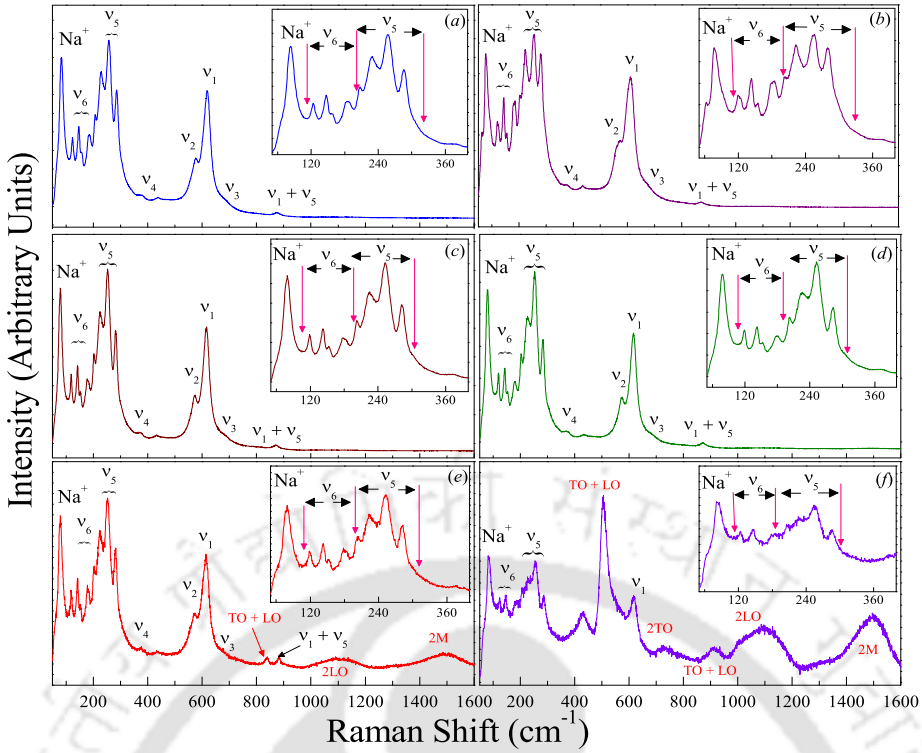

Figure 4.5. Room temperature Raman spectra of (*a*) x = 0.05, (*b*) x = 0.10, (*c*) x = 0.30, (*d*) x = 0.50, (*e*) x = 0.70 and (*f*) x = 0.95 for (1−x) $NaNbO_3$ + x NiO recorded by a laser source of wavelength λ = 514nm between 50cm^{-1} and 1600cm^{-1}. Insets show the enlarged view of the spectrum between 50cm^{-1} and 400cm^{-1}.

4.4 Temperature Dependent Raman Spectra:

In this section, we discuss the low-temperature Raman spectra of the investigated system in detail and the role of NiO on the lattice dynamics of $NaNbO_3$. Figures 4.5(*a–f*) show the vibrational Raman spectra for various compositions (x) of $NaNbO_3$ + NiO composites [(1−x) $NaNbO_3$ + x NiO] recorded at room temperature between 50cm^{-1} and 1600cm^{-1} using a laser source of wavelength λ = 514nm. The insets of this figure show the spectra at lower wavenumbers (between 50 and 400cm^{-1}). For all the compositions, we noticed a sharp peak at 83cm^{-1} (p_1) corresponding to the translational modes of Na^+. However, this peak (between 50 and 110cm^{-1}) can be deconvoluted into three Gaussian peaks with centres 66.0cm^{-1}, 82.2cm^{-1} and 91.3 cm^{-1} which are consistent with previously reported data (61, 75 and 93cm^{-1} as shown in figure 4.6) by Lima *et al.* and Shen *et al.* [201,218]. However, the centres of these peaks shift towards higher wavenumbers as the NiO composition increases to x = 0.95. For x = 0.10, p_1 splits into two distinct peaks, one centred at 61.43cm^{-1} and other at 77.43cm^{-1} and the latter peak at 77.43cm^{-1} can be deconvoluted into two Lorentzian peaks at 77.4cm^{-1} and 86.7cm^{-1}. The bands designated by ν_6 (109cm^{-1}–200cm^{-1}) and ν_5 (200cm^{-1}– 310cm^{-1}) are associated with the rotational and liberational (rotational vibrations) modes of NbO_6 [218,219].

Except for the decrease in the intensity of both these bands, no significant shift was noticed. These two bands together with additional modes ν_4 (379cm^{-1} and 437cm^{-1}) have a significant intensity for all the compositions $x \leq$ 0.95, which originate due to vibrations of the NbO_6 group [218]. The crystal field

Assignment	Ref [221] (300K) cm^{-1}	Ref [201] (295K) cm^{-1}	Current Work (297K in cm^{-1})					
			x = 0.05	*x* = 0.10	*x* = 0.30	*x* = 0.50	*x* = 0.70	*x* = 0.95
Na^+	62.4	60.2	66.02	61.53	62.69	62.82	60.36	63.29
Na^+	75.4	73.0	82.26	77.43	78.50	78.17	78.14	82.61
	92.3	89.5	91.34	86.66	92.26	90.17	93.74	105.85
NbO_6 lib.	119.4	115.1	119.58	119.58	118.76	118.91	119.06	-
	124.0	121.0	124.67	124.67	-	-	-	123.12
	144.2	142.1	142.99	142.99	142.15	142.02	142.19	145.42
	155.7	157.0	155.24	155.24	153.47	153.34	153.11	-
$\nu_6(F_{2\nu})$	186.1	183.2	184.76	182.01	179.23	178.60	179.71	182.42
	203.4	201.0	206.62	202.80	202.30	202.19	202.48	205.74
	230.7	230.4	228.65	222.88	224.92	225.25	224.02	227.81
$\nu_5(F_{2g})$	258.4	255.1	257.77	254.41	253.34	253.01	253.01	256.30
	279.4	276.1	286.61	280.57	283.99	283.19	282.22	287.02
	294.1	295.9	304.19	293.45	300.14	303.75	304.53	323.16
$\nu_4(F_{1u})$	380.5	378.5	379.90	377.85	372.21	370.67	377.85	-
	436.0	435.3	437.88	434.29	432.75	432.75	437.88	-
$\nu_2(E_g)$	559.8	557.2	574.79	564.20	571.36	571.59	569.75	-
$\nu_1(A_{1g})$	604.0	602.6	618.18	609.84	615.58	615.61	613.68	-
$\nu_3(F_{1u})$	672.6	671.5	692.01	683.74	679.69	679.65	689.56	-
	-	-	-	-	-	-	838.08*	-
$\nu_1 + \nu_5$	872.0	867.3	876.56	871.95	871.43	872.97	883.23	-

Table 4.1. Wavenumbers of Raman bands and their assignments at room temperature for various compositions (*x*) of (1- *x*) $NaNbO_3$ + *x* NiO. The asterisk (*) represent the new mode for *x* = 0.70.

environment plays a major role in the symmetry and orientation of the NbO_6 group and its vibrational bands, which lead to four additional modes at ν_2 = 574cm^{-1}, ν_1= 616cm^{-1}, ν_3 = 676cm^{-1} and $\nu_1 + \nu_5$ = 871cm^{-1}. All the modes depicted above 500cm^{-1} are mostly due to the motion of oxygen ions in NbO_6 [198]. Such modes are severely affected by the incorporation of NiO inside the $NaNbO_3$ matrix, except for a new mode centred at 838cm^{-1} (shown by the red arrow in figure 4.5(*e*)) due to the coupling of longitudinal and translational optical modes (LO + TO) of NiO [220]. At high wave numbers (> 700cm^{-1}), NiO modes dominate over the niobate modes for higher values of *x*. In particular, a broad Two-Magnon mode (1496cm^{-1}) associated with the antiferromagnetic ordering of NiO dominates between 1343cm^{-1} and 1598cm^{-1} (figure 4.7). In addition,

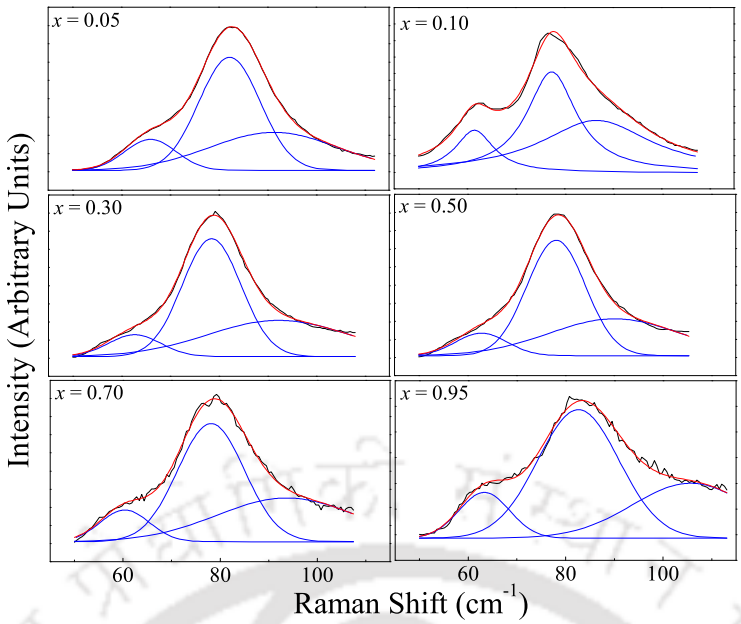

Figure 4.6. Gaussian curve fitting of the Raman peaks in the low wavenumber range (50-120cm^{-1}) corresponding to the translational mode of Na^+, for various compositions (*x*) of NiO in (1-*x*) $NaNbO_3$ + *x* NiO.

moderately intense broad LO modes (2LO) at 1096cm^{-1} and a weak translational optical mode (2TO) at 726cm^{-1} are the noteworthy features observed for higher wavenumbers and compositions which are associated with the vibrational spectra of NiO. Table 4.1 summarizes all the Raman modes below 1000cm^{-1} observed in this work together with previously reported data.

It is well known that the low-temperature rhombohedral phase (space group *R-3c*) of $NaNbO_3$ has six formula-units per unit-cell which results in 90 fundamental vibrational degrees of freedom, out of which three are acoustic modes and the rest are optical modes [194,219]. From the factor group analysis, the optical modes (T_{opt}) are quantified as: $20A_1 + 9A_2 + 29E$, out of these A_1 and E modes are both Raman

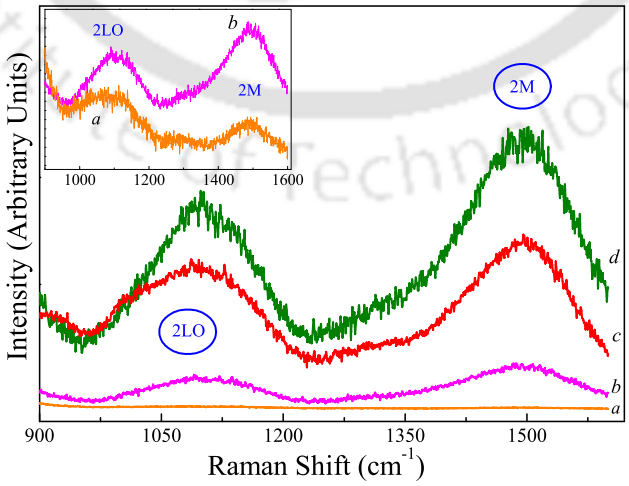

Figure 4.7. Room temperature Raman spectra showing the Two-Magnon mode and longitudinal–optical (LO) phonon mode associated with antiferromagnetic NiO dispersed in NNO for the following compositions: (*a*) *x* = 0.50, (*b*) *x* = 0.70, (*c*) *x* = 0.90, (*d*) *x* = 0.95.

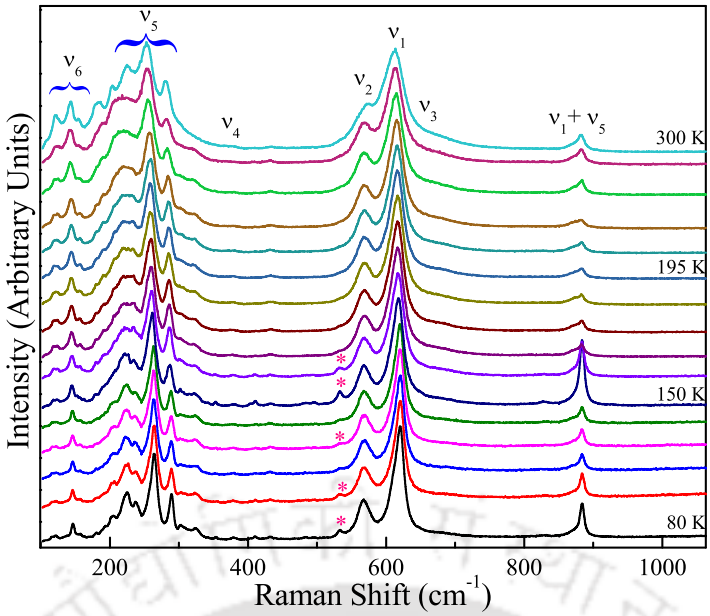

Figure 4.8. Raman spectra of NNO5 recorded at various temperatures between 80K and 300K during the cooling cycle in the range 100–1100cm^{-1}. Various modes associated with the rotation, vibration and liberation of NbO_6 octahedra are labelled as ν_n (n = 1, 2, 3, 4, 5, 6).

and infrared active whereas the A_2 mode is inactive both in Raman and infrared. In this situation, total of 49 Raman active phonon modes are expected. Similarly, at ambient temperature, the orthorhombic phase (space group *Pbcm*) has eight formula-units per unit-cell [194,219]. From the group theory analysis, the irreducible representation of the vibrational modes of orthorhombic phase at room temperature is $T_{opt} = 15A_g + 17B_{1g} + 15B_{2g} + 13B_{3g} + 13A_u + 14B_{1u} + 16B_{2u} + 14B_{3u}$, where A_g , B_{1g}, B_{2g} and B_{3g} modes

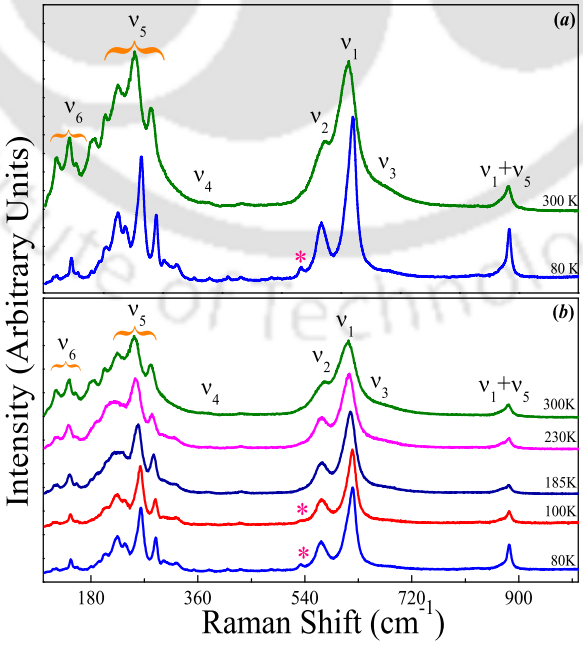

Figure 4.9. Raman spectra of NNO5 recorded at (*a*) 300K and at 80K and (*b*) at selected temperatures between 80K and 300K. The new mode at $\nu_p \sim 533$cm^{-1} is labelled by an asterisk.

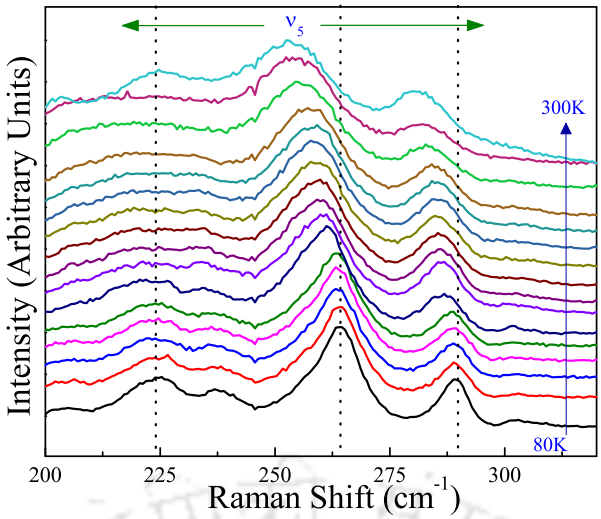

Figure 4.10. Raman spectra of NNO5 showing the liberational mode (ν_5) of NbO_6 octahedra, measured at different temperatures between 80K and 300K in the wavenumber range 200–320cm^{-1}.

are Raman active, whereas the mode A_u is inactive both in Raman and IR modes B_{1u}, B_{2u} and B_{3u} are only infrared active. Thus, altogether sixty Raman active optical phonons are anticipated in $NaNbO_3$ [173,219,220]. In addition, we expect phonon modes from NiO since the system under investigating is a two-phase composite comprising of both alkaline niobate as well as an antiferromagnetic Mott insulator. Figure 4.8 and 4.9 show the Raman spectra recorded at various temperatures between 80K and 300K for the bulk sample with NiO composition x = 0.05 in $NaNbO_3$ under back scattering configuration in the frequency range 100-1200cm^{-1} (with laser wavelength of 432nm as the source). From figure 4.9(*a*) and (*b*), it can be noticed that the spectra recorded for T = 80K exhibits very different feature from that of the spectra recorded at room temperature, signifying that $NaNbO_3$ exists in a different crystal structure at low temperatures.

On closer examination, we can see that overall linewidth or full width at half maximum (FWHM) has reduced for few modes and at the same time few new modes have emerged. On gradual cooling from room temperature to about 170K, the peaks associated with the NbO_6 liberations (ν_5) merge together as a result of transformation from orthorhombic to a low symmetric rhombohedral phase which is consistent with previous reports [219]. With decreasing temperature, few modes gradually diminished in intensities and dissolve into the background. It can be noted that on cooling, Raman bands become progressively sharper (figure 4.9(*b*)) due to the freezing of phonons at low temperatures. With decreasing temperature, most of the modes are found to shift towards a higher wavenumber as a result of contraction of bond length, resulting an increase in the force constant [221].

Figure 4.10 and 4.11 show the temperature variation of ν_5 (200cm^{-1} to 300cm^{-1}), ν_1, ν_2 and ν_3 (between 505cm^{-1} and 705cm^{-1}). It is noticeable that the modes shift to higher wavenumber with decreasing temperature. A new mode gradually emerges at $\nu_p \sim$ 533cm^{-1} (as shown in figure 4.11(*a*) indicated by an asterisk) for lower temperature and becomes more discernible at 150K and 80K. Most of the low

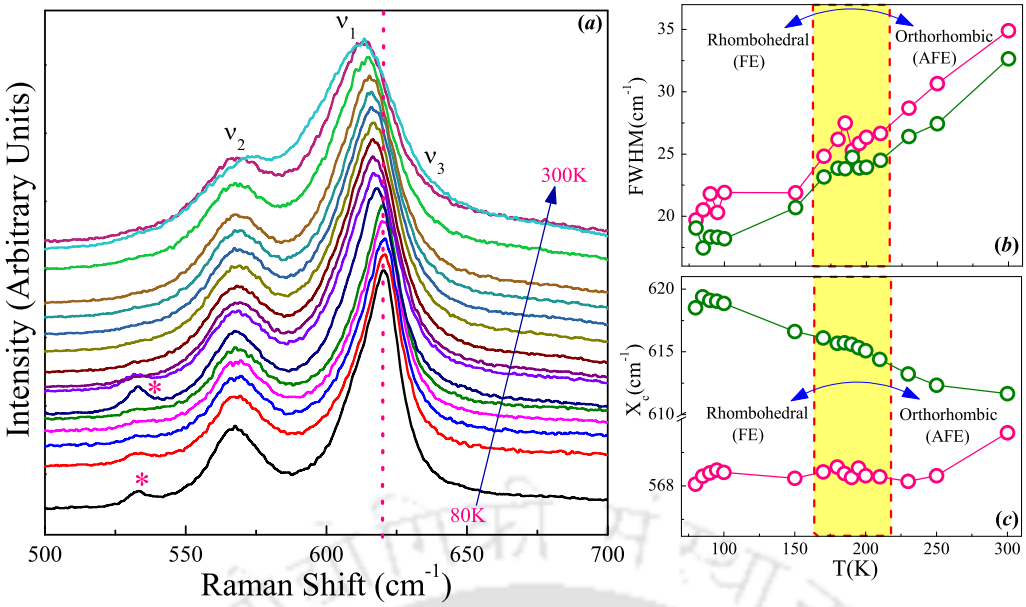

Figure 4.11. (*a*) Raman spectra of NNO5 recorded at different temperatures between 80K and 300K in the wavenumber range 500–700cm^{-1}. The new mode ν_p arising at 533cm^{-1} is marked by an asterisk. (*b*) Variation of the linewidth (FWHM) as a function of temperature for the modes ν_1 and ν_2. (*c*) Temperature dependence of peak position X_C for the ν_1 and ν_2 modes of NNO5. The green and pink symbols in (*b*) and (*c*) represent the ν_1 and ν_2 modes, respectively. The yellow shaded area represents the modulation region where a structural phase transition is anticipated in the NNO5 system.

wavenumber (between 100cm^{-1} and 250cm^{-1}) Raman modes arise due to the Na^+ and NbO_6 ions. On cooling from 300K to 150K, these modes (ν_5 and ν_6 at 120cm^{-1} and 154cm^{-1} respectively) merge and disappear into the background (figure 4.9(*a*)). This is mainly due to the fact that in the N-phase (ferroelectric) only one type of Na–O bond exists and the Na–O distance is reduced at low temperatures [201]. Figure 4.12 clearly shows the temperature dependence of ν_p, ν_1 and ν_2 peak positions analysed by fitting experimental data with the

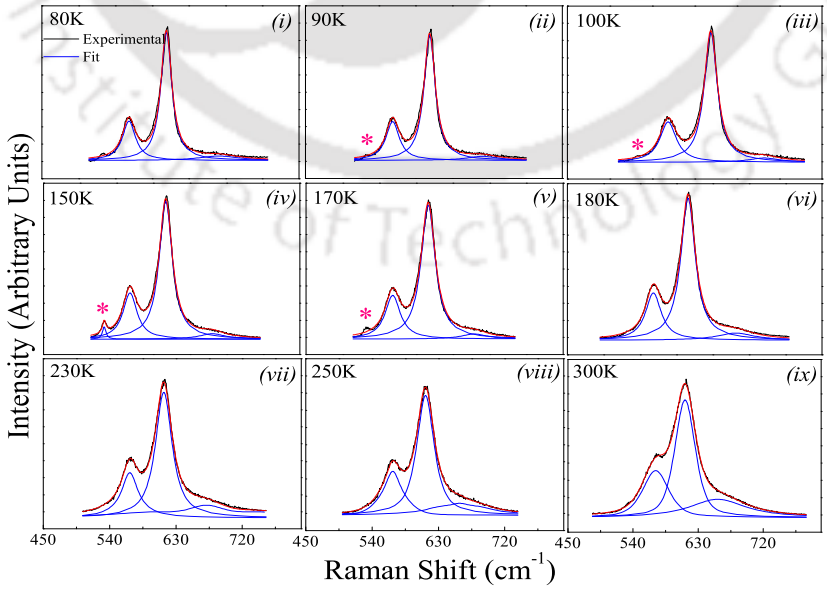

Figure 4.12. Lorentzian curve fitting of the Raman peaks of NNO5 at different temperatures in the wavenumber range 450-800cm^{-1} corresponding to the vibrational modes (ν_1, ν_2 and ν_3) of NbO_6 octahedra. The new mode ν_p is labelled by an asterisk (*).

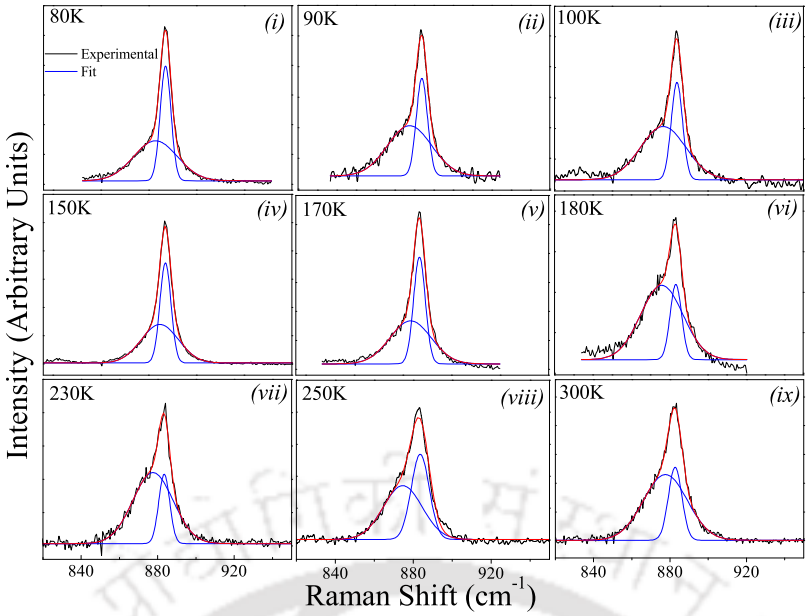

Figure 4.13. Lorentzian curve fitting of the Raman peaks of NNO5 at different temperatures in the wavenumber range 800-1000cm^{-1} corresponding to the vibrational mode ν_1 + ν_5 of NbO_6 octahedra, centred at 880cm^{-1} which is deconvoluted into two peaks.

Lorentzian fits (blue solid lines) in which ν_1 and ν_2 are deconvoluted into three peaks centred at 568cm^{-1}, 616cm^{-1} and 679cm^{-1}. On the other hand, figure 4.13 shows the ν_1 + ν_5 mode, which is deconvoluted into two clearly distinguishable Lorentzian peaks centred at 884cm^{-1} and 879cm^{-1}. It is also evident that the rotational degree of freedom of NbO_6 octahedra is drastically affected with temperature. As the measuring temperature decreases, low-wavenumber modes associated with NbO_6 gradually merges up to a critical temperature (193K) and start to reappear for T < 180K, suggesting that the transition from the antiferroelectric P-phase to the ferroelectric N-phase is a slow process which might be taking place in more

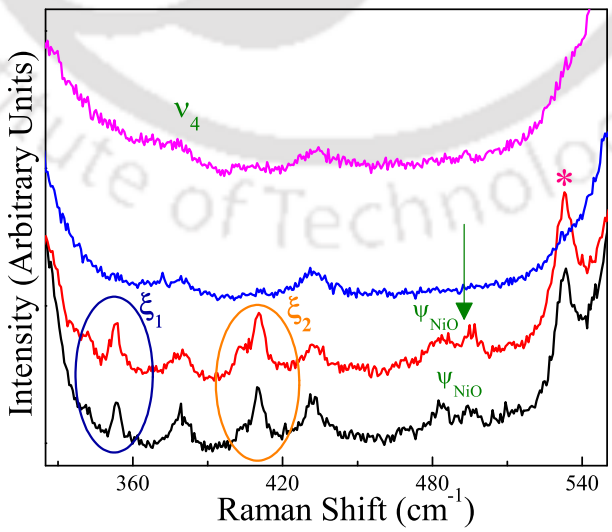

Figure 4.14. Raman spectra of NNO5 in the wavenumber range 320–550cm^{-1}, shown for selected temperatures (from bottom) T = 80K, 150K, 200K and 300K. Encircled are the new modes at 353cm^{-1} (ξ_1) and 410cm^{-1} (ξ_2). The green arrow represents the NiO phonon mode (1P).

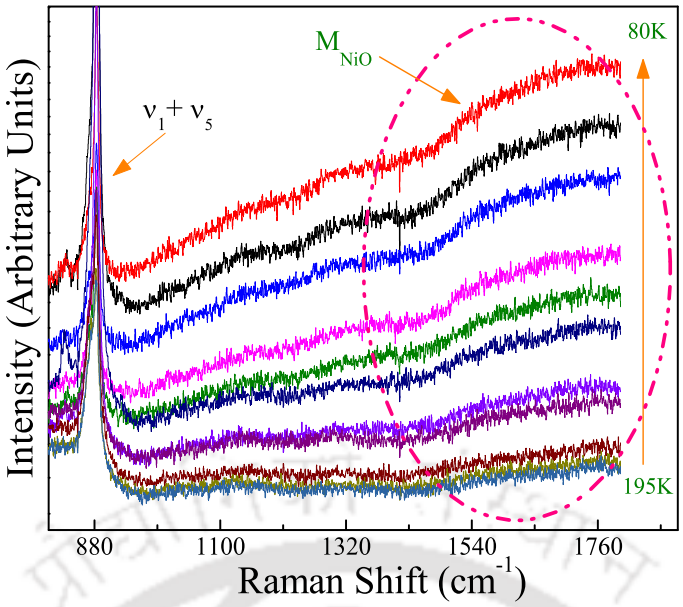

Figure 4.15. Raman spectra of NNO5 showing the NiO Two-Magnon mode (M_{NiO}) in the high wavenumber region (> 1200cm^{-1}) measured at different temperatures in the range 80K ≤ T ≤ 195K.

than one step. Figures 4.11(*b*) and (*c*) show the temperature variation of the linewidth (FWHM) and peak position (X_C) where one can clearly notice the modulated regions (shown by yellow rectangle) across the phase transition (antiferroelectric orthorhombic to rhombohedral ferroelectric). Initially as the temperature is lowered from 300K to 180K the bands associated with the liberations of NbO_6 octahedra in the orthorhombic state is slightly distorted. On further decreasing the temperature, the rhombohedral configuration becomes stable (T < 180K) and the NbO_6 octahedra realign from the distorted state.

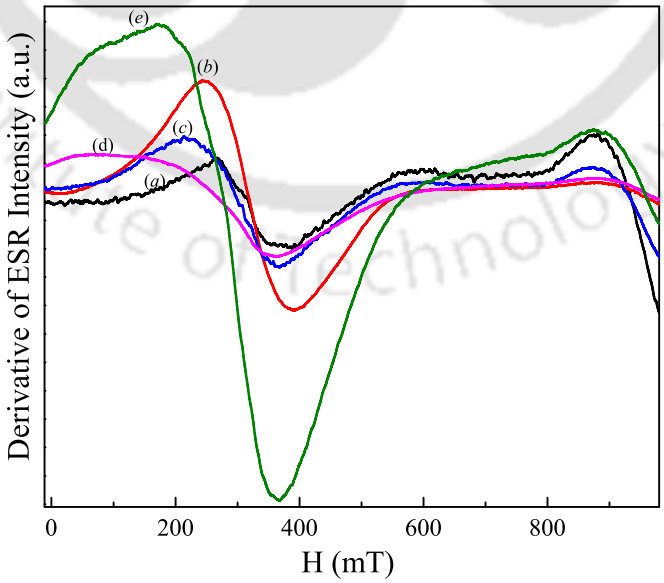

Figure 4.16. First derivative of electron spin resonance (ESR) spectra of (1-*x*) $NaNbO_3$ + *x* NiO recorded at room temperature for various compositions: (*a*) *x* = 0.0, (*b*) *x* = 0.05, (*c*) *x* = 0.10, (*d*) *x* = 0.50 and (*e*) *x* = 0.70.

Such tilting and re-tilting of the NbO_6 octahedra (believed to be first-order in nature) plays a significant role in the low wavenumber Raman spectra of $NaNbO_3$ [201]. Sharp and distinct Raman peaks emerge (ξ_1 and ξ_2) across 353cm^{-1} and 410cm^{-1}, along with ν_p (533cm^{-1}), which are associated with the changes occurring in the NbO_6 octahedra due to the incorporation of antiferromagnetic NiO. It is interesting to see the presence of NiO phonon modes ψ_{NiO} (figure 4.14) at 483cm^{-1} and 495cm^{-1} and the Two-Magnon mode (M_{NiO}) at 1543cm^{-1} (as indicated by the dotted circle in figure 4.15), although NiO exists in small quantities (x = 0.05) in the $NaNbO_3$ matrix [124,216,217,222–226]. From the above results, we conclude that antiferromagnetic properties of NiO play a significant role in the global vibrational spectra and dielectric behaviour of $NaNbO_3$. These results are consistent with the previous studies of Ulmane *et al.* who reported the Two-Magnon mode in nano-sized NiO at a wavenumber of 1500cm^{-1}; this becomes more intense and sharper with decreasing temperature down to 10K [220]. From the ESR spectra (figure 4.16), the resonance field H_r obtained from the zero-crossing of the ESR spectra exhibits a significant shift from the free electron position. Value of g-factor measured for x = 0 for the zero-crossing field comes out to be 2.17 which shows a deviation from the value of the g-factor of a free-electron. This indicates that all the samples have long-range magnetic ordering as a result of the NiO, due to which we observed the Magnon modes for all the compositions.

4.5 Summary:

To sum up, the temperature dependence of ac-resistivity and dielectric measurements performed at constant ac driving frequencies (0.5MHz and 1.0MHz) under heating and cooling cycles unveil a large thermal hysteresis ($\Delta T_{hys}\sim$ 38℃) in ε_r and ρ_{ac} between 200℃ and 400℃ signifying the first-order nature of the transition. We performed a detailed analysis of vibrational Raman spectra for various compositions of (1-x) $NaNbO_3$ + x NiO ($0.05 \leq x \leq 0.95$) which reveals the existence of a new mode centred at 838cm^{-1} for x = 0.70. For all the composites with $x \geq 0.50$ a broad Two-Magnon mode centred at 1496cm^{-1} was noticed which is associated with the antiferromagnetic ordering of NiO present in the niobate system. In addition to this feature, a broad longitudinal optical mode (2LO) at 1096cm^{-1} and a weak translational optical mode (2TO) at 726cm^{-1} are the main results obtained in this system.

A detailed low temperature (80K $\leq T \leq$ 300K) Raman measurements were performed for NNO5 sample which reveals peculiar features in the Raman modes of NbO_6 octahedra which are associated with the structural transition from orthorhombic P-phase to rhombohedral N-phase that usually occurs in un-doped $NaNbO_3$ and is linked with the ordering of domains from antiferroelectric state to a ferroelectric arrangement (~ 180 ± 10K). In addition to this, a new mode ν_p at 530cm^{-1} is evident between 150K and 80K. Two distinct Raman modes emerge at $\xi_1 \sim$ 350cm^{-1} and $\xi_1 \sim$ 410cm^{-1}, have also been observed along with ν_p ; these are associated with the vibrations of NbO_6 octahedra. Nevertheless, NiO phonon modes across 485cm^{-1} and 490cm^{-1} are clearly distinguishable even for low compositions of NiO in the $NaNbO_3$ matrix. But

Two-Magnon mode of antiferromagnetic NiO is visible only at low temperatures below 200K. Tuning of the Magnon mode across room temperature in these systems play a constructive role in designing the Magnon transistors.

Chapter 5
Dielectric and Raman Spectroscopic Studies of $NaNbO_3$-MnO_2

In this chapter, we present the structural, dielectric and Raman spectroscopy studies of manganese dioxide containing $NaNbO_3$ system. The first section focuses on basic introduction related to the improvement of the density and hygroscopic resistance of the $NaNbO_3$ system. The second section deals with the experimental details together with the synthesis method. Third section deals with the crystal structure, temperature-dependent dielectric and Raman spectra of $NaNbO_3$-MnO_2 system followed by brief summary of results.

5.1 Introduction:

As mentioned in the introduction chapter, the low mechanical strength and thermal sensitivity of alkaline niobates make them undesirable for rugged applications. Moreover, it is difficult to retain the dipole alignment of alkaline niobates during the fabrication process [227]. Many attempts have been made to improve the density and strength of niobate based ceramics. Among them, novel heat treatment methods like microwave sintering, sintering aids and additives are some of the important techniques [227–231]. Besides, Eshghi *et al.* achieved low dielectric loss and high density of 99% for $KNbO_3$ system prepared by sol-gel method [228]. These authors also observed a significant increase in the magnitude of dielectric permittivity (ε_r = 6200 at T_C), much higher than that of single crystal $KNbO_3$ (ε_r = 3900 at T_C) [228]. Matsubara *et al.* reported high densification of $K_{0.5}Na_{0.5}NbO_3$ (KNN) systems using $K_4CuNb_8O_{23}$ as a sintering aid [229]. This additive resulted in liquid phase sintering at 1020°C, leading to effective packing of grains [229]. Small amounts of additives such as $LaFeO_3$, $BiFeO_3$, and MnO_2 were also found to improve the densification and electrical properties, but some of these additives disturbed the poling process [227,230,231]. High densities have been attained also by optimizing sintering techniques, for instance, Kim *et al.* prepared $KNbO_3$ samples with 95% of the theoretical density by employing liquid-phase sintering technique [232]. However, dealing with improvement on the density of $NaNbO_3$ based systems by adding the binary manganese oxides as additives is minimal.

Ximing *et al.* reported the effects of MnO_2 doping on the structure, dielectric and piezoelectric properties of complicated lead-free ceramics based on $NaNbO_3$–$Ba_{0.6}(Bi_{0.5}K_{0.5})_{0.4}TiO_3$ [233]. Similarly, Mgbemere *et al.* reported that different amounts of MnO_2 doping in $(K_{0.44}Na_{0.52}Li_{0.04})(Nb_{0.86}Ta_{0.1}Sb_{0.04})O_3$ significantly improved the density of the system [234]. Studies carried out by Molak *et al.*, on Mn-doped $NaNbO_3$ single crystals reported that the transition between insulator to metal can be induced by oxygen non-stoichiometry [124]. In a similar experiment, Molak *et al.* reported that Mn dopant was found to bring down the phase transition temperatures in $NaNbO_3$ [235] with change in Mn concentration. Also, the low-temperature transition of $NaNbO_3$ shifts from P to N-phase when Mn-ions replaces Na-ions, which is

accompanied with the gradual change in the local symmetry around the doped Mn ions [236]. Studies carried out by Saravanan *et al.* on single crystals of Mn-doped $K_{0.5}Na_{0.5}NbO_3$ resulted in very high dielectric permittivity with low-loss compared to its undoped counterpart [237]. These authors also found that the ferroelectric Curie temperature and the structural transition from orthorhombic to tetragonal (T_{O-T}) shift to a lower temperature regime after the incorporation of Mn. It is also claimed that MnO_2 doping can be used to reduce leakage current and high remnant polarization in alkaline niobates [238,239].

Owing to their non-toxicity and possible applications in Li-ion batteries and as catalysts, Mn-oxides are extensively preferred in ceramics. Also, among the binary transition metal oxides, manganese oxides such as MnO_2, Mn_2O_3, Mn_3O_4 and MnO show paramagnetic behaviour at room temperature while exhibiting antiferromagnetic long-range ordering at low temperatures. Among the afore-mentioned oxides, Mn_3O_4 displays very high magneto-crystalline anisotropy with massive moment due to its dominant ferrimagnetic order below 43.75K [54,240]. It is very interesting that the magnetic properties of Mn_3O_4 strongly depend on dislocations, vacancies, crystallite size, and lattice parameters. This affirms that crystal structure and its properties play an exclusive role in controlling magnetic strength in Mn_3O_4 that can be exploited in magnetic data storage applications. Also, Mn_3O_4 exists as normal spinal structure, in which Mn^{+2} and Mn^{+3} occupies tetrahedral and octahedral positions respectively [241,242]. Recently, Saputra *et al.* reported that the catalytic activity in the oxides of manganese for decomposition of phenolic followed the trend, Mn_2O_3 > MnO > Mn_3O_4 > MnO_2, is related to its redox potential [243]. All the above-mentioned literature studies motivated us to investigate the MnO_2-$NaNbO_3$ system to analyse the changes occurring in the density, crystal structure and dielectric behaviour. Nevertheless, no report is available on the MnO_2 stabilized $NaNbO_3$ system with a detailed study of their structural and dielectric properties with a comprehensive analysis of low-temperature Raman spectroscopy.

5.2 Experimental Details:

For the synthesis of MnO_2-doped $NaNbO_3$, we employed standard solid-state reaction technique with highly pure sodium carbonate (Na_2CO_3, from EMPLURA, 99.9%) and niobium pentoxide (Nb_2O_5, from SRL Pvt. Ltd., 99.95%) as starting materials. Appropriate amounts of these compounds were thoroughly mixed using a planetary Ball-Milling for 5h with distilled water as the milling medium. The obtained products were heated above 100℃ in air overnight to remove the water content and then calcined at 700℃ for 4h in air to obtain pure $NaNbO_3$. Stoichiometric amounts of MnO_2 powder were added to pure $NaNbO_3$ to obtain desired compositions of (1-*x*) $NaNbO_3$ + *x* MnO_2 (from hereafter this composition will be referred to as NMO100*x*, for example, NMO10 implies *x* = 0.10 of (1-*x*) $NaNbO_3$ + *x* MnO_2) two-phase composites. This mixture was then pressed into cylindrical pellets of diameter ~13mm using hydraulic press with a load not exceeding 5ton-cm^{-2} and finally sintered at 1040℃ for 4h in air. The phase purity and crystal structure were examined using X-ray diffraction measurements performed using a Rigaku X-ray diffractometer (model: TTRAX-III) with Cu-K_α radiation (λ = 1.54056Å). Further, for the dielectric measurements, we used these samples in the form

of hard pellets obtained after sintering at 1040℃ with silver coating on either side of the parallel-plate capacitor geometry for the metallic contacts. As discussed in the chapter 2, an impedance analyser from Solatron (Model SI1260) was used for the temperature dependent dielectric measurements in the frequency range 100Hz - 20MHz with 100mV ac peak-to-peak amplitude of the electric field.

Low-temperature Raman spectroscopy was performed in the backscattering geometry using a He-Ne laser of wavelength 473nm coupled with a Labram-HR800 micro Raman spectrometer equipped with a 50× objective. An appropriate notch filter and Peltier-cooled charge-coupled device detector were used in the above equipment. The laser power was kept at 25mW for excitation. No melting or phase transformation was found in the sample due to this power. For the low-temperature measurements, the sample was mounted on a THMS600 stage from Linkam, UK, and a 1800gr-mm^{-1} grating was used in the high-resolution dispersive geometry. The samples were first mounted in the cold stage setup, equipped with a temperature controller which is capable of maintaining a steady temperature of 80K. Samples were not more than 1mm in thickness to reduce temperature gradient. Cooling was provided by passing dry nitrogen gas from a thermally sealed container filled with liquid nitrogen. Lakeshore based temperature controller was able to hold the temperature fluctuations within a range ±1K by regulating this gas flow. In order to achieve very high positional accuracy, the grating was kept stationary during the entire temperature scan enabling a spectral window of ~1800cm^{-1}. Thermal analysis of the sintered products was carried out using a high temperature (from room temperature to 1100℃ with heating rate 10℃/min in Argon ambiance with flow rate 60ml/min) differential scanning calorimeter and thermogravimetric analyser from Netzsch (Model: STA449F3A00). In the following sections, we discuss the results and their interpretation.

5.3 Result and Discussion:

5.3.1 Crystal structure studies using X-Ray Diffraction (XRD):

Figure 5.1 shows the XRD pattern of the sample before and after calcination. It can be clearly seen that the XRD pattern of calcined product corresponds to orthorhombic $NaNbO_3$ with phase group *P21ma*(26). It is also possible that at room temperature, both antiferroelectric phase with space group *Pbcm* and ferroelectric phase with *R-3c* space group coexist in high temperature (1150℃) sintered $NaNbO_3$ [244]. This type of phase co-existence was also previously reported by Mishra *et al.* while investigating the ferroelectric-antiferroelectric interactions through neutron diffraction studies [105].

The key feature that sets apart *Pbcm* from *P21ma* is the diffraction peak occurring at a diffraction angle of $2\theta \sim 36.5°$ [244]. The XRD pattern for various compositions of (1-*x*) $NaNbO_3$ + *x* MnO_2 are shown in figures 5.2 and 5.3. Here, figure 5.2 shows the XRD for the mixture sintered for 1000℃ and figure 5.3 for 1040℃. From figures 5.1 and 5.2, it can be seen that the XRD pattern for low and dilute compositions of MnO_2, the peaks are analogous to orthorhombic $NaNbO_3$ with phase group *P21ma*(26).

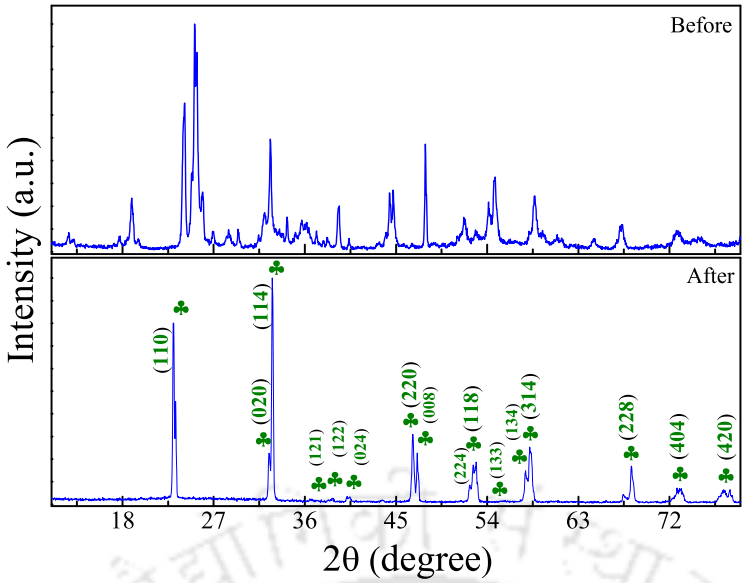

Figure 5.1. This figure shows the X-ray diffraction (XRD) pattern of the sample before and after calcination of the Ball-Milled precursors.

For the samples heated at 1000°C, the secondary phase emerging out was that of Mn_2O_3. This is due to the thermal decomposition of MnO_2 into Mn_2O_3 and oxygen (this phase is stable up to below 1000°C). The reverse reaction occurs at a slower rate at lower temperatures (~ 300°C). Whereas, for the samples heated at 1040°C reveals the formation of tetragonal Mn_3O_4 (as shown in the chemical reactions given below).

$$2MnO_2 \rightarrow Mn_2O_3 + ½\ O_2$$

$$3Mn_2O_3 \rightarrow 2Mn_3O_4 + ½\ O_2$$

Previous studies reveal that all the reduction reaction of these oxides of Mn are highly endothermic and requires high amount of thermal energy [245]. Figure 5.4 shows the reduction reaction of the oxides of manganese. The above report also reveals that these phases of manganese oxides form based on thermodynamic variables such as Temperature (T) and Oxygen Partial Pressure (P-O_2). The above reactions are thermodynamically feasible at a partial pressure of P-$O_2 \sim 10^{-1}$atm (assuming oxygen constitutes 20% of atmospheric gases) [245]. The XRD pattern for Mn_3O_4 can be differentiated from Mn_2O_3 by the peak emerging out at Bragg angle $2\theta \sim 18.6^{o}$ (101) (as shown in figure 5.3(*c*)). Manganese exists in two oxidation states in Mn_3O_4 (+2 and +3) which is represented as $MnO.Mn_2O_3$. Williamson-Hall (W-H) analysis was carried out to estimate the average grain size (D) and micro-strain (η) using equation 5.4 [199,246]. This relation is a combination of two separate relations assuming that the contribution towards broadening due to particle size and strain are independent of each other. Also, the peak broadening occurs due to instrumental broadening. To ratify the instrumental contributions towards broadening, standard silicon sample was used

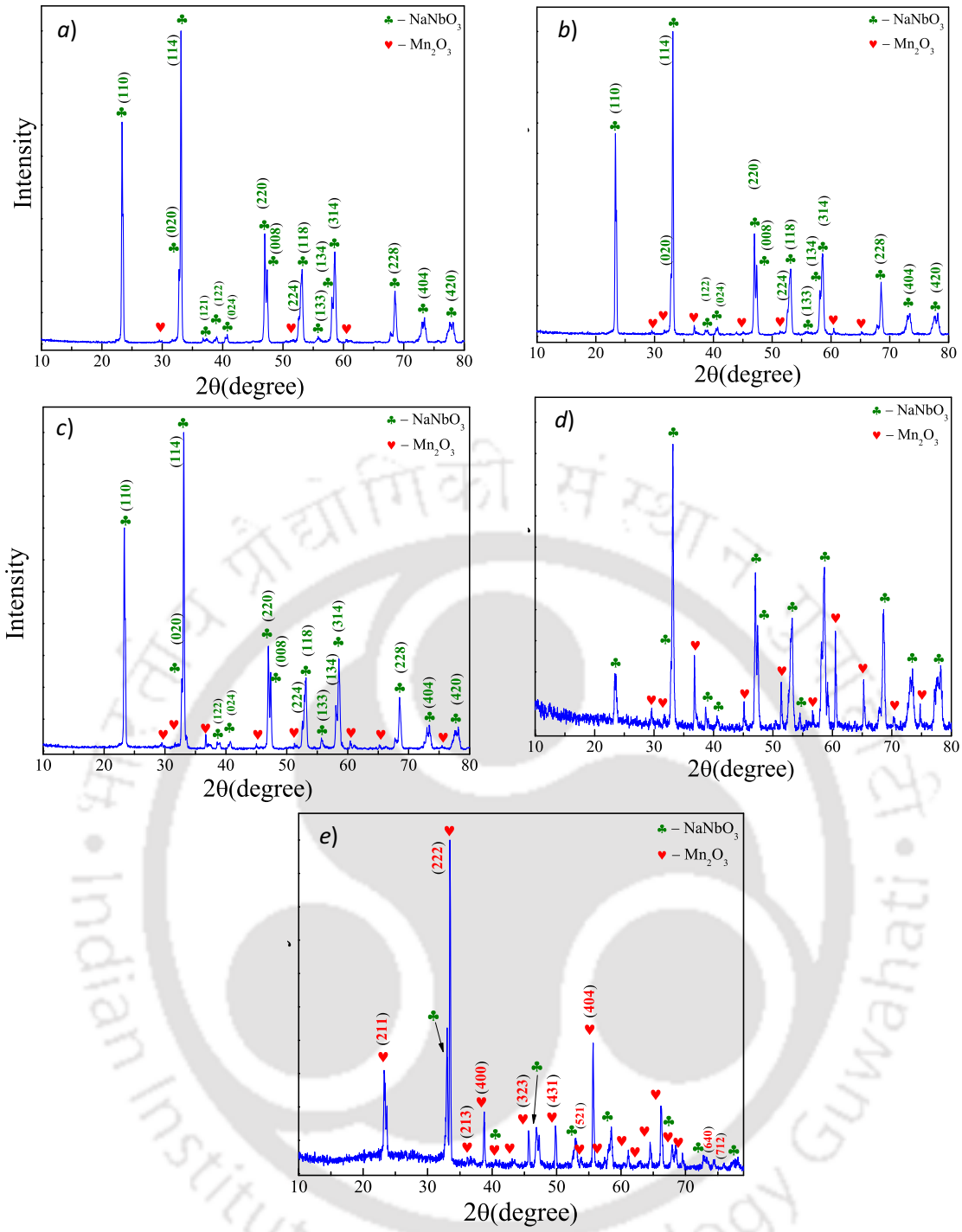

Figure 5.2. X-Ray diffraction pattern of (1-*x*) $NaNbO_3$ + *x* MnO_2 for various compositions (*a*) *x* = 0.02 (*b*) *x* = 0.04 (*c*) *x* = 0.10 (*d*) *x* = 0.30 and (*e*) *x* = 0.70 sintered at 1000°C for 4h in air. Secondary phases suggest formation of Mn_2O_3 from MnO_2.

at first to determine the instrumental broadening. The corrected broadening β_{hkl} was calculated using the equation 5.1.

$$\beta_{hkl} = \left(\beta^2_{measured} - \beta^2_{instrumental}\right)^{\frac{1}{2}} \qquad (5.1)$$

Line-broadening of Bragg reflection originating due to smaller size of crystals follows the Scherrer equation $\beta_s = K\lambda/(DCos\theta_{hkl})$ and the strain-induced broadening (β_η) follows the Wilson's formula, $\beta_\eta = 4\eta Tan\theta_{hkl}$, which are combined to give β_{hkl} as given below, [247]

$$\beta_{hkl} = \beta_s + \beta_\eta \tag{5.2}$$

$$\beta_{hkl} = \frac{K\lambda}{DCos\theta_{hkl}} + 4\eta Tan\theta_{hkl} \tag{5.3}$$

$$\beta_{hkl} Cos\theta_{hkl} = \frac{K\lambda}{D} + 4\eta Sin\theta_{hkl} \tag{5.4}$$

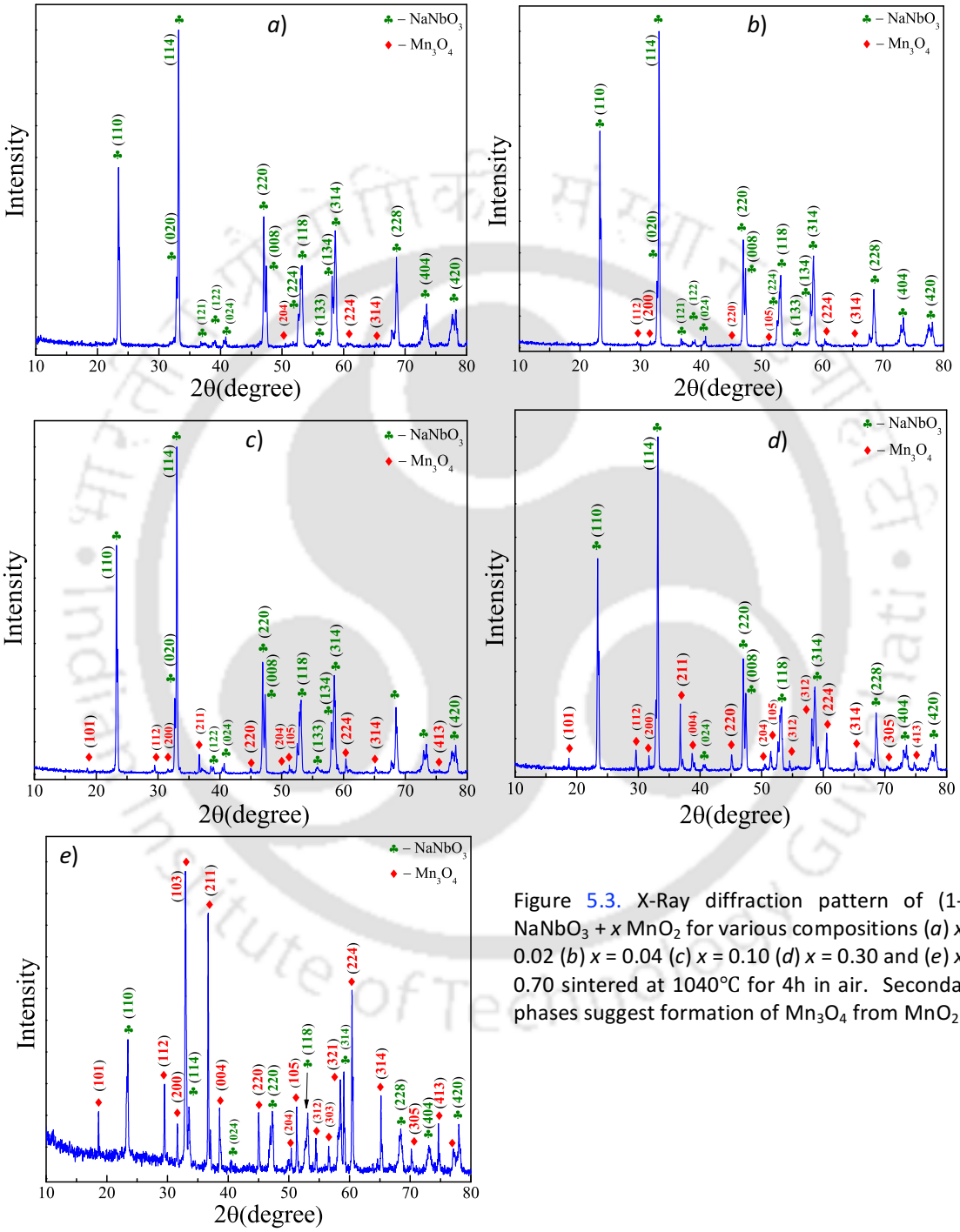

Figure 5.3. X-Ray diffraction pattern of (1-*x*) $NaNbO_3$ + *x* MnO_2 for various compositions (*a*) *x* = 0.02 (*b*) *x* = 0.04 (*c*) *x* = 0.10 (*d*) *x* = 0.30 and (*e*) *x* = 0.70 sintered at 1040°C for 4h in air. Secondary phases suggest formation of Mn_3O_4 from MnO_2.

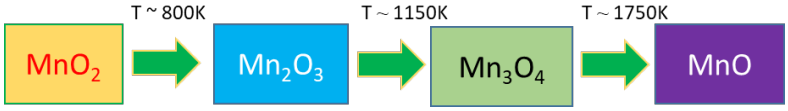

Figure 5.4. This figure shows various oxide forms of Manganese and their respective formation temperature of formation.

where β represents the full-width at half maximum (FWHM) of diffraction peak, K represents the shape factor (= 0.89 assuming spherical geometry) and λ is the wavelength of Cu-K_α X-ray radiation (= 1.5406Å). Figure 5.5 shows the variation of micro-strain (η) and average particle size (D) obtained from the slope and intercept of the W-H plot ($\beta Cos\theta$ versus $Sin\theta$) for various compositions (x) of $NaNbO_3$-MnO_2 composites using equation 5.4. It was observed that the average particle size lies in the range of 58-320nm and the micro-strain is in the order of 10^{-3} for x = 0.30. A significant drop in η and D was noticed in the samples containing Mn_2O_3 and Mn_3O_4, but for $x \geq 0.30$ (Mn_2O_3 dominant samples) both η and D exhibit anomalous changes such as non-uniform strain effects [248].

5.3.2 Probing the Phase Transitions using Thermogravimetric and Differential Scanning Calorimetry:

We performed the DSC-TG experiments to investigate the thermal stability of the composites in Argon ambience. Figure 5.6(*a*) and (*b*) show the DSC-TG curves of the precursors of NMO10 and NMO70 heated recorded from 20°C to 1000°C. Considerable amount of weight-loss is observed in both the samples (for NMO10 (~ 9%) and NMO70 (~ 5%)) between 80°C and 150°C which is attributed to the removal of water of crystallization which is evident as an endothermic peak in DSC [211]. The amount of heat (Q_{H_2O}) absorbed during this process is approximately 4.99J and 1.44J for NMO10 and NMO70, respectively. This endothermic peak is closely overlapping with an exothermic peak for T < 80°C (which is labelled by 'I' in figure 5.6(*a*)). Exothermic peak before 80°C is linked with the loss of the organic solvent (iso-propyl alcohol) used for cleaning the crucible, for which temperature of vaporization is T~ 81°C [249]. With further increase of temperature, the rate of mass loss slows down up to about T~ 447°C (labelled 'II' in figure 5.6(*b*)) for both the samples. At T~ 630°C, an endotherm is clearly visible for NMO70 (double-headed arrow) corresponding to the formation of Mn_2O_3, similar to what Hahn *et al.* observed while performing TGA of MnO_2 [250]. Such signatures were masked in NMO10 due to phase formation of $NaNbO_3$. This endotherm peak reaches its maximum at T_m ~ 626°C for NMO70. The Heat of fusion for this endotherm is ~102.2J/g.

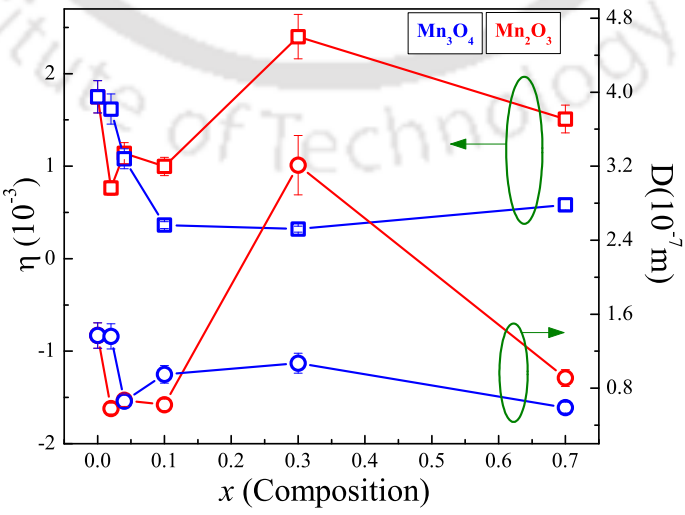

Figure 5.5. Shows variation of micro-strain (η) and average particle size (D) obtained from the slope and intercept respectively of the W-H plot for various composition of $NaNbO_3$-MnO_2 two phase composite.

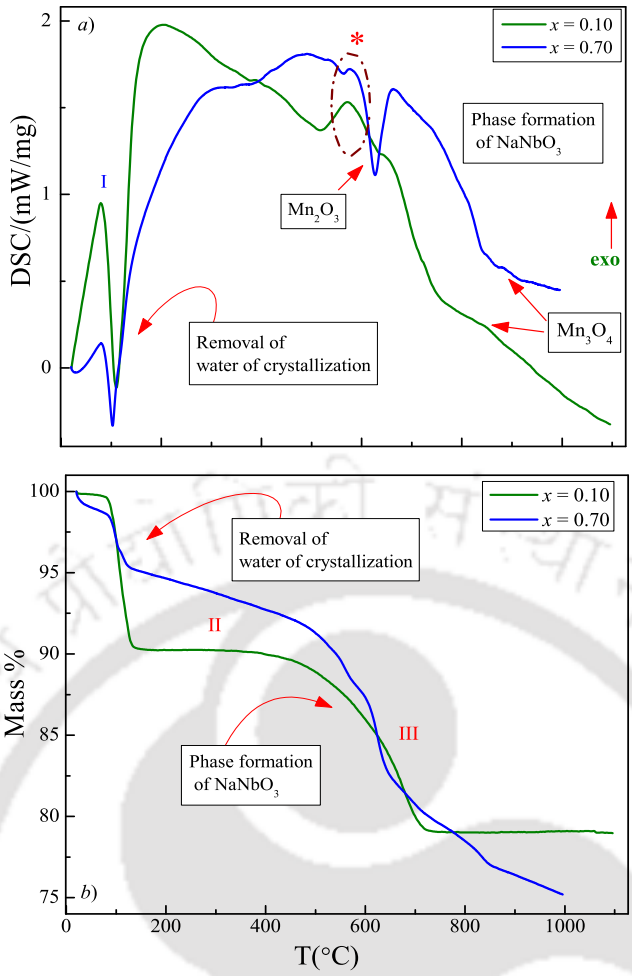

Figure 5.6. *a*) Shows the DSC curves and *b*) shows the TGA curves of the precursors NMO10 and NMO70 respectively, heated from 20℃ to 1000℃.

Along with the formation of Mn_2O_3, crystallization of $NaNbO_3$ and the elimination of residual carbon occur simultaneously. This phase formation records the highest weight-loss in the TGA for both samples in the temperature range of 450-770℃ (NMO10 shows a drop of ~ 11% and NMO70 is about ~13%). The exothermic peak (labelled using an asterisk symbol) appearing in both the mixtures (NMO10 and NMO70) across the avalanche of weight-loss suggests the emission of residual CO and CO_2 [212]. The temperature of crystallization peaks at ~ 575℃ (T_C) with a release of 1.4J as heat. A small but distinct hump visible for NMO70 at T~ 880℃ correlates to the phase transformation from Mn_2O_3 to Mn_3O_4. Investigation of the thermochemical cycle of Mn_2O_3/MnO by Marugán *et al.* also report that the stable and dominant phase appears in the temperature regime of 770℃ - 1400℃ (at P_{total} = 1bar) is Mn_3O_4 [251].

5.3.3 High temperature Dielectric Studies:

In order to understand the role of MnO_2 on the overall dielectric response of the material, we measured the variation of relative dielectric permittivity as a function of temperature ($\varepsilon_r(T)$) for varying frequencies of ac signal. Figure 5.7(*a-f*) shows the temperature dependence of relative dielectric permittivity (ε_r) and dielectric loss ($Tan\delta$) measured under various ac-frequencies (0.2kHz ≤ f ≤ 2MHz) for NMO10,

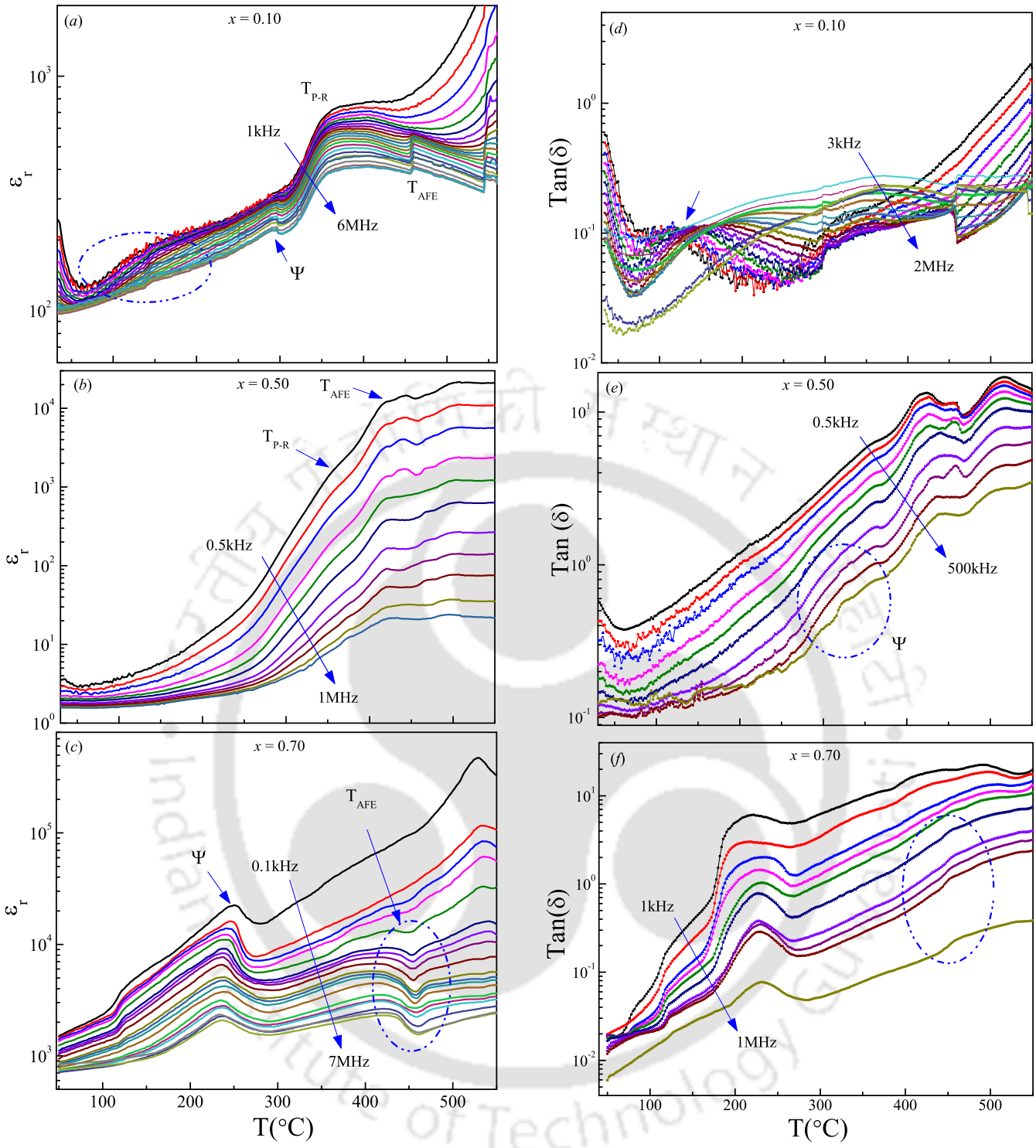

Figure 5.7. (*a-c*) Shows the temperature dependence of relative dielectric permittivity (ε_r) and (*d-f*) shows dielectric loss ($tan\delta$) measured under various ac-frequencies (0.2kHz ≤ f ≤ 2MHz) for x = 10, x = 0.50 and x = 0.70 for temperatures between 27°C and 600°C with a temperature interval ΔT = 2°C.

NMO50 and NMO70 for temperatures between 27°C and 630°C. In general, for all the compositions ε_r increases progressively with increase in temperature. For NMO10 (figure 5.7(*a*)), for T < 50°C, a tiny anomaly in ε_r was observed which is associated with the structural transition between temperature 275K (2°C) and 290K (17°C). Such anomalous change in ε_r also has its signature in the low-temperature vibrational spectroscopy which will be discussed in section 5.3.5. With further increase in temperature, a giant cusp was

observed between 310℃ and 460℃, which peaks at $T\sim$ 370℃. This cusp is associated with the transition from Orthorhombic-P to R phase without altering its antiferroelectric domains [189,194]. Similar features were observed by us in case of $NaNbO_3$-NiO at $T\sim$ 392℃ [252]. This transition for pure $NaNbO_3$ occurs at 370℃ [189]. Dissipation factor during this transition is observed as low as 0.1 (at 20kHz). This cusp can be noticed as a shoulder-like feature in NMO50, whereas it has completely disappeared in NMO70. In figure 5.7(*a*) one can also observe a soft anomaly at 80℃ $\leq T \leq$ 260℃ (encircled in blue) which is centred at $T\sim$ 150℃. Dissipation factor also reveals the signature of this anomaly across the same temperature gradient. Similar transitions are also reported earlier in $NaNbO_3$-NiO, $KNbO_3$-NiO, $KNbO_3$-$NaNbO_3$, and (Li/K,Na)NbO_3 systems due to the rhombohedral distortion in the perovskite structure [131,156,157,158,199,252]. However, this transition is feeble in NMO50 and completely absent in NMO70. Further above this transition, at $T\sim$ 300℃, a small kink-like feature was observed in NMO10 for f > 30kHz, whereas this feature appears as a major cusp in NMO70 sample (marked as Ψ in the figures 5.7(*a*) and (*c*)). This feature is not visible up to f ~ 50kHz, but gradually emerges out to be a feeble anomaly for higher frequencies in NMO50 ('Ψ' overlaps with the second-order transition). Such anomalous change is also noticed in the temperature dependence of the dissipation factor. Berbenni *et al.* reported that the oxidation behaviour of mechanically activated Mn_3O_4 yields an exothermic peak in DSC at $T\sim$ 200℃ (oxidation from Mn_3O_4 → Mn_5O_8) [253]. Such oxidation from Mn_3O_4 to Mn_5O_8 was also reported by Feitknecht *et al.* which takes place during the heating of Mn_3O_4 particles at temperatures between 245℃ and 550℃ in an atmosphere containing more than 5% O_2 [254]. Furthermore, small but sharp humps were observed for $f > 10^5$Hz at $T\sim$ 462℃ which are associated with the standard antiferroelectric to paraelectric (T_{AFE}) transition accompanied by orthorhombic-R to S crystallographic phase transition of NNO [105,189].

Ac-resistivity (ρ_{ac}) measurement was performed in order to determine the temperature and frequency dependence of transport of charge carriers. Figure 8(*a-c*) depict $\rho_{ac}(T)$ for various ac-driving frequencies for the samples NMO10, NMO50 and NMO70. For dilute composition of MnO_2, i.e. NMO10, the system exhibits very large resistivity (~ $2\times10^6\Omega$-m) at room temperature for f = 6kHz. For all the compositions at a given frequency, resistivity is maximum between temperatures 27℃ and 127℃ exhibiting a cusp (labelled 1 in figure 5.8). This cusp gradually diminishes with increasing frequency for all the compositions. This frequency dependence of resistivity is mostly due to the relaxation process arising in mobile charge carriers. Further at low frequencies, charge conduction process takes place via infinite path through long-range translation motion of carriers [199]. Also, one cannot rule out the contribution of charge accumulation with different relaxation time across the interface of the two materials (Maxwell-Wagner (MW) polarization discussed in section 1.3.5) [255]. This is also coupled with the second-order transition near the incommensurate state leading to cusp like feature which diminishes with increasing frequency. Both NMO50 and NMO70 also show similar feature at lower temperature spectrum. At high temperatures, NMO10 shows

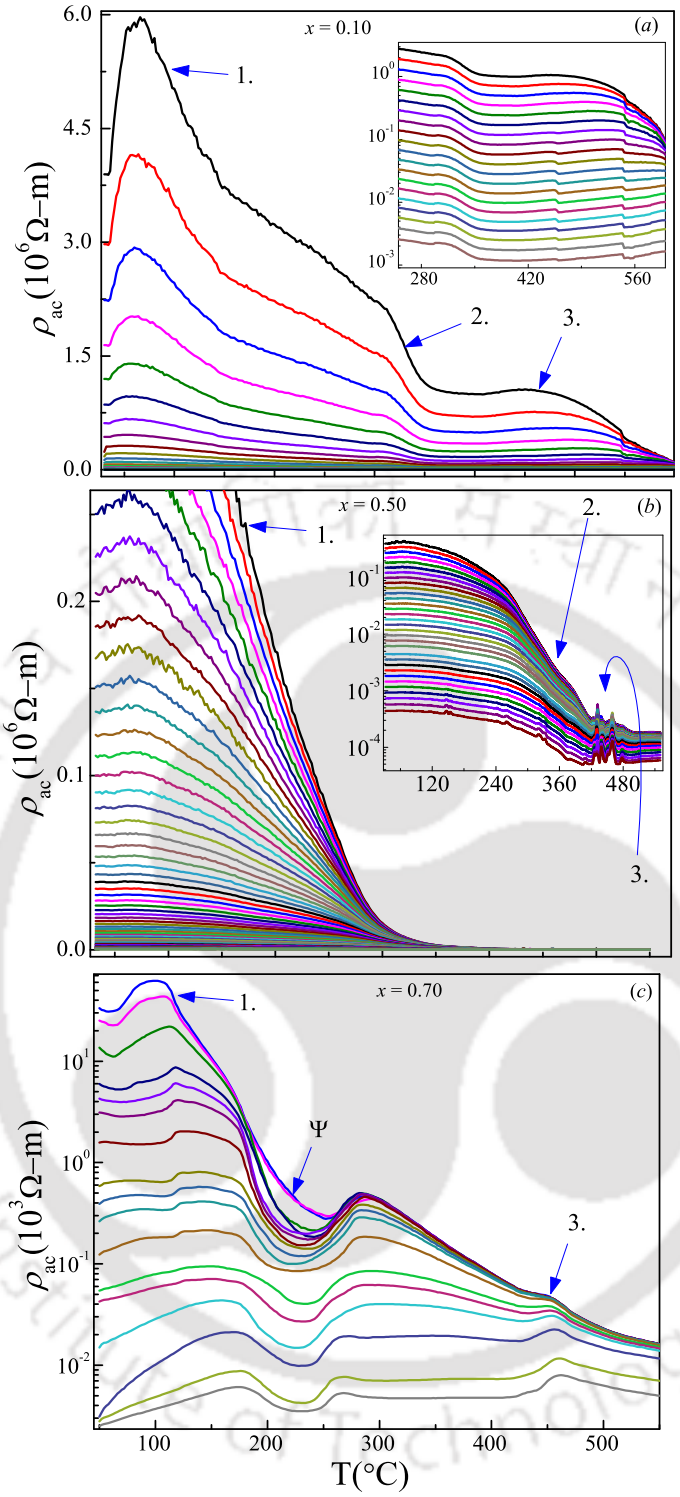

Figure 5.8. Temperature variation in ac-resistivity ($\rho_{ac}(T)$) for (*a*) *x* = 0.10, (*b*) *x* = 0.50 and (*c*) *x* = 0.70 for frequency ranging between 1kHz and 2MHz.

a steep fall in the resistivity at $T\sim$ 360°C, which is associated with the phase transition of the perovskite from orthorhombic-P to R (T_{P-R}) phase (labelled by 2 in figure 5.8). However, this feature is completely absent in NMO70. Signatures of antiferroelectric to paraelectric transition of $NaNbO_3$ are also visible in resistivity (labelled by 3 in figure 5.8) as a broad hump across T = 460°C in NMO10, whereas in NMO50 and NMO70, it is quite diminished but still discernible. Also, the resistivity decreases (alternatively conductivity increases)

with increase in the temperature for all the composites. In order to understand the charge conduction mechanism in these composites, we conducted a detailed analysis of the ac-resistivity using the Mott's Variable Range Hopping (VRH) model. According to this model, charge conduction of localized charge carriers in d-dimension is;

$$\rho = \rho_0 \exp\left(\frac{T_0}{T}\right)^{\frac{1}{1+d}} \quad (5.5)$$

where, ρ_0 represents the pre-exponent factor and T_0 the characteristic temperature. For 3-dimension case, the equation reduces to,

$$\rho = \rho_0 \exp\left(\frac{T_0}{T}\right)^{\frac{1}{4}} \quad (5.6)$$

where the parameters ρ_0 and T_0 are extracted from the intercept and slope of the $ln\rho_{ac}$ versus $T^{-0.25}$ plots for desired frequencies. In order to confirm VRH method of charge conduction, we have plotted the double logarithm of $[\rho/\rho_0]$ versus lnT for few selected frequencies as shown in figure 5.9. The slope of these plots was found to be ~ -0.25 which ratifies the validity of equation 5.6 and hence providing significant evidence for VRH. Oxygen vacancies and Mn-ions contribute towards the localized charge carriers, and these localized charge carriers deliver finite number of electronic states near Fermi level [199,156]. The Density of electronic states ($N(\Sigma_F)$) thus formed due these localized charge carriers depend on the T_0 given by the equation,

$$N(\Sigma_F) = 16\alpha^3/k_B T_0 \quad (5.7)$$

where α^{-1} is known as the localization length (decay length) or in other words the spatial extension of the wave function $e^{(-\alpha R)}$ which takes the value 10^{-7}cm [199]. Making use of $N(\Sigma_F)$ obtained from equation 5.7, we have calculated the average hopping distance ($\mathcal{R}_H$) and Hopping Energy ($\mathcal{E}_H$) using the following relations [158,256]

$$\mathcal{R}_H = \left[\frac{3}{(2\pi\alpha N(\Sigma_F)k_B T)}\right]^{1/4} \quad (5.8)$$

$$\mathcal{E}_H = \frac{3}{4\pi N(\Sigma_F)\mathcal{R}_H^3} \quad (5.9)$$

The values of $\mathcal{R}_H$ and $\mathcal{E}_H$ calculated from the above equations along with the slope obtained from the VRH analysis are listed together in Table 5.1. The value of $N(\Sigma_F)$ for a given composite increases with increase in frequency.

5.3.4 Room Temperature Raman Spectroscopy:

Figure 5.10 shows room temperature Raman spectra recorded at room temperature between wavenumber 40cm^{-1} and 1200cm^{-1} using laser of wavelength λ = 473nm for various compositions of the samples (1-*x*) $NaNbO_3$ + *x* MnO_2. This figure also contains the tentative assignment of peaks with appropriate

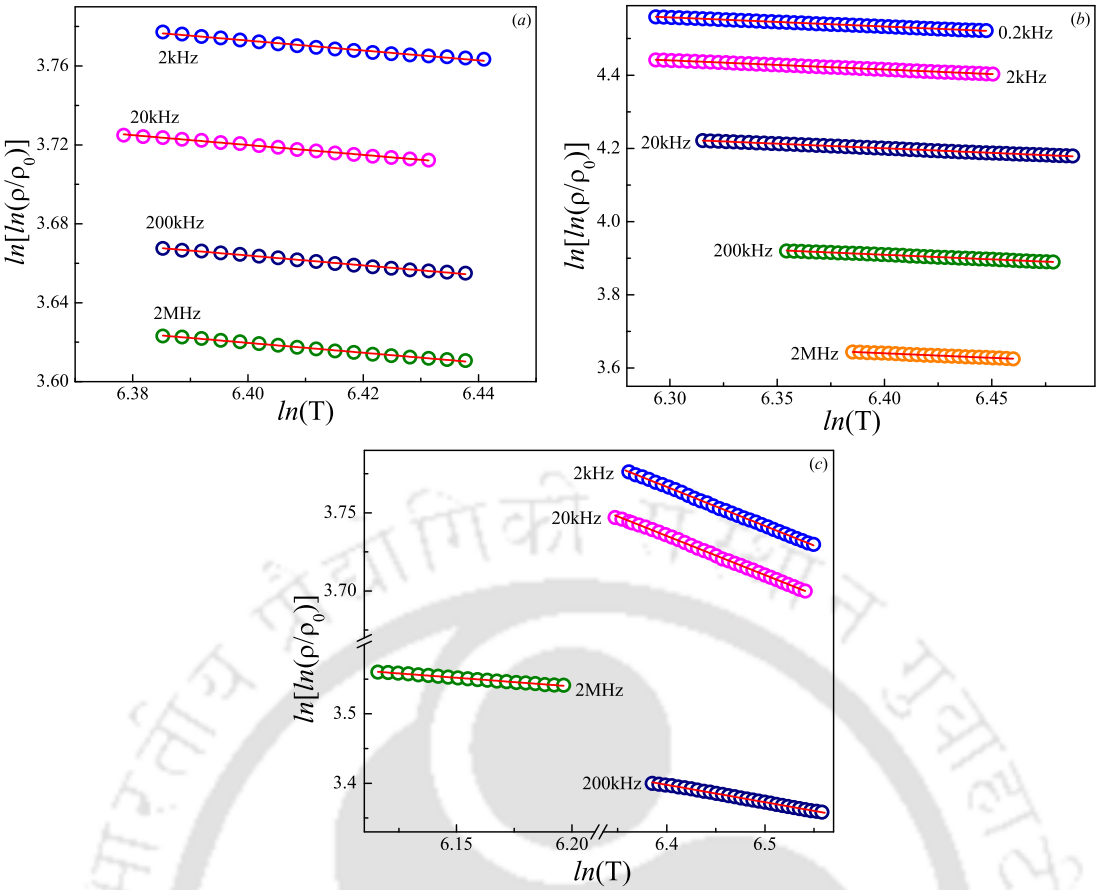

Figure 5.9. The double logarithmic variation of (ρ/ρ_0) as a function of $ln(T)$ for few selected frequencies for (*a*) *x* = 0.10, (*b*) *x* = 0.50 and (*c*) *x* = 0.70.

x	*f* (kHz)	$N(\Sigma_F)$ ($\times 10^{35}$ $J^{-1}cm^{-3}$)	$\mathcal{R}_H$ (μcm)	$\mathcal{E}_H$ (eV)	Slope from VRH
0.10	2	5.38	1.80	0.157	-0.2498
	20	6.64	1.71	0.149	-0.2500
	200	8.31	1.62	0.141	-0.2499
	2000	9.92	1.55	0.135	-0.2499
0.50	0.2	0.257	3.84	0.343	-0.2499
	2	0.411	3.41	0.305	-0.2500
	20	0.973	2.75	0.246	-0.2499
	200	3.11	2.06	0.184	-0.2500
	2000	9.14	1.57	0.140	-0.2500
0.70	2	5.51	1.78	0.159	-0.2500
	20	6.25	1.73	0.154	-0.2500
	200	24.1	1.23	0.110	-0.2500
	2000	16.7	1.35	0.121	-0.2499

Table 5.1. List of parameters: density of states $[N(\Sigma_F)]$, average hopping length $(\mathcal{R}_H)$, and average hopping energy $(\mathcal{E}_H)$, obtained from VRH analysis for the compositions mentioned.

transitions following the references [201,218,219]. The inset of the figures shows the low wavenumber regime (< 370cm^{-1}) of the spectra. In general, $NaNbO_3$ at room temperature exhibits orthorhombic structure (point group D_{2h}^{11}) with space group *Pbcm* which corresponds to eight molecular units per unit cell. The irreducible representation of the vibrational modes at zero wave-vector is,

$$\Gamma = 15A_g + 17B_{1g} + 15B_{2g} + 13B_{3g} + 13A_u + 14B_{1u} + 16B_{2u} + 14B_{3u} \quad (5.10)$$

where A_u mode is inactive, B_{1u}, B_{2u} and B_{3u} are infrared active and A_g, B_{1g}, B_{2g}, and B_{3g} are the only modes that are Raman active [219,252]. The bands appearing in the low wavenumber regions between 50cm^{-1} and 100cm^{-1} are mainly attributed to the cationic translations of Na^+ [219,221]. The mode positioned at 74cm^{-1} is the result of this cationic translation. This mode is suppressed in the background for the samples NMO02 and NMO30, whereas for other compositions, this mode is completely or partially submerged into the background. The bands lying in between 100cm^{-1} and 170cm^{-1} along with ν_5 and ν_6 are mainly due to the rotational vibrations (liberations) of NbO_6 octahedra [218]. The bands in spectral region between 340cm^{-1} and 940cm^{-1} associated with the NbO_6 group are labelled with ν_1 , ν_2 , ν_3 and ν_4. Here ν_1 and ν_2 are linked with the stretching of NbO_6 octahedron [218,221]. Studies by Bouziane *et al.* suggested that these three modes namely ν_1 , ν_2 and ν_3 mainly occur due to the motion of oxygen ions [198]. The $\nu_1 + \nu_5$ band (labelled with asterisk symbol in figure 5.10) is a combination of two fundamental modes. Moreover, Raman bands assigned by ν_2 and ν_3 are present as low-intensity bands as a shoulder to ν_1. All Raman modes in the range 170-950cm^{-1} are related to internal vibrations of the NbO_6 octahedra [201,219]. On a closer look into the room temperature Raman spectra (as shown in figure 5.11), one can notice that there are irregular shifts in the Raman bands with change in concentration (*x*). Figure 5.11(*b*) shows the Raman spectra in the higher wavenumber regime where all the modes deviate from the standard position (602.60cm^{-1}) [201]. The mode ν_1 shifts to (598.28cm^{-1}) lower energy spectrum for NMO02 system and further increases to 610.56cm^{-1} for the samples NMO04, 609.27cm^{-1} for NMO10, 600.22cm^{-1} for NMO30 and 615.08cm^{-1} for NMO70. Whereas,

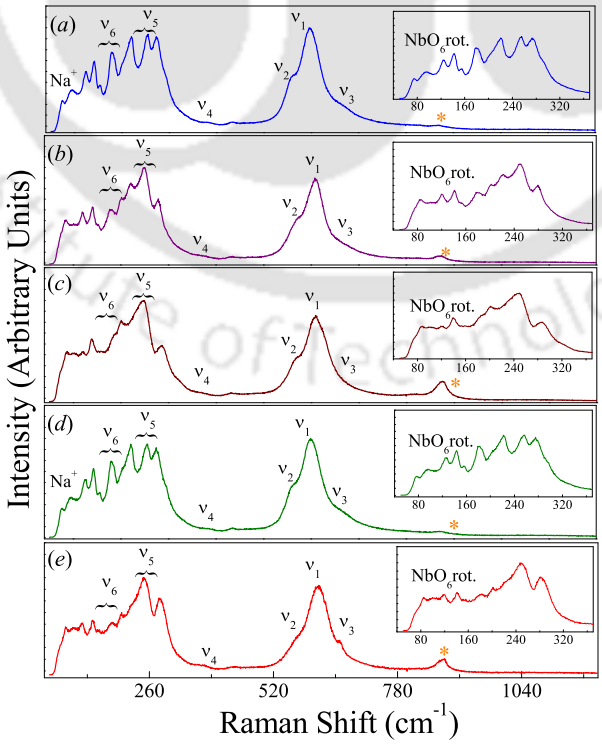

Figure 5.10. Room temperature Raman spectra for various compositions of (1 -*x*) $NaNbO_3$ + *x* MnO_2 showing various modes with their tentative assignments.

in the low wavenumber regime the Raman bands assigned by ν_5 and ν_6 show irregularities (represented with an arrow symbol in figure 5.11(*a*)) with the change in composition. This observation implies that the Mn^{2+} or Mn^{3+} ions might be occupying the interstitial positions due to their smaller ionic radii, such size difference significantly affects the vibrational and the liberational modes of the NbO_6 octahedra. However, the ν_4 band seems to be unaltered with the change in concentration. Also, the crystal field environment and measuring temperature play a vital role in the spatial orientation and vibration of the NbO_6 octahedra [252]. Hence, to understand such effects we performed the temperature dependence of vibrational Raman spectroscopy which is discussed in the following subsections.

5.3.5 Low Temperature Raman Spectroscopy:

Rhombohedral phase of $NaNbO_3$ has six molecular units per unit-cell (space group *R-3c*) which gives the following irreducible representation of the factor group O_h at zero wave-vector:

$$\Gamma = 20A_1 + 9A_2 + 29E \qquad (5.11)$$

In the above equation, A_1 and E are both Raman and IR active. On the other hand, A_2 is inactive for both Raman and IR vibrations [194,219]. Raman spectra for various compositions of (1-*x*) $NaNbO_3$ + *x* MnO_2 (0.02 ≤ *x* ≤ 0.30) were studied in the temperature range 85-300K (depicted in figure 5.12), and from 10K to 300K for *x* = 0.70 (as shown in figure 5.15). It should be noted that for NMO02 and NMO04, the spectra have been recorded during the cooling cycle, whereas, for NMO10 and NMO30, during the heating cycle. The low-temperature Raman bands are assigned with reference to the room temperature assignments. It can be seen from figure 5.12(*a-d*), that all the modes become progressively sharper with decreasing temperature. This

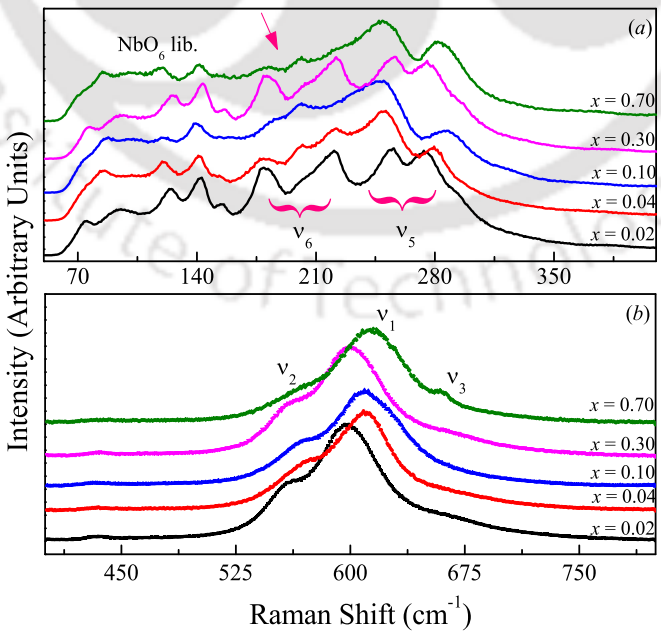

Figure 5.11. Room temperature Raman spectra for various compositions of (1-*x*) $NaNbO_3$ + *x* MnO_2 in the wavenumber range (*a*) 60-400cm^{-1} and *b*) 400-800cm^{-1}. The arrow mark in (*a*) points to visible irregularities displayed by the ν_5 and ν_6 mode.

suggests that at low-temperatures the vibrational amplitude decreases and harmonicity of the vibrations increases [201,252]. With decreasing temperature, majority of the modes are found to shift towards higher wavenumber due to contraction of bond length, hence resulting in an increase in force constant [221,252].

Studies carried out by Mishra *et al*. on pure $NaNbO_3$ suggest that the Raman modes in the orthorhombic phase have larger temperature coefficient than the modes in the rhombohedral phase implying that the anharmonicity of the antiferroelectric phase is higher than that in the ferroelectric phase [219]. Table 5.2 summarizes the temperature coefficients (dv^*/dt) calculated for a few selected Raman modes for various compositions of (1 - *x*) $NaNbO_3$ + *x* MnO_2. Nonetheless, the magnitude of these coefficients is not consistent with the values reported in literature. Temperature coefficients are relatively different for each composition because the phonons are from two different molecular origins, $NaNbO_3$ and MnO_2. But the striking feature is the positive temperature coefficients for the Raman modes. There is no clear explanation for such positive temperature coefficient. However, studies conducted by Burn claim that this anomalous temperature dependence of the Raman modes is attributed to intra and intermolecular couplings which are observed previously for rhombohedral, α-monoclinic and trigonal phases of selenium [257,258]. Figure 5.13 shows the low-wavenumber region (45-370cm^{-1}) of the vibrational Raman spectra recorded for various compositions of (1-*x*) $NaNbO_3$ + *x* MnO_2 ($0.02 \leq x \leq 0.30$) between 80K and 300K.

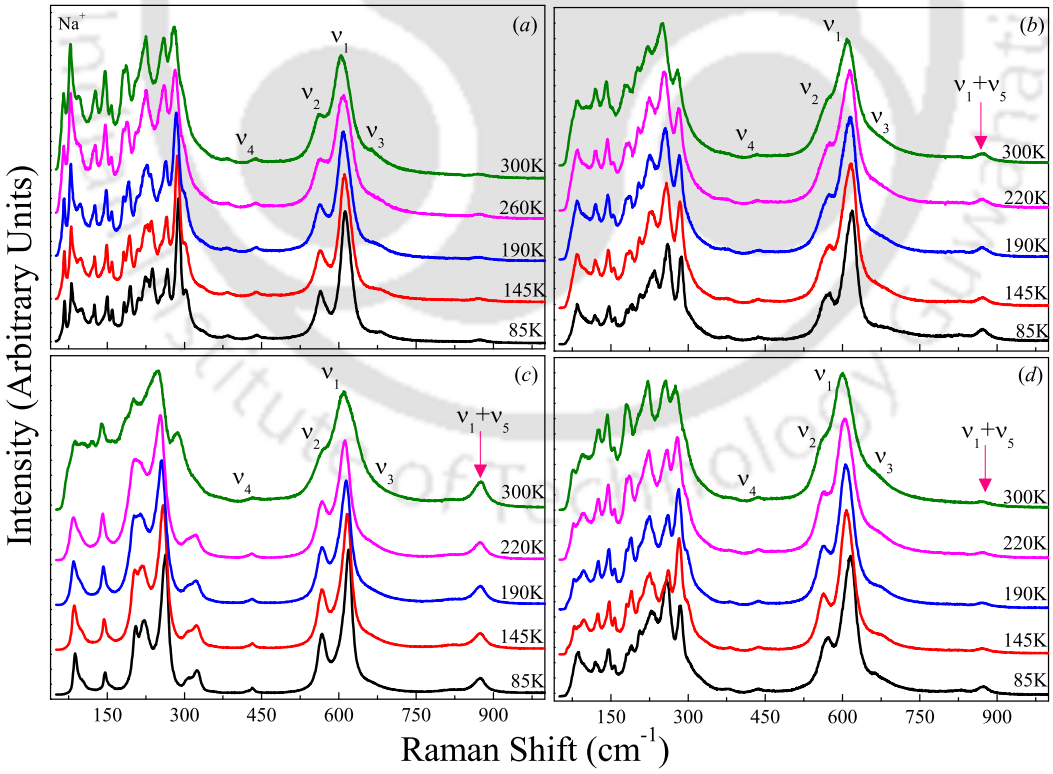

Figure 5.12. Low temperature Raman spectra for various compositions of (1 - *x*) $NaNbO_3$ + *x* MnO_2: (*a*) *x* = 0.02, (*b*) *x* = 0.04, (*c*) *x* = 0.10 and (*d*) *x* = 0.30 measured at different temperatures, 80K ≤ *T* ≤ 300K.

Composition (x)	Temperature Range	$\nu_1 \times 10^{-3}$ cm^{-1}/K	$\nu_2 \times 10^{-3}$ cm^{-1}/K	$\nu_3 \times 10^{-3}$ cm^{-1}/K	NbO_6 lib. $\times 10^{-3}$ cm^{-1}/K	$\nu_5 \times 10^{-3}$ cm^{-1}/K
x = 0.02	300-190K	-36.42	-17.67	-40.16	-23.68	-42.63
	190-85K	-34.17	-15.89	-53.58	-14.89	-39.70
x = 0.04	300-190K	-29.73	-3.24	-88.92	-31.14	-55.29
	190-85K	-35.05	-16.51	+30.25*	-19.58	-45.03
x = 0.10	300-190K	-14.95	-32.40	-70.65	-44.65	-73.75
	190-85K	-48.75	-1.62	+17.76*	-26.10	-70.74
x = 0.30	300-190K	-55.88	-23.61	-83.42	-18.68	-49.10
	190-85K	-71.00	-68.67	-14.30	+6.52*	+32.15*
x = 0.70	300-190K	+20.73*	-35.36	-39.82	-6.23	-55.3
	190-85K	-45.05	-2.67	-12.10	-32.62	-64.31
	85-10K	-4.27	+57.07*	+59.07*	+42.49	-1.59

Table 5.2. List of the temperature coefficients (dv^*/dt) calculated for few selected Raman modes for various compositions (1-x) $NaNbO_3$ + x MnO_2. The '*' sign denotes those modes which has anomalous positive temperature coefficients.

It is evident that for NMO04 and NMO10 (Fig 5.13(*b*) and (*c*)) the rotational degree of freedom of NbO_6 octahedra is drastically affected. Similar to our previous results, as we decrease the measuring temperature, all the low-wavenumber modes associated with NbO_6 diminishes [252]. The spectra of NMO02 and NMO30 have clearly distinguishable Na^+ translational mode whereas, in NMO04 and NMO10, the same seems to be absent or may be dissolved in the background intensity. Also, the Raman spectra for NMO10 and NMO70 has much less discernible Raman modes compared to other compositions (figure 5.15).

According to the studies carried out by Shen *et al*. in 1998 on bulk $NaNbO_3$ system, no Raman-active band was observed (ν_6 mode) within the ferroelectric phase (~ 185K) [201]. For NMO02 and NMO30 (figure 5.13(*a*) and (*d*)), the ν_6 mode clearly deconvolutes into two distinct peaks with decreasing temperature. But for the former, the deconvoluted peaks gets sharper. Whereas, for latter, the deconvoluted peaks soften with cooling and for NMO04, the ν_6 mode diminishes with decreasing temperature. However, for NMO10 (figure 5.13(*c*)), ν_6 mode is partially present as a shoulder for higher temperature (> 280K), but, completely disappears below 280K. In figure 5.13(*a*), that mode ν_6 (encircled) at 225.07cm^{-1} deconvolutes into four discernible peaks at 80K (210.99cm^{-1}, 224.02cm^{-1}, 229.76cm^{-1}, and 238.09cm^{-1}). A sharp change in the NbO_6 liberational mode was noticed (∇ sign in figure 5.13(*c*) and 5.15(*c*)) between 292K and 288K ($\Delta T \sim$ 4°C). A new structural transition is anticipated in this region of the temperature spectrum (between 275K and 290K).

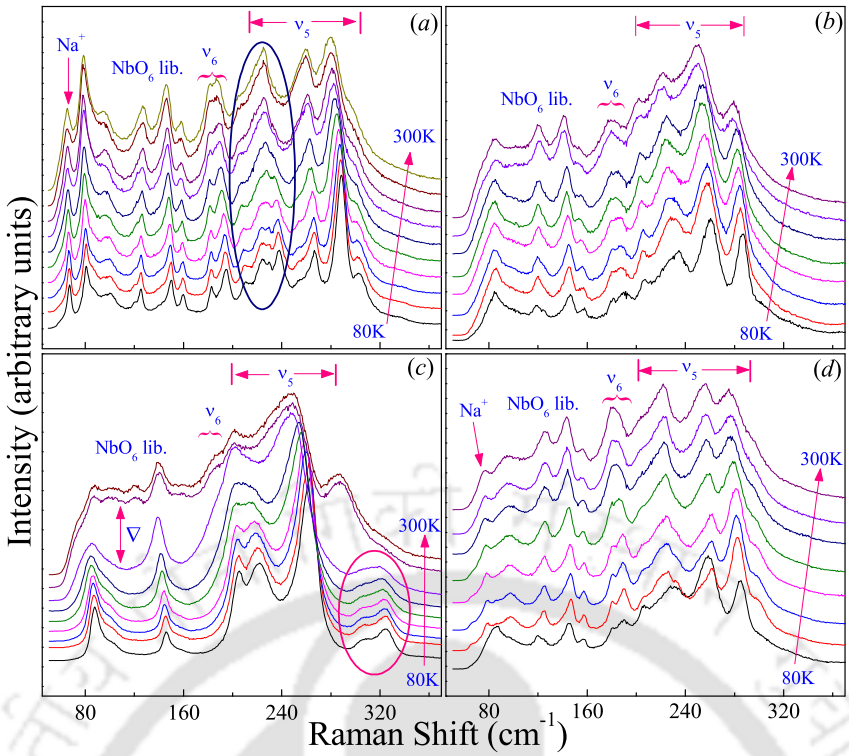

Figure 5.13. Shows the low wavenumber regime (45-370cm^{-1}) of the vibrational Raman spectra measured for various compositions (1-*x*) $NaNbO_3$ + *x* MnO_2 (0.02 ≤ *x* ≤ 0.30) recorded for temperatures between 80K and 300K. The '∇' symbol denotes a sharp anomaly in the NbO_6 liberational mode regime with temperature changing from 292K to 288K.

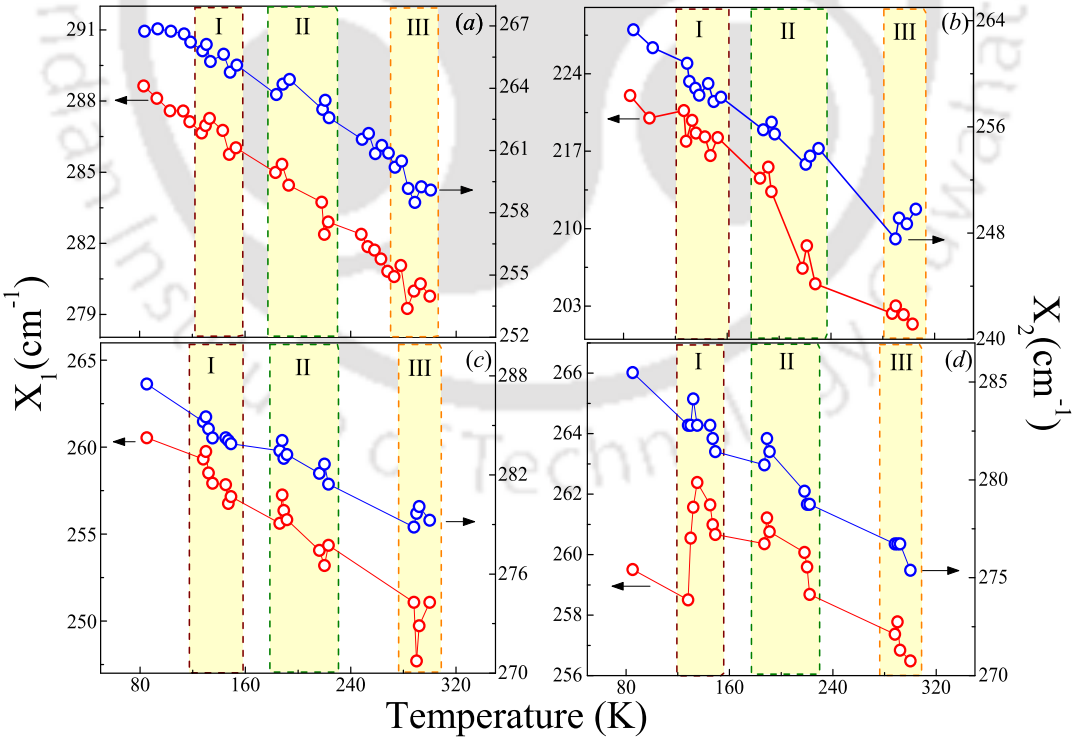

Figure 5.14. Shows the temperature variation of peak-position of two peaks in the ν_5 mode for various compositions of (1-*x*) $NaNbO_3$ + *x* MnO_2: (*a*) *x* = 0.02, (*b*) *x* = 0.04, (*c*) *x* = 0.10 and (*d*) *x* = 0.30. Modulated regions are highlighted where the positional anomalies are anticipated.

Figure 5.14 and 5.16 show the temperature variation of peak-position of two peaks in the ν_5 mode. The highlighted portions represent modulated regions where the positional anomaly is observed. Clearly, all the compositions display irregularities in the peak positions (denoted by Region-III). These irregularities exist in both the heating cycle ($dT/dt > 0$) and the cooling cycle ($dT/dt < 0$) which clearly signifies the existence of a transition in this vicinity of Region-III. Region-II represents the area where the antiferroelectric-ferroelectric transition is anticipated. However, Region-I does not show any anomaly for the samples with dilute substitution of MnO_2 (figure 5.14(*a-c*)). But for higher compositions (figure 5.14(*d*) and 5.16) this region shows considerable amount of positional anomaly signifying the dominant role of Mn^{2+}/Mn^{3+} substitution inside the NNO matrix which hinders the modes related to the vibrations of NbO_6 octahedra.

Figure 5.15 shows the vibrational Raman spectra for the sample NMO70 for various temperatures in the range of 10-300K. The ν_6 band has completely disappeared and there are no Raman active bands for ν_6 mode in the ferroelectric phase which is consistent with the previously reported results by Shen *et al.* [201]. Nevertheless, the mode centred at 249.13cm^{-1} for the ν_5 band has become more sharper and the variation of its peak position with temperature is shown in figure 5.14 (blue symbols). As reported earlier, the slopes of the curve reduce with decrease in temperature denoting the fact that the rhombohedral ferroelectric phase has smaller temperature coefficient than the orthorhombic antiferroelectric phase [219]. The spectra at 300K and 10K clearly distinguish the ferroelectric phase from the antiferroelectric phase. Remarkable changes are observed with the decrease in temperature for the region below 350cm^{-1}. Although the ν_4 band remains weak in intensity, it does not show much variation with change in temperature. In earlier reports [201,218,221,252], the ν_3 and ν_2 band exist as a shoulder to ν_1 , in which the ν_2 band separates out while lowering temperature. Similarly, the ν_3 mode separates out from the main body of the ν_1 mode while lowering the temperatures. Similar features have been observed in the NMO70 sample. We also observed a Raman mode that emerges out at ~ 320cm^{-1} (labelled with an asterisk in figure 5.15(*b*)) at T = 222K. It is also observed that at this temperature, the mode at 215cm^{-1} starts to deconvolute into two distinct peaks centred at 203cm^{-1} and 216cm^{-1} with cooling (encircled region in figure 5.15(*d*)). This mode is also observed in previous reports on pure $NaNbO_3$ bulk sample [201,221,219]. Previous report by Shen *et al.* claims that the emergence of the two-peak behaviour in NNO (at 201cm^{-1} and 318cm^{-1}) indicates the emergence of the ferroelectric phase [201]. These authors also reported the possibility of antiferroelectric-ferroelectric transition to be first-order which involves the re-arrangement of Na^+ ions in the perovskite lattice. A tiny hysteresis is clearly visible in both the peaks for NMO70 as shown in the figure 5.16.

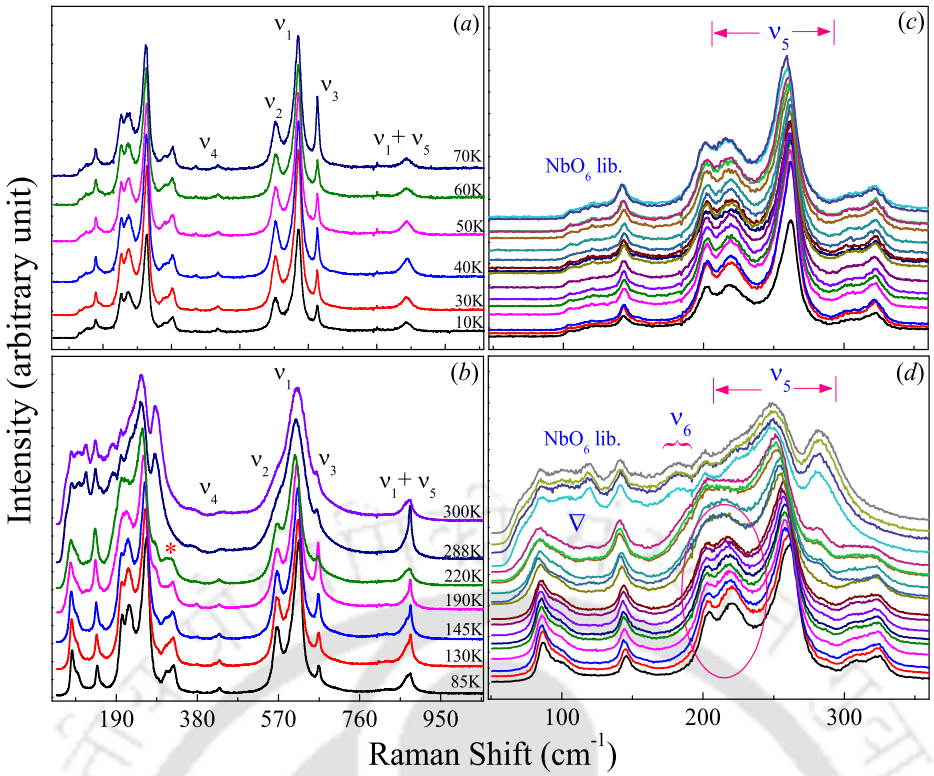

Figure 5.15. Figures (*a*) and (*c*) shows Raman spectra of NMO70 in the temperature range 10K ≤ T ≤ 70K and, (*b*) and (*d*) for the temperature range 85K ≤ T ≤ 300K.

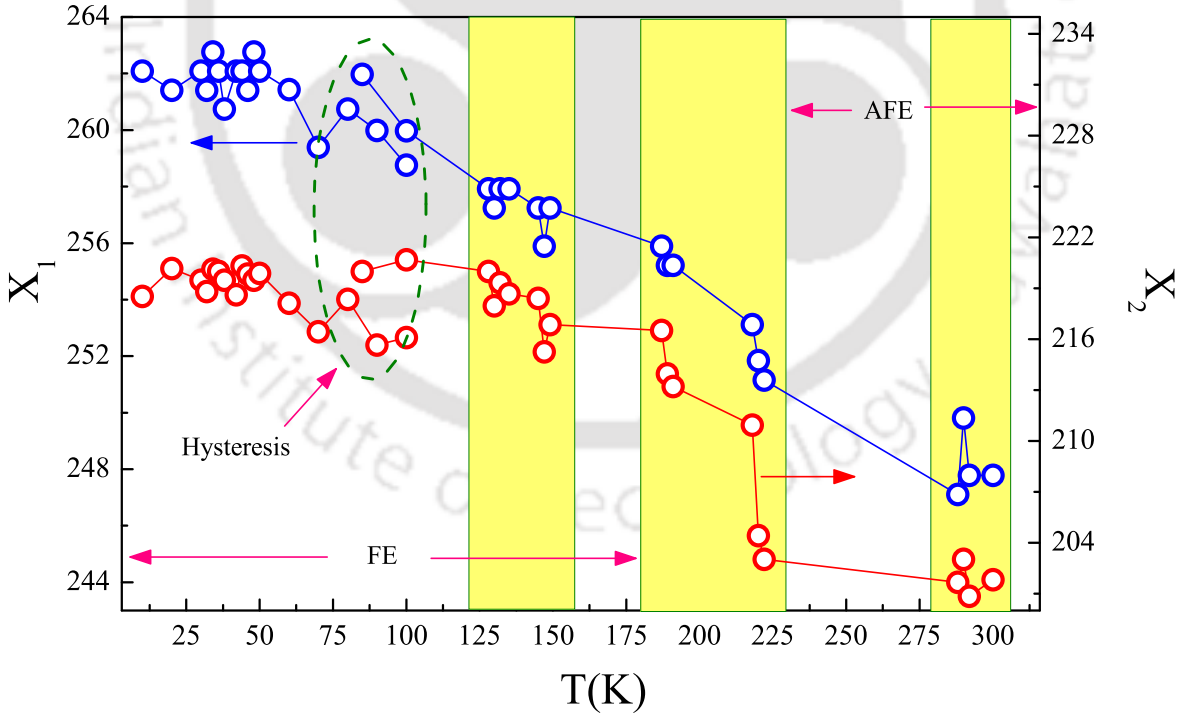

Figure 5.16. Shows the temperature variation of peak-position of two peaks in the ν_5 mode for NMO70 in the temperature range 10K ≤ T ≤ 300K. Encircled region shows a possible positional hysteresis that was observed while measuring during heating and cooling cycle.

5.4 Summary

We have presented here an overview of the structural, vibrational and impedance spectroscopy of $NaNbO_3$-MnO_2 two-phase composite. Main results along with their conclusions are presented below.

- Preliminary XRD analysis after heat treatment of the precursors reveals orthorhombic $NaNbO_3$ with space group *P21ma.*
- Structural analysis also reveals that samples heat-treated at 1000℃ have Mn_2O_3 as the secondary phase and those heat-treated at 1040℃ have Mn_3O_4 as the secondary phase.
- Non-uniform strain effects on the lattice planes of NNO matrix were evident from the micro-strain analysis carried out by W-H analysis.
- DSC-TG of NMO10 and NMO70 uncovers evidence for the phase formation of Mn_2O_3 and Mn_3O_4. For x = 0.70, formation of Mn_2O_3 is evident in the DSC curve with a latent-heat-of-fusion of ~102.2J/g.
- For T< 50℃, a soft anomaly is visible in both ε_r and $tan\delta$ which is not reported elsewhere. The signatures of this transition are also evident in the temperature-dependent Raman spectroscopy.
- Permittivity was found to increase with increasing concentration of the MnO_2. Loss-factor of < 1 was observed for x = 0.10
- Apart from the transitions, dielectric spectroscopy reveals the existence of soft anomaly in the region 80℃ ≤ T ≤ 260℃. This additional phase transition is within the proximity of a second order transition due to rhombohedral distortion in the perovskite structure.
- Resistivity and permittivity curves also reveals an anomaly associated with the oxidation of Mn_3O_4 to Mn_5O_8. With increasing concentration, resistivity is found to decrease for the composite.
- Resistivity analysis provided substantial evidence to support Variable Range Hopping mechanism of charge carrier transport. Slopes from the VRH analysis came out to -0.25.
- The room temperature vibrational Raman spectroscopy shows anomalous change in the vibrational and liberational modes of NbO_6 octahedra with the substitution of Mn in NNO lattice. We also noticed some irregular shifts in the vibrational bands with change in x. In the higher wavenumber regime, ν_1 shifts to lower energy spectrum (598.28cm^{-1}) for NMO02, and further increases to 610.56cm^{-1} for NMO04, 609.27cm^{-1} for NMO10, 600.22cm^{-1} for NMO30 and 615.08cm^{-1} for NMO70. Whereas, in the low wavenumber regime the ν_5 and ν_6 modes exhibit irregularities with change in concentration.
- With decreasing temperature, most of the modes are found to shift towards the higher wavenumber as a result of contraction of bond length. Low-temperature (80K - 300K) vibrational Raman spectra reveals a yet another possible structural transition between 275K and 290K in all the investigated samples. Signatures of this transition are also revealed in the dielectric spectroscopy.
- Few modes exhibited positive temperature coefficients with decreasing temperature. Temperature coefficients are relatively different for each composition which may be due to the fact that the

phonons are from two different molecular origins.

- For Ultra-low vibrational spectroscopy, *x* = 70 exhibits positional hysteresis which is associated with the change in the NbO_6 octahedra location. Also, this mode is found to have smaller temperature coefficient with decreasing temperature.
- Ferroelectric phase has much fewer number of modes compared to the antiferroelectric phase of $NaNbO_3$.
- For x = 0.02 and NMO30, the ν_6 mode clearly deconvolutes into two distinct peaks with decreasing temperature. For the former, these peaks get sharper whereas, for the latter, the deconvoluted peaks soften with cooling and for NMO04, the ν_6 mode diminishes with decreasing temperature. Further, all the compositions display irregularities in the peak position independent of whether the measurements were taken in the heating or cooling cycle.

Chapter 6
Ferroelectric $KNbO_3$ and Antiferromagnetic NiO composites

This chapter deals with the structural phase changes, dielectric behaviour and Raman spectroscopy of ferroelectric $KNbO_3$ – antiferromagnetic NiO composites [(1-*x*) $KNbO_3$ + *x* NiO ($0 \leq x \leq 1$)]). In the first section, we briefly discuss about the properties of $KNbO_3$ and challenges associated with its physical properties to use them in devices along with the gaps in the literature. Second section provides detailed experimental details followed by the results and analysis of our data as third section. Our main aim in choosing this system to check whether there is any improvement in the moisture sensitivity or density of the $KNbO_3$ system after the incorporation of NiO within the perovskite lattice. The temperature dependence of dielectric permittivity studies reveals two major transitions across 445°C and 220°C which are associated with the cubic to tetragonal and tetragonal to orthorhombic phase transitions of $KNbO_3$, respectively. We also noticed a new anomaly in dielectric permittivity across 320°C originating from the antiferromagnetic ordering of NiO. Details of these results and their discussions are presented below.

***6.1 Introduction*:**

Potassium Niobate ($KNbO_3$) is the sister compound to $NaNbO_3$ which exhibits almost identical physical properties except its ferroic-ordering; $KNbO_3$ exhibits ferroelectric ordering, whereas, $NaNbO_3$ show antiferroelectric properties. In this section, we provide few basic properties of $KNbO_3$ and challenges associated with its physical properties. $KNbO_3$ and its composites are widely investigated due to their potential applications in electronic memory devices, holographic storage, optical data processing, pyroelectric detectors and phase conjugation devices [259,260]. In particular, very high photorefractive sensitivity and large electro-optic coefficients of $KNbO_3$ (r_{42} = 380×10^{-12}m/V) have garnered immense research interest in the field of tunable optoelectronics [261]. Large nonlinear piezoelectric coefficients (d_{31} ~ 52pC/N, d_{33} = 80pC/N), high dielectric permittivity (ε_r > 2000), high ferroelectric Curie temperature (T_C ~ 430 ± 5℃) and high coupling factor (~ 31%) of $KNbO_3$ makes it a promising candidate for electro-mechanical coupling devices operating above room temperature [259]. Recently, Ganeshkumar *et al.* reported excellent sensing performance, including ultrafast response (≤ 2s) and quick recovery time (10s), with good linearity and reproducibility, in $KNbO_3$ nanofibers, which can act as an excellent humidity sensor due to the high moisture retentivity of $KNbO_3$, together with a porous structure [262]. This also becomes a limitation when $KNbO_3$ is used as a dielectric [263]. Among perovskite photo-catalysts, $KNbO_3$ possesses nontoxicity and high photo-stability, in addition to the excellent dielectric and piezoelectric response [262,263]. Zhang *et al.* reported very high photo-reactivity (30.64×10^{-3} min^{-1}) of Ag nanoparticles supported on well-defined orthorhombic $KNbO_3$ synthesized by photo-reduction technique [264]. Although $KNbO_3$ is very versatile from an application point of view, its implementation is severely limited by its low density and hygroscopic nature,

which prevent its being fully employed in compact high-frequency devices, decrease its reliability and shorten its lifetime. Also, the low mechanical strength and thermal sensitivity of $KNbO_3$ make it undesirable for rugged applications, and make it difficult to retain the dipole alignment during the fabrication process [227].

Many attempts have been made to improve the density and strength of potassium niobate ceramics, such as novel heat treatment methods like microwave sintering, sintering aids, additives, etc [227–231]. Eshghi *et al.* reported a high density of 99%, and low dielectric losses for a $KNbO_3$ system prepared by sol-gel methodology [228]. These authors also observed a huge magnitude of dielectric permittivity (ε_r = 6200 at T_C), much higher than that of single crystal $KNbO_3$ (ε_r = 3900 at T_C) [228]. Matsubara *et al.* reported high densification of KNN systems using $K_4CuNb_8O_{23}$ as a sintering aid [229]. This additive resulted in liquid phase sintering at 1020°C, leading to effective packing of grains [229]. Small amounts of additives such as $LaFeO_3$, $BiFeO_3$, and MnO_2 were also found to improve the densification and electrical properties, but some of these additives disturbed the poling process [227,230,231]. High densities have also been achieved by optimizing sintering techniques, for example, Kim *et al.* prepared $KNbO_3$ samples with 95% of the theoretical density by employing liquid phase sintering [232]. These samples exhibited high dielectric constant (ε_r= 540), good electromechanical coupling factor (k_p = 29%), high piezoelectric coefficient (d_{33} = 109pC-N^{-1}), and a Quality factor of 197 [232]. Recently, Lu *et al.*, studied phase morphology and corresponding piezoelectricity in ferroelectric solid solutions using a phenomenological theory considering the phase coexistence [265]. These authors found that piezoelectricity can be enhanced by manipulating the stress-field [265]. Very recently, Schmidbauer *et al.*, obtained a high piezoelectric coefficient d_{zz} = 29pmV^{-1} by deliberate manipulation of the ferroelectric domain pattern in 25nm $K_{0.9}Na_{0.1}NbO_3$ films grown on $SrRuO_3$ by means of anisotropic strain engineering [266]. Using the Landau theory, Ke *et al.* have proved the existence of monoclinic (M) phase in ferroelectric solid solutions having compositions at the morphotrophic phase boundary (MPB) between the tetragonal and rhombohedral phases, which is responsible for the extraordinary piezoelectric properties [267].

Yoshida *et al.* reported a significant suppression of deliquescence in $KNbO_3$ ceramic on addition of small quantity of Bi_2O_3 and $MnCO_3$ during ball-milling followed by conventional heat treatment conditions [268]. These additives also improved the electromechanical coupling factor and piezoelectric coefficients (k_{33} = 30% and d_{33} = 101pC-N^{-1} respectively) [231]. Despite such improvements, deliquescence remained a problem. Previous studies have conclusively reported that the strong deliquescence in $KNbO_3$ is due to the porous microstructure of the alkali metal [269]. The reduction of the pores can be attained by either optimum densification, or by engaging those pores with fillers (additives) which are an-hygroscopic as well as dense [270]. Xiang *et al.* reported a massive reduction in deliquescence of $KNbO_3$ upon using ZnO as an additive [270]. Zinc is a d-block element, and all transition metal oxides (TMOs) are relatively denser (~ 5-

8g-cm^{-3} for oxides of IVth period transition metals) as compared to alkaline niobate systems (~ 3-4g-cm^{-3}). Therefore, incorporation of TMOs within the $KNbO_3$ matrix should result in improvement in density, reduce the deliquescence and enhance the frequency response of the dielectric properties. Although, there has been studies on doping of different TMOs in $KNbO_3$, aiming to improve various physical properties, there are still considerable gaps in the literature when it comes to overall rectification of all the limitations simultaneously. In this work, we have incorporated Mott insulator NiO inside the $KNbO_3$ matrix, and performed detailed structural and dielectric studies. Among all the $3d$ TMOs, NiO has attracted a great deal of attention due to its wide range of application in spin-valves, solar cells, varistors, thin-film transistors (TFTs), lithium-ion batteries and gas-sensors. In this work, our main idea in adding NiO to $KNbO_3$ is to understand the effect of the rhombohedral- to-cubic structural phase transition of NiO (at T_N~ 250°C antiferro-to-paramagnetic) on the global dielectric behaviour of the $KNbO_3$. Another motivating aspect in adding NiO is that the antiferromagnetic ordering of this compound may significantly influence (control) the ferroelectric ordering of the parent compound (similarly to extrinsic multiferroic-like systems), which is the main focus of this work, since the T_N of NiO is in the range accessible from room temperature, i.e. which can be tuned down to room temperature for possible device application [226]. The wide energy bandgap (E_g = 3.5–5eV) and high dielectric permittivity of $Ni_{1-x}Li_xO$ finds attractive applications such as transparent electronic devices, spin-valves, thermistors and as electrode material in electrochemical cells [271–273]. In order to achieve a good dielectric response in combination with dopants such as Li and Ti, Lin *et al.* studied dielectric behaviour of $Li_{0.01}Si_xNi_{0.99-x}O$, a derivative of NiO which shows high permittivity (~2000 for 100kHz) [131,274–279]. All the above studies motivated us to synthesize the two-phase composites [(1−*x*) $KNbO_3$ + *x* NiO (0 ≤ *x* ≤ 1)], aiming to improve the electrical properties of the parent niobate.

***6.2 Experimental Details*:**

In this section first we discuss about the synthesis procedure and then characterization details. Standard solid state reaction method has been adopted to synthesize various compositions of (1−*x*) $KNbO_3$ + *x* NiO (0 ≤ *x* ≤ 1) similar to previous chapters, except potassium carbonate (K_2CO_3) in place of sodium carbonate (Na_2CO_3) as precursor. For this, highly pure potassium carbonate (K_2CO_3) (Merck Co, purity 98%), niobium pentoxide (Nb_2O_5) (Sisco Research Laboratories, purity 99.95%) and NiO (Alfa Aesar Co, purity 99%) were taken as raw materials. Appropriate amounts of K_2CO_3 and Nb_2O_5 were first mixed by ball-milling method for 5h with distilled water as the milling medium in order to prepare pure $KNbO_3$. Stoichiometric amounts of $KNbO_3$ and NiO were mixed in an agate mortar with pestle for 4h to attain homogeneity. The obtained product was heated above 100°C in air, overnight, to remove moisture. The powder was then calcined at 700°C in air for 4h and re-milled for 10h for various compositions (*x*) of NiO. The powders obtained were pressed into pellets of 13mm diameter and 1–2mm thickness, using a hydraulic press with a maximum load of 5tons-cm^{-2}. These pellets were finally sintered at 1040°C for 4h in air.

The phase purity and crystal structure were examined by X-ray diffraction measurements using a Rigaku X-ray diffractometer (model: TTRAX-III) with Cu–K_α radiation (λ = 1.54056Å), followed by Rietveld refinement of the diffraction patterns using FullProf suite (Open source software module). The microstructure of the samples was examined with a field emission scanning electron microscope (FESEM, Sigma, Zeiss), using secondary electron mode. The frequency and temperature dependent dielectric measurements over a frequency range 10Hz to 32MHz were performed using an RF Impedance-Gain-phase analyser (Solatron SI-1260) assembled with a high-temperature furnace. Raman spectra were recorded on the powder samples at room temperature using a micro-Raman spectrometer from Horiba Jobin Vyon (LabRam HR) equipped with Ar^+ ion excitation laser source under high-resolution dispersive geometry with wavelength λ = 488nm and an 1800line-mm^{-1} grating.

6.3 Results and Discussion:

6.3.1 Crystal Structure Analysis:

Figure 6.1 shows the X-ray diffraction pattern of polycrystalline $KNbO_3$ and NiO composite samples, along with their Rietveld refinement, performed using Fullproof suite. The diffraction pattern of pure $KNbO_3$ (figure 6.1(*a*)) sample is consistent with the standard orthorhombic crystal structure having space group *Amm2*(38). On the other hand, the diffraction pattern of the pure NiO sample (figure 6.1(*b*)) exhibits Rhombohedral crystal structure with space group *R-3m*(166). Figure 6.1(*c*) shows the X-ray diffraction pattern together with the Rietveld refinement data of $0.995KNbO_3$ + 0.005NiO composite. The diffraction pattern of this composite (*x* = 0.005) was nearly identical to that of pure $KNbO_3$, indicating no appreciable

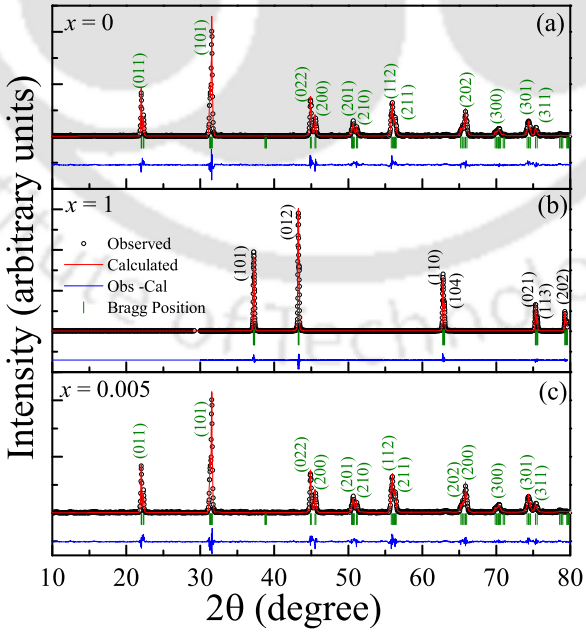

Figure 6.1. The X-ray diffraction pattern together with Rietveld refined data of (1−*x*) $KNbO_3$ + *x* NiO samples for (*a*) *x* = 0 (*b*) *x* = 1 and (*c*) *x* = 0.005, sintered at 1040°C for 4h in air.

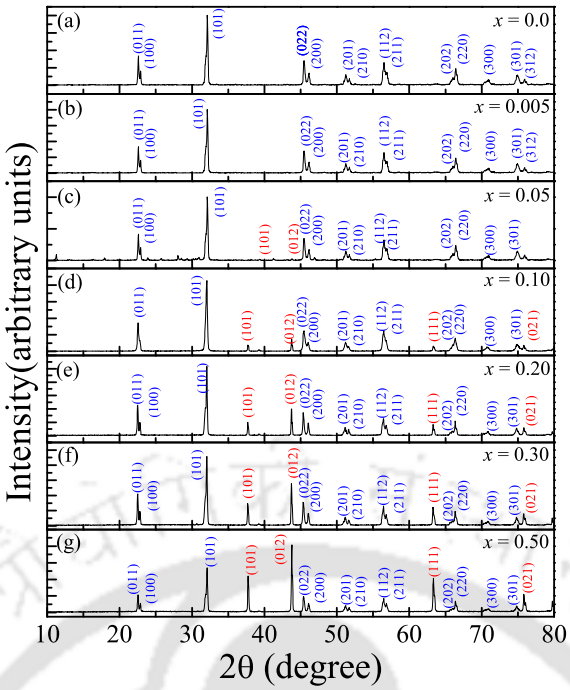

Figure 6.2. The X-ray diffraction pattern recorded at room temperature of (1–*x*) $KNbO_3$ + *x* NiO ($0 \le x \le 1$) composites (*a*) *x* = 0, (*b*) *x* = 0.005, (*c*) *x* = 0.05, (*d*) *x* = 0.10, (*e*) *x* = 0.20, (*f*) *x* = 0.30, and (*g*) *x* = 0.50; sintered at 1040°C for 4h.

variation in the lattice parameters (obtained from refinement analysis) and absence of NiO peaks in the diffraction pattern. Incorporation of NiO in the $KNbO_3$ matrix causes Ni atoms to occupy Nb-sites. The difference in ionic radii results in a slight increase in the unit cell volume which is expected because the ionic radius of the divalent Ni^{2+} (0.69Å) is greater than the ionic radius of the pentavalent Nb^{5+} (0.64Å). However, no significant alteration in the lattice parameters were noticed for *x* = 0.005 sample except a slight increase in the bond lengths: K–O = 2.66 ± 0.01Å (from 2.53 ± 0.01Å) and Nb–O = 1.99 ± 0.01Å (from 1.95 ± 0.01Å) with Nb–O–Nb bond angle 170.22±0.71° (from = 172.29 ± 0.71°).

System	Lattice parameters (Å)	Inter-axial angles	Bond lengths (Å)	Bond angle
$KNbO_3$	*a* = 3.97 ± 0.01 *b* = 5.72 ± 0.01 *c* = 5.69 ± 0.02	α = 90º β = 90º γ = 90º	K-O = 2.53 ± 0.01 Nb-O = 1.95 ± 0.01	K-O-Nb = 89.32° ± 0.42º Nb-O-Nb = 172.29° ± 0.71º
NiO	*a* = 2.96 ± 0.01 *b* = 2.96 ± 0.01 *c* = 7.24 ± 0.02	α = 90º β = 90º γ = 120º	O-O = 2.95 ± 0.01 Ni-O = 2.09 ± 0.01 Ni-Ni = 2.96 ± 0.01	Ni-O-Ni = 89.94° ± 0.41º O-Ni-O = 90.05° ± 0.61º

Table 6.1. The list of lattice parameters, bond lengths and bond angles obtained from Rietveld Refinement for pure $KNbO_3$ and NiO.

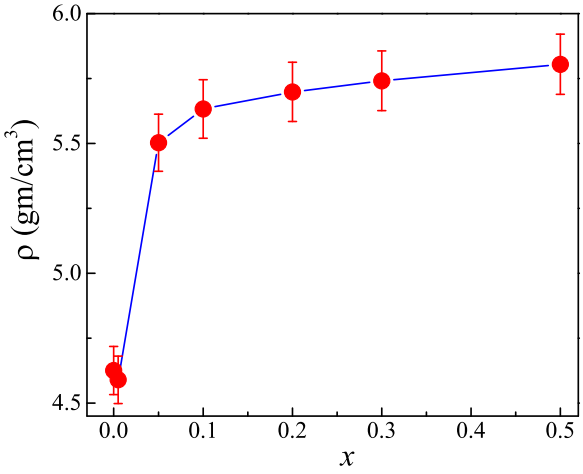

Figure 6.3. The variation of unit-cell density with NiO concentration *x* of (1−*x*) $KNbO_3$ + *x* NiO two-phase composites calculated using X-ray diffraction data.

Table 6.1 summarizes all the list of parameters determined from the Rietveld refinement analysis. Moreover, after a critical concentration $x \geq 0.05$ the secondary phase of NiO emerges out distinctly at higher doping levels as shown in figure 6.2. The weight percentage of both the phases, i.e. Rhombohedral NiO and orthorhombic $KNbO_3$, were quantitatively analysed using the following equation [277].

$$W_{NiO} = [1/(1 + 1.265(\frac{I_{KNbO_3}}{I_{NiO}})]\times 100 \qquad (6.1)$$

The parameter W_{NiO} in the equation indicates the weight fraction of the NiO phase; I_{NiO} and I_{KNbO_3} represent the strongest X-ray diffraction line intensities of NiO and $KNbO_3$ respectively. In our analysis, we considered (101) diffraction peak for $KNbO_3$, and (012) peak for NiO as highest intensity peaks for the respective phases. Using the above equation, the evaluated weight percentage (*x*) of NiO within the $KNbO_3$ matrix were determined to be *x* = 0.043, 0.12, 0.32, 0.54, and 1, well-nigh consistent with the theoretically assessed weighed fractions of 0.05, 0.10, 0.30, 0.50 and 1 respectively. Moreover, using these XRD patterns,

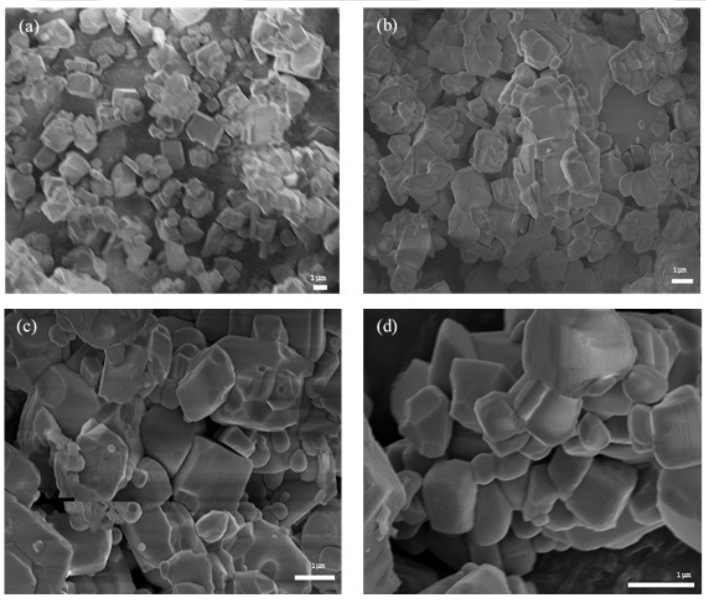

Figure 6.4. FESEM micrographs recorded in the secondary-electron mode for different compositions of (1−*x*) $KNbO_3$ + *x* NiO (*a*) *x* = 0.1 (*b*) *x* = 0.2 (*c*) *x* = 0.3 (*d*) *x* = 0.5, bulk grain size pellets.

we calculated the unit-cell density for different concentrations of NiO ($0 \leq x \leq 0.50$) as shown in figure 6.3. The FESEM micrograph of (1−*x*) $KNbO_3$ + *x* NiO (*x* = 0.1, 0.2, 0.3, and 0.5) recorded under secondary electron mode are shown in figure 6.4. From the figure, we observed polygonal grains with average sizes 1.42, 1.04, 0.66 and 0.41μm, respectively.

6.3.2 High Temperature Dielectric Studies:

Figure 6.5 shows the temperature dependence of relative dielectric permittivity $\varepsilon_r(T)$ of (1–*x*) $KNbO_3$ + *x* NiO ($0.1 \leq x \leq 0.3$) composites measured under various ac-frequencies (*f*) between 500Hz and 20MHz. All these samples show huge ε_r values ($\sim$ 1500 at *f* = 2kHz), and exhibit a major peak in ε_r between 415℃ and 455℃ with a hump across 220℃. In particular, for *x* = 0.1 the maximum in ε_r occurs across the critical temperature $T^* \sim$ 445℃ associated with the ferroelectric Curie temperature (T_C) accompanied by a structural phase transition from tetragonal to cubic phase (figure 6.5(*a*)) [131,278,279]. The second broad hump across $T_1 \sim$ 220℃ is associated with another crystallographic phase transition (orthorhombic to tetragonal) of $KNbO_3$ [131,278]. In the present case for *x* = 0.1, T^* is shifted by 10℃ towards high temperature (as compared to bulk single crystal $KNbO_3$, Curie temperature $T_C(\infty)$ ~ 435℃, at high frequencies) [131,278,279]. We believe the shifting of T^* towards higher temperature is due to the deviation of stoichiometry in the polycrystalline $KNbO_3$ brought about by the addition of NiO. Recently, Marcos *et al.*, reported that substitution of Sb^{5+} ion (by an amount 8wt%) at the B-site of the 0.96 $[(K_{0.48}Na_{0.52})_{0.95}Li_{0.05}Nb_{1-x}Sb_xO_3]$ − 0.04$[BaZrO_3]$ composites reduced the Curie temperature by 80℃. These authors reported that the co-existence of rhombohedral and tetragonal phase at (T_C) gives rise to increase in the dielectric constant [280]. The inset (*i*) of figure 6.5(*a*) shows the temperature dependence of loss-tangent ($Tan\delta(T)$) for *x* = 0.1 measured at different values of f between 500Hz and 20MHz. Our system exhibits very low dielectric loss of $\sim$ 0.051 in the vicinity of room temperature for *f* = 2kHz, as compared to $tan\delta \sim$ 0.3 for standard single crystal $KNbO_3$ [281]. However, as the temperature increases the dielectric loss increases and attains a local maximum across T_1 and T^*. Fukuda *et al.* reported $\varepsilon_r \sim$ 1200 for orthorhombic $KNbO_3$ single domain crystal along the principle axes at room temperature. They observed prominent and sharp changes in the $\varepsilon_r(T)$ with a thermal hysteresis width of ΔT = 22℃ across the transition T_1 on the heating and cooling cycle measurements of $\varepsilon_r(T)$ [281]. But these temperature dependent measurements are confined only up to 300℃, and a detailed ac-conductivity study with respect to frequency and temperature is lacking. Thus, there is insufficient information about the transition across $T^* \sim$ 445℃ at which the system undergoes a tetragonal-to-cubic structural phase transition [131,278]. The phase transition temperatures T_1 and T^* are not only predisposed to the stoichiometry of the crystal, but also subject to the external pressure and electric field [282].

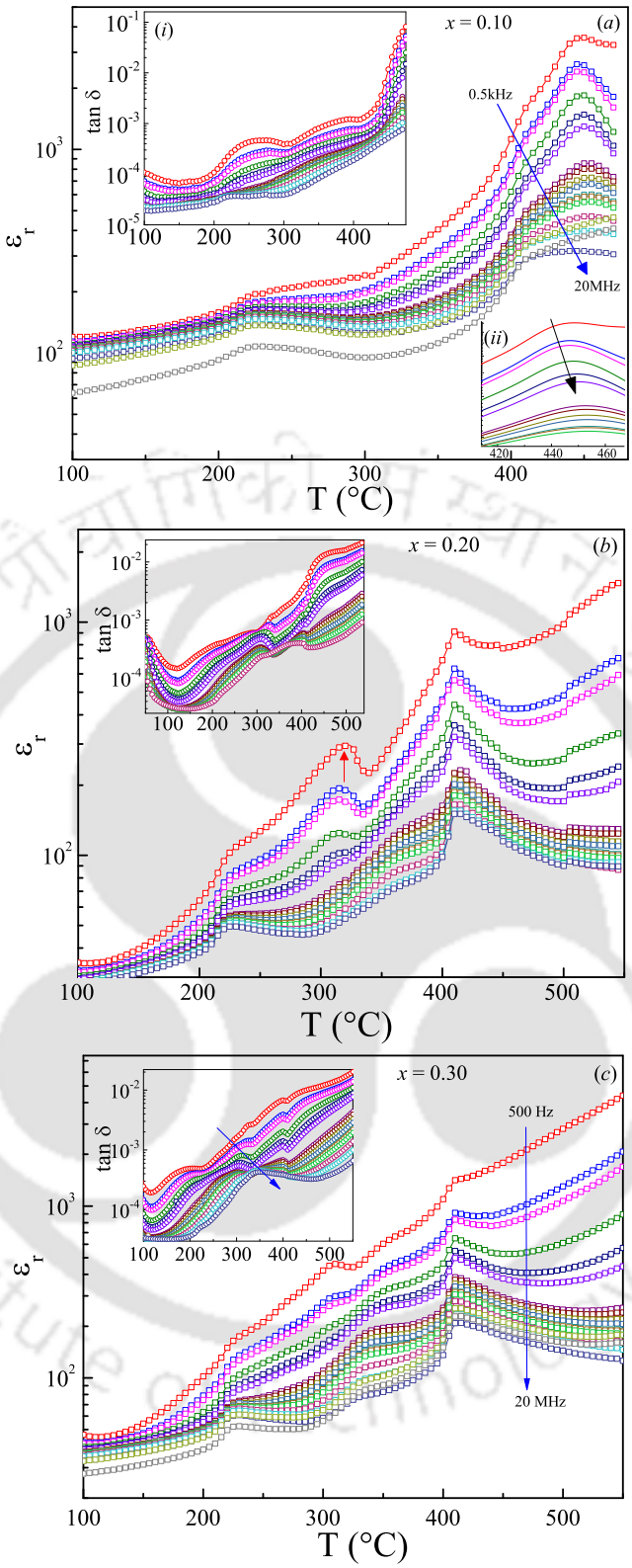

Figure 6.5. Temperature variation of the relative dielectric permittivity $\varepsilon_r(T)$ of the two-phase composites (1−*x*) $KNbO_3$ + *x* NiO for (a) *x* = 0.10, (b) *x* = 0.20 and (c) *x* = 0.30, measured at various frequencies ranging from 500Hz to 20MHz. The insets show the temperature dependence of the dissipation factor $Tan\delta$ for the respective compositions recorded at various frequencies (500Hz ≤ *f* ≤ 20MHz). The inset (*ii*) of figure 6.5(*a*) shows the zoomed view of dielectric anomaly at critical temperature T clearly depicting the frequency dispersion behavior.

Liang *et al.* employed the Landau–Ginzburg–Devonshire theory to probe the ferroelectric phase transitions, and performed a systematic study on the effect of hydrostatic pressure and external electric field on the phase transition temperature of single domain $KNbO_3$ [282]. Pressure dependent studies revealed a significant shift in the transitions towards lower temperatures with increasing pressure: orthorhombic to tetragonal phase transition shifts from 277°C (2GPa) to −17°C (10GPa), and tetragonal to cubic phase transition shifts from 422°C (2GPa) to 127°C (10GPa) [282]. In the present case, we observed a significant shift of T^* towards higher temperature (445°C – 455°C, for x = 0.1) with increasing frequency. Such diffusive nature of the dielectric peak maximum is commonly characterized as relaxor ferroelectric behaviour (inset (*ii*) of figure 6.5(*a*)). It is well known that the ferroelectric behaviour in $KNbO_3$ originates from the displacement of the Nb^{5+} cations away from a centro-symmetric position within the NbO_6 octahedron, and that the distortion is driven by the hybridization of the empty *d*-orbitals of the transition metals (TM) with the p-orbitals of Oxygen ions [283]. In the present case, incorporation of Ni inside the $KNbO_3$ lead to a compositional disordering, which often leads in turn to the formation of polar- nanoregions due to the difference in the ionic radius (r) of the substituent Ni^{2+} (r_{Ni} = 0.69Å) as compared to Nb^{5+} (r_{Nb} = 0.64Å). Formation of such polar-nanoregions and compositional heterogeneity disturbs the long-range ferroelectric ordering and likely generates a diffusive phase transition such as that observed in the present system [283,121]. Similar frequency dispersion in $\varepsilon_r(T^*)$ was noticed for the compositions x = 0.20 and 0.30, as shown in figures 6.5(*b*) and (*c*), and the corresponding $tan\delta$ is shown in the insets. To oversee the composition dependent relaxor behaviour in this system, we performed precise frequency dependent measurements (100Hz ≤ f ≤ 20MHz) of a higher composition sample x = 0.90 with very closely spaced temperature intervals (ΔT = 2°C); the $\varepsilon_r(T)$ data is presented in figure 6.6. A clear shift of the peak position T^* towards higher temperatures is evident from this figure. In order to confirm the presence of relaxor

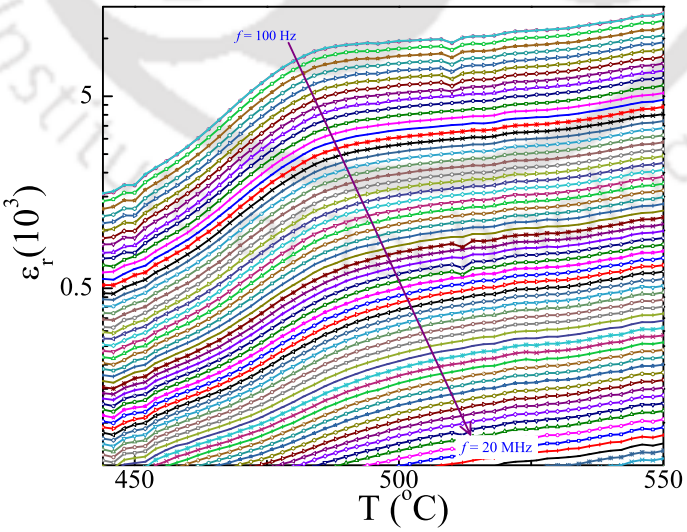

Figure 6.6. Temperature dependent relative dielectric permittivity $\varepsilon_r(T)$ measured at various frequencies (100Hz ≤ f ≤ 20MHz) for $0.10KNbO_3$ + 0.90NiO with very closely spaced temperature intervals (ΔT = 2°C) and temperature ranging from 440°C to 550°C.

behaviour theoretically, we analysed the frequency dependence of the T^* (second dielectric maximum $\varepsilon_r(T_C = T^*)$) using the Vogel–Fulcher law given by the following relation [121,284–286]:

$$f = f_0\left(-\frac{E_A}{k_B(T^*-T_g)}\right) \qquad (6.2)$$

where E_A is the activation energy, T^* is the critical temperature, T_g is the freezing temperature of the polarized domains, k_B is the Boltzmann constant and f_0 is the attempt frequency. The temperature dependent dynamic behaviour of dipole- reorientation in most mixed ferroelectric-glass phases, in which the short-range and long-range polar orders coexist, obey Vogel–Fulcher law and this law is widely used to characterize the relaxor ferroelectrics as well as spin-glasses/ super-paramagnets in magnetic systems [121,284,287].

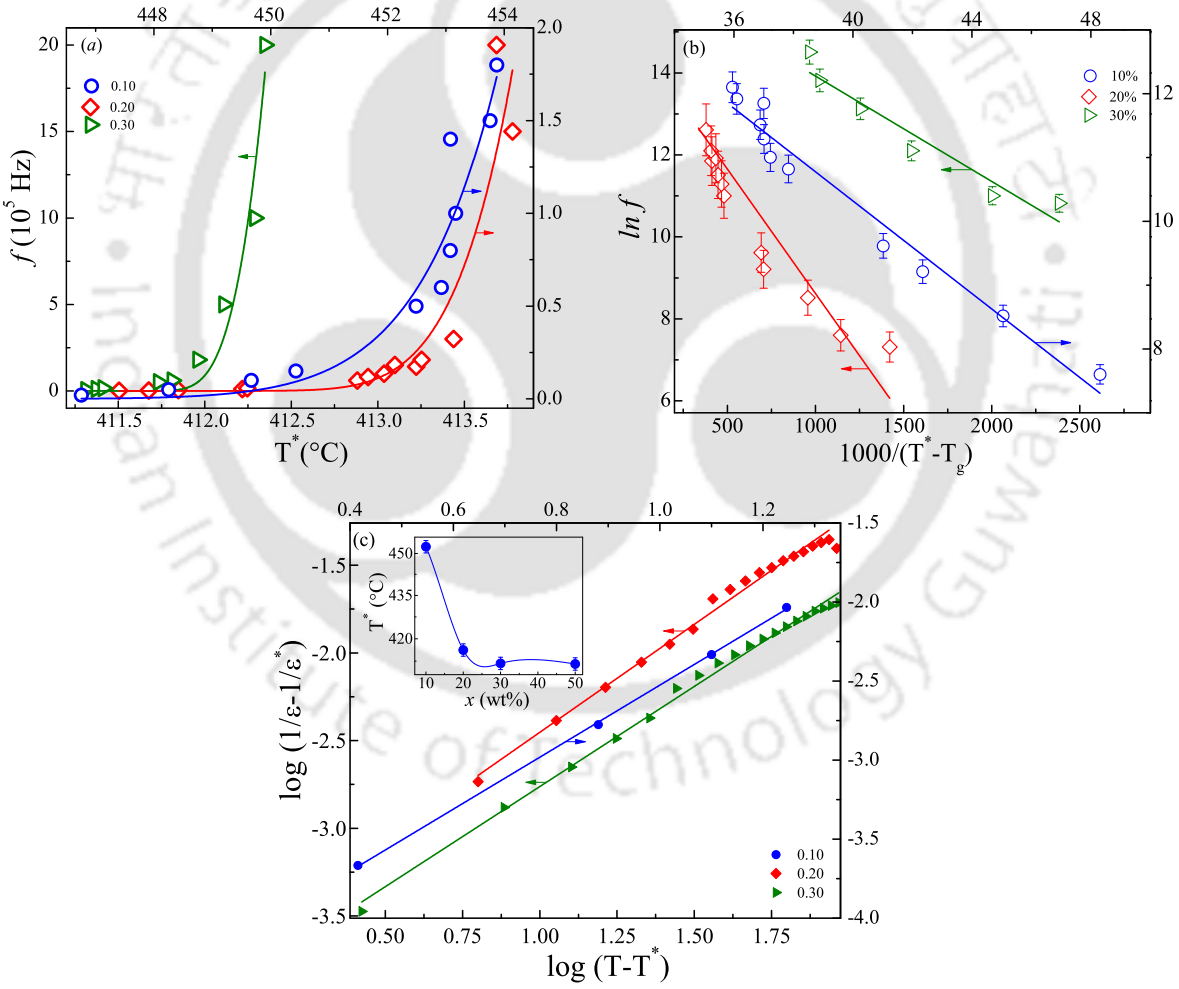

Figure 6.7. (*a*) The frequency variation of transition temperature T^* (shown by hollow symbols) and the corresponding solid continuous lines are the best fits to the Vogel–Fulcher law (*b*) The linear dependence of lnf on $1000/(T^* - T_g)$, and (*c*) Logarithmic variations of the difference in the reciprocal values of the relative dielectric permittivity, $log(1/\varepsilon - 1/\varepsilon^*)$as a function of $log\ (T - T^*)$ for *x* = 0.10 (blue), 0.20 (green), and 0.30 (red). The inset of figure 6.7(*c*) shows the variation of critical temperature T^* as a function of *x*.

The scattered hollow symbols shown in figure 6.7(*a*) represent the T^* values for different magnitudes of f which are obtained from the above discussed experimental data for the three different compositions *x* = 0.10, 0.20 and 0.30. The solid continuous lines are the best fits to the equation 6.2 which is in good agreement with the experimental data. This fitting analysis yields the following parameters, f_0 = 1.03×10^{14}Hz, 1.66×10^{10}Hz, and 7.28×10^{8}Hz; T_g = 426°C, 410°C and 411°C; and E_A = 48meV, 2meV and 0.5meV for *x* = 0.10, 0.20 and 0.30, respectively. The linear variation of lnf versus $1000/(T^* - T_g)$, as shown in figure 6.7(*b*), further confirms the validity of the Vogel–Fulcher relation for (1−*x*) $KNbO_3$ + *x* NiO composites (0.1 ≤ *x* ≤ 0.3). The attempt frequencies (f_0) obtained in the present case are in accordance with those observed for standard relaxor-ferroelectrics, which lie between 10^{9}Hz and 10^{14}Hz. However, as the NiO concentration increases, the value of attempt frequency decreases from 10^{14}Hz to 10^{8}Hz, signifying a deviation from ideal relaxor behaviour in which strong correlated antiferromagnetic clusters dominate the overall dielectric properties, leading to weakly coupled relaxor ferroelectric behaviour [131,288–290]. Recently, Luisman *et al.* observed such weakly coupled relaxor behaviour in Bi and Yb doped $KNbO_3$ ceramics caused by the local lattice strain induced by the larger Yb^{3+} combined with the presence of Bi^{3+}, which finally leads to the formation of polar nanoregions [283]. However, the temperature dependence of X-ray diffraction measurements reported in [286] did not point to any change in the crystal symmetry, and the system remained cubic over the complete temperature region from 30°C to 480°C [283]. The frequency dependence of dielectric permittivity follows Arrhenius law yielding the attempt jump frequency of ~ 10^{16}Hz, which is much larger than the Debye frequency (~ 10^{13}Hz), signifying the presence of weakly coupled relaxor behaviour in these systems [283].

Besides the Vogel–Fulcher law, we also employed the empirical scaling relation based on the Uchino–Nomura criterion (equation 6.3) to confirm the relaxor-like ferroelectric characteristics [121,291,292].

$$\frac{1}{\varepsilon} - \frac{1}{\varepsilon^*} = \frac{(T-T^*)^\gamma}{C} \qquad (6.3)$$

where C is the Curie constant, γ is a diffuseness coefficient and ε^* represents the maximum dielectric constant at T^*. For typical ferroelectrics, γ values should be close to unity. However, for relaxor systems the γ value should range between 1 and 2 [121,291,292]. The logarithmic variation of $(1/\varepsilon - 1/\varepsilon^*)$ versus $log\ (T - T^*)$ shown in figure 6.7(c), follows a linear behaviour. From the slope of these straight lines we obtained the γ (= 1.96 for *x* = 0.10), which is very close to 2, signifying an ideal relaxor. As the composition increases, γ values decrease to 1.23 (for *x* = 0.20) and 1.14 (for *x* = 0.30), indicating departure from relaxor like behaviour. These results are consistent with the Vogel–Fulcher analysis discussed above, in which the attempt frequency decreases with increasing *x*. The inset of figure 6.7(c) shows the composition dependence of T^* showing a monotonic decrease of these two ordering temperatures with increasing NiO (Mott insulator) concentration in the system. Usually, for $T > T^*$ (= T_C) the dielectric susceptibility of all ferroelectric systems follows the *Curie–Weiss law* $(1/\varepsilon_r = (T - T^*)/C)$, where C is the Curie constant [121,285,293,294].

However, the disruption of long-range ferroelectric ordering leads to a deviation from the standard Curie–Weiss behaviour, and the temperature below which the system deviates from the Curie–Weiss law is called *Burns temperature* (T_d). T_d is the temperature at which the formation of localized polar-clusters occurs [295,296]. Such deviation from the Curie–Weiss law is treated as a direct signature of the relaxor ferroelectric behaviour [295,296]. The difference between Burns temperature and Curie temperature, $\Delta T_d = T_d - T_C$ is often treated as a characteristic parameter which represents the degree of deviation from high-temperature linearity. In the present case ΔT_d = 29.28°C, 92.01°C and 80.91°C for *x* = 0.10, 0.20 and 0.30 respectively. Moreover, the high-temperature slope of inverse dielectric permittivity ($1/\varepsilon_r$) versus temperature (T) is described by an empirical Lorentz-type relation (given below) where the degree of diffuseness of peak is quantified by δ-often known as the shape parameter [296]:

$$\frac{\varepsilon_A}{\varepsilon_r} - 1 = \frac{(T-T_A)^2}{2\delta^2} \qquad (6.4)$$

Fitting the experimental data with the above equation gives the magnitude of δ, T_A, and ε_A across the saddle point (Lorentz cusp). The calculated values of δ from the fitting analysis lie in the range 24°C–123.86°C for compositions *x* = 0.10 – 0.30. It is interesting to note that a new anomaly across T_2 = 320°C was noticed (indicated by arrow mark in figures 6.5(*b*) and (*c*)) between T^* and T_1 for higher NiO concentration (*x* = 0.20 and 0.30) of NiO. This new transition may be associated with the antiferromagnetic ordering of NiO. It is well known that bulk grain sized NiO undergoes antiferromagnetic to paramagnetic transition at Néel temperature T_N (253°C), and that this magnetic ordering is accompanied by the crystal structure change from rhombohedral phase (low temperatures) to cubic (at high-temperatures) [121,140,293,297]. Usually, such change in the magnetic order in undoped NiO occurs across 250 ± 6°C; however, in the present composites a vast shift of T_2 (~ 70°C) towards higher temperature is noticed, due to the inter-diffusion of the alkali metals inside NiO grains, which can alter its magnetic ordering substantially. Although a diffusive behaviour of this peak ($\varepsilon_r(T_2)$) is observed with increasing frequency, from 315°C (1.5kHz) to 320°C (20MHz) for *x* = 0.2; from 315°C (1.5kHz) to 334°C (20MHz) for *x* = 0.3, the dispersion however was not found to follow either the Vogel – Fulcher law or the Uchino – Nomura criterion.

6.3.3 Frequency and temperature dependent ac-resistivity:

In order to understand the frequency (500Hz ≤ f ≤ 10MHz) and temperature (100°C ≤ T ≤ 500°C) dependence of the charge transport mechanism in the present composite system, we investigated the ac-resistivity $\rho_{ac}(T)$ through measurements performed by applying a 100mV peak-to-peak driving electric field (E_{ac}) of varying frequency. Figure 6.8(*a*) depicts $\rho_{ac}(T)$ for different values of 'f' for *x* = 0.10, wherein we noticed two anomalies across T_1 and T^* associated with the morphotrophic phase boundaries of $KNbO_3$. Figure 6.8(*b*) shows the variation of $ln(\rho_{ac})$ with respect to $T^{-1/4}$ for various compositions at f = 2kHz, which follows a linear behaviour giving signatures of Mott-variable range hopping (VRH) process: $\rho = \rho_0 \, exp\left(\frac{T_0}{T}\right)^{1/4}$ [121,298]; here ρ_0 (pre-exponent factor) and T_0 (characteristic temperature coefficient) for

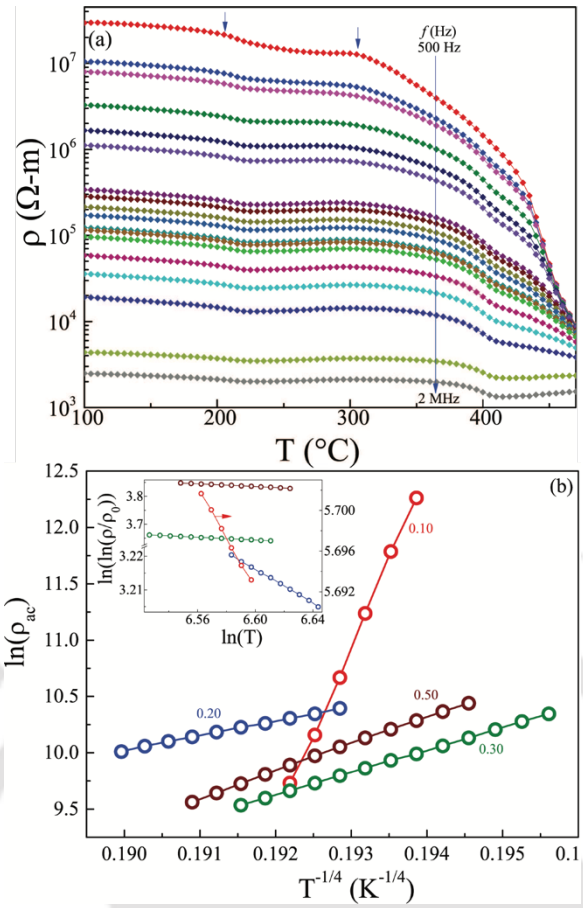

Figure 6.8. (*a*) Temperature variation of ac-resistivity $\rho_{ac}(T)$ for *x* = 0.10 recorded at various frequencies (500Hz ≤ f ≤ 2MHz). (b) Logarithmic dependence of ac-resistivity, i.e. $ln(\rho_{ac})$ versus $T^{-1/4}$; inset shows the double logarithmic variation of $[\rho/\rho_0]$ versus $ln(T)$ for *x* = 0.10, 0.20, 0.30, and 0.50.

different compositions were extracted from the intercepts and slopes (figure 6.8(*b*)). Depending upon the nature of the hopping process, the power of the exponential factor varies; in particular, for variable range hopping, the exponential value should be approximately -0.25 [121,298]. In order to confirm the hopping mechanism, we plotted the double logarithm of $[\rho/\rho_0]$ against $ln(T)$ as shown in the inset of figure 6.8(*b*). Consequently, we obtained the slope values −0.25 for all the compositions, which confirms the variable range hopping process of charge carriers in the (1−*x*) $KNbO_3$ + *x* NiO (0.10 ≤ *x* ≤ 0.50) systems.

Moreover, using the VRH model we evaluated the most probable hopping distance R_H (also known as characteristic hopping length) and hopping energy W_H between the localized sites, which depend upon the parameters ρ_0 and T_0, which are obtained from the slopes and intercepts of figure 6.8(*b*) [121,298-301]. The average hopping length R_H and hopping energy W_H are given by the following expressions [121,256,298-301]:

$$R_H = \left(\frac{3}{2\pi\alpha N(\epsilon_F)k_B T}\right)^{1/4} \quad (6.5)$$

$$W_H = \left(\frac{3}{4\pi N(\epsilon_F)R^3}\right) \quad (6.6)$$

In the above equations $N(\epsilon_F)$ is the density of states of the charge carriers across the Fermi level, α is the measure of the extent of localized wave function $exp(-\alpha R)$, and k_B is the Boltzmann constant [186,256]. According to Mott's VRH theory for the ensemble of localized states randomly distributed in space and energy, the characteristic temperature T_0 depends on the density of states of the charge carriers across the Fermi level, given by the relation:

$$N(\epsilon_F) = \left(\frac{16\alpha^3}{k_B T_0}\right) \qquad (6.7)$$

Substituting the value of decay length α ~ 10^7 cm^{-1} and density of states $N(\epsilon_F)$ (calculated from the above relation) to the equations 6.5 and 6.6, we obtained R_H and W_H values which are listed in table 6.2. For *x* = 0.10 and 0.50 the hopping length decreases from 4.19nm to an absurdly small value, suggesting a probable deviation of the variable range hopping mechanism for higher *x* values. With increasing composition, the average hopping length R_H and hopping energy W_H decrease significantly indicating the formation of additional localized states due to incorporation of NiO into the $KNbO_3$ system.

Composition 'x'	$N(\epsilon_F)$ (eV^{-1} cm^{-3})	R_H (nm)	W_H (eV)
0.10	4.490×10^{18}	4.192	0.722
0.20	8.038×10^{21}	0.644	0.112
0.30	1.559×10^{30}	0.0054	0.0009
0.50	1.122×10^{29}	0.0105	0.0018

Table 6.2. The calculated Mott parameters of (1-*x*) $KNbO_3$+ *x* NiO two-phase composite.

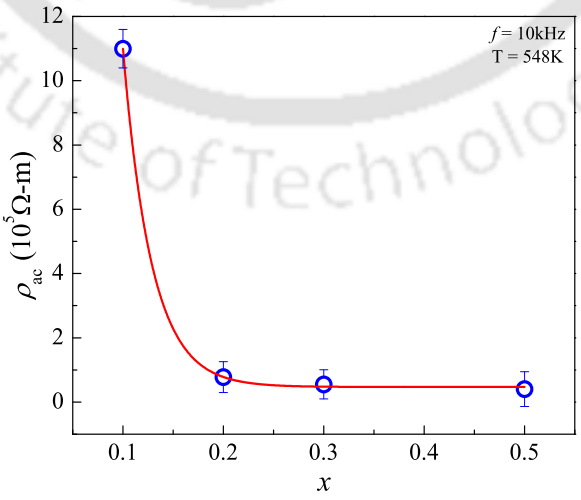

Figure 6.9. The variation of ac-resistivity ρ_{ac} as a function of NiO concentration (*x*) measured at constant *f* = 10kHz and T = 275°C.

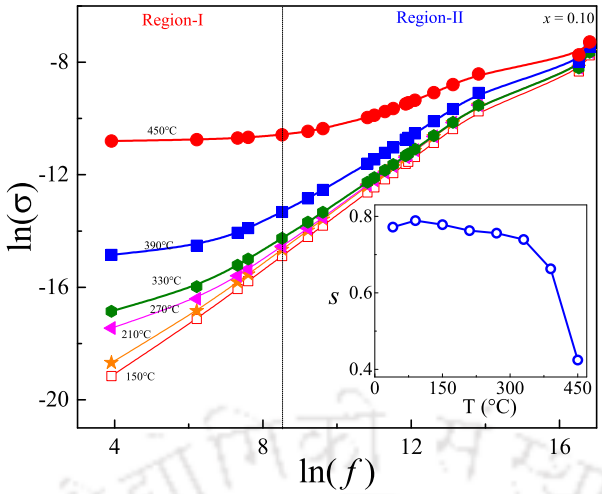

Figure 6.10. Log–log plot of ac-conductivity (σ_{ac}) versus frequency (*f*) measured at different temperatures for *x* = 0.10. The inset shows the temperature dependence of frequency exponent '*s*' calculated from the Jonscher's power law relation.

Nevertheless, there are few reports dealing with the dependence of hopping conductivity on the disordered systems in which the charge is transported via phonon-induced tunnelling of electrons between localized states randomly distributed in energy and position [302]. Dinno and Schwartz [303] reported that the ac-electrical conductivity increases progressively with increasing grain size of tellurium thin- films (2D). These authors also reported that the electron mobility depends on the number of defects generated by quenching and annealing processes. For the present system (3D-bulk) we are able to plot the composition dependence of ρ_{ac} at a specific frequency and temperature (f ~ 10kHz, 275°C) (figure 6.9). This analysis yields the following relation between the resistivity and the composition: $\rho = \rho_0 + Aexp(-x/B)$, where A and B are constants. From this relation, we can understand that as we increase the composition, the grain size and the resistivity decrease simultaneously. Consequently, the conductivity increases, which causes the increase of carrier concentration and the mobility of the charge carriers. As a result, the hopping process enhances as additional localized states are created near the Fermi level.

Figure 6.10 shows the frequency response of conductivity $\sigma_{ac}(f)$ measured at different temperatures for all the compositions of the system. Usually, the relationship between σ_{ac} and angular frequency ω is characterized by the well-known Jonscher's power law relation [301,304–306]:

$$\sigma_{ac} = \sigma_{dc} + A\omega^s \ (0 < s < 2) \qquad (6.8)$$

where A is the temperature dependent constant, ω is the angular frequency, and s is an exponent factor which depends on both f and T. From the logarithmic variation of σ_{ac} with respect to *f* ($ln\sigma_{ac}$ versus $ln(f)$ for *x* = 0.10 we observed a frequency independent plateau region in the low-frequency range (50Hz – 5kHz), as shown by the vertical dotted line in figure 6.10 (region-1). The σ_{ac} values in this regime are mainly attributed to the dc-contribution σ_{dc}.

Temperature (°C)	's'			
	x = 0.10	*x* = 0.20	*x* = 0.30	*x* = 0.50
90	0.789	1.047	1.087	1.160
150	0.778	1.043	1.058	0.910
210	0.762	1.330	1.332	1.281
270	0.756	1.208	1.332	1.013
330	0.739	0.838	0.723	0.773
390	0.662	0.849	0.883	0.943
450	0.424	1.080	1.030	1.047

Table 6.3. The temperature dependence of *s* evaluated using equation 6.8 for different NiO compositions.

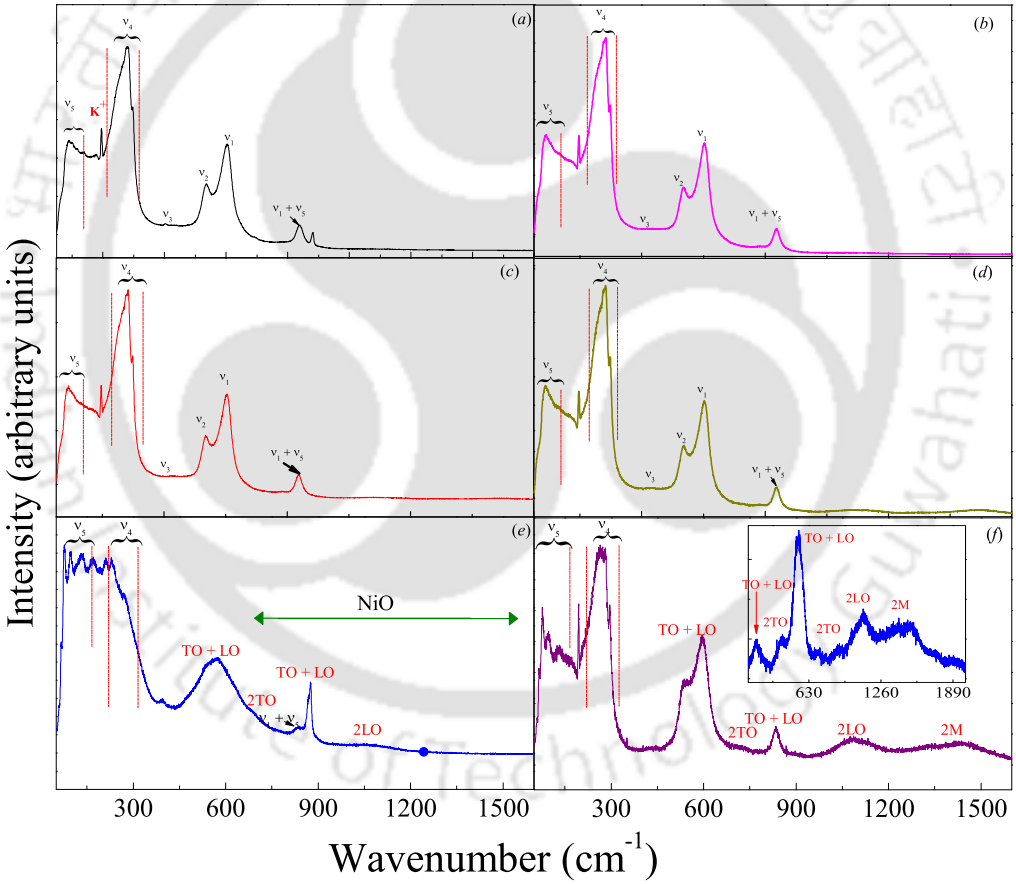

Figure 6.11. Raman spectra of (1 − *x*) $KNbO_3$ + *x* NiO two-phase composites recorded at room temperature for the compositions (*a*) *x* = 0.05, (*b*) *x* = 0.20, (*c*) *x* = 0.30, (*d*) *x* = 0.50, (*e*) *x* = 0.80 and (*f*) *x* = 0.95.

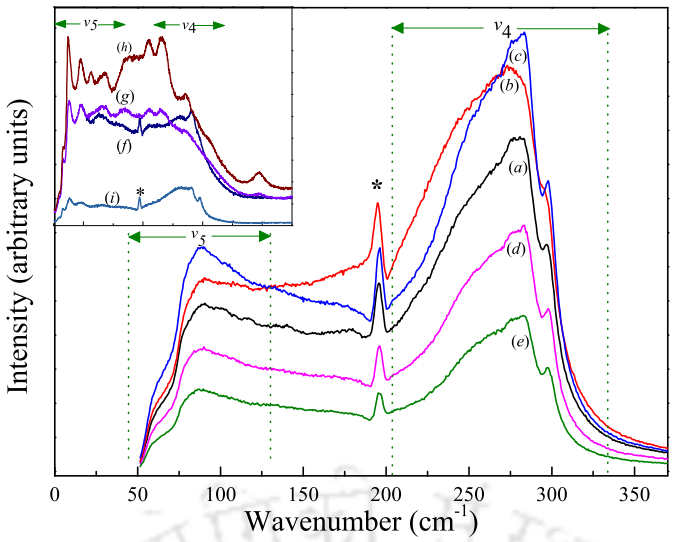

Figure 6.12. Raman spectra shown in the wavenumber range 50–400cm^{-1} for various compositions: (*a*) x = 0.05, (*b*) x = 0.10, (*c*) x = 0.20, (*d*) x = 0.30, and (*e*) x = 0.50. The inset depicts spectra for higher compositions ($0.70 \le x \le 0.95$) between 50cm^{-1} and 400cm^{-1}.

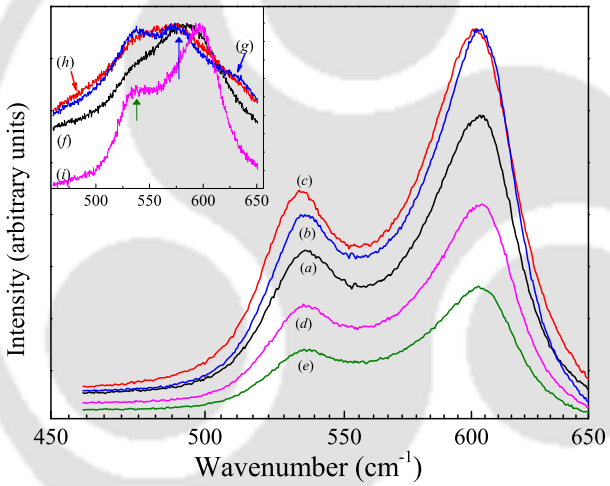

Figure 6.13. Raman spectra of (1–x) $KNbO_3$ + x NiO system for different compositions: (*a*) x = 0.05, (*b*) x = 0.10, (*c*) x = 0.20, (*d*) x = 0.30, and (*e*) x = 0.50 (between the wavenumbers 450cm^{-1} and 650cm^{-1}). The inset depicts spectra for higher compositions ($0.7 \le x \le 0.95$) between 450cm^{-1} and 650cm^{-1}.

However, at higher frequencies (> 5kHz, region-2) the conductivity increases linearly, and follows a frequency variation defined by the second term in equation 6.8 (i.e. $A\omega^s$). In order to estimate the values of A and *s*, the high frequency linear region (region-2) of figure 6.10 is fitted to the equation 6.8. From the intercepts and slopes of this linear fit, values of parameters A and *s* are obtained; the s values are listed in table 6.3. Normally, perovskites and other semiconducting transition metal oxides (such as $BaTiO_3$, $PbTiO_3$, $MgMnO_3$, MnO_2) follow either quantum-mechanical tunnelling (QMT) model or the correlated barrier hopping (CBH) model [299,301,304-308]. According to the QMT model, the charge transport process is mainly dominated by tunnelling of the charge carriers driven by thermal energy. This model predicts the linear dependence of

conductivity on temperature, and that the behaviour of s is independent of temperature, mathematically given by [305]:

$$s = 1 + \frac{4}{ln(\omega\tau_0)} \quad (6.9)$$

where τ_0 is the characteristic relaxation time for the charge carriers. However, for the present scenario the value of s is temperature dependent and decreases from 0.78 to 0.42 as the temperature varies from 90°C to 420°C. Such temperature dependence of s, as shown in the inset of figure 6.10, is not in agreement with the QMT model where phonon-assisted tunnelling of charge carriers take place. CBH model differs in a way that it describes the charge carriers hopping over the potential barrier rather than taking tunnelling into account. This model describes the temperature dependence of s by the following relation [305]:

$$s = 1 - \frac{6k_BT}{W_{OBG}} \quad (6.10)$$

where, W_{OBG} is the optical band gap. In the present system temperature dependence of s follows equation 6.10 where the value of s decreases with increasing temperature and hence the charge carriers transport is mainly dominated by the hopping process instead of tunnelling of charge carriers through the barrier [305]. Usually, the localized charge carriers (mainly generated by the defects) play a major role in the hopping conduction mechanism [283,309]. The formation of oxygen vacancies in the investigated composites leads to non-stoichiometry and an increase in the defect states, according to the following relation [283]:

$$K_K \rightarrow K + V_K' + h \quad (6.11)$$

$$O_o \rightarrow \frac{1}{2}(O_2) + V_{O}'' + 2e' \quad (6.12)$$

where V_K' is a potassium vacancy with a negative charge and V_{O}'' is an oxygen vacancy with two positive charges. The released electrons in the above reaction may be captured by Nb^{+5}, converting it to Nb^{+3}, since Nb is multivalent with oxidation states +3 and +5. At low frequencies, high conductivity may arise due to short range translational hopping of electrons among Nb^{+5} and Nb^{+3}. At high frequencies, the conductivity arises due to localized hopping of charge carriers among Nb^{+5} and Nb^{+3} [309].

6.3.4 Raman spectroscopy:

Figure 6.11 shows the Raman spectra of various compositions of the composites (1−*x*) $KNbO_3$ + *x* NiO recorded at room temperature. It is well known that $KNbO_3$ belongs to orthorhombic phase with space group C_{2v}^{14}, (*Amm2*), with one formula group in the unit-cell. According to the group theory analysis, the spectrum should consist of 12 optical modes in the C_{2v} point group represented by $4A_1 + 4B_1 + 3B_2 + A_2$ [283,310-315]. All these modes are both Raman and IR active except the A_2 mode. On the other hand, the vibrations of the NbO_6 octahedra consist of $1A_{1g}(\nu_1) + 1E_g(\nu_2) + 2F_{1u}(\nu_3, \nu_4) + F_{2g}(\nu_5) + F_{2u}(\nu_6)$; out of these vibrations, $1A_{1g}(\nu_1) + 1E_g(\nu_2) + 1F_{1u}(\nu_3)$ are stretching modes and the rest are bending modes [311]. For $x \geq 0.7$, the Raman modes corresponding to NiO emerge between 650cm^{-1} and 950cm^{-1}, as indicated by the arrow in figures 6.11(*e*) and (*f*). These modes are associated with transverse (TO) and longitudinal (LO) optical phonon modes of NiO [70].

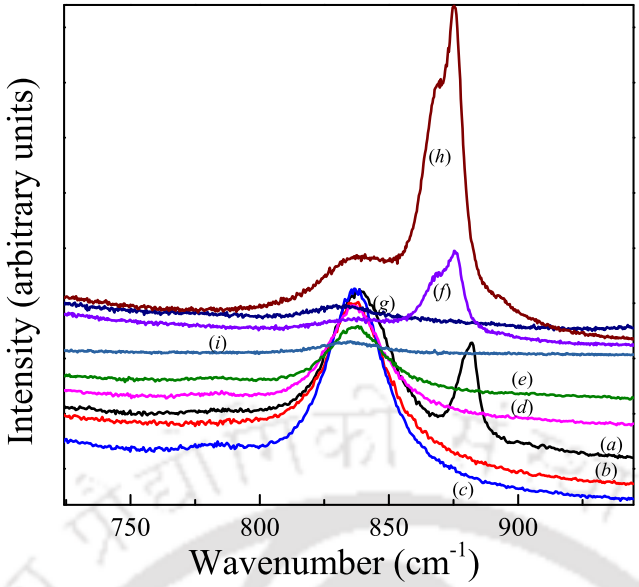

Figure 6.14. Zoomed view of the Raman spectra (from 750cm^{-1} to 950cm^{-1}) for (*a*) *x* = 0.05, (*b*) *x* = 0.10, (*c*) *x* = 0.20, (*d*) *x* = 0.30, (*e*) *x* = 0.50, (*f*) *x* = 0.70, (*g*) *x* = 0.80, (*h*) *x* = 0.90 and (*i*) *x* = 0.95 recorded at room temperature.

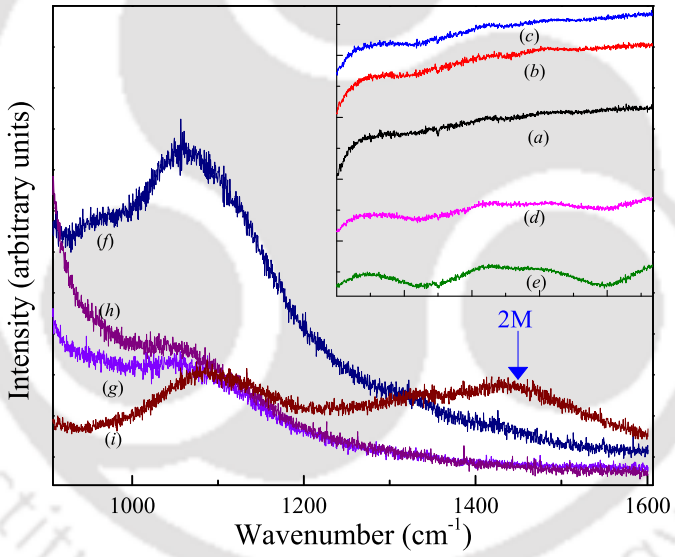

Figure 6.15. Raman spectra in the wavenumber range 950cm^{-1} to 1600cm^{-1} for high compositions: (*f*) *x* = 0.70, (*g*) *x* = 0.80, (*h*) *x* = 0.90 and (*i*) *x* = 0.95. The inset shows spectra for low compositions: (*a*) *x* = 0.05, (*b*) *x* = 0.10, (*c*) *x* = 0.20, (*d*) *x* = 0.30 and (*e*) *x* = 0.50.

At higher wavenumbers (≥ 1000cm^{-1}), the Two-Magnon modes also appear, and are prominent for *x* = 0.95. In order to understand the role of antiferromagnetic NiO clusters on the Raman spectra of $KNbO_3$, we separated the spectra into four different regions, as shown in figures 6.12 – 6.15. The main panel of the figure 6.12 shows the low frequency Raman active modes for the compositions *x* ≤ 0.5, and the inset shows the Raman spectra for *x* > 0.5. The modes appearing at wavenumbers lower than 150 cm^{-1} (ν_5) can be assigned to the combination of translational modes of monovalent potassium cations and rotational modes of NbO_6 octahedra. The modes around 195cm^{-1} (denoted by asterisk) and 296cm^{-1} arising because of the

translational modes of K^+ cations indicate the onset of long-range polar-order [283]. The Raman bands above 200 cm^{-1} (ν_4) occur mainly due to the internal vibrations of the NbO_6 octahedra [309]. For $x > 0.50$, we noticed few additional modes (inset of figure 6.11) associated with the dilute substitution of Ni^{2+} cations at the octahedral sites of the parent perovskite matrix. Similar features were also observed in $(1 - x)\ K_{0.5}Na_{0.5}NbO_3 + x\ LiNbO_3$ for compositions $x \geq 0.70$ [305]. The modes appearing at 130cm^{-1} and 160cm^{-1} are completely absent for $x < 0.7$ (figure 6.12); however, these bands are prominent for $x \geq 0.7$. Disappearance of these bands is ascribed to the waning of the tilt-angle between the adjacent NbO_6 octahedra [312]. Figure 6.13 shows the Raman spectra between wavenumber range 450cm^{-1} to 650cm^{-1} wherein we observed two main modes centred at 535cm^{-1} and 600cm^{-1} ($x < 0.7$). Both of these modes arise mainly due to the doubly degenerate O–Nb–O symmetric stretching-vibration, which is sensitive to the phase change [313]. For $x > 0.50$, the vibrational modes at ~ 530cm^{-1} can be assigned to the one-phonon (1P) transverse optical (TO) and longitudinal optical (LO) modes of NiO (inset of figure 6.13). Usually, higher defect levels and antiferromagnetic ordering ($T < T_N$) enhance the intensity of optical phonon modes [314]. Thus, the peak centred at 580cm^{-1} is likely due to the combined effect of vibrational modes of NbO_6 octahedra and optical phonon modes of NiO. In figure 6.14, the cusp centred at 835cm^{-1} for $x \leq 0.5$ is attributed to the combined effect of inter-bond angle vibration of O–Nb–O and asymmetry vibration of NbO_6 octahedra, which diminishes as x increases beyond 0.5 [123,220,314]. For $x > 0.5$, we observe a sharp peak at 875cm^{-1}, along with a hump at $\sim$ 868 cm^{-1} corresponding to the two-phonon (2P) TO + LO mode [123]. At higher wavenumbers (figure 6.15), the dominant Raman modes at $\sim$ 906 cm^{-1} and at $\sim$ 1090 cm^{-1} correspond to TO + LO and 2LO modes of NiO, respectively [123,314,315]. A wide hump around 1500cm^{-1} arises due to a Two-Magnon (2M) scattering associated with the antiferromagnetic ordering of NiO [123,314,315]. The positions of all these modes (LO + TO and 2M) are in close agreement with the Raman spectra of $NiO_{1-\delta}$ sintered at high temperature (inset of figure 6.11(*f*)). For lower compositions ($x \leq 0.20$), the phonon and Magnon-modes are absent; however, the features around 1000cm^{-1} and 1300cm^{-1} start appearing for x = 0.30 and 0.50 without any significant shift. The modes broaden and the intensity of the peak decreases due to the decrease in the grain size (increase of micro-strain) as the NiO clusters increase within the $KNbO_3$ matrix.

6.4 Summary:

In this chapter the nature of dielectric behaviour of various compositions of ferroelectric $KNbO_3$ and antiferromagnetic NiO two-phase composites were studied in detail. All these systems exhibit a clear dielectric transition across T^*(~ 445°C), along with a hump at T_1 (~ 220°C), associated with the cubic to tetragonal and tetragonal to orthorhombic structural phase transitions, respectively. The incorporation of NiO inside the $KNbO_3$ matrix results in the shifting of T^* towards higher temperatures along with the emergence of a new anomaly across 320°C associated with the antiferromagnetic ordering of NiO accompanied by the crystal structure change from rhombohedral to cubic phase. For $T > T^*$ the dielectric

permittivity cusp follows the empirical Lorentz-type relation with the shape parameter value δ varying from 24℃ to 123.86℃ for the compositions *x* = 0.10 to 0.30. The dynamic variation of the dispersion in the $\varepsilon_r(T)$ at temperatures close to T^* follows Vogel–Fulcher law which confirms the relaxor-like behaviour. However, with increasing NiO content the system deviates from strongly coupled relaxor behaviour ($f_0 \sim 1.03 \times 10^{14}$Hz, *x* = 0.10) to weak relaxor ($f_0 \sim 7.28 \times 10^{8}$Hz, *x* = 0.30). These results are consistent with the empirical scaling relation of the Uchino–Nomura criterion, where the values of diffuseness exponent *γ* decreases from 1.96 (γ = 2, for perfect relaxor) to 1.14 (γ = 1, for ideal ferroelectrics) as *x* increases from 0.10 to 0.30. From the analysis of frequency and temperature dependent ac-conductivity $\sigma_{ac}(f,T)$ we demonstrated that variable range hopping of localized charge carriers between Nb^{+5} and Nb^{+5} ions dominates the charge transport mechanism. The average distance between two successive hops R_H, and the associated hopping energy W_H, are 4.19nm and 0.722eV respectively for *x* = 0.10. The addition of NiO to $KNbO_3$ significantly improves the density and relative dielectric permittivity ε_r (∼1500 at f = 2kHz) and brings down the dielectric-loss factor $Tan\delta(T)$ to ∼ 0.051. Raman spectroscopy results reveal that the main contribution to the vibrational spectra (in low wavenumber region ≤ 150cm^{-1}) is from the combination of translational modes of K^+ cations along with the rotations of the NbO_6 octahedra of $KNbO_3$. However, at higher concentration (≥ 0.70) and higher wavenumbers (≥ 950cm^{-1}) LO + TO and Magnon Raman (2M) modes appear, which mainly correspond to antiferromagnetic NiO.

Chapter 7
Conclusions and Future Scope

7.1 Conclusions:

This chapter contains all the important findings of the present research work together with a brief summary of future scope arising from these studies. As discussed in the previous chapters, we mainly focused on the structural, dielectric and Raman spectroscopy of alkaline niobates and wide-bandgap transition-metal-oxides; the similarities and differences of their structural, spectroscopic and dielectric properties are recapitulated here. The structural and dielectric properties of all the investigated systems have shown several interesting features including the thermally driven structural phase transition leading to a dielectric anomaly that can be exploited to develop spin-valve, Magnon transistors and ferroelectric memory devices.

In Chapter 3 we have demonstrated that the Orthorhombic (*Pmna*) crystal structure of $NaNbO_3$ transforms to a lower symmetry monoclinic phase (*Pbma*) after the dilute dispersion of NiO. The X-ray photoelectron spectroscopy revealed pentavalent 'Nb', monovalent 'Na' and divalent 'Ni' states along with the signatures of non-local screening effects. The antiferroelectric to paraelectric transition (T_{AFE}) accompanied by the structural change from orthorhombic to tetragonal phase shifts by 55°C towards low-temperature side, however, the morphotropic phase boundary (T_{O-M}) shifts towards high temperatures by 28°C for nominal substitutions of NiO ($x \leq 0.10$). The generalized Lyddane-Sachs-Teller expression $\frac{\epsilon_0 - S'}{\epsilon_\infty} = \left(\frac{\omega_l}{\omega_t}\right)^2$ and thermodynamic free energy models are employed to understand the anomalous behaviour of temperature dependence of relative dielectric permittivity ($\varepsilon_r(T)$) across T_{AFE} and T_{O-M}. The frequency dependence of ac-conductivity $\sigma_{ac}(f)$ follows Jonscher's power law ($\sigma_{ac} = \sigma_0 + A\omega^s$) suggesting the phonon-assisted hopping mechanism, whereas the frequency-independent term (σ_0) was explained by Funke's Jump-Relaxation-Model. In the next chapter, we extended the study of $NaNbO_3$-NiO system for dilute compositions of NiO and made a systematic study of the dielectric hysteresis and temperature-dependent vibrational excitations. The temperature dependence of relative-dielectric permittivity, $\varepsilon_r(T)$, exhibits an anomalous change in its magnitude across three distinct phase transitions of $NaNbO_3$ at 176°C, 392°C and 478°C. These are, respectively, associated with a second-order phase transition occurring due to incommensurate phase between two orthorhombic antiferroelectric orderings, change from orthorhombic P to R-phase (T_{P-R}) without altering the antiferroelectric structure, and an orthorhombic R to S-phase transition accompanied by a change from antiferroelectric to paraelectric transition. A large thermal hysteresis ($\Delta T_{hys} \sim$ 38°C) was evident in ε_r and ac-resistivity (ρ_{ac}) between the temperatures 200°C and 400°C signifying the first-order nature of the T_{P-R} transition. At room temperature, for higher NiO content,

a new mode centered at 838cm^{-1} was observed in Raman spectra along with the Two-Magnon mode at 1496cm^{-1}, a broad longitudinal optical mode (2LO) at 1096cm^{-1}, and a weak translational optical mode (2TO) at 726cm^{-1}. At low temperatures, down to 80K, several peculiar features are evident in the Raman spectra of NbO_6 octahedra which are associated with the structural and antiferromagnetic transitions of $NaNbO_3$ and NiO, respectively.

In Chapter 5 the structural, dielectric and spectroscopic properties of MnO_2 containing $NaNbO_3$ polycrystalline composites have been investigated. Our results confirmed that the undoped system exhibits orthorhombic phase of $NaNbO_3$ with space group *P21ma* which is different as compared to *Pbcm* space group of $NaNbO_3$ and *R3c* space group of ferroelectric $NaNbO_3$. Depending upon the heat treatment conditions of the composites MnO_2 decomposes and gives rise to other secondary phases. For example, samples heat-treated at 1000℃ has Mn_2O_3 as the major phase along with $NaNbO_3$, however, samples heat-treated at 1040℃ contains Hausmannite Mn_3O_4 along with Mn_2O_3. The W-H analysis reveals that few compositions having significant amount of Mn_3O_4 which exhibits non-uniform strain effects on the lattice planes within the core $NaNbO_3$ matrix. The room temperature vibrational Raman spectra show anomalous change in the location of vibrational and liberational modes of NbO_6 octahedra due to the occupation of the manganese ions at interstitial positions of Perovskite lattice. With decreasing temperature, most of the NbO_6 modes are found to shift towards the higher wavenumbers as a result of contraction of bond length, and hence resulting in an increase in force constant. The anomalous changes occurring in the Raman shift between 80K and 300K for all the compositions reveal the existence of yet another possible structural transition. In particular, the Raman modes of NbO_6 octahedra, ν_6 (109-200cm^{-1}) and ν_5 (200-310cm^{-1}) exhibit anomalies in their position (X_C) between 275K and 290K. It is interesting to note that these modes exhibit positive temperature coefficients and shows significant hysteresis in their positions (4cm^{-1} across 80K). For the compositions x = 0.04 and x = 0.10, the rotational degree of freedom of NbO_6 liberational modes are drastically affected as the temperature approaches to 300K from 80K. For x = 0.02 and x = 0.30, the ν_6 mode clearly deconvolutes into two distinct peaks with decreasing temperature. For the former, these peaks get sharper whereas, for the latter, the deconvoluted peaks soften with cooling and for x = 0.04, the ν_6 mode diminishes gradually with decreasing the temperature. For all the compositions, ν_5 and $\nu_6$modes display anomalous change in its position between 170K and 220K which is associated with the structural phase transition of $NaNbO_3$ from rhombohedral to orthorhombic structure accompanied by the ferroelectric to antiferroelectric phase transition. The high-temperature impedance spectroscopic studies ($\varepsilon_r(T)$ and $\rho_{ac}(T)$) of these composites exhibits cusps at orthorhombic-P to -R phase transition together with a new soft-anomaly across 147℃ associated with the second-order incommensurate phase. A small but distinct hump was observed in $\varepsilon_r(T)$ and $\rho_{ac}(T)$ across 462℃ for frequencies greater than 105kHz which is associated with the standard antiferroelectric to disorder PE (T_{AFE}) phase transition accompanied by a change from orthorhombic-R to S phase. Furthermore, the ρ_{ac} analysis provided substantial evidence to the

variable range hopping mechanism of charge carriers in all these samples.

In Chapter 6 we summarized the results of structural, dielectric, ac-conductivity and Raman scattering of ferroelectric $KNbO_3$ and antiferromagnetic NiO two-phase composites [(1-*x*) $KNbO_3$ + *x* NiO]. Two major transitions were observed in the temperature-dependent dielectric permittivity $\varepsilon_r(T)$; the first one across 445°C (T^*) and the second at 220°C (T_1), associated with the structural transitions from tetragonal to cubic and orthorhombic to tetragonal phase, respectively. In addition, a new anomaly across $T_2 \sim 320$°C has been observed in $\varepsilon_r(T)$ and the loss-tangent ($Tan\delta$), which may be associated with the combined effect of antiferromagnetic ordering of NiO and ferroelectric coupling of $KNbO_3$. The dispersive nature of T^* and its Vogel–Fulcher's temperature dependence of the characteristic relaxation frequency reveals the existence of relaxor-like behaviour which is further supported by Uchino-Nomura criteria (for $x \leq 0.10$) but departs from relaxor behaviour for $x > 0.10$. The temperature-dependent ac-resistivity analysis $\rho_{ac}(T)$ provides strong evidence for Mott's variable-range-hopping process of charge carriers between the localized states with average hopping length of 4.2nm and hopping energy 0.72eV. The variation of T^*, T_1 and T_2 as a function of *x* has been discussed in consonance with the crystal structure. Raman spectroscopic studies were carried out to study the local structure of the (1-*x*) $KNbO_3$ + *x* NiO two-phase composites, which shows a significant increase of tilt-angle between the adjacent NbO_6 octahedra as the divalent Ni occupies octahedral sites of the $KNbO_3$ matrix. All the Raman-active modes of these composites are indexed as lattice translations, specifically, the motion of K^+ (190cm^{-1}), the core vibrations of the NbO_6 octahedra (220cm^{-1} ≤ ν ≤ 320cm^{-1}) and their collective modes (50cm^{-1} ≤ ν ≤ 150cm^{-1}), and Magnon modes (2M ~ 1500cm^{-1}) associated with the antiferromagnetic ordering of NiO.

7.2 Future Scope of work

The results obtained in the present study come out from a systematic study and thorough investigation into their response towards changing external parameters like electric and magnetic field and temperature. However, this is not the end of road for this area of research. Here, we proposed some future work as follows:

1. Since we explored dominantly only the dielectric properties, that wide opens the doors for exploring the magnetic properties and how the magnetic properties can change with altering the electric field and vice-versa.
2. We have only used one mode of sample preparation technique i.e. the solid-state reaction technique followed by high-temperature sintering with no parameters controlling the environment. Earlier reports also suggest that phase formation also occurs in much lower calcination temperatures with much more cheaper precursors. Hence we have scope of exploring what changes in the properties are possible by improving on the preparation and sintering techniques.
3. In the present study, we have not explored one variable parameter i.e. pressure. Pressure-

dependent studies are available on the parent system in earlier literatures. Hence, we can also take into account for future work.

4. In the current study, we have explored only two of the d-block elements in their oxide form i.e. MnO_2 and NiO. Copper, strontium are also other potential transition metal-oxides that can be used.
5. All the studies involved here are either on $NaNbO_3$ or $KNbO_3$. However, there also scope for the multi-perovskite composite like $NaNbO_3$-$KNbO_3$ and can be explored for enhanced properties.

Bibliography

[1] A.J. Dekker, "Solid State Physics", *Macmillan* (2014).
[2] D. Richerson, "Modern Ceramic Engineering: Properties, Processing and Use in Design. 2nd ed.", *Marcel Dekker* (1992).
[3] C. Zhao, C.Z. Zhao, M. Werner, S. Taylor and P. Chalker, *Nanoscale Res. Lett.*, **8**, 456 (2013)
[4] K.S. Cole and R.H. Cole, *J. Chem. Phys*., **9**, 341 (1941).
[5] D.W. Davidson and R.H. Cole, *J. Chem. Phys*., **19**, 99 (1951).
[6] S. Havriliak and S. Negami, *J. of Polym. Sci: C*, **14**, 99 (1966).
[7] J.C. Maxwell, "A Treatise on Electricity and Magnetism", *Clarendon Press Series* (1954).
[8] M. Iwamoto, *Encyclopedia of Nanotechnology*, 1 (2014).
[9] T. Hao, "Dielectric properties of non-aqueous heterogeneous systems", *Studies in Interface Science*, **22**, 341 (2005).
[10] J. Robertson, *Comprehensive semiconductor Science and Technology*, **4**, 132 (2011).
[11] R.H. Lyddane, R.G. Sachs and E. Teller, *Phys. Rev.*, **59**, 673 (1941),
[12] M. Shur, "Physics of Semiconductor Devices", *Prentice-Hall* (1990).
[13] C. Kittel, "Introduction to Solid State Physics – 8th edn." *Wiley and Sons* (2005).
[14] M. Schubert, *arXiv:1602.08785* (2016).
[15] D. W. Berreman and F. C. Unterwald, *Phys. Rev.*, **174**, 791 (1968).
[16] G.H. Haertling, *J. Am. Ceram. Soc.*, **82**, 797 (1999)
[17] A. J. Moulson and J. M. Herbert, Electroceramics: Materials, Properties Applications, *Wiley* (2003).
[18] http://xrayweb.chem.ou.edu/notes/symmetry.html
[19] A.L. Kholkin, N.A. Pertzev, and A.V. Goltsev, "Piezoelectricity and Crystal Symmetry", *Springer* (2008).
[20] T. Ikeda, "Fundamentals of Piezoelectricity", *New York: Oxford University Press* (1990).
[21] D. Damjanovic, *Rep. Prog. Phys.*, **61**, 1267 (1998).
[22] J. F. Nye, "Physical Properties of Crystals", *Oxford: Oxford University Press*. (1985)
[23] B. Jaffe, W.R. Cook Jr. And H. Jaffe, "Piezoelectric Ceramics" *Academic Press London and New York*, 1971.
[24] A. Moulson, and J. Herbert, "Electroceramics Materials, Properties, Applications. 2nd edn." *Wiley & Sons, Inc.* (2003).
[25] M. Srinivasan, *Bull. Mater. Sci.*, **6**, 317 (1984).
[26] E.T. Jaynes, "Ferroelectricity", *Princeton University Press* (1953).
[27] R.C. Vernon, *Am. J. Phy.*, **23**, 183 (1955).
[28] M. Trainer, *Eu.J. Phys*, **21**, 459 (2000).
[29] P. Ghosez and J. Junquera, *arXive:cond-mat*/0605299 (2006).
[30] P. Chandra and P.B. Littlewood, *arXive:cond-mat*/0609347 (2006).
[31] L.D. Landau: *Phys. Z. Sowjun.*, **11**, 26 (1937).
[32] L.D. Landau: *Zh. Eksp. Teor.Fiz.*, **7**, 627 (1937).
[33] D. ter Haar (Ed.): Collected papers of L.D. Landau (Pergamon, Oxford 1965) contains Eng. transl. of [30] and [31].
[34] H. Ehrenreich and F. Spaepen, Solid state physics advances in research and applications, *Academic Press*, San Diego (2001).
[35] A. F. Devonshire, *Phil. Mag. J. Sci.*, **40**, 1040 (1949).
[36] A. F. Devonshire: *Phil. Mag. J. Sci.*, **42**, 1065 (19451).
[37] E. Fatuzzo, W. M. Mertz: Ferroelectricity (North-Holland, Amsterdam 1967).
[38] M. E. Lines and A. M. Glass, "Principles and Applications of Ferroelectrics and Related Materials", *Oxford University Press* (1977).
[39] W. Cochran, *Phys. Rev. Lett.*, **3**, 412 (1959).
[40] R. Blinc, *Ferroelectrics*, **74**, 301 (1987).
[41] C.V. Raman and T.M.K. Nedungadi, *Nature*, **145**, 147 (1940).
[42] L.L. Boyer, R.E. Cohen, H. Krakauer and W.A. Smith, *Ferroelectrics*, **111**, 1 (1990).
[43] M. E. Lines and A. M. Glass, "Principles and Applications of Ferroelectrics and Related Materials", *Cambridge University Press* (1977).
[44] B.K. Mani, R. Herchig, E. Glazkov, S. Lisenkov and I. Ponomareva, *Nanotechnology*, **27**, 195705 (2016).

[45] K.M. Rabe, "Antiferroelectricity in Oxides: A Re-examination", *Wiley* (2013)
[46] C. Kittel, *Phys. Rev.*, **82**, 5 (1951).
[47] B. Wul, *J. Phys. U.S.S.R.*, **10**, 95 (1946).
[48] A.F. Devonshire, *Phil. Mag.*, **40**, 1040 (1949).
[49] J.C. Slater, *Phys. Rev.*, **78**, 748 (1950).
[50] IUPAC, *Compendium of Chemical Terminology*, 2nd ed. (the "Gold Book") (1997). Online corrected version (2006).
[51] A.M. Páez, *J. Chem. Educ.*, **71**, 381 (1994).
[52] S.V. Vonsovsky, Y.A. Izyumov and E.Z. Kurmaev, "Superconductivity of Transition Metals", *Springer* (1982).
[53] J. G. Bednorz, K. A. Müller, *Z.Phys. B*, **64**, 189 (1986).
[54] C.N.R. Rao, *Annu. Rev. Phys. Chem.*, **40**, 291 (1989).
[55] N.P. Novák, "Transition Metal Oxides: Magnetism", *Elsevier* (1996).
[56] K.I. Kugel and D.I. Khomskii, *Soviet Physics Uspekhi,* **25**, 231 (1982).
[57] N. F. Mott, *Proc. Phys. Soc. A*, **62**, 416 (1949).
[58] Y. Tokura and N. Nagosa, *Science*, **288**, 462 (2000).
[59] J. Orenstein and A.J. Millis, *Science*, **288**, 468 (2000).
[60] J. Wu, C. Nan, Y. Lin and Y. Deng, *Phys. Rev. Lett.*, **89**, 217601 (2002).
[61] A. A. Dakhel, *Ceram. Int.,* **39**, 4263 (2013).
[62] S. Thota, J. H. Shim and M. S. Seehra, *J. Appl. Phys.*, **114**, 214307 (2013).
[63] J. Hlinka, D. Nuzhnyy, J. Petzelt, P. Kuzel, C. Kadlec, P. Vanek, I. Ponomareva and L. Bellaiche, *Phys. Rev. Lett.,* **101**, 167402 (2008).
[64] M. L. Volpe and J. Reddy, *J. Chem. Phys.*, **53**, 1117 (1970).
[65] C. C. Homes, T. Vogt, S. M. Sharipo, S. Wakimoto and A. P. Ramirez, *Science*, **293**, 673 (2001).
[66] A.M. Glass, K. Nassau, *J. Appl. Phys.*, **49**, 4808 (1978).
[67] N. Chaiyo, B. Boonchom, N. Vittayakorn, *J. Mater. Sci.*, **45**, 1443 (2010).
[68] A. D. McNaught and A. Wilkinson, IUPAC. Compendium of Chemical Terminology, 2nd ed. (the "Gold Book"), *Blackwell Scientific Publications* (1997).
[69] S.J.L. Kang, "Sintering, Densification, Grain growth & Microstructure", *Elsevier* (2005).
[70] P. Gabbott, "Principles and Applications of Thermal Analysis", *Blackwell Publishing Ltd.* (2008)
[71] W.H. Bragg and W.L. Bragg, "The reflection of X-rays by crystals", *Proceedings of the Royal Society of London. Series A, Containing Papers of a Mathematical and Physical Character* (1913).
[72] P.P. Ewald, "The Principles of X-ray Diffraction", *Springer* (1962).
[73] R.A. Young, *The Rietveld method*, **5**, 1 (1993).
[74] R. A. Young, "The Rietveld Method", *Oxford University Press* (1995).
[75] A. Einstein, *Ann. Physik*, **17**, 132 (1905).
[76] H. Konno, "X-ray Photoelectron Spectroscopy", *Elsevier* (2016).
[77] J. Goldstein, D.E. Newbury, D.C. Joy, C.E. Lyman, P. Echlin, E. Lifshin, L. Sawyer, J.R. Michael, "Scanning Electron Microscopy and X-ray Microanalysis", *Plenum Press* (2003),
[78] Cik Rohaida Che Hak, C.T. Foo, and N.A.F. Othman., Field Emission Scanning Electron Microscope (FESEM) Facility in BTI., (2015).
[79] A. Bogner, P.H. Jouneau, G. Thollet, D. Basset and C. Gauthier, *Micron*, **38**, 390 (2007).
[80] C.V. Raman, *Nature*, 121(3048), 501 (1928).
[81] C.V. Raman, *Nature*, 121(3051), 619 (1928).
[82] J.R. Ferraro, "Introductory Raman Spectroscopy", *Elsevier Science* (2003).
[83] A. Lund, M. Shiotani, S. Shimada, "Principles and Applications of ESR spectroscopy", *Springer Science* (2011).
[84] G.R. Eaton, S.S. Eaton, K.M. Salikhov, "Foundations of Modern EPR", *World Scientific* (1998).
[85] H. Kawaji, "Handbook of Advanced Ceramics 2nd edn.", *Materials, Applications, Processing, and Properties* (2013).
[86] Y. Saito, H. Takao, T. Tani, T. Nonoyama, K. Takatori, T. Homma, T. Nagaya, and M. Nakamura, *Nature*, **432**, 84 (2004).
[87] G. Xing, "Method of dry etching PZT capacitor stack to form high-density ferroelectric memory devices," U.S. patent 6, **492**, 222 (2002).

[88] K. Niwa, Y. Kotaka, M. Tomotani, H. Ashida, Y. Goto, and S. Otani, *Acta. Mater.*, **48**, 4755 (2000).
[89] Z.-Y. Shen, J.-F. Li, R. Chen, Q. Zhou, and K. K. Shung, *J. Am. Ceram. Soc.*, **94**, 1346 (2011).
[5,90] I. Aulika, V. Zauls, K. Kundzins, M. Kundzins, and S. Katholy, *J. Optoelectron. Adv. Mater.*, **5**, 755 (2003), available at https://joam. inoe.ro/arhiva/pdf5_3/Aulika1.pdf.
[91] S. T. Lau, C. Cheng, S. Choy, D. Lin, K. Kwok, and H. L. Chan, *J. Appl. Phys.*, **103**, 104105 (2008).
[92] V. Manglani and A. Agnihotri, *Int. J. Recent Res. Rev.*, **1**, 16 (2012).
[93] M. Saliba, J.P. Correa-Baena, M. Grätzel, A. Hagfeldt and A. Abate, *Angew. Chem. Int. Ed.*, **57**, 2554 (2018).
[94] M. Johnsson and P. Lemmens, *arXive:cond-mat*/0506606 (2005).
[95] V. M. Goldschmidt, Die gesetze der krystallochemie, *Naturwissenschaften*, **14**, 477 (1926).
[96] V. M. Goldschmidt, ‘‘Geochemische Verteilungsgesetze der Elemente. VII: Die Gesetze der Krystallochemie,’’ Skrifter utgitt av det Norske Videnskaps-Akademi I Oslo, Shrifter Norskevidenskop Akad. *I. Matem.-Naturvid. Klasse*, **2**, 5 (1926).
[97] J. Rödel, W. Jo, K. T. Seifert, E. M. Anton, T. Granzow, and D. Damjanovic, Perspective on the development of lead-free piezoceramics, *J. Am. Ceram. Soc.*, **92**, 1153 (2009).
[98] W. Travis, E.N.K. Glover, H. Bronstein, D.O. Scanlon and R.G. Palgrave, *Chem. Sci.*, **7**, 4548 (2016).
[99] V. Shanker, S. Samal, G. Pradhan, C. Narayana, and A. Ganguli, *Solid State Sci.*, **11**, 562 (2009).
[100] E. Valdez, C. B. de Ara ujo, and A. Lipovskii, *Appl. Phys. Lett.*, **89**, 031901 (2006).
[101] E. Hollenstein, M. Davis, D. Damjanovic, and N. Setter, *Appl. Phys. Lett.*, **87**, 182905 (2005).
[102] E. Falcão-Filho, C. Bosco, G. Maciel, L. Acioli, C. B. de Araujo, A. Lipovskii, and D. Tagantsev, *Phys. Rev. B*, **69**, 134204 (2004).
[103] G. Maciel, N. Rakov, C. B. de Araujo, A. Lipovskii, and D. Tagantsev, *Appl. Phys. Lett.*, **79**, 584 (2001).
[104] S. Prosandeev, *Phys. Solid State*, **47**, 2130 (2005).
[105] S. Mishra, N. Choudhury, S. Chaplot, P. Krishna, and R. Mittal, *Phys. Rev. B*, **76**, 024110 (2007).
[106] K. E. Johnston, J. M. Griffin, R. I. Walton, D. M. Dawson, P. Lightfoot, and S. E. Ashbrook, *Phys. Chem. Chem. Phys.*, **13**, 7565 (2011).
[107] J. Koruza, J. Tellier, B. Malicˇ, V. Bobnar, and M. Kosec, *J. Appl. Phys.*, **108**, 113509 (2010).
[108] A. Aydi, S. Chkoundali, H. Khemakhem, A. Simon, and R. Von Der Mühll, *J. Alloys Compd.*, **465**, 222 (2008).
[109] D. Kobertz, M. Müller, and A. Molak, *Calphad*, **48**, 55 (2015).
[110] J. Brous, I. Fankuchen, and E. Banks, *Acta Crystallogr.*, **6**, 67(1953).
[111] E. Almeida, K. C. Jorge, L. d. S. Menezes, C. B. de Araújo, and A. A. Lipovskii, *J. Opt. Soc. Am. B: Opt. Phys.*, **30**, 1284 (2013).
[112] K. Kioka, T. Honma, K. Oh-ishi, S. Reibstein, N. Da, L. Wondraczek, and T. Komatsu, *J. Non-Cryst. Solids*, **358**, 1523 (2012).
[113] J. Lv, T. Kako, Z. Li, Z. Zou, and J. Ye, *J. Phys. Chem. C*, **114**, 6157 (2010).
[114] I. Raevski, S. Prosandeev, K. Abdulvakhidov, L. Shilkina, S. Raevskaya, V. Eremkin, V. Smotrakov, and L. Jastrabik, *J. Appl. Phys.*, **95**, 3994 (2004).
[115] I. Raevski, S. Raevskaya, S. Prosandeev, V. Shuvaeva, A. Glazer, and M. Prosandeeva, *J. Phys.: Condens. Matter*, **16**, L221 (2004).
[116] A. Burkhanov, P. Bondarenko, S. Raevskaya, A. Shil’nikov, and I. Raevskaya, *Phys. Solid State*, **48**, 1114 (2006).
[117] V. Titov, V. Shuvaeva, S. Raevskaya, A. Semenchev, A. Glazer, S. Shevtsova, I. Raevski, and M. Malitskaya, *Ferroelectrics*, **374**, 58 (2008).
[118] Y.-J. Hsiao, Y.-H. Chang, T.-H. Fang, Y.-S. Chang, and Y.-L. Chai, *J. Alloys Compd.*, **430**, 313 (2007).
[119] X.-g. Zhao, P. Liu, Y.-C. Song, A.-p. Zhang, X.-m. Chen, and J.-p. Zhou, *Phys. Chem. Chem. Phys.*, **17**, 23132 (2015).
[120] F. Li, B. Shang, P. Liang, L. Wei, and Z. Yang, *J. Electron. Mater.*, **45**, 5178 (2016).
[121] D. Joshi, S. Thota, S. Nayak, D. Harish, P. Mahesh, A. Kumar, D. Pamu, and M. Qureshi, *J. Phys. D: Appl. Phys.*, **47**, 435305 (2014).
[122] S. Mukherjee, S. Chatterjee, S. Rayaprol, S. Kaushik, S. Bhattacharya, and P. Jana, *J. Appl. Phys.*, **119**, 134103 (2016).
[123] D. Joshi, S. Nayak, A. Kumar, A. Mohanta, D. Pamu, and S. Thota, *J. Appl. Phys.*, **119**, 074303 (2016).

[124] A. Molak, K. Szot, A. Kania, J. Friedrich, and H. Penkalla, *Phase Trans.*, **81**, 977 (2008).
[125] J. Wu, C.-W. Nan, Y. Lin, and Y. Deng, *Phys. Rev. Lett.*, **89**, 217601 (2002).
[126] S. Mandal, S. Pal, A. K. Kundu, K. S. Menon, A. Hazarika, M. Rioult, and R. Belkhou, *Appl. Phys. Lett.*, **109**, 092906 (2016).
[127] J. Li, F. Li, X. Zhu, D. Lin, Q. Li, W. Liu, and Z. Xu, *J. Alloys Compd.*, **692**, 375 (2017).
[128] W. Tuichai, S. Danwittayakul, S. Maensiri, and P. Thongbai, *RSC Adv.*, **6**, 5582 (2016).
[129] E. Erünal, P. Jakes, S. Körbel, J. Acker, H. Kungl, C. Elsässer, M. J. Hoffmann, and R.A. Eichel, *Phys. Rev. B*, **84**, 184113 (2011).
[130] S. Lanfredi, M. Lente, and J. Eiras, *Appl. Phys. Lett.*, **80**, 2731 (2002).
[131] G. Shirane, R. Newnham, and R. Pepinsky, *Phys. Rev.*, **96**, 581 (1954).
[132] Y. Shiratori, A. Magrez, W. Fischer, C. Pithan, and R. Waser, *J. Phys. Chem. C*, **111**, 18493 (2007).
[133] S. Gupta, S. Huband, D. S. Keeble, D. Walker, P. Thomas, D. Viehland, and S. Priya, *CrystEngComm*, **15**, 6790 (2013).
[134] F. Fresno, P. Jana, P. Reñones, J. Coronado, D. Serrano, and V. de la Peña O'Shea, *Photochem. Photobiol. Sci.*, **16**, 17 (2017).
[135] Y. Zhen and J.-F. Li, *J. Am. Ceram. Soc.*, **89**, 3669 (2006).
[136] B. Noheda, D. Cox, G. Shirane, J. Gonzalo, L. Cross, and S. Park, *Appl. Phys. Lett.*, **74**, 2059 (1999).
[137] A. Mohanta and R. Thareja, *J. Appl. Phys.*, **103**, 024901 (2008).
[138] H. S. Kang, J. W. Kim, J. H. Kim, S. Y. Lee, Y. Li, J.-S. Lee, J.-K. Lee, M. Nastasi, S. Crooker, and Q. Jia, *J. Appl. Phys.*, **99**, 066113 (2006).
[139] P. Dutta, M. Seehra, S. Thota, and J. Kumar, *J. Phys.: Condens. Matter*, **20**, 015218 (2007).
[140] S. Thota and J. Kumar, *J. Phys. Chem. Solids*, **68**, 1951 (2007).
[141] D. Joshi, P. Pramanik, S. Nayak, K. Dasari, R. Choudhary, and S. Thota, *J. Phys. D: Appl. Phys.*, **50**, 325002 (2017).
[142] K. Barick, M. Aslam, V. P. Dravid, and D. Bahadur, *J. Colloid Interface Sci.*, **349**, 19 (2010).
[143] F. Hai-Bo, Y. Shao-Yan, Z. Pan-Feng, W. Hong-Yuan, L. Xiang-Lin, J. Chun-Mei, Z. Qin-Sheng, C. Yong-Hai, and W. Zhan-Guo, *Chin. Phys. Lett.*, **24**, 2108 (2007).
[144] D. Briggs, "XPS: Basic principles, spectral features and qualitative analysis in Surface Analysis by Auger and X-Ray Photoelectron Spectroscopy", *IM Publications and SurfaceSpectra Limited* (2003).
[145] D. Joshi, S. Nayak, P. Suresh, K. Suresh, B. Kumar, and S. Thota, *Phys. Status Solidi B*, **252**, 2323 (2015).
[146] M. Kruczek, E. Talik, and A. Kania, *Solid State Commun.*, **137**, 469 (2006).
[147] A. Sakowski-Cowley, K. Łukaszewicz, and H. D. Megaw, Acta Crystallogr., Sect. B, **25**, 851 (1969).
[148] E. Ksepko, E. Talik, A. Ratuszna, A. Molak, Z. Ujma, and I. Gruszka, *J. Alloys Compd.*, **386**, 35 (2005).
[149] J. Mohapatra, D. Mishra, S. Kamilla, V. Medicherla, D. Phase, V. Berma, and S. Singh, *Phys. Status Solidi B*, **248**, 1352 (2011).
[150] F. Zhang, Z. Wu, B. Sun, G. Li, and W. Zhang, *APL Mater.*, **3**, 104501 (2015).
[151] K. Gaskell, A. Starace, and M. Langell, *J. Phys. Chem. C*, **111**, 13912 (2007).
[152] D. Watanabe, J. Castles, A. Jostsons, and A. Malin, *Acta Crystallogr.*, **23**, 307 (1967).
[153] J. Gautier, E. Trollund, E. Ríos, P. Nkeng, and G. Poillerat, *J. Electroanal. Chem.*, **428**, 47 (1997).
[154] G. Tyuliev, D. Panayotov, I. Avramova, D. Stoichev, and T. Marinova, *Mater. Sci. Eng. C*, **23**, 117 (2003).
[155] T. Chuang, C. Brundle, and D. Rice, *Surf. Sci.*, **59**, 413 (1976).
[156] I. Raevskii, L. Reznichenko, V. Smotrakov, V. Eremkin, M. Malitskaya, E. Kuznetsova, and L. Shilkina, *Tech. Phys. Lett.*, **26**, 744 (2000).
[157] I. Raevski and S. Prosandeev, *J. Phys. Chem. Solids*, **63**, 1939 (2002).
[158] R. Soni, R. T. George, D. C. Joshi, S. Nayak, P. Pramanik, S. Pittala, T. A. Dar, and S. Thota, *J. Phys. D: Appl. Phys.*, **50**, 415305 (2017).
[159] I. Chang, *Phys. Rev. B*, **14**, 4318 (1976).
[160] L. Landau, "Course of Theoretical Physics", *Pergamon Press* (1958).
[161] A.K. Jonscher, *Nature*, **267**, 673 (1977).
[162] J.L. Ndeugueu and M. Aniya, *J. Phys. Soc. Jpn.*, **79**, 72 (2010).
[163] K. Funke, *Solid State Ionics*, **94**, 27 (1997).
[164] A. Jonscher, *J. Mater. Sci.*, **13**, 553 (1978).
[165] A. K. Jonscher, *Nature*, **267**, 673 (1977).

[166] Y.-J. Hsiao, Y.-S. Chang, T.-H. Fang, Y.-L. Chai, C.-Y. Chung, and Y.-H. Chang, *J. Phys. D: Appl. Phys.*, **40**, 863 (2007).
[167] J. R. Macdonald, *J. Appl. Phys.*, **58**, 1971 (1985).
[168] A. K. Jonscher, *IEEE Trans. Electr. Insul.*, **27**, 407 (1992).
[169] S. Kumar and K. Varma, *Curr. Appl. Phys.*, **11**, 203 (2011).
[170] K. Funke, *Prog. Solid State Chem.*, **22**, 111 (1993).
[171] D. Almond, A. West, and R. Grant, *Solid State Commun.*, **44**, 1277 (1982).
[172] S. Sumi, P. P. Rao, M. Deepa, and P. Koshy, *J. Appl. Phys.*, **108**, 063718 (2010).
[173] C. Darlington and K. Knight, *Phys. B: Condens. Matter*, **266**, 368 (1999).
[174] G. A. Smolenskii, V. A. Bokov, V. A. Isupov, N. N. Krainik, R. E. Pasynkov, and A. I. Sokolov, "Ferroelectrics and Related Materials", *Gordon & Breach Sci. Publishers* (1984).
[175] C. Homes, T. Vogt, S. Shapiro, S. Wakimoto, and A. Ramirez, *Science*, **293**, 673 (2001).
[176] J. Macutkevic, A. Molak, and J. Banys, *Ferroelectrics*, **479**, 48 (2015).
[177] I. Tomeno, Y. Tsunoda, K. Oka, M. Matsuura, and M. Nishi, *Phys. Rev. B*, **80**, 104101 (2009).
[179] J.T. Devreese, *arXive:cond-mat/0004497*.
[180] H. Fröhlich, *Adv. Phys.*, **3**, 325 (1954).
[181] J. Yamashita and T. Kurosawa, *J. Phys. Chem. Solids*, **5**, 34 (1958).
[182] A.J. Bosman and H.J. van Daal, *Adv. Phys.*, **19**, 1 (1970).
[183] L. Friedman and T. Holstein, *Ann. Phys.*, **21**, 494 (1963).
[184] D. Emin and T. Holstein, *Ann. Phys.*, **53**, 439 (1969).
[185] N.F. Mott, *Philos. Mag.*, **19**, 835 (1969).
[186] R. Hill, *Phys. Status Solidi A*, **34**, 601 (1976).
[187] N. Mott, The Philosophical Magazine, **19**, 835 (1969).
[188] D. Yu, C. Wang, B. L. Wehrenberg, and P. Guyot-Sionnest, *Phys. Rev. Lett.*, **92**, 216802 (2004).
[189] H.D. Megaw, *Ferroelectrics* **7**, 87 (1974).
[190] V. Lingwal and N. Panwar, *J.Appl. Phys.*, **94**, 4571 (2003).
[191] Y. Guo, K.I. Kakimoto and H. Ohsato, *Mater. Lett.*, **59**, 241 (2005).
[192] T. Arioka, H. Taniguchi, M. Itoh, K. Oka, R. Wang and D. Fu, *Ferroelectrics*, **401**, 51 (2010).
[193] A. Chauhan, S. Patel and R. Vaish, *Appl. Phys. Lett.*, **106**, 172901 (2015).
[194] C. Darlington and H.D. Megaw, *Acta Cryst. B*, **29**, 2171 (1973).
[195] P. Seidel and W. Hoffmann, *Z. Kristallogr. Cryst. Mater.*, **143**, 444 (1976).
[196] S. Solov'ev, Y.N. Venevtsev and G. Zhanov, *Sov. Phys. Crystallogr.*, **6**, 171 (1961).
[197] C. Darlington and K. Knight, *Acta Crystallogr. Sec. B*, **55**, 24 (1999).
[198] E. Bouziane, M. Fontana and M. Ayadi, *J. Phys. Condens. Matter*, **15**, 1387 (2003).
[199] R.T. George, D.C. Joshi, S. Nayak, N. Tiwari, R. Chauhan, P. Pramanik, T.A. Dar, S. Ghosh and S. Thota, *J. Appl. Phys.*, **123**, 054101 (2018).
[200] A. Kania and J. Kwapulinski, *J. Phys. Condens. Matter*, **11**, 8933 (1999).
[201] Z. Shen, X. Wang, M. Kuok and S. Tang, *J. Raman Spectrosc.*, **29**, 379 (1998).
[202] L. Pardo, P. Duran-Martin, J. Mercurio, L. Nibou and B. Jimenez, *J. Physics and Chemistry of Solids*, **58**, 1335 (1997).
[203] L. Gao, H. Guo, S. Zhang and C. A. Randall, *J. Appl. Phys.*, **120**, 204102 (2016).
[204] S. Thota, J. Shim and M. Seehra, *J. Appl. Phys.*, **114**, 214307 (2013).
[205] J. Chen and D. Feng, *Phys. Status Solidi A*, **109**, 427 (1988).
[206] I. Raevskii, L. Reznichenko, V. Smotrakov, V. Eremkin, M. Malitskaya and E. Kuznetsova, *Ferroelectrics* **265** 129 (2002).
[207] S. Raevskaya, L. Reznitchenko, A. Semenchev, S. Lisitsina, V. Smotrakov, V. Eremkin and E. Dul'kin, *Ferroelectrics* **307**, 227 (2004).
[208] A. Molak, *Solid State Commun.*, **62**, 413 (2004).
[209] M.A.L. Nobre, E. Longo, E. Leite and J.A. Varela, *Mater. Lett.*, **28**, 210 (1996).
[210] Y. Lu, T. Karaki and T. Fujii, *Ceram. Int.*, **41**, S174 (2015).
[211] Q. Gu, K. Zhu, J. Liu, P. Liu, Y. Cao and J. Qiu, *RSC Adv.*, **4**, 15104 (2014).
[212] W. Liu, H. Wang and K. Li, *J. Sol–Gel Sci. Technol.*, **55**, 229 (2014).
[213] S. Pogatscher, D. Leutenegger, J. Schawe, P.J. Uggowitzer and J.F. Löffler, *Nat. Commun.*, **7**, 11113

(2016).
[214] A. Molak, *J. Phys.: Condens. Matter*, **9**, 11263 (1997).
[215] G. Srinivasan, *Phys. Rev. B*, **28**, 1 (1983).
[216] A.J. Sievers, III and M. Tinkham, *Phys. Rev.*, **129**, 1566（1963).
[217] M.T. Hutchings and E. Samuelsen, *Phys. Rev. B*, **6**, 3447 (1972).
[218] R. Lima, P. Freire, J. Sasaki, A. Ayala, F. Melo, F.J. Mendes, K. Serra, S. Lanfredi, M. Lente and J. Eiras, *J. Raman Spectrosc.*, **33**, 669 (2002).
[219] K. Mishra, V. Sivasubramanian and A. Arora, *J. Raman Spectrosc.*, **42**, 517 (2011).
[220] N. Mironova-Ulmane, A. Kuzmin, I. Steins, J. Grabis, I. Sildos and M. Pärs, *Journal of Physics: Conference Series*, **93**, p012039 (2007).
[221] S. Lin, D. Chiang, Y. Chen, C. Peng, H. Liu, J. Mei, W. Tse, T.R. Tsai and H.P. Chiang, *Journal of Raman Spectroscopy*, **37**, 1442 (2006).
[222] D. Lockwood, M. Cottam and J. Baskey, *J. Magn. Magn. Mater.,* **104**, 1053 (1992).
[223] P. Gielisse, J. Plendl, L. Mansur, R. Marshall, S. Mitra, R. Mykolajewycz and A. Smakula, *J. Appl. Phys.*, **36**, 2446 (1965).
[224] R. Dietz, G. Parisot and A. Meixner, *Phys. Rev. B,* **4**, 2302 (1971).
[225] C. Perry, E. Anastassakis and J. Sokoloff, *Phys. Rev.*, **114**, 1507 (1971).
[226] R. Newman and R. Chrenko, *Phys. Rev.*, **114**, 1507 (1959).
[227] K.I. Kakimoto, I. Masuda, and H. Ohsato, *Jpn. J. Appl. Phys*, **42**, 6102 (2003).
[228] A. Nazeri-Eshghi, A.X. Kuang, and J.D. Mackenzie, *J. Mater. Sci.*, **25**, 3333 (1990).
[229] M. Matsubara, T. Yamaguchi, K. Kikuta, and S. Hirano, *Jpn. J. Appl. Phys.*, **43**, 7159 (2004).
[230] K.I. Kakimoto, I. Masuda and H. Ohsato, *Jpn. J. Appl. Phys.*, **43**, 6706 (2004).
[231] J.H. Choi, J.S. Kim, S.B. Hong, K.W. Chae, and C.I. Cheon, *J. Korean Phys.*, **61**, 956 (2012).
[232] D.H. Kim, M.R. Joung, I.T. Seo, J. Hur, J.H. Kim, B.Y. Kim, H.J. Lee, and S. Nahm, *J. Eur. Ceram. Soc.*, **34**, 4193 (2014).
[233] X. Fan, D. Lin, Q. Zheng, H. Sun, Y. Wan, X. Wu, L. Wu, *Phys. Status Solidi A*, **209**, 2610 (2012).
[234] H.E. Mgbemere, R.P. Herber, G.A. Schneider, *J. Eur. Ceram. Soc.*, **29**, 1729 (2009).
[235] A. Molak, *J. Phys. Condens. Matter*, **13**, 9561 (2001).
[236] A. Molak and J. Pichet, *Acta. Phys. Polon*, **A66**, 251 (1984).
[237] R. Saravanan, D. Rajesh, S.V. Rajashekaran, R. Perumal, M. Chitra and R. Jayavel, *Int. J. Appl. Phys. Math.,* **2**, 3 (2012).
[238] Y. Inagaki and K. Kakimoto, *Appl. Phys. Exp*., **1**, 061602 (2008).
[239] Y. Kizaki, Y. Noguchi and M. Miyayama, *Appl. Phys. Lett.*, **89**, 142910 (2006).
[240] J.P. Zheng, T.R. Jow, *J. Electrochem. Soc.*, **142**, L6 (1995).
[241] H. Wang, Z. Li, J. Yang, Q. Li and X. Zhong, *J. Power Sources*, **194**, 1218 (2009).
[242] Pasero D., Reeves N and West A.R., *J. Power Sources*, **141**, 156 (2005).
[243] E. Saputra, H. Zhang, Q. Liu, H. Sun, S. Wang, *Appl. Catal. B: Environmental*, **142**, 729 (2013).
[244] X. Lin, Z-F. Li and L-F. Shu, *J. Ceram. Sci. Technol.*, **08**, 209 (2017).
[245] F.E. Sesen, *J. Chem. Tech. App.*, **1**, 1 (2017).
[246] G.K Willaimson and W.H. Hall, *Acta. Metall. Mater.*, **1**, 22 (1953).
[247] V. Biju, N. Sugathan, *J. Mater. Sci*., **43**, 1175 (2008).
[248] A. K. Zak, W.H.A. Majid, M.A. Abhrishami and R. Yousefi, *Solid State Sci.*, **13**, 251 (2011).
[249] G.S. Parks and W.K. Nelson, *J. Phys. Chem.*, **32**, 61 (1928).
[250] R. Hahn and K. Tempel, *HiTEN*, **2015**, 000142 (2015).
[251] J. Marugán, J.A. Botas, M. Martín, R. Molina and C. Herradón, *Int. J. Hydrog. Energy*, **37**, 7017 (2012).
[252] R.T. George, T.A. Dar, D.C. Joshi, V. Sathe, A.K. Rathore and S. Thota, *J. Phys. D: Appl. Phys.*, **52**, 115301 (2019).
[253] V. Berbenni and A. Marini, *Mater. Res. Bull.*, **38**, 1859 (2003).
[254] W. Feitknecht, *Pure Appl. Chem.*, **9**, 423 (1964).
[255] M. Iwamoto, Springer, *Encyclopedia of Nanotechnology*, 1276 (2012).
[256] V. Ambegaokar, B.I. Halperin and J.S. Langer, *Phys. Rev. B*, **4**, 2612 (1971).
[257] G.R. Burns, *J. Phys. Chem. Solids*, **47**, 681 (1986).
[258] K. Nagata, T. Ishikawa and Y. Miyamoto, *Jpn. J. Appl. Phys.*, **22**, 1129 (1983).
[259] S. Wada, A. Seike, and T. Tsurumi, *Jpn. J. Appl. Phys.,* **40**, 5690 (2001).

[260] K. Nakamura, T. Tokiwa, and Y. Kawamura, *J. Appl. Phys.*, **91**, 9272 (2002).
[261] M. Adachi, Y. Akishige, T. Asahi, K. Deguchi, K. Gesi, K. Hasebe, T. Hikita, T. Ikeda, Y. Iwata, M. Komukae, *Springer*, **36A1**, 1 (2001).
[262] R. Ganeshkumar, K.V. Sopiha, P. Wu, C.W. Cheah, and R. Zhao, *Nanotechnology*, **27**, 395607 (2016).
[263] M. Ishikawa, Y. Kadota, N. Takiguchi, H. Hosaka, and T. Morita, *Jpn. J. Appl. Phys.*, **47**, 7673 (2008).
[264] T. Zhang, W. Lei, P. Liu, J.A. Rodriguez, J. Yu, Y. Qi, G. Liu, and M. Liu, *J. Phys. Chem.*, **120**, 2777 (2016).
[265] X. Lu, H. Zhang, L. Zheng, W. Cao, *AIP Adavnces*, **6**, 105208 (2016).
[266] M. Schmidbauer, D. Braun, T. Markurt, M. Hanke, J. Schwarzkopf, *Nanotechnology*, **28**, 24LT02 (2017).
[267] X.Q. Ke, D. Wang, X. Ren, Y. Wang, *Phys. Rev. B*, **88**, 214105 (2013).
[268] T. Yoshida, H. Nagata, and T. Takenaka, *Key Engineering Materials*, **301**, 19 (2006).
[269] K.I. Kakimoto, I. Masuda, and H. Ohsato, *J. Eur. Ceram. Soc.*, **25**, 2719 (2005).
[270] X. Lv, Z. Li, J. Wu, D. Xiao, and J. Zhu, *ACS Appl. Mater. Interfaces*, **8**, 30304 (2016).
[271] K.V. Rao and A. Smakula, *J. Appl. Phys.*, **36**, 2031 (1965).
[272] N.F. Mott and L. Friedman, *Philos. Mag.*, **30**, 389 (1974).
[273] J.H. de Boer and E.J.W. Verwey, *Proc. Phys. Soc.*, **49**, 59 (1937).
[274] Y. Lin, L. Jiang, R. Zhao, and C. Nan, *Phys. Rev. B*, **72**, 014103 (2005).
[275] B. Gokul, P. Matheswaran, K.M. Abhirami and R. Sathyamoorthy, *J. Non. Cryst. Solids*, **363**, 161 (2013).
[276] S. Kabashima and T. Kawakubo, *J. Phys. Soc. Japan*, **24**, 493 (1968).
[277] T. Asanuma, T. Matsutani, C. Liu, T. Mihara, and M. Kiuchi, *J. Appl. Phys.*, **95**, 6011 (2015).
[278] V.A. Shuvaeva, K. Yanagi, Y. Kenichiro, S. Kiyoshi, and T. Hikaru, *Solid State Commun.*, **106**, 335 (1998).
[279] F. Jona, G. Shirane, "Ferroelectric Crystals", *Dover Publications* (1962).
[280] F. Rubio-Marcos, R. L´opez-Ju´arez, R.E. Rojas-Hernandez, A.D. Campo, N. Razo-P´erez, J.F. Fernandez, *Appl. Mater. Interfaces* **7**, 23080 (2015).
[281] T. Fukuda, H. Hirano, Y. Uematsu, and T. Ito, *Jpn. J. Appl. Phys.*, **13**, 1021 (1974).
[282] L. Liang, Y.L. Li, L.Q. Chen, S.Y. Hu, and G.H. Lu, *J. Appl. Phys.*, **106**, 104118 (2009).
[283] L. Luisman, A. Feteira, and K. Reichmann, *Appl. Phys. Lett.*, **99**, 1 (2011).
[284] V.V. Laguta, M.D. Glinchuk, I. Kondakova, *Phys. Solid State.*, **46**, 1262 (2004).
[285] D. Viehland, S.J. Jang, L.E. Cross, M. Wuttig, *Phys. Rev. B*, **46**, 8003 (1992).
[286] D. Viehland, S.J. Jang, L.E. Cross, M. Wuttig, *J. Appl. Phys.*, **68**, 2916 (1990).
[287] H. Shim, A. Manivannan, M.S. Seehra, K.M. Reddy, A. Punnoose, *J. Appl. Phys.*, **99**, 08Q503 (2006).
[288] A.P. Ramirez, M.A. Subramanian, M. Gardel, G. Blumberg, D. Li, T. Vogt, S.M. Shapiro, *Solid State Commun.*, **115**, 217 (2000).
[289] E. Buixaderas, V. Bovtun, M. Kempa, M. Savinov, D. Nuzhnyy, F. Kadlec, P. Vank, J. Petzelt, M. Eriksson, Z. Shen, *J. Appl. Phys.*, **107**, 014111 (2010).
[290] E. Buixaderas, D. Nuzhnyy, I. Gregora, S. Kamba, M. Berta, B. Mali, and M. Kosec, *IEEE Transactions on Ultrasonics, Ferroelectrics, And Frequency Control*, **9**, 1843 (2009).
[291] T.R. Shrout and J. Fielding, *IEEE Symp. Ultrason.*, **711**, (1990).
[292] K. Uchino and S. Nomura, *Ferroelectrics*, **44**, 55 (1982).
[293] M. Trainer, *Ferroelectrics and the Curie Weiss law*, **21**, 459 (2000).
[294] J.G. Hyun, S. Lee, S.D. Cho, K.W. Paik, *Proc. Electronic Components and Technology Conf. Proceedings.*, **31**, 1241 (2005).
[295] G. Burns, *Phys. Rev. B*, **13**, 215 (1976).
[296] A.A. Bokov, Y.H. Bing, W. Chen, Z.G. Ye, S.A. Bogatina, I.P. Raevski, S.I. Raevskaya, E.V. Sahkar, *Phys. Rev. B*, **68**, 052102 (2003).
[297] M. Tadic, D. Nikolic, M. Panjan, G.R. Blake, *J. Alloys Compd.*, **647**, 1061 (2015).
[298] D.C. Joshi, K. Dasari, S. Nayak, R. Palai, P. Suresh, S. Thota, *J. Electron. Mater.*, **45**, 2059 (2016).
[299] P. Mahesh, S. Thota, D. Pamu, *IEEE Trans. Dielectr. Electr. Insul.*, **22**, 3668 (2015).
[300] I. Rawal, A. Kaur, *J. Appl. Phys.*, **115**, 043717 (2014).
[301] S. Upadhyay, O. Parkash, D. Kumar, *J. Alloys Compd.*, **432**, 258 (2007).
[302] A.S. Ioselevich and V.V. Sivak, *Phys. Rev. B*, **95**, 214205 (2017).
[303] M.A. Dinno, M. Schwartz, B. Giammara, *J. Appl. Phys.*, **45**, 3328 (1974).
[304] K. Funke, *Solid State Ionics*, **28**, 100 (1988).
[305] A. Qureshi, A. Altindal, A. Mergen, *Sens. Actuators. B Chem.*, **138**, 71 (2009).

[306] D.K. Pradhan, R.N. Choudhary, B.K. Samantaray, *Int. J. Electrochem. Sci.*, **3**, 597 (2008).
[307] A. Osak, J. Piwowarczyk, *Czasopismo Techniczne. Nauki Podstawowe,* **108**, 59 (2011).
[308] D.P. Almond, C.R. Bowen, *Phys. Rev. Lett.*, **92**, 157601 (2004).
[309] B. Sundarakannan, K. Kakimoto, H. Ohsato, *J. Appl. Phys.*, **94**, 5182 (2003).
[310] Z.X. Shen, Z.P. Hu, T.C. Chong, C.Y. Beh, S.H. Tang, M.H. Kuok, *Phys. Rev. B.*, **52** 3976 (1995).
[311] K.I. Kakimoto, K. Akao, Y. Guo, H. Ohsato, *Jpn. J. Appl. Phys.*, **44**, 7064 (2005).
[312] Z. Wang, H. Gu, Y. Hu, K. Yang, M. Hu, D. Zhou, J. Guan, *Cryst Eng Comm.*, **12**, 3157 (2010).
[313] S. Sun, Y. Ge, Y. Zhao, X. Yuan, Y. Zhao, H. Zhou, *RSC Advances*, **6**, 113038 (2016).
[314] R.E. Dietz, W.F. Brinkman, A.E. Meixner, H.J. Guggenheim, *Phys. Rev. Lett.*, **27** 814 (1971).
[315] Y. Zhang, J. Hao, C.L. Mak, X. Wei, *Optics express.*, **19**, 1824 (2011).